

# **Seismic Response and Reliability of Electrical Substation Equipment and Systems**

**Junho Song**

**Armen Der Kiureghian**

**Jerome L. Sackman**

Structural Engineering, Mechanics & Materials  
Department of Civil & Environmental Engineering  
University of California, Berkeley  
Berkeley, California 94720

A report to sponsor  
Pacific Gas & Electric Co.  
San Francisco, California

Report No. PEER **???? /??**  
Pacific Earthquake Engineering Research Center  
College of Engineering  
University of California  
Berkeley, California

**????** 2004



## ABSTRACT

Continued operation of critical lifelines after a major earthquake is essential for reduction of losses, timely delivery of emergency services, and post-earthquake recovery. An important element within the power transmission lifeline is the electrical substation, which serves to transform the power voltage for distribution in local grids. The electrical substation typically consists of a complex set of equipment items that are interconnected through either assemblies of rigid bus and flexible connectors or flexible cable conductors.

Estimating the seismic response and reliability of an electrical substation is a challenging task because: (1) Connected equipment items cannot be analyzed individually due to the presence of dynamic interaction between them; (2) the connecting elements (either rigid-bus-flexible-connector or flexible cable conductor) behave nonlinearly; (3) the earthquake ground motion is stochastic in nature; and (4) the substation is a complex system subjected to a stochastic loading, whose reliability cannot be directly deduced from the marginal reliabilities of its components. This report aims at developing analytical models and methods for assessing the seismic response of electrical substation equipment connected by assemblies of rigid bus and flexible connectors, and the reliability of electrical substation systems subjected to stochastic earthquake loading. A parallel aim is to develop practical guidelines for design of connected equipment items to reduce the adverse effect of dynamic interaction under earthquake loading. Attention is also given to developing systematic methods for identifying critical components and cut sets within the electrical substation system.

An electrical substation equipment item is idealized as a single-degree-of-freedom oscillator by describing its deformation in terms of an assumed displacement shape function. The validity and accuracy of this idealization for interaction studies is examined for an example pair of connected equipment items. The hysteretic behaviors of several rigid bus connectors are described by differential equation models fitted to experimental data or to hysteresis loops predicted by detailed finite element analysis. Efficient nonlinear time history and random vibration analysis methods are developed for determining the seismic response of the connected equipment items. Based on the developed analytical models and methods, the effect of interaction in the connected equipment system is investigated through extensive parametric studies. The results lead to practical guidelines for the seismic design of interconnected electrical substation equip-

ment.

In order to estimate the seismic reliability of the electrical substation system, linear programming is used to compute bounds on the system reliability in terms of information on marginal- and joint-component failure probabilities. This methodology is also used to systematically identify critical components and cut sets within the electrical substation system. Finally, to apply this methodology to the electrical substation system under stochastic earthquake loading, new formulations and results are developed for the joint first-passage probability of a vector process. Example applications are used throughout the report to demonstrate the newly developed models and methods.

## **ACKNOWLEDGMENTS**

This research is supported by the Lifelines Program of the Pacific Earthquake Engineering Research Center funded by the Pacific Gas & Electric Co. and the California Energy Commission. Partial support was also provided by the Earthquake Engineering Research Centers Program of the National Science Foundation under Award No. EEC-9701568. These supports are gratefully acknowledged. The authors wish to thank Eric Fujisaki of PG&E for valuable support during the course of this study.



# TABLE OF CONTENTS

<b>Abstract</b> .....	<b>iii</b>
<b>Acknowledgments</b> .....	<b>v</b>
<b>Table of Contents</b> .....	<b>vii</b>
<b>List of Figures</b> .....	<b>xi</b>
<b>List of Tables</b> .....	<b>xvii</b>
<b>1 Introduction</b> .....	<b>1</b>
1.1 Motivation .....	1
1.2 Objectives and Scope .....	2
1.3 Organization .....	4
<b>2 Single-Degree-of-Freedom Idealization of Electrical Equipment</b> .....	<b>7</b>
2.1 Introduction .....	7
2.2 Modeling of Connected Equipment Items Using SDOF Idealization .....	8
2.3 Accuracy of SDOF Models in Interaction Studies .....	11
2.3.1 The Example System .....	11
2.3.2 Results .....	13
<b>3 Analytical Modeling and New Design for Rigid Bus Connectors</b> .....	<b>31</b>
3.1 Introduction .....	31
3.2 Generalized Bouc-Wen Hysteresis Model for Rigid Bus - Flexible Strap Connectors .....	32
3.3 Bi-linear Hysteresis Model for Slider Connector .....	38
3.4 Development and Analytical Modeling of S-FSC .....	41
3.4.1 Development of S-FSC .....	41

3.4.2	Bouc-Wen Hysteresis Model for <i>S</i> -FSC .....	45
<b>4</b>	<b>Seismic Response of Equipment Items Connected by Rigid Bus Conductors .....</b>	<b>67</b>
4.1	Introduction .....	67
4.2	Dynamic Analysis of Equipment Items Connected by Rigid Bus Conductors .....	67
4.3	Evaluation of Analytical Models for Connected Equipment System .....	70
4.3.1	Generalized Bouc-Wen Model for RB-FSC .....	70
4.3.2	Bi-linear Model for SC .....	72
4.3.3	Bouc-Wen Model for <i>S</i> -FSC .....	73
4.4	Nonlinear Random Vibration Analysis of Connected Equipment by the Equivalent Linearization Method .....	74
4.5	Application of ELM to Investigation of Interaction Effect in Equipment Items Connected by Rigid Bus .....	77
4.5.1	Generalized Bouc-Wen Model for RB-FSC .....	78
4.5.2	Bi-linear Model for SC .....	83
4.5.3	Bouc-Wen Model for <i>S</i> -FSC .....	85
<b>5</b>	<b>Effect of Interaction on Connected Electrical Equipment .....</b>	<b>105</b>
5.1	Introduction .....	105
5.2	Effect of Interaction in Linearly Connected Equipment Items .....	106
5.3	Effect of Interaction in Equipment Items Connected by Nonlinear Rigid Bus Conductors .....	110
5.4	Design Guidelines .....	113
5.4.1	Characterization of Equipment Items as SDOF Oscillators .....	114
5.4.2	Modeling of the Rigid-Bus Connector .....	114
5.4.3	Characterization of Input Ground Motion .....	114
5.4.4	Evaluation of the Effect of Interaction on the Higher-Frequency Equipment .....	115



5.4.5	Reducing the Effect of Interaction on the Higher-Frequency Equipment Item .....	116
<b>6</b>	<b>Reliability of Electrical Substation Systems .....</b>	<b>131</b>
6.1	Introduction .....	131
6.2	Bounds on System Reliability by Linear Programming .....	132
6.2.1	Formulation and Estimation of System Reliability .....	133
6.2.2	Bounds on System Reliability by Linear Programming .....	137
6.3	Application to Electrical Substation Systems .....	142
6.3.1	Single-Transmission-Line Substation .....	144
6.3.2	Single-Transmission-Line with a Parallel Sub-system of Circuit Breakers .....	146
6.3.3	Two-Transmission-Line Substation .....	147
6.4	Identification of Critical Components and Cut Sets .....	148
6.4.1	Importance Measures by LP Bounds .....	149
6.4.1.1	Fussell-Vesely Importance Measure .....	150
6.4.1.2	Risk Achievement Worth .....	151
6.4.1.3	Risk Reduction Worth .....	153
6.4.1.4	Boundary Probability .....	154
6.4.1.5	Fussell-Vesely Cut-set Importance Measure .....	155
6.4.2	Applications to Electrical Substation Systems .....	155
<b>7</b>	<b>First-Passage Probability of Systems and Applications to Electrical Substations .....</b>	<b>163</b>
7.1	Introduction .....	163
7.2	Marginal First-Passage Probability .....	164
7.3	Joint First-Passage Probability .....	167
7.3.1	Joint First-Passage Probability of Two Processes .....	168

7.3.2	Joint First-Passage Probability of Three Processes .....	170
7.4	Verification by Monte Carlo Simulation .....	172
7.4.1	Verification of Joint First-Passage Probability of Two Processes .....	173
7.4.2	Verification of Joint First-Passage Probability of Three Processes .....	174
7.5	Applications to Electrical Substation Systems .....	175
<b>8</b>	<b>Conclusions .....</b>	<b>189</b>
8.1	Summary of Major Findings .....	189
8.2	Recommendations for Future Studies .....	190
	<b>References .....</b>	<b>193</b>
	<b>Appendix A Mean Crossing Rates of Vector Processes over Finite Edges</b>	<b>199</b>
	<b>Appendix B Joint Distribution of Envelopes of Two Gaussian Processes</b>	<b>203</b>
	<b>Appendix C Nataf Approximation of the Joint Distribution of Envelopes of Gaussian Processes .....</b>	<b>207</b>
	<b>Appendix D Statistical Moments of Single-Degree-of-Freedom Oscillator Response to White Noise Input .....</b>	<b>211</b>

## LIST OF FIGURES

Figure 2.1	Mechanical models of equipment items connected by rigid bus connectors: (a) RB-FSC-connected system, (b) Bus-slider-connected system, and (c) Idealized system with SDOF equipment models .....	19
Figure 2.2	Definition of shape functions for SDOF idealization of 3D frame element: (a) configuration and end responses, (b) shape functions .....	20
Figure 2.3	A 230kV disconnect switch in service (Courtesy: PG&E) .....	21
Figure 2.4	FE model for 230kV disconnect switch with three-pole, two-post porcelain insulators (unit of length: meter) .....	22
Figure 2.5	A 230kV bus support in service (Courtesy: PG&E) .....	23
Figure 2.6	FE model for 230kV bus support with three-pole, two-post porcelain insulators (unit of length: meter) .....	24
Figure 2.7	Fundamental mode of a 230kV disconnect switch (dashed line: initial configuration of the system) .....	25
Figure 2.8	FE model for 230kV disconnect switch and bus support connected by three rigid bus connectors .....	26
Figure 2.9	Ground motions used in the dynamic analyses; <i>x</i> -axis: time (sec), <i>y</i> -axis: acceleration (g) .....	27
Figure 2.10	Response ratios of lower-frequency equipment (bus support) .....	28
Figure 2.11	Response ratios of higher-frequency equipment (disconnect switch) .....	29
Figure 3.1	Rigid bus conductors fitted with flexible strap connectors: (a) asymmetric FSC (PG&E No. 30-2021), (b) symmetric FSC (PG&E No. 30-2022), (c) FSC with long leg (PG&E No. 30-2023) .....	48
Figure 3.2	Hysteretic behavior of RB-FSC as observed in UCSD tests and as predicted by the fitted generalized Bouc-Wen model: (a) symmetric FSC (30-2022) and (b) asymmetric FSC (30-2021) .....	49

Figure 3.3	Hysteresis loops by Bouc-Wen model ( $A=1, n=1$ ) (a) $\gamma=0.5, \beta=0.5$ , (b) $\gamma=0.1, \beta=0.9$ , (c) $\gamma=0.5, \beta=-0.5$ and (d) $\gamma=0.75, \beta=-0.25$ .....	50
Figure 3.4	Values of shape-control functions for (a) original Bouc-Wen model, (b) model by Wang & Wen .....	51
Figure 3.5	Values of the shape-control function for the generalized Bouc-Wen model ..	51
Figure 3.6	Hysteretic behavior of RB-FSC as observed in UCSD test and as predicted by the FE model: (a) symmetric FSC (30-2022), (b) asymmetric FSC (30-2021) ....	52
Figure 3.7	Hysteretic behavior of RB-FSC as observed by UCSD tests and as predicted by the fitted modified Bouc-Wen model: (a) symmetric FSC (30-2022), (b) asymmetric FSC (30-2021) .....	53
Figure 3.8	Slider connector specimens: (a) PG&E Type 221A, 30-4462, (b) improved model (Photo courtesy: UCSD) .....	54
Figure 3.9	Coulomb slider-spring representation of slider connector .....	55
Figure 3.10	Experimental hysteresis loops of slider connectors (Filiatrault <i>et al.</i> 1999 and Stearns & Filiatrault 2003) .....	55
Figure 3.11	Ideal bi-linear hysteresis loop .....	56
Figure 3.12	Bi-linear hysteresis as observed in UCSD tests and as predicted by the differential equation model: (a) PG&E Type 221A, 30-4462 and (b) improved slider connector .....	57
Figure 3.13	PG&E 30-2021: (a) undeformed shape, (b) extreme compressed shape and (c) extreme elongated shape .....	58
Figure 3.14	PG&E 30-2022: (a) undeformed shape, (b) extreme compressed shape and (c) extreme elongated shape .....	59
Figure 3.15	PG&E 30-2023: (a) undeformed shape, (b) extreme compressed shape and (c) extreme elongated shape .....	60
Figure 3.16	Displacement load cycles used for RB-FSC .....	61
Figure 3.17	S-FSC (1) .....	62

Figure 3.18	<i>S</i> -FSC (1): (a) undeformed shape, (b) extreme compressed shape and (c) extreme elongated shape .....	63
Figure 3.19	Hysteresis loops of <i>S</i> -FSC .....	64
Figure 3.20	Hysteretic behavior of <i>S</i> -FSC as observed in UCSD tests and as predicted by the fitted Bouc-Wen model: (a) first specimen, (b) second specimen .....	65
Figure 4.1	Displacement time histories of the lower-frequency equipment item in the RB-FSC (symmetric, 30-2022)-connected system for the TabasLN record: (a) modified Bouc-Wen model; (b) generalized Bouc-Wen model .....	89
Figure 4.2	Displacement time histories of the higher-frequency equipment item in the RB-FSC (symmetric, 30-2022)-connected system for the TabasLN record: (a) modified Bouc-Wen model; (b) generalized Bouc-Wen model .....	90
Figure 4.3	Force-elongation hysteresis loops of the RB-FSC (symmetric, 30-2022) in the interconnected system subjected to the Tabas LN record .....	91
Figure 4.4	Acceleration time histories of shake-table motions for (a) Test RB-79 (Tabas 50%); (b) Test RB-112 (Newhall 100%) .....	92
Figure 4.5	Displacement time histories of equipment items in the bus-slider-connected system for the table motion of Test RB-79: (a) lower frequency equipment item; (b) higher-frequency equipment item .....	93
Figure 4.6	Displacement time histories of equipment items in the bus-slider-connected system for the table motion of Test RB-112: (a) lower-frequency equipment item; (b) higher-frequency equipment item .....	94
Figure 4.7	Force-elongation hysteresis loops of the bus slider in the connected system: (a) Test RB-79; (b) Test RB-112 .....	95
Figure 4.8	Acceleration time histories for shake table motions of (a) Test RC-86 (Newhall 100%); (b) Test RC-88B (Tabas 100%) .....	96
Figure 4.9	Displacement time histories of the lower-frequency equipment item of Test RC-86 and RC-88B when excited in its stand-alone configuration (Test RC-64): (a) analysis based on the reported equipment frequency $f_1 = 1.88$ Hz; (b) analysis based on the adjusted frequency $f_1 = 1.81$ Hz .....	97

Figure 4.10	Displacement time histories of equipment items in the <i>S</i> -FSC-connected system for the table motion of Test RC-86: (a) lower-frequency equipment item; (b) higher-frequency equipment item .....	98
Figure 4.11	Displacement time histories of equipment items in the <i>S</i> -FSC-connected system for the table motion of Test RC-88B: (a) lower-frequency equipment item; (b) higher-frequency equipment item .....	99
Figure 4.12	Force-elongation hysteresis loops of the <i>S</i> -FSC in the connected system: (a) Test RC-86; (b) Test RC-88B .....	100
Figure 4.13	Response ratios for equipment items connected by RB-FSC 30-2022: (a) lower-frequency equipment item; (b) higher-frequency equipment item .....	101
Figure 4.14	Response ratios for equipment items connected by bus slider: (a) lower-frequency equipment item; (b) higher-frequency equipment item .....	102
Figure 4.15	Response ratios for equipment items connected by <i>S</i> -FSC: (a) lower-frequency equipment item; (b) higher-frequency equipment item .....	103
Figure 5.1	Response ratios for $l_1 / m_1 = l_2 / m_2$ , $f_2 = 5$ Hz, $\zeta_1 = \zeta_2 = 0.02$ and $c_0 = 0$ based on the Kanai-Tajimi power spectral density with $\omega_g = 5\pi$ rad/s and $\zeta_g = 0.6$ .....	118
Figure 5.2	Response ratios for $l_1 / m_1 = l_2 / m_2$ , $f_2 = 10$ Hz, $\zeta_1 = \zeta_2 = 0.02$ and $c_0 = 0$ based on the Kanai-Tajimi power spectral density with $\omega_g = 5\pi$ rad/s and $\zeta_g = 0.6$ .....	119
Figure 5.3	Response ratios for $l_1 / m_1 = l_2 / m_2$ , $f_2 = 5$ Hz, $\zeta_1 = \zeta_2 = 0.02$ and $c_0 = 0$ based on the Kanai-Tajimi power spectral density with $\omega_g = \pi$ rad/s and $\zeta_g = 0.3$ .....	120
Figure 5.4	Effect of equipment damping on the response ratio $R_2$ for $l_1 / m_1 = l_2 / m_2$ , $f_2 = 10$ Hz and $c_0 = 0$ , based on the Kanai-Tajimi power spectral density with $\omega_g = 5\pi$ rad/s and $\zeta_g = 0.6$ .....	121
Figure 5.5	Effect of energy dissipation of the connecting element on response ratios for $m_1 / m_2 = 2$ , $l_1 / m_1 = l_2 / m_2$ , $f_2 = 10$ Hz, $\kappa = 0.5$ and $\zeta_1 = \zeta_2 = 0.02$ , based on the Kanai-Tajimi power spectral density with $\omega_g = 5\pi$ rad/s and $\zeta_g = 0.6$ ..	122

Figure 5.6	Range of response ratios of higher-frequency equipment item connected by PG&E: 30-2021 .....	123
Figure 5.7	Range of response ratios of higher-frequency equipment item connected by PG&E: 30-2022 .....	124
Figure 5.8	Range of response ratios of higher-frequency equipment item connected by PG&E: 30-2023 .....	125
Figure 5.9	Range of response ratios of higher-frequency equipment item connected by Slider Connector (old) .....	126
Figure 5.10	Range of response ratios of higher-frequency equipment item connected by Slider Connector (new) .....	127
Figure 5.11	Range of response ratios of higher-frequency equipment item connected by <i>S</i> -FSC .....	128
Figure 5.12	Response ratios for $l_1 / m_1 = l_2 / m_2 = 1$ , $f_1 = 1$ Hz, $f_2 = 5$ Hz, $m_1 = 500$ kg, $m_2 = 100$ kg, $\zeta_1 = \zeta_2 = 0.02$ , $c_0 = 0$ based on the Kanai-Tajimi power spectral density with $\omega_g = 5\pi$ rad/s and $\zeta_g = 0.6$ .....	129
Figure 5.13	Response ratios for $l_1 / m_1 = l_2 / m_2 = 1$ , $f_1 = 1$ Hz, $f_2 = 10$ Hz, $m_1 = 100$ kg, $m_2 = 100$ kg, $\zeta_1 = \zeta_2 = 0.02$ , $c_0 = 0$ based on the Kanai-Tajimi power spectral density with $\omega_g = 5\pi$ rad/s and $\zeta_g = 0.6$ .....	130
Figure 6.1	Basic MECE events $e_i$ for a three-event sample space .....	160
Figure 6.2	Example single-transmission-line substation system .....	161
Figure 6.3	System versus circuit-breaker failure probabilities .....	161
Figure 6.4	Example single-transmission-line substation with a parallel sub-system of circuit breakers .....	162
Figure 6.5	Example two-transmission-line substation system .....	162
Figure 7.1	Trajectories of a vector process and relation to the joint failure event .....	179
Figure 7.2	Unconditional mean crossing rates and corresponding thresholds for a 2-dimensional vector process .....	180

Figure 7.3	Unconditional mean crossing rates and corresponding thresholds for a 3-dimensional vector process .....	181
Figure 7.4	Comparison between analytical estimates and Monte Carlo simulation for the ‘Medium-Medium’ category of: (a) $P_i(a_i, \tau)$ , (b) $P_j(a_j, \tau)$ , (c) $P_{i+j}(a_i, a_j, \tau)$ , (d) $P_{ij}(a_i, a_j, \tau)$ .....	182
Figure 7.5	Joint first-passage probability $P_{ij}(a_i, a_j, \tau)$ for (a) ‘Medium-Low’, (b) ‘Medium-High’, (c) ‘Narrow-Medium’, (d) ‘Wide-Medium’ categories .....	183
Figure 7.6	Joint first-passage probability $P_{ij}(a_i, a_j, \tau)$ for (a) ‘Narrow-Low’, (b) ‘Narrow-High’, (c) ‘Wide-Low’, (d) ‘Wide-High’ categories .....	184
Figure 7.7	Comparison between analytical estimates and Monte Carlo simulation for the ‘Medium-Medium’ category: (a) $P_{i+k}(a_i, a_k, \tau)$ , (b) $P_{j+k}(a_j, a_k, \tau)$ , (c) $P_{i+j+k}(a_i, a_j, a_k, \tau)$ , (d) $P_{ijk}(a_i, a_j, a_k, \tau)$ .....	185
Figure 7.8	Joint first-passage probability $P_{ijk}(a_i, a_j, a_k, \tau)$ for (a) ‘Medium-Low’, (b) ‘Medium-High’, (c) ‘Narrow-Medium’, (d) ‘Wide-Medium’ categories .....	186
Figure 7.9	Joint first-passage probability $P_{ijk}(a_i, a_j, a_k, \tau)$ for (a) ‘Narrow-Low’, (b) ‘Narrow-High’, (c) ‘Wide-Low’, (d) ‘Wide-High’ categories .....	187
Figure 7.10	Substation system with five equipment items .....	188
Figure 7.11	Equipment and system fragility estimates by (a) extended Poisson approximation; (b) extended VanMarcke approximation .....	188



## LIST OF TABLES

Table 2.1	Parameters of SDOF models of equipment items .....	16
Table 2.2	Response ratios of lower-frequency equipment (bus support) .....	17
Table 2.3	Response ratios of higher-frequency equipment (disconnect switch) .....	18
Table 3.1	Values of the shape-control function for the generalized Bouc-Wen model ..	46
Table 3.2	Comparison of FSC characteristics .....	47
Table 4.1	Expressions for $E_i$ , $i = 1, \dots, 8$ , in (4.32)-(4.34), for computing the coefficients of the linearized equations for the generalized Bouc-Wen model for $n = 1$ .....	88
Table 6.1	Coefficients $c_i$ of the object functions $\mathbf{c}^T \mathbf{p}$ for three-component systems .....	157
Table 6.2	Failure probabilities of circuit breaker and corresponding system failure probabilities .....	157
Table 6.3	Failure probabilities of single-transmission-line substation with parallel subsystem of $k$ correlated circuit breakers .....	158
Table 6.4	Failure probabilities of single-transmission-line substation with parallel subsystem of $k$ uncorrelated circuit breakers .....	158
Table 6.5	Failure probabilities of two-transmission-line substation system .....	158
Table 6.6	Component importance measures for the two-transmission-line substation system (maximum IM's are highlighted) .....	159
Table 6.7	Fussell-Vesely cut-set importance measures for the two-transmission-line substation system .....	159
Table 7.1	Parameters of two SDOF oscillators and statistical moments of the responses under white noise excitation ( $f_i = 2$ Hz) .....	177
Table 7.2	Parameters of three SDOF oscillators and statistical moments of the responses under white noise excitation ( $f_i = 2$ Hz) .....	178

Table C.1	Relative error $\varepsilon_r$ (%) in estimate of $P_{i+j}(a_i, a_j, \tau)$ based on the Nataf approximation of the bi-variate PDF of envelopes .....	210
-----------	---	-----

# 1 Introduction

## 1.1 MOTIVATION

Lifelines, such as power transmission and communication networks, gas- and water-distribution systems, and transportation networks operate as critical backbones of urban communities. Recent earthquakes in Loma Prieta (1989), Northridge (1995) and Kobe (1996) have demonstrated that damage to critical lifelines can cause severe losses to an urban society and economy. Moreover, the failure of lifeline systems may hamper emergency services and delay post-earthquake recovery. Therefore, it is important to reinforce critical lifeline systems so as to assure their functionality during future earthquakes.

An important element within the power transmission network is the electrical substation, which consists of a complex set of interconnected equipment items, such as transformers, circuit breakers, switches and surge arrestors. Many of these equipment items are connected to each other through assemblies of rigid bus and various types of flexible connectors. To assure a desired level of functionality of the electrical substation during future earthquakes, it is essential to have analytical models and methods for assessing the seismic response and reliability of electrical substation equipment and system. It is also necessary to have practical guidelines for seismic design and retrofitting of electrical substation equipment and system.

The problems described above are not straightforward for the following reasons: (1) Connected equipment items cannot be analyzed individually because of dynamic interaction between them. This interaction is known to cause significant amplification in the response of the higher-frequency equipment item (Der Kiureghian *et al.* 1999). (2) The rigid bus connectors behave nonlinearly (Der Kiureghian *et al.* 2000, Filiatrault *et al.* 1999, Stearns & Filiatrault 2003) and analysis methods based on linear models may lead to significant errors. (3) Ground motions are stochastic in nature and equipment and system responses to future earthquakes can only be assessed in a statistical sense. Deterministic analysis with one or a few selected ground motions may lead to erroneous conclusions. (4) The substation is a complex system of interconnected

components. The reliability of such a system cannot be directly deduced from marginal component reliability estimates.

The motivation behind this study is the need for the development of new models and analysis methods for improved estimation of the seismic response of interconnected electrical substation equipment and the seismic reliability of substation systems.

## 1.2 OBJECTIVES AND SCOPE

The primary objective of this study is to develop the needed analytical models and methods that can account for the effect of dynamic interaction between connected equipment items, the nonlinear hysteretic behavior of rigid bus connectors, the stochastic nature of earthquake ground motions, and the systems aspects of the electrical substation. This study also aims at providing practical guidelines and decision frameworks for seismic design of connected equipment, and systematic methods for identifying critical components within a substation for reliability enhancement. Towards these ends, the development of the models and methods is tailored such that extensive parametric studies can be performed with efficiency and accuracy. Particular attention is also given to estimating and improving the reliability of complex substation systems. New methods to estimate narrow bounds on the reliability of general systems are developed and applied to example substation systems.

Considering the plethora of equipment types and configurations in a substation, and the dearth of available information about their characteristics, simple modeling of equipment items is essential. Following Der Kiureghian *et al.* (1999), in this study an electrical substation equipment item is idealized as a single-degree-of-freedom (SDOF) oscillator by use of a displacement shape function. Details of the idealization procedure are provided for beam-type structures and 3-dimensional (3D) frame and truss structures. A set of response ratios originally introduced by Der Kiureghian *et al.* (1999) are used to quantify the interaction effect. In order to demonstrate the procedure and examine the accuracy of the SDOF idealization for interaction studies, a connected system consisting of a disconnect switch and a bus support is examined in great detail. The response ratios predicted by the SDOF models are compared with those obtained by 3D finite-element dynamic analysis. Based on these results, recommendations are made on the best choice of the shape functions for the SDOF idealization.

The hysteretic behavior of rigid bus connectors is described by differential-equation-type models for use in nonlinear time history and random vibration analyses of the interconnected electrical substation equipment. For the existing designs of Flexible Strap Connector's (FSC), a generalized Bouc-Wen model is developed that is capable of describing the highly asymmetric hysteresis behavior. This model is appropriate for use in conjunction with nonlinear random vibration analysis by the equivalent linearization method (ELM). For the Slider Connector, a bilinear model in the form of a differential equation is adopted (Kaul & Penzien 1974). This study also introduces a new S-shaped FSC, called *S*-FSC, which has enhanced flexibility and is highly effective in reducing the adverse effect of dynamic interaction between the connected equipment items. The hysteretic behavior of the *S*-FSC is modeled by the original Bouc-Wen model (Wen 1976). These theoretical models are fitted to available experimental results (Filiatrault *et al.* 1999, Stearns & Filiatrault 2003) and finite element predictions (Der Kiureghian *et al.* 2000), and then are used to conduct a comprehensive parametric study of the interaction effect.

Analysis methods are developed for estimating the seismic response of equipment items connected by nonlinear rigid bus conductors. The analysis methods use the SDOF models for equipment items and the differential-equation-type hysteresis models for the rigid bus connectors. For deterministic time-history analysis, the adaptive Runge-Kutta-Fehlberg algorithm (Fehlberg 1969) is used. For stochastic dynamic analysis, the ELM is used (Wen 1980). For each connector hysteretic model, closed-form expressions are derived for the coefficients of the equivalent linear system in terms of the second moments of the response. Numerical simulations verify the accuracy of the proposed models and methods.

Employing nonlinear random vibration analysis with the developed models and methods, the effect of interaction in the connected equipment system is investigated through extensive parametric studies. For each connector, parametric charts of the amplification in the response of the higher-frequency equipment item relative to its stand-alone configuration are developed, which describe the influences of important system parameters over wide ranges of values. The performances of the various connectors under identical conditions are then compared in terms of the amplification in the response of the higher-frequency equipment item. Based on this parametric investigation, simple design guidelines are suggested for reducing the hazardous effect of the seismic interaction in practice. The design guidelines utilize the parametric charts and an interpolation/extrapolation formula for easy estimate of the interaction effect in practice.

In order to assess and improve the seismic reliability of electrical substation systems, a method is developed for computing bounds on the reliability of general systems by use of Linear Programming (LP). The procedure and merits of the methodology are described in a detail. The usefulness of the methodology for assessing the seismic reliability of complex electrical substation systems is demonstrated by applications to three transmission-line-substation examples. It is also shown that the proposed LP formulation provides a convenient framework for a systematic identification of critical components and cut sets of the system. Numerical examples with the two-transmission-line substation system demonstrate the proposed methodology.

In order to obtain narrow bounds on the reliability of an electrical substation system under stochastic loading, the new concept of “joint first-passage probability of a vector process” is introduced and new formulations for Gaussian vector processes are derived. The accuracy of the proposed formulas is verified by comparing the analytical estimates with Monte Carlo simulation results. By synthesis of the analytical models and methods developed in this study, a general methodology for estimating the reliability of an electrical substation system subjected to a stochastic ground excitation is proposed. The methodology is demonstrated for an example electrical substation system.

### **1.3 ORGANIZATION**

Following this introductory chapter, Chapter 2 describes the SDOF idealization of electrical substation equipment and examines the validity and accuracy of this idealization for interaction studies. In Chapter 3, analytical models are developed to describe the hysteretic behavior of rigid bus connectors. Chapter 4 describes the deterministic and stochastic analysis methods for estimating the seismic response of equipment items connected by nonlinear rigid bus conductors. In Chapter 5, the effect of interaction in the connected equipment system is investigated through extensive parametric studies. This chapter also provides practical guidelines for the seismic design of interconnected electrical substation equipment. Chapter 6 presents the LP formulation for computing bounds on the reliability of general systems and a convenient framework for systematic identification of critical components and cut sets of the system. The use of LP bounds for estimating and improving the seismic reliability of example electrical substation systems is demonstrated. In Chapter 7, approximate formulas are developed for the joint first-passage probabil-

ity of a vector process, so as to achieve narrow bounds on the failure probability of general systems under stochastic loading. A general methodology for estimating the reliability of an electrical substation system subjected to a stochastic ground excitation is developed by synthesizing the models and methods developed in this study. Finally, a summary of the major findings and suggestions for further study are presented in Chapter 8.





## 2 Single-Degree-of-Freedom Idealization of Electrical Equipment

### 2.1 INTRODUCTION

Recent studies on dynamic interaction between interconnected electrical substation equipment (Der Kiureghian *et al.* 1999, 2000; Filiatrault *et al.* 1999) have used single-degree-of-freedom (SDOF) models for characterizing the equipment items. In this approach, each equipment item is idealized as a SDOF oscillator by describing its deformation in terms of an assumed displacement “shape” function. This procedure leads to effective mass, stiffness, damping and external inertia force values of each equipment item. The connected system then is idealized as a 2-degree-of-freedom system defined by the effective properties of each equipment item and the properties of the connecting element. This chapter examines the validity and accuracy of this idealization for interaction studies.

In Section 2.2, the procedure for determining the effective mass, stiffness, damping and external inertia force for a selected displacement shape function is described. Details are given for beam-type structures and for 3-dimensional (3D) frame and truss structures. The equations of motion for a system consisting of two such idealized equipment items connected by a rigid bus and subjected to base motion are presented. The measure of dynamic interaction considered is the ratio of peak response of each equipment in the connected system to its peak response in a stand-alone configuration.

In Section 2.3, a system consisting of a 230 kV disconnect switch and a 230 kV bus support connected by a rigid bus (RB) fitted with a flexible-strap connector (FSC) is examined in great detail. Four different displacement shapes for each equipment item are considered. The response ratios computed for these idealized models are compared with response ratios obtained by 3D finite-element dynamic analyses of the connected and stand-alone systems for a selected set

of recorded ground motions. Based on these results, recommendations are made on the best choice of the shape functions for SDOF idealization of equipment items in interaction studies.

## 2.2 MODELING OF CONNECTED EQUIPMENT ITEMS USING SDOF IDEALIZATION

Consider two electrical substation equipment items connected by a rigid bus conductor, such as a RB-FSC in Figure 2.1a or a slider connector in Figure 2.1b. In estimating the displacements of the equipment items either by deterministic or probabilistic methods, it is convenient to idealize each equipment item as a SDOF oscillator characterized by its effective mass, stiffness and damping values and an effective external inertia force. This idealization is depicted in Figure 2.1c. As Der Kiureghian *et al.* (1999) have argued, in addition to the need for simplicity, this SDOF idealization is necessary from a pragmatic standpoint because of the extremely diverse configurations of equipment types and connections in a typical electrical substation, as well as the dearth of information that is available on the dynamic characteristics of equipment items.

The SDOF idealization begins with the assumption that the displacement of the equipment can be decomposed into spatial and time coordinates, i.e.  $u(y,t) = \psi(y)z(t)$ . Herein,  $y$  is the spatial coordinate,  $\psi(y)$  is a displacement shape function, which is normalized to have a unit value at the attachment point, and  $z(t)$  is the generalized coordinate reflecting the variation of the displacement shape with time. For an equipment item modeled as a beam with length  $L$ , the effective structural parameters of the SDOF model are computed based on the principle of virtual work (Clough & Penzien 1993). The effective mass,  $m$ , stiffness,  $k$ , damping coefficient,  $c$ , and the effective mass producing the external inertia force,  $l$ , are given as (Der Kiureghian *et al.* 1999)

$$m = \int_0^L \rho(y)[\psi(y)]^2 dy \quad (2.1)$$

$$k = \int_0^L EI(y)[\psi''(y)]^2 dy \quad (2.2)$$

$$c = 2\zeta\sqrt{mk} \quad (2.3)$$

$$l = \psi(y) \int_0^L \rho(y) \psi(y) dy \quad (2.4)$$

where  $\rho(y)$  is the mass density per unit length,  $EI(y)$  is the flexural rigidity function and  $\zeta$  is the damping ratio.

In the case of a complex 3-dimensional structure composed of frame-type members, the idealization procedure should account for all the deformation modes of the constituent members: axial, torsional, and transverse displacements in two orthogonal directions. Figure 2.2a shows the  $k$ -th frame member in an equipment item, which has length  $L_k$ , mass density  $\rho_k(s)$ , axial rigidity  $EA_k(s)$ , torsional rigidity  $GJ_k(s)$ , and flexural rigidities  $EI_k^{(2)}(s)$  and  $EI_k^{(3)}(s)$  for bending around axes 2 and 3, respectively. The member is subject to 12 kinematic conditions related to the end displacements  $v_1, v_2, \dots, v_6$ , and end rotations  $\theta_1, \theta_2, \dots, \theta_6$ . One can assume a set of four displacement shape functions:  $\psi_k^{(a)}(s)$  for the axial displacements,  $\psi_k^{(t)}(s)$  for the torsional displacements around axis  $\mathbf{e}_1$ ,  $\psi_k^{(2)}(s)$  for the transverse displacements along axis  $\mathbf{e}_2$ , and  $\psi_k^{(3)}(s)$  for the transverse displacements along axis  $\mathbf{e}_3$  (see Figure 2.2b). These displacement shape functions must of course satisfy the kinematic conditions complying with the assumed displacement of the entire structure. According to the principle of virtual work, the effective parameters of the idealized SDOF oscillator for such a structure are given by

$$m = \sum_{k=1}^N \int_0^{L_k} \rho_k(s) \{ [\psi_k^{(a)}(s)]^2 + [\psi_k^{(2)}(s)]^2 + [\psi_k^{(3)}(s)]^2 \} ds \quad (2.5)$$

$$k = \sum_{k=1}^N \int_0^{L_k} EA_k(s) [\psi_k^{(a)}(s)]^2 + EI_k^{(3)}(s) [\psi_k^{(2)}(s)]^2 + EI_k^{(2)}(s) [\psi_k^{(3)}(s)]^2 + GJ_k(s) [\psi_k^{(t)}(s)]^2 ds \quad (2.6)$$

$$l = \sum_{k=1}^N \int_0^{L_k} \rho_k(s) [(\mathbf{e}_1 \cdot \mathbf{E}) \psi_k^{(a)}(s) + (\mathbf{e}_2 \cdot \mathbf{E}) \psi_k^{(2)}(s) + (\mathbf{e}_3 \cdot \mathbf{E}) \psi_k^{(3)}(s)] ds \quad (2.7)$$

where  $N$  is the number of frame members in the equipment item and  $\mathbf{E}$  denotes the direction of vibration of the idealized SDOF oscillator. The damping value  $c$  is obtained from (2.3) using (2.5) and (2.6).

In many practical situations, it is difficult to carry out the SDOF idealization as described

above. The complexity of the equipment item and lack of information about its properties are serious impediments. In many cases, the total mass and the fundamental frequency of the equipment are all the information that is available. Even when a computer model of the equipment is available, it may not be easy to compute the second derivatives of the shape function at the element level, which are needed in (2.2) and (2.6) to compute the effective stiffness. In such cases, we recommend computing the effective mass based on an assumed displacement shape, and the fundamental or other appropriate modal frequency having a mode shape similar to the assumed displacement shape of the system. The effective stiffness can then be computed by multiplying the square of the natural circular frequency by the effective mass. Thus, in general, considerable amount of engineering judgment must be exercised in selecting the properties of the idealized SDOF model. The purpose of this chapter is to examine the accuracy of this SDOF idealization for specific example equipment.

Using the equivalent SDOF model for each equipment item, the equation of motion of the connected system in Figure 2.1c is described in a matrix form as

$$\mathbf{M}\ddot{\mathbf{u}} + \mathbf{C}\dot{\mathbf{u}} + \mathbf{R}(\mathbf{u}, \dot{\mathbf{u}}, z) = -\mathbf{L}\ddot{x}_g \quad (2.8)$$

where

$$\mathbf{u} = \begin{Bmatrix} u_1(t) \\ u_2(t) \end{Bmatrix}, \quad \mathbf{M} = \begin{bmatrix} m_1 & 0 \\ 0 & m_2 \end{bmatrix}, \quad \mathbf{C} = \begin{bmatrix} c_1 + c_0 & -c_0 \\ -c_0 & c_2 + c_0 \end{bmatrix} \quad (2.9)$$

$$\mathbf{R}(\mathbf{u}, \dot{\mathbf{u}}, z) = \begin{Bmatrix} k_1 u_1(t) - q(\Delta u(t), \Delta \dot{u}(t), z(t)) \\ k_2 u_2(t) + q(\Delta u(t), \Delta \dot{u}(t), z(t)) \end{Bmatrix}, \quad \mathbf{L} = \begin{Bmatrix} l_1 \\ l_2 \end{Bmatrix} \quad (2.10)$$

where  $\ddot{x}_g$  is the base acceleration,  $u_i(t)$  is the displacement of the  $i$ -th equipment item at its attachment point,  $\Delta u(t) = u_2(t) - u_1(t)$  is the relative displacement between the two equipment items,  $z$  is an auxiliary variable representing the plasticity of the inelastic connector;  $m_i$ ,  $c_i$ ,  $k_i$  and  $l_i$ ,  $i = 1, 2$ , are the effective mass, damping, stiffness and external inertia force values of the equipment items, respectively, and  $c_0$  denotes the effective viscous damping of the rigid bus connector. The function  $q(\Delta u(t), \Delta \dot{u}(t), z(t))$  denotes the resisting force of the inelastic rigid bus connector based on an assumed hysteretic model. Usually, this type of mathematical modeling of the inelastic behavior requires an auxiliary equation that describes how the variable  $z$  evolves

during the hysteretic behavior. Chapter 3 describes in great detail the mathematical models that are used to describe the inelastic behavior of various rigid bus connectors. Note that for a linear connector, we have  $q = k_0 \Delta u$ , where  $k_0$  denotes the stiffness of the connector. Throughout this study,  $i = 1$  refers to the lower-frequency equipment item (as measured in the stand-alone configuration) and  $i = 2$  refers to the higher-frequency equipment item.

In order to quantify the effect of dynamic interaction, Der Kiureghian *et al.* (1999) introduced a pair of response ratios:

$$R_i = \frac{\max |u_i(t)|}{\max |u_{i0}(t)|}, \quad i = 1, 2 \quad (2.11)$$

where  $u_i(t)$  and  $u_{i0}(t)$  respectively denote the displacements of equipment  $i$  in the connected and stand-alone configurations at time  $t$ . It should be obvious that a response ratio with a value greater (resp. smaller) than unity indicates that the interaction effect amplifies (resp. de-amplifies) the response of the corresponding equipment item in the connected system relative to its response in its stand-alone configuration. Thus,  $R_i$ 's are good measures of the dynamic interaction effect between connected equipment items. It is noted that, since forces in a SDOF oscillator are proportional to its displacement, the response ratios (2.11) also apply to the maximum forces acting on each equipment.

## 2.3 ACCURACY OF SDOF MODELS IN INTERACTION STUDIES

The accuracy of the SDOF idealization of a complex structure strongly depends on the selected shape function. This section examines several alternatives for selecting the shape functions for two typical electrical substation equipment in a connected system. Since the aim of this study is to evaluate the effect of interaction between the connected equipment items, the accuracy of the SDOF idealization with different shape functions is examined in terms of the response ratios defined in (2.11) instead of the absolute responses.

### 2.3.1 The Example System

An electrical substation has a large variety of equipment items. Some of these equipment are

well described by SDOF models, others are not. For the present investigation, a system consisting of a 230kV disconnect switch and a 230kV bus support connected to each other by a rigid bus fitted by a flexible strap connector is considered. The disconnect switch has a complicated 3-dimensional frame structure, which is not easily idealized by a SDOF model. The bus support, on the other hand, is a simple 2-dimensional frame and is more easily idealized as a SDOF oscillator. Therefore, the considered system provides a challenging case for investigating the validity of SDOF equipment models for interaction studies.

Since the switch and bus support are made of typical frame elements with known properties, they are relatively easy to analyze by the finite element method as compared to other electrical substation equipment, such as transformer bushings and circuit breakers. The FE model allows us to obtain fundamental mode shapes and displacement shapes of each structure under various kinds of static loading. The response ratios are obtained by FE dynamic analysis for selected ground motions. These are then compared with the response ratios obtained for SDOF idealizations of each equipment item by use of different displacement shapes.

A disconnect switch controls the flow of electricity by connecting or disconnecting equipment items in a substation. Figure 2.3 shows an actual 230kV disconnect switch in service. Most disconnect switches have three poles, each pole consisting of two or three posts (porcelain insulators). The posts on the outer lines are connected to other equipment items through rigid bus connectors or cables. The poles are usually supported by a frame structure, such as the one shown in Figure 2.3.

The SAP2000 (CSI Inc. 1997) finite element code is used to develop a model of the disconnect switch. Each pole is assumed to have three two-piece porcelain insulators connected by a vertical break pole (Gilani *et al.* 2000). Figure 2.4 shows the finite element model of a switch in ‘open’ condition, where information on the geometry and member characteristics are given. For the supporting structure beneath the poles, typical steel frame members such as W8×31, 4×3×1/4 double angle, L3×3×1/4, and L4×3×1/4 are used. The porcelain posts show complicated seismic behavior, which cannot be easily modeled with linear frame members. Gilani *et al.* (2000) performed a series of earthquake simulator tests on the 230kV disconnect switch to obtain an approximate SDOF model for each post. To develop a finite element model for the switch, lumped-mass SDOF models of the posts were combined with the finite element model of supporting structure. In the present finite element analysis, for the sake of simplicity,

porting structure. In the present finite element analysis, for the sake of simplicity, the posts are modeled as frame members that have solid circular cross sections with uniformly-distributed mass. Each post has two 1.02 m long porcelain insulators weighing 54.4 kg each. The upper piece has a diameter of 0.105 m and the lower post has a diameter of 0.125 m. Young's modulus for the porcelain is assumed to be 96.5 GPa.

Bus supports are used to support rigid bus connectors between electrical equipment items separated by long distance. Figure 2.5 shows a 230kV bus support in service with three porcelain insulators. For this example, a three-post bus support structure consisting of two pipes (Pipe 8 std.) and a tube (Ts 7×7×0.25) is chosen. Figure 2.6 shows the finite element model of the example bus support structure. It is assumed that the same insulators which are used for the 230kV disconnect switch are mounted on the frame structure of the bus support.

### 2.3.2 Results

Three types of shape functions are considered for the SDOF idealization: (a) The fundamental mode shape, (b) the displacement shape under identical point loadings at the connection points, and (c) the displacement shape under self-weight in the direction of interest, i.e., parallel to the rigid bus connectors between the two equipment. The fundamental mode shape, which is obtained by eigenvalue analysis of the finite element model, reflects the most dominant vibration mode in most cases. However, for a complex structure such as the disconnect switch, the fundamental mode shape may correspond to the local vibration of a slender member and not the entire structure. As shown in Figure 2.7, the fundamental mode represents the local vibration of a member at the top of the supporting structure. For this reason, the first lateral mode shape of the structure is also considered as a shape function. The displacement shape based on the point loadings at the connection points is intended to simulate the forces acting on the interconnected equipment items. The displacement shape under lateral self-weight is intended to simulate the effective inertia force in the direction of ground motion (Clough & Penzien 1993).

Polynomial functions are used to describe the shape functions  $\psi_k^{(a)}(s)$  (linear),  $\psi_k^{(l)}(s)$  (linear),  $\psi_k^{(2)}(s)$  (cubic) and  $\psi_k^{(3)}(s)$  (cubic) for each member, satisfying the end displacements and rotations obtained from the finite element analysis for the prescribed loading or mode shape. These are used in (2.5)-(2.7) to compute the parameters of the idealized SDOF model for each

case. Table 2.1 lists the computed parameters of the SDOF model for each shape function and equipment item. The last column of the table lists the natural frequency of the resulting SDOF oscillator obtained in terms of the effective mass and stiffness from the expression

$$f_i = \frac{1}{2\pi} \sqrt{\frac{k_i}{m_i}} \quad (2.12)$$

It is seen that the disconnect switch has a higher frequency than the bus support in all cases. As mentioned above, the fundamental mode of the disconnect switch represents a local mode of vibration and not that of the entire system. That is why the SDOF parameters for the disconnect switch based on the first mode are not consistent with the SDOF parameters for the other displacement shapes.

To investigate the effect of interaction, we assume the two equipment items are connected at the top of their respective three posts by a set of three rigid buses, each fitted with a PG&E 30-2021 flexible strap connector (see Figure 2.8). Although this RB-FSC in general may exhibit nonlinear behavior (See Chapter 3), for the sake of simplicity in this analysis the connector is modeled as a linear spring with its initial stiffness of 49.2 kN/m. Ten recorded acceleration time histories, shown in Figure 2.9, are used to compute the response ratios for both the finite element model and the SDOF idealized systems, thus allowing us to examine the effect of variability in the ground motion on the response ratios.

Tables 2.2 and 2.3 respectively list the response ratios of the lower (bus support) and higher (disconnect switch) frequency equipment items for the 10 recorded ground motions. The first four columns are for the SDOF-idealized systems with each of the selected displacement shapes, and the last column is based on the 3D finite element dynamic analysis. It is seen that the response ratio for the lower frequency equipment item is generally less than 1 (the interaction tends to deamplify the response), whereas that of the higher frequency item is greater than 1, indicating that the interaction tends to amplify the response of the disconnect switch relative to its response in the stand-alone configuration. The last rows in Tables 2.2 and 2.3 list the root-mean-square (rms) errors in the computed response ratios based on each SDOF-idealized model with respect to the corresponding finite element analysis over the ensemble of ground motions. Figures 2.10 and 2.11 show the same results for the response ratios in a graphical form.



The results in Tables 2.2 and 2.3 and Figures 2.10 and 2.11 show that the SDOF-idealized models provide reasonable approximations of the response ratios for the given interconnected equipment system. For the lower-frequency equipment item, no single displacement shape function can be distinguished as the best. The rms errors narrowly range from 0.164 to 0.225. However, for the higher frequency equipment item, the displacement shape function based on the lateral self-weight clearly gives superior results. The rms error for this case is 0.123, whereas the errors for the other three shape functions range from 0.331 to 0.585. On this basis, we can state that the displacement shape under the lateral self-weight is best representing the vibration shape of the interconnected disconnect switch and bus support. Further studies with other equipment models are needed before one can conclusively recommend appropriate shape functions for SDOF modeling of electrical substation equipment.

It is noteworthy that there is significant variability in the estimated response ratios over the ensemble of ground motions for each of the structural models. The sample coefficients of variation of the response ratios estimated by 3D finite element analyses are 25.6 % (bus support) and 15.4 % (disconnect switch), respectively. This points to the need for stochastic modeling of the ground motion in the analysis of dynamic interaction between connected equipment items. These topics are addressed in later chapters of this report.

Table 2.1 Parameters of SDOF models of equipment items

230kV Support	$m_1$ (kg)	$k_1$ (N/m)	$l_1$ (kg)	$f_1$ (Hz)
1 <sup>st</sup> mode	192	$2.03 \times 10^5$	356	5.18
3 point loading	156	$1.86 \times 10^5$	308	5.50
Self-weight	236	$2.84 \times 10^5$	406	5.52

230kV Switch	$m_2$ (kg)	$k_2$ (N/m)	$l_2$ (kg)	$f_2$ (Hz)
1 <sup>st</sup> mode	$4.0 \times 10^{10}$	$1.69 \times 10^{14}$	350	10.3
1 <sup>st</sup> lateral	2386	$1.74 \times 10^7$	363	13.6
3 point loading	300	$7.70 \times 10^6$	500	25.5
Self-weight	661	$2.00 \times 10^7$	1131	27.7

Table 2.2 Response ratios of lower-frequency equipment (bus support)

$R_1$	1 <sup>st</sup> – 1 <sup>st</sup>	1 <sup>st</sup> lateral – 1 <sup>st</sup>	3 point loading	Self-weight	3D FEM
Northridge	0.395	0.405	0.399	0.525	0.610
Tabas LN	0.544	0.560	0.624	0.724	0.518
Tabas TR	0.507	0.512	0.483	0.604	0.473
Imperial Valley	0.715	0.720	0.879	0.854	0.665
Loma Prieta	0.518	0.532	0.548	0.672	0.851
San Fernando	0.600	0.576	0.593	0.546	0.704
Kobe	0.581	0.583	0.571	0.904	0.404
Turkey	0.897	0.929	0.448	0.934	0.650
Parkfield	0.895	0.911	0.570	0.882	0.928
Victoria	0.528	0.541	0.660	0.666	0.556
rms error	0.164	0.166	0.203	0.225	X

Table 2.3 Response ratios of higher-frequency equipment (disconnect switch)

$R_2$	1 <sup>st</sup> – 1 <sup>st</sup>	1 <sup>st</sup> lateral – 1 <sup>st</sup>	3 point loading	Self-weight	3D FEM
Northridge	1.72	1.58	1.36	1.12	1.20
Tabas LN	1.49	1.82	1.99	1.51	1.32
Tabas TR	2.29	1.94	1.77	1.27	1.22
Imperial Valley	1.17	1.14	1.26	0.91	0.85
Loma Prieta	1.62	1.13	1.22	1.22	1.08
San Fernando	1.42	1.05	1.22	0.99	1.04
Kobe	1.92	1.95	1.31	1.35	1.23
Turkey	1.30	1.43	1.10	1.07	0.894
Parkfield	1.96	1.88	1.32	1.13	1.13
Victoria	1.19	1.29	0.989	1.05	0.868
rms error	0.585	0.505	0.331	0.123	X

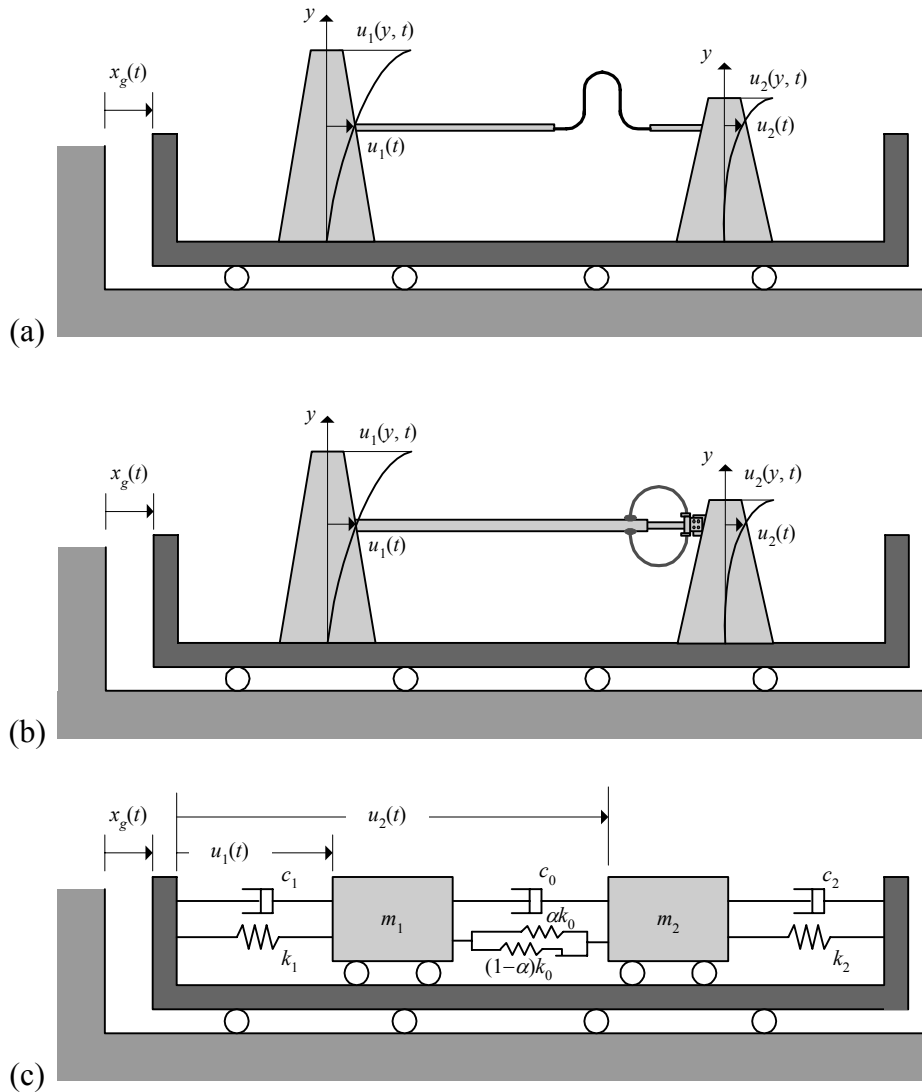


Figure 2.1 Mechanical models of equipment items connected by rigid bus connectors: (a) RB-FSC-connected system, (b) Bus-slider-connected system, and (c) idealized system with SDOF equipment models

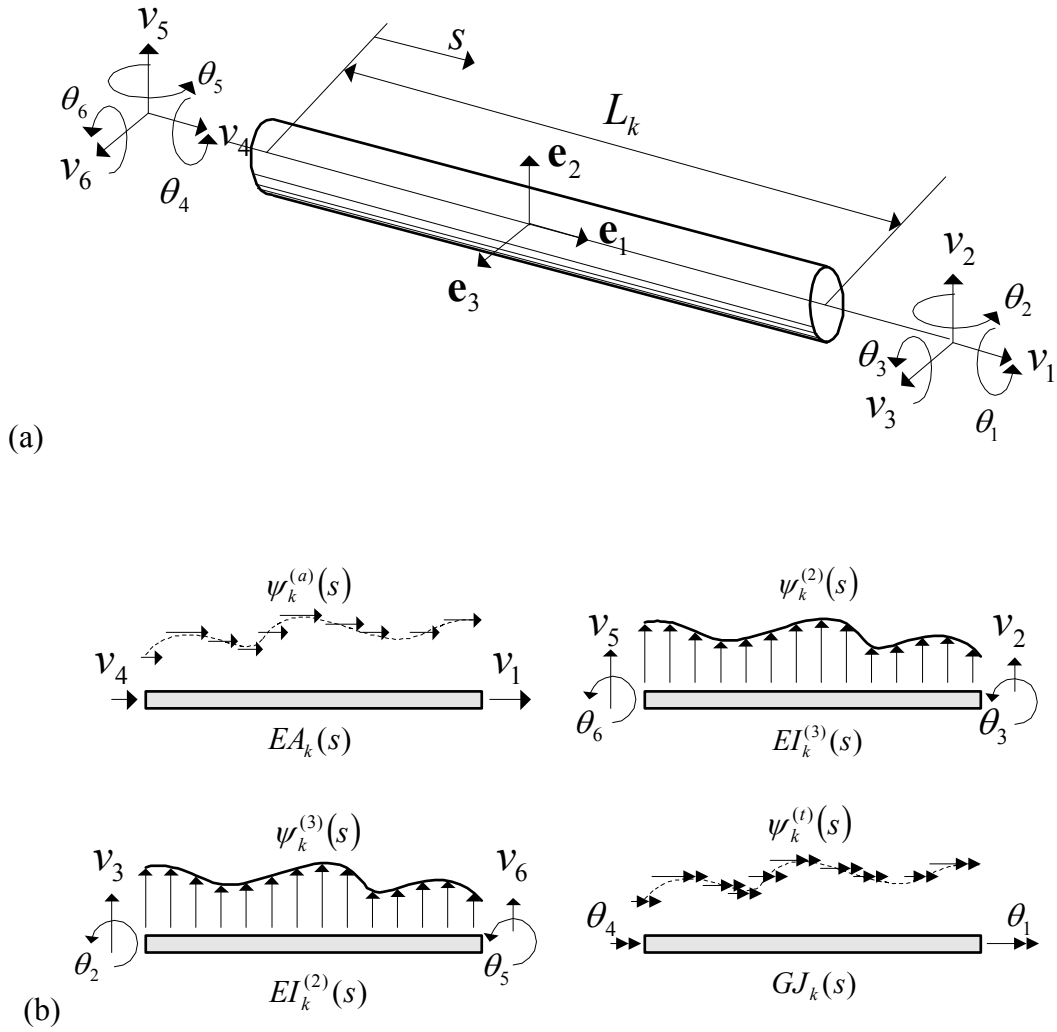


Figure 2.2 Definition of shape functions for SDOF idealization of 3D frame element: (a) configuration and end responses, (b) shape functions



Figure 2.3 A 230kV disconnect switch in service (Courtesy: PG&E)

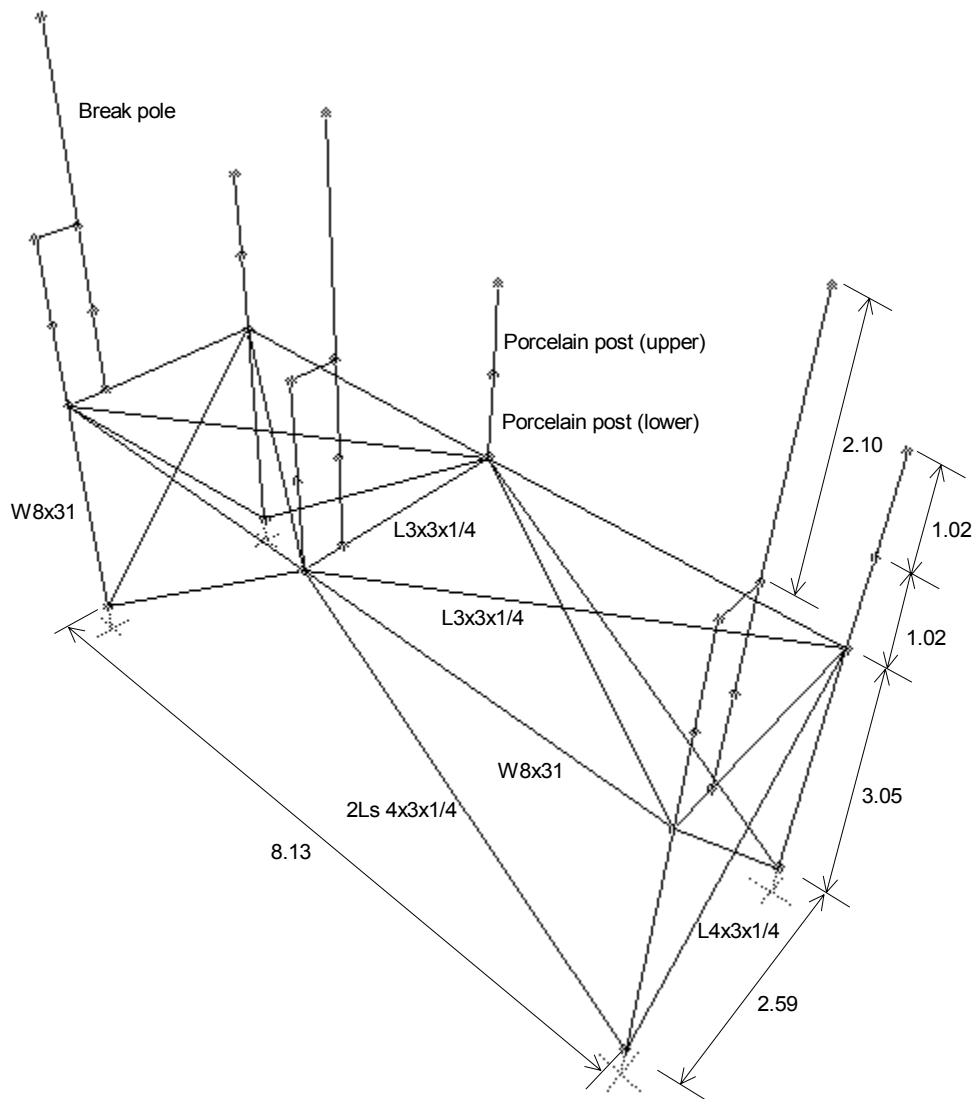


Figure 2.4 FE model for 230kV disconnect switch with three-pole, two-post porcelain insulators (unit of length: meter)





Figure 2.5 A 230kV bus support in service (Courtesy: PG&E)

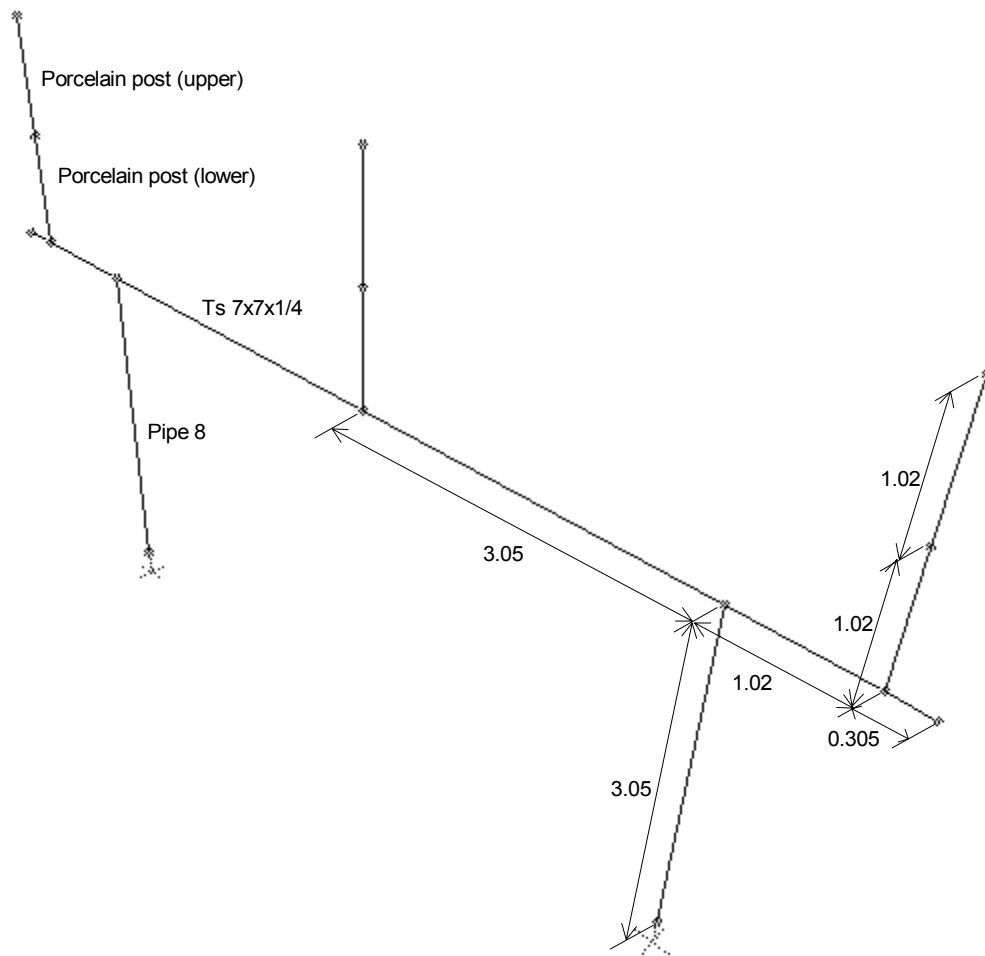


Figure 2.6 FE model for 230kV bus support with three-pole, two-post porcelain insulators (unit of length: meter)

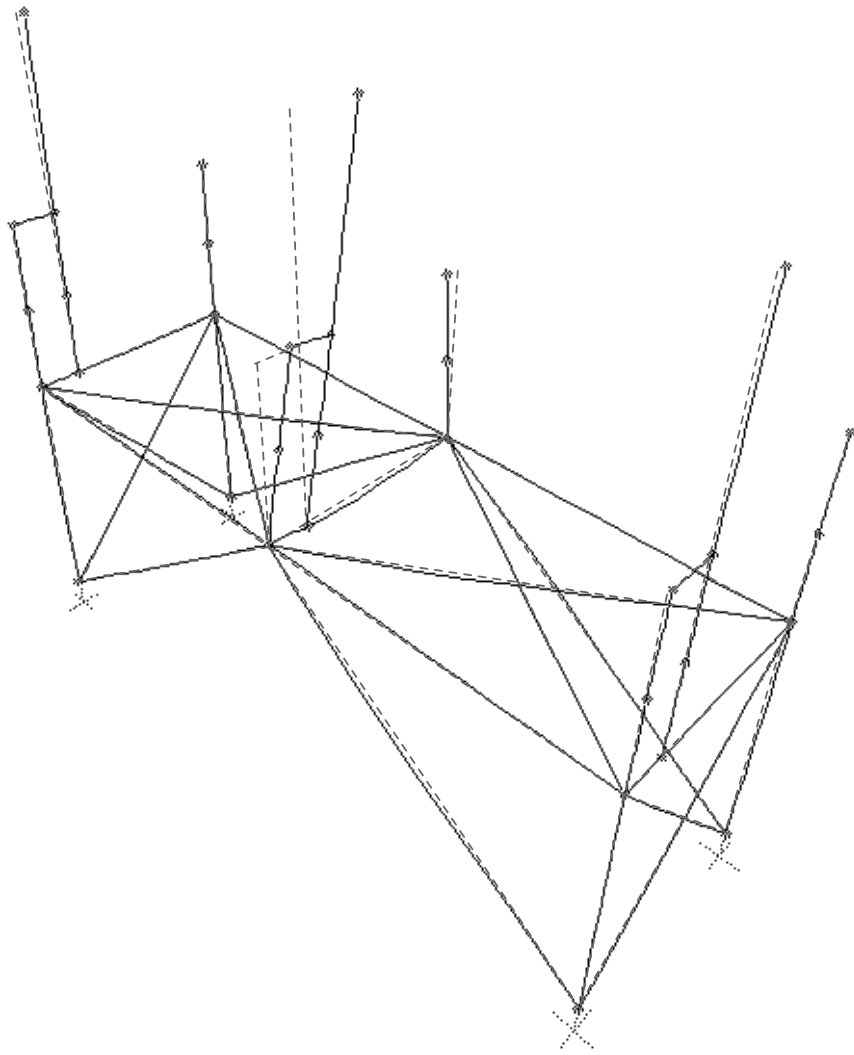


Figure 2.7 Fundamental mode of a 230kV disconnect switch (dashed line: initial configuration of the system)

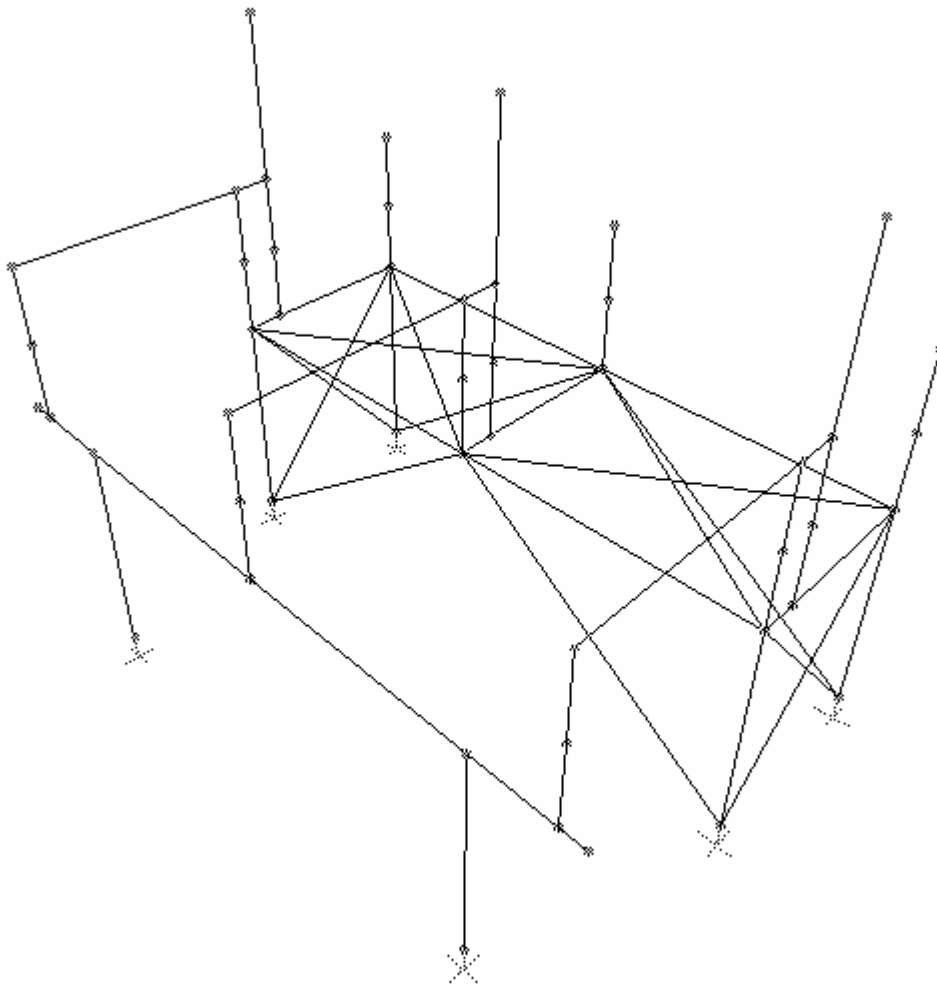


Figure 2.8 FE model for 230kV disconnect switch and bus support connected by three rigid bus connectors

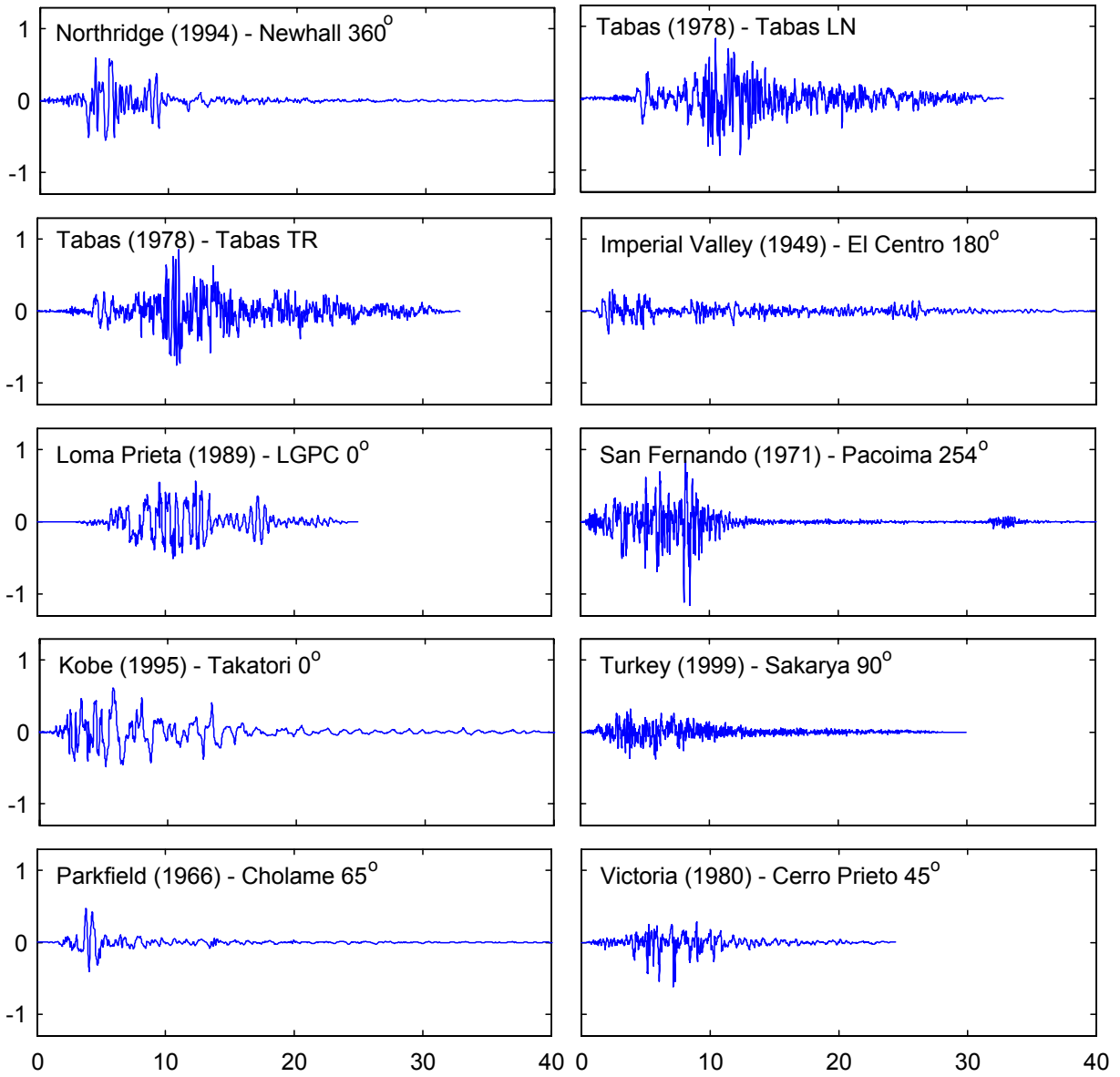


Figure 2.9 Ground motions used in the dynamic analyses; x-axis: time (sec), y-axis: acceleration (g)

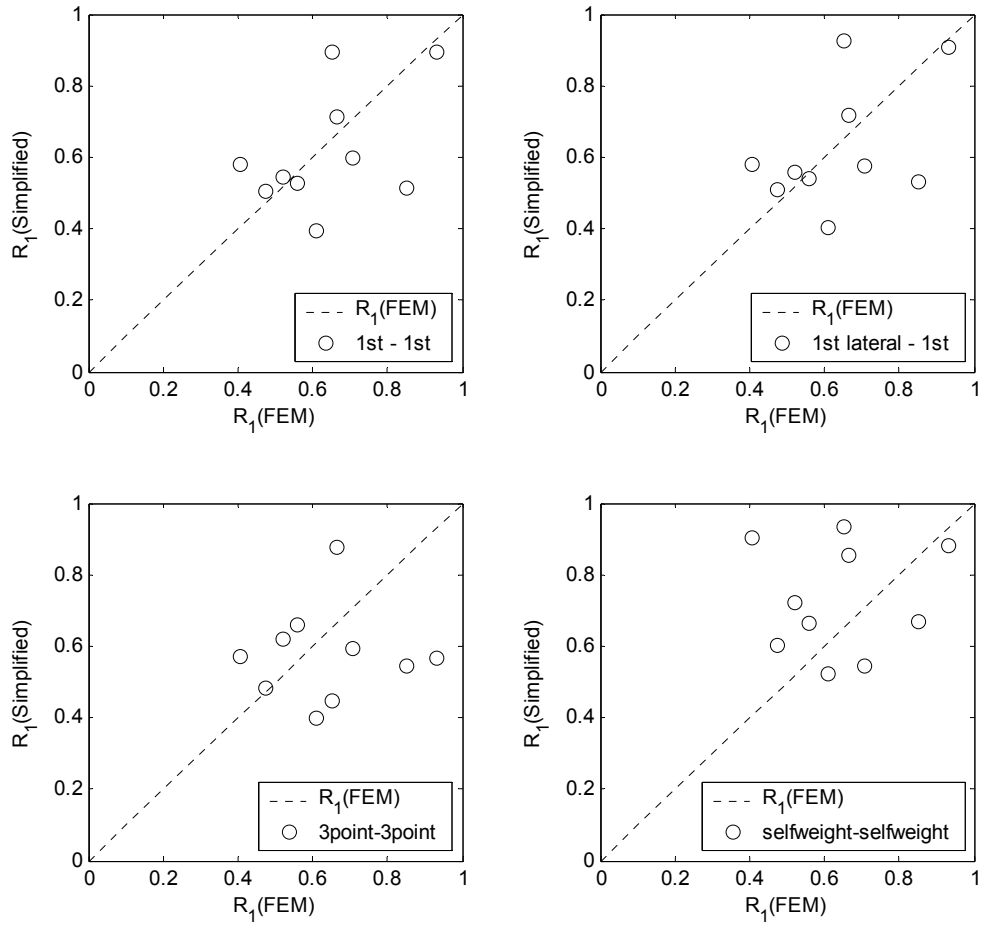


Figure 2.10 Response ratios of lower-frequency equipment (bus support)

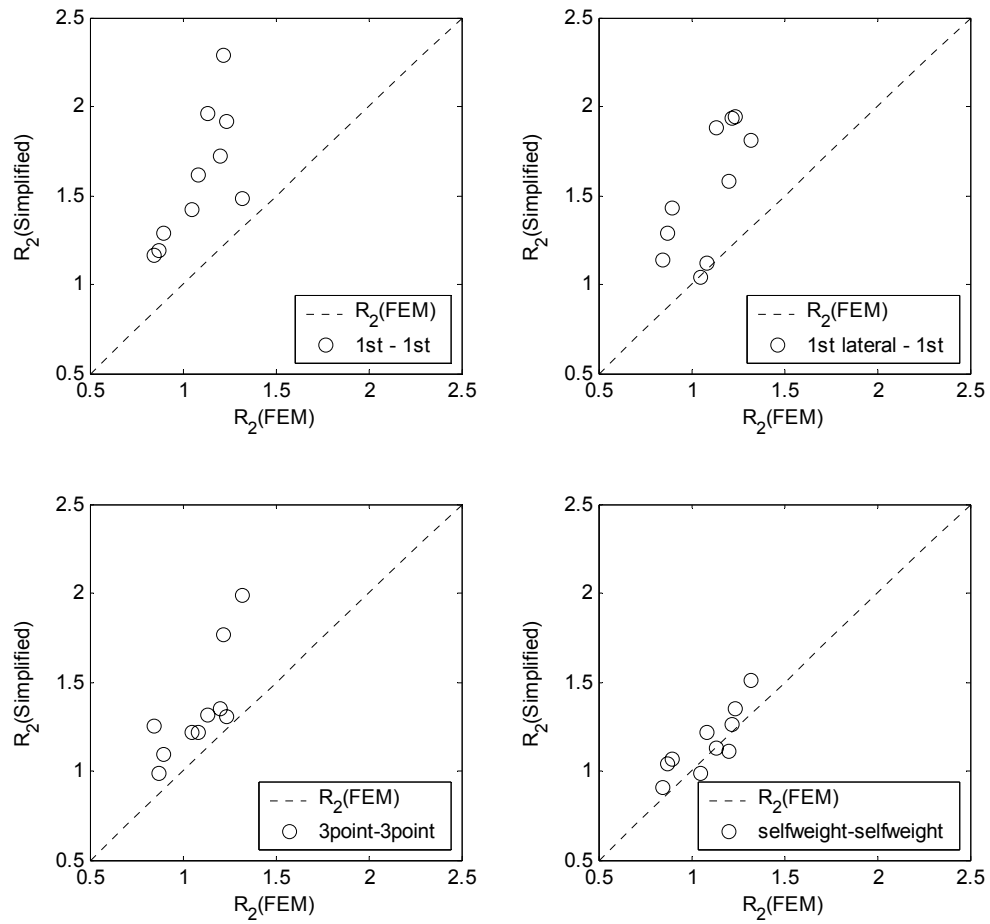


Figure 2.11 Response ratios of higher-frequency equipment (disconnect switch)





## 3 Analytical Modeling and New Design for Rigid Bus Connectors

### 3.1 INTRODUCTION

This chapter provides analytical models to describe the hysteretic behavior of rigid bus connectors for use in time history and random vibration analyses of interconnected electrical substation equipment. Two types of connectors are considered: The Flexible Strap Connector (FSC) and the Slider Connector (SC), both of which are attached to the rigid bus (RB) conductor in order to provide flexibility in the axial direction. In experiments conducted by Filiatrault *et al.* (1999) and in analytical finite element (FE) studies conducted by Der Kiureghian *et al.* (2000), it has been found that existing FSC's exhibit highly asymmetric hysteresis behavior. In the first part of this chapter, a generalized Bouc-Wen class mathematical model is developed to describe this behavior. Unlike a model previously developed by Der Kiureghian *et al.* (2000), the proposed model has constant coefficients so it can be used in nonlinear random vibration analysis by use of the equivalent linearization method (ELM). Comparison of the fitted model with experimental hysteresis loops demonstrates the accuracy of the proposed model. For the slider connector, a bi-linear model in the form of a differential equation that describes the behavior of the combination of a linear spring and a Coulomb slider is adopted. Comparison of this model with experimental results shows close agreement. Lastly, the design of a new S-shaped FSC, called *S*-FSC, is introduced. Due to its shape, this FSC has a small stiffness in the axial direction of the rigid bus and, as a result, is highly effective in reducing the adverse dynamic interaction between the connected equipment items. The hysteretic behavior of the *S*-FSC is modeled by the original Bouc-Wen model, which is found to provide good agreement in comparison with experimental results.

### 3.2 GENERALIZED BOUC-WEN HYSTERESIS MODEL FOR RIGID BUS – FLEXIBLE STRAP CONNECTORS

Many electrical substation equipment items are connected to each other through a rigid conductor bus, typically an aluminum pipe. An inverted U-shaped flexible strap connector made of copper bars is usually inserted at one end of the rigid bus to allow thermal expansion. Figure 3.1 illustrates typical RB-FSC's. The FSC's shown in the figure, FSC No. 30-2021 (asymmetric), No. 30-2022 (symmetric) and No. 30-2023 (long leg) of Pacific Gas & Electric Company, are made of three parallel straps, each strap consisting of a pair of copper bars 7.62 cm wide and 3.18 mm thick. Because of its flexibility relative to the RB, this type of FSC reduces the adverse effect of interaction between interconnected equipment items during an earthquake excitation. As pointed out by Der Kiureghian *et al.* (2000), additional reduction results from the energy dissipation capacity of the FSC.

Filiatrault *et al.* (1999) have conducted quasi-static tests of selected RB-FSC's to determine their hysteretic behavior under large deformation cyclic loading. The resulting hysteretic curves, shown as dashed lines in Figure 3.2 for the symmetric and asymmetric FSC's, incorporate geometric nonlinearity due to the large deformation, material nonlinearity due to inelastic action, and contact and friction between the bars. To investigate dynamic interaction effects in equipment items connected by the RB-FSC with this kind of complicated hysteretic behavior, the following three-stage modeling and analysis procedure was employed in Der Kiureghian *et al.* (2000): (a) detailed analysis of the FSC under cyclic loading by use of a nonlinear FE model, which is verified by comparison to experimental results; (b) global modeling of the RB-FSC by fitting a modified Bouc-Wen model to the FE results, or to experimental results if available for the particular FSC; and (c) nonlinear dynamic analysis of the RB-FSC-connected equipment system by use of the global RB-FSC model.

In their study of the cyclic behavior of the FSC's, Der Kiureghian *et al.* (2000) found that the FE analysis provided accurate estimates of the hysteretic behavior, as compared to experimental results, if material inelasticity and large deformation effects were properly accounted for. This type of analysis is useful as a virtual experimental tool. Once the FE model is verified for a particular type of FSC, it can be used to accurately predict the hysteretic behavior of other FSC's that are moderately different in shape, size or material properties, thus avoiding costly experi-

ments. Indeed, repeated but inexpensive virtual experiments by use of FE models helped us design a new FSC, which significantly reduces the adverse interaction effects. The details of the nonlinear FE models for FSC's and their usage in designing the new FSC are described later in this chapter.

For the purpose of dynamic analysis of the RB-FSC-connected system, a modified Bouc-Wen model was developed in Der Kiureghian *et al.* (2000) to mathematically represent the global hysteretic behavior of the RB-FSC. As mentioned earlier, this model was fitted either to the experimental hysteretic loop or to its prediction by a detailed FE model. Of course one could conduct nonlinear dynamic analysis of the connected system using the detailed FE model. However, the global model of the RB-FSC is much less costly, while providing sufficient accuracy for the interaction analysis. Furthermore, it allows a large number of parametric studies, which is essential for a full understanding of the interaction effect. To account for the asymmetric shape of the hysteresis loop, Der Kiureghian *et al.* (2000) developed a modified Bouc-Wen model with parameters that are functions of the time-varying responses. Unfortunately, such a model cannot be used for nonlinear random vibration analysis. Therefore, this study develops a generalized Bouc-Wen type model that has response-invariant parameters but is capable of modeling asymmetric hysteresis loops with reasonable accuracy. Before describing the details of this model, a brief review of the original Bouc endochronic model is presented below.

A memory-dependent multi-valued relation between the load and displacement of a material specimen is called hysteresis. Many mathematical models have been developed for describing and analyzing the hysteretic behavior of materials. One of the most popular is the Bouc endochronic model (Bouc 1967, Wen 1976). The model has the advantage of computational simplicity, because only one auxiliary nonlinear ordinary differential equation is needed to describe the hysteresis. Moreover, the form of the model makes it feasible for use in nonlinear random vibration analysis by the ELM (Wen 1980). Due to these benefits, the Bouc endochronic model has been widely used in the structural engineering field in spite of the fact that it violates Drucker's postulate (Bažant 1978).

Consider a SDOF oscillator with hysteresis described by a Bouc endochronic model, satisfying the dynamic equilibrium equation

$$\ddot{x} + 2\zeta_0\omega_0\dot{x} + \alpha\omega_0^2x + (1 - \alpha)\omega_0^2z = f(t)/m \quad (3.1)$$

where  $x$ ,  $\dot{x}$  and  $\ddot{x}$  denote the displacement, velocity and acceleration of the oscillator, respectively,  $m$  is the mass of the oscillator,  $\omega_0$  is the natural frequency,  $\zeta_0$  is the viscous damping ratio,  $f(t)$  is the external force,  $\alpha$  is the post to pre-yield stiffness ratio, and  $z$  is the auxiliary or internal variable (Capecchi & de Felice 2001) that represents the plasticity of the oscillator. The evolution of  $z$  is determined by an auxiliary ordinary differential equation involving  $z$ ,  $\dot{z}$ ,  $x$  and  $\dot{x}$ .

The auxiliary differential equation originally proposed by Bouc (1967) is

$$\dot{z} = \dot{x} \{ A - |z| [\beta + \gamma \operatorname{sgn}(\dot{x}z)] \} \quad (3.2)$$

where  $A$  is the parameter scaling the hysteresis loop,  $\beta$  and  $\gamma$  are the parameters controlling the shape of the hysteresis loop, and  $\operatorname{sgn}(\cdot)$  is the signum function. Wen (1976) generalized this model, so as to control the sharpness of the hysteresis in transition from elastic to inelastic region, to the form

$$\dot{z} = \dot{x} \{ A - |z|^n [\beta + \gamma \operatorname{sgn}(\dot{x}z)] \} \quad (3.3)$$

where  $n$  is the parameter controlling the sharpness. The case  $n \rightarrow \infty$  corresponds to the perfect elasto-plastic material. Figure 3.3 depicts the relation between  $x$  and  $z$  for selected values of parameters  $\gamma$  and  $\beta$  as determined by (3.2) for  $A=1$  or (3.3) with  $A=1$  and  $n=1$ . It is observed that a variety of hysteresis shapes can be achieved by proper selection of the shape-control parameters  $\beta$  and  $\gamma$ .

Wen (1980) demonstrated the use of the Bouc-Wen model for nonlinear random vibration analysis by use of the ELM. With this method, one can approximately obtain the second moments (variances and covariances) of the responses of a hysteretic oscillator subjected to random Gaussian excitation. Chapter 4 deals with the details of this analysis method. It is important to note that this method does not rely on the Krylov-Bogoliubov (K-B) technique (Krylov & Bogoliubov 1943), which assumes that the response process is narrow-band and well represented by a sinusoidal oscillation. The responses of a multi-degree-of-freedom inelastic structure can be quite wide band. Due to its narrow-band assumption, the K-B technique could overestimate the energy dissipation capacity of a structure, which may lead to unconservative results. In this sense, the ELM with a Bouc endochronic model may provide more accurate solutions to the broad-band

response of inelastic structures.

To effectively use the ELM with a Bouc endochronic model following the method proposed by Wen, it is essential to derive closed form solutions for the expectations of the derivatives of the nonlinear function in the auxiliary differential equation (3.2) or (3.3) with respect to the state variables, and express them in terms of the second moments of the response quantities. If the parameters in the auxiliary equation are complicated or are algorithmic functions of the state variables, then one cannot practically use the Bouc endochronic model for random vibration analysis by the ELM. Such is the case for the modified Bouc-Wen model developed in Der Kiureghian *et al.* (2000), where the model parameters are made functions of time in order to closely fit the asymmetric hysteresis loop.

Over the years, the Bouc endochronic model has been modified in order to account for various types of hysteresis-related phenomena, such as degrading behavior (Baber & Wen 1979), pinching behavior (Baber & Noori 1986) and asymmetric hysteresis (Wang & Wen 1998). Wang & Wen's asymmetric hysteretic model has the auxiliary differential equation

$$\dot{z} = \dot{x} \left\{ \frac{A}{\eta} - |z|^n \frac{\nu}{\eta} [\beta \operatorname{sgn}(\dot{x}z) + \gamma + \phi(\operatorname{sgn}(z) + \operatorname{sgn}(\dot{x}))] \right\} \quad (3.4)$$

where  $\eta$  is a parameter that controls the pre-yielding stiffness,  $\nu$  is a parameter that controls the ultimate strength, and  $\phi$  is a parameter that accounts for the asymmetric yielding behavior. As shown later in this chapter, even the above model provides little flexibility in describing the highly asymmetric hysteresis of the RB-FSC's. Therefore, the need arises to develop a new endochronic model that not only has sufficient degree of freedom to accurately describe the highly asymmetric hysteretic behavior of RB-FSC's, but also has a simple form such that random vibration analysis by the ELM is possible. Toward that end, the shape-control mechanism of the Bouc endochronic model is analyzed and the model is generalized such that the shape can be controlled by use of a set of response-invariant model parameters in each phase determined by the signs of the state variables.

In general, the auxiliary differential equation of the Bouc endochronic model can be written in the form.

$$\dot{z} = \dot{x} [A - |z|^n \psi(x, \dot{x}, z)] \quad (3.5)$$

where  $\psi(x, \dot{x}, z)$  is a nonlinear function of  $x$ ,  $\dot{x}$  and  $z$ . Multiplying both sides of (3.5) by  $dt/dx$ , one obtains

$$\frac{dz}{dx} = A - |z|^n \psi(x, \dot{x}, z) \quad (3.6)$$

The above equation shows that the slope of the hysteresis loop in the  $x-z$  plane,  $dz/dx$ , is controlled by the ‘shape-control’ function  $\psi(\cdot)$  within each phase determined by the signs of  $x$ ,  $\dot{x}$  and  $z$ . Therefore, the more independent values the shape-control function  $\psi(\cdot)$  can assume within the different phases determined by the signs of  $x$ ,  $\dot{x}$  and  $z$ , the higher flexibility the model will have in shaping the hysteresis loop.

The shape-control functions of the original Bouc-Wen model (Wen 1976) and the model by Wang & Wen (1998), respectively, are

$$\Psi_{\text{Bouc-Wen}} = \beta + \gamma \operatorname{sgn}(\dot{x}z) \quad (3.7)$$

$$\Psi_{\text{Wang-Wen}} = \frac{\nu}{\eta} \{ \beta \operatorname{sgn}(\dot{x}z) + \gamma + \phi [\operatorname{sgn}(z) + \operatorname{sgn}(\dot{x})] \} \quad (3.8)$$

It is evident that the shape-control functions of the above two models can have four different phases defined by the signs of  $\dot{x}$  and  $z$ . The four phases are: (a) ( $z \geq 0, \dot{x} \geq 0$ ), (b) ( $z \geq 0, \dot{x} \leq 0$ ), (c) ( $z \leq 0, \dot{x} \leq 0$ ) and (d) ( $z \leq 0, \dot{x} \geq 0$ ). Figure 3.4 shows the values of the shape-control functions for the above models within the four phases in the  $x-z$  plane during a full-cycle test. The original Bouc-Wen model has only two independent values for the shape-control function:  $\beta + \gamma$  for phases (a) and (c), and  $\beta - \gamma$  for phases (b) and (d). The model by Wang and Wen has three independent values for the same four phases:  $\nu/\eta (\beta + 2\phi + \gamma)$  for phase (a),  $\nu/\eta (\beta - 2\phi + \gamma)$  for phase (c), and  $\nu/\eta (-\beta + \gamma)$  for phases (b) and (d). Therefore, one can say that the Bouc-Wen model is a two-degree-of-freedom shape-control model, and the model by Wang & Wen is a three-degree-of-freedom shape-control model.

As can be seen in Figure 3.2, the hysteresis loops of the RB-FSC’s are affected not only by the signs of  $\dot{x}$  and  $z$ , but also by the sign of the displacement  $x$ , because the hysteretic behavior of the FSC’s in tension is different from that in compression. That is the reason for the existing models not being able to fit well with the experimental data, unless the parameters are

made functions of the response quantities. Naturally, it would be desirable to develop a shape-control function that can assume different values for all the phases determined by the signs of  $x$ ,  $\dot{x}$  and  $z$ . With this motivation, the following shape-control function is proposed:

$$\psi = \beta_1 \operatorname{sgn}(\dot{x}z) + \beta_2 \operatorname{sgn}(x\dot{x}) + \beta_3 \operatorname{sgn}(xz) + \beta_4 \operatorname{sgn}(\dot{x}) + \beta_5 \operatorname{sgn}(z) + \beta_6 \operatorname{sgn}(x) \quad (3.9)$$

where  $\beta_1, \dots, \beta_6$  are response-invariant parameters. The proposed model can control the value of the shape-control function at six phases, i.e., it is a six-degree-of-freedom shape-control model. Figure 3.5 shows the six different phases of the model determined by the combinations of the signs of  $x$ ,  $\dot{x}$ , and  $z$  during a full-cycle test. In this figure,  $\psi_i$ ,  $i = 1, \dots, 6$ , denotes the value of the shape-control function  $\psi(x, \dot{x}, z)$  at the  $i$ -th phase. Table 3.1 lists the sign combinations of  $x$ ,  $\dot{x}$ , and  $z$  for the six different phases in Figure 3.5 and the corresponding values of the shape-control function.

The linear relationship between the values of  $\psi_i$  and  $\beta_i$  observed in Table 3.1 can be described in the matrix form

$$\begin{bmatrix} \psi_1 \\ \psi_2 \\ \psi_3 \\ \psi_4 \\ \psi_5 \\ \psi_6 \end{bmatrix} = \begin{bmatrix} 1 & 1 & 1 & 1 & 1 & 1 \\ -1 & -1 & 1 & -1 & 1 & 1 \\ 1 & -1 & -1 & -1 & -1 & 1 \\ 1 & 1 & 1 & -1 & -1 & -1 \\ -1 & -1 & 1 & 1 & -1 & -1 \\ 1 & -1 & -1 & 1 & 1 & -1 \end{bmatrix} \begin{bmatrix} \beta_1 \\ \beta_2 \\ \beta_3 \\ \beta_4 \\ \beta_5 \\ \beta_6 \end{bmatrix} \quad (3.10)$$

Since the transformation matrix in (3.10) is non-singular, one can solve for  $\beta_i$ 's in terms of the desired values of the shape-control function values  $\psi_i$  by matrix inversion:

$$\begin{bmatrix} \beta_1 \\ \beta_2 \\ \beta_3 \\ \beta_4 \\ \beta_5 \\ \beta_6 \end{bmatrix} = \frac{1}{4} \begin{bmatrix} 1 & 0 & 1 & 1 & 0 & 1 \\ 0 & -1 & -1 & 0 & -1 & -1 \\ 1 & 1 & 0 & 1 & 1 & 0 \\ 1 & -1 & 0 & -1 & 1 & 0 \\ 0 & 1 & -1 & 0 & -1 & 1 \\ 1 & 0 & 1 & -1 & 0 & -1 \end{bmatrix} \begin{bmatrix} \psi_1 \\ \psi_2 \\ \psi_3 \\ \psi_4 \\ \psi_5 \\ \psi_6 \end{bmatrix} \quad (3.11)$$

A systematic procedure for fitting the model in (3.9) to experimental data can now be developed by use of the above matrix equation. First, one selects a set of trial values of the  $\psi_i$ 's and com-

putes the corresponding parameters  $\beta_i$  by use of (3.11). The theoretical hysteresis loops are then plotted and compared with the experimental loops. Adjustments in the  $\psi_i$ 's are then made to reduce the difference between the theoretical and experimental loops by a suitable measure. For example, one can use an optimization algorithm to determine values of  $\psi_i$  that minimize the sum of squared errors over each phase or over the entire hysteresis loop. Next, the parameters  $\beta_i$  are computed for the adjusted  $\psi_i$  values by use of (3.11). This process is continued until a set of the model parameters that minimize the difference between the theoretical and experimental hysteresis loops is achieved.

Figure 3.2 compares the hysteresis loops of RB-FSC 30-2022 (Figure 3.2a) and RB-FSC 30-2021 (Figure 3.5b) based on the proposed model (solid lines) with those obtained in the experiments conducted by Filiatrault *et al.* (1999) (dashed lines). The model parameters for RB-FSC 30-2022 are  $k_0 = 35.5$  kN/m,  $\alpha = 0.1$ ,  $A = 1.0$ ,  $n = 1$ ,  $\beta_1 = 0.419$ ,  $\beta_2 = -0.193$ ,  $\beta_3 = 0.174$ ,  $\beta_4 = 0.0901$ ,  $\beta_5 = -0.156$  and  $\beta_6 = -0.0564$ . The parameters for RB-FSC 30-2021 are  $k_0 = 49.2$  kN/m,  $\alpha = 0.1$ ,  $A = 1.0$ ,  $n = 1$ ,  $\beta_1 = 0.470$ ,  $\beta_2 = -0.118$ ,  $\beta_3 = 0.0294$ ,  $\beta_4 = 0.115$ ,  $\beta_5 = -0.121$  and  $\beta_6 = -0.112$ . It is evident that the model is able to represent the hysteretic behavior of the RB-FSC's with good accuracy, including the strong asymmetry in the loops. The model yields almost as accurate results as the FE model (see Figure 3.6) or the modified Bouc-Wen model developed by Der Kiureghian *et al.* (2000) (see Figure 3.7). It is noteworthy that the good agreement of the proposed model is accomplished by defining the model parameters as constants throughout the loading history, and not as complicated functions of the responses as done in Der Kiureghian *et al.* (2000). This feature greatly simplifies the dynamic analysis of the interaction problem. Furthermore, it allows us to conduct nonlinear random vibration analysis of the RB-FSC-connected equipment items by use of the ELM.

### 3.3 BI-LINEAR HYSTERESIS MODEL FOR SLIDER CONNECTOR

A second type of connector used with rigid bus conductors is the slider connector (SC). Figure 3.8 shows the specimens of two SC's investigated in this study. They are the 'old' SC (PG&E Type 221A, 30-4462) in Figure 3.8a and the 'improved' SC in Figure 3.8b. In the 'old' SC, the shaft or plunger is aligned with the axis of the aluminum bus pipe, which is held by two flexible cables welded at the outside of the pipe. As the two connected equipment items move relative to



one another, the shaft slides against the inner surface of the pipe, while the cables provide resisting forces. Beyond the displacement limit in compression, the aluminum pipe makes contact with the terminal pad, in which case the slider bus loses its flexibility. Beyond the tension limit, the shaft comes out of the aluminum pipe, in which case the assembly may entirely fail to function. These horizontal displacement limits, or maximum strokes, for the old SC are measured as  $\pm 8.89$  cm (Filiatrault *et al.* 1999). The ‘improved’ SC has the maximum strokes  $\pm 12.7$  cm (Stearns & Filiatrault 2003). It also has four cables spread out equally around the pipe to avoid possible damage by torsion. The cables are welded to the connector’s own tube, in which the shaft slides. To prevent the shaft from sliding out of the tube, a stopper is installed at the end of the plunger.

As the SC experiences relative displacement, a friction force arises from the shaft sliding against the inner surface of the pipe, while the cables provide elastic resisting forces. Therefore, the slider bus can be considered as a Coulomb-friction element coupled with elastic springs, as shown in Figure 3.9. The mechanical behavior of the springs can be analytically predicted by use of a FE model. However, it is difficult to construct a FE model for the Coulomb-friction element. This is because the friction force is strongly dependent on the alignment of the shaft, which is practically impossible to predict for field conditions. Therefore, this study constructs a mathematical model of the RB-SC by fitting to hysteresis loops obtained in experiments.

Quasi-static tests of two rigid bus assemblies with the SC were conducted at the University of California, San Diego, by Filiatrault *et al.* (1999) and Stearns & Filiatrault (2003) to investigate the hysteretic behavior of the sliders. The test specimen of the older SC in Figure 3.8a consists of a 3.05-meter long, 10.2-cm diameter aluminum pipe with a SC PG&E Type 221A, 30-4462 attached at one end. The specimen was subjected to cyclic displacements in the axial direction of the pipe within the range  $\pm 8.89$  cm. The improved SC in Figure 3.8b was tested through cyclic displacements within the range  $\pm 10.2$  cm.

Figure 3.10 shows the hysteresis loops of the SC’s as obtained by Filiatrault *et al.* (1999) and Stearns & Filiatrault (2003) under a specified load protocol. It is observed that the hysteresis loops have almost a perfect bi-linear shape. A slight stiffening effect is observed in the tension zone. This is probably caused by the stiffening of the connecting cables as they are stretched. The yielding force for the Coulomb slider of the old slider was estimated by Filiatrault *et al.*

(1999) as 236 N. The yielding displacement was measured as 0.0203 cm. The post-yielding stiffness is estimated as 14.5 kN/m. Since the parameters for the improved SC were not reported in Stearns & Filiatrault (2003), the yielding force and displacement, and the post-yielding stiffness are roughly estimated as 236 N, 0.0203 cm and 7.71 kN/m, respectively, from the model fitting.

Several analytical models exist for describing the bi-linear hysteresis behavior with initial stiffness  $k_0$ , yielding displacement  $x_y$ , and post-to-pre-yield stiffness ratio  $\alpha$ , as defined in Figure 3.11. One possible method is to use a system of nonlinear differential equations. First, we represent it as a parallel assembly of a linear spring (*Spring I*) and a Coulomb friction slider in series with a second linear spring (*Spring II*), as shown in Figure 3.9. Let *Spring I* have the stiffness  $\alpha k_0$  and *Spring II* have the stiffness  $(1-\alpha)k_0$ . Assume the Coulomb slider does not slide until its force reaches the yielding force,  $(1-\alpha)k_0 x_y$ . Since up to that point the system acts as a parallel assembly of two linear springs, the total initial stiffness is simply the sum of the two stiffnesses, i.e.,  $\alpha k_0 + (1-\alpha)k_0 = k_0$ . When the yield level is exceeded and the Coulomb slider starts sliding, the *Spring II*-friction slider series assembly does not produce any resisting force. Therefore, the post-yielding stiffness is  $\alpha k_0$ . It is obvious that the relative displacement of the spring attached to the Coulomb slider equals the total displacement  $x$  whenever  $-x_y < x < x_y$ , and it equals  $x_y$  or  $-x_y$  otherwise.

The differential equation in (3.1) can be used to describe the mechanical behavior of the above assembly. In this case, the auxiliary variable  $z$  describes the relative displacement of the spring in the series assembly in Figure 3.9. The aforementioned conditions on the variable  $z$  are satisfied by the auxiliary nonlinear differential equation (Kaul & Penzien 1974):

$$\dot{z} = \dot{x} [u(z + x_y) - u(z - x_y) + u(z - x_y)u(-\dot{x}) + u(-z - x_y)u(\dot{x})] \quad (3.12)$$

where  $u(\cdot)$  denotes the unit step function. This study employs the above differential equation together with (3.1) to describe the behavior of the slider bus. The model is fitted to the parameter values measured by Filiatrault *et al.* (1999) and Stearns & Filiatrault (2003), i.e.,  $x_y = 0.0203$  cm,  $k_0 = 1,163$  kN/m, and  $\alpha = 0.0125$  for the old SC and  $x_y = 0.0203$  cm,  $k_0 = 1,163$  kN/m, and  $\alpha = 6.64 \times 10^{-3}$  for the improved SC. Figure 3.12 compares the theoretical hysteresis loops obtained for this model under the same quasi-static loading as in the test performed in UCSD. This numerical result was obtained by an adaptive Runge-Kutta-Fehlberg method (Fehlberg 1969), which automatically varies the integration time step with a relative tolerance of  $10^{-6}$ . It is seen in

Figure 3.12 that the above theoretical model provides a reasonably accurate representation of the hysteresis behavior of the slider bus.

This modeling approach adopted in this chapter helps to avoid complicated and algorithmic mechanical models in static or time history analysis of connected equipment items. Furthermore, the analytical models developed herein allow nonlinear random vibration analysis by use of the ELM. Chapter 4 deals with this topic.

### **3.4 DEVELOPMENT AND ANALYTICAL MODELING OF S-FSC**

#### **3.4.1 Development of S-FSC**

Parametric studies by Der Kiureghian *et al.* (1999) of linearly connected equipment items have shown that the dynamic interaction effect can strongly amplify the response of the higher-frequency equipment item. Furthermore, it is found that lowering the stiffness of the connecting element can help reduce the adverse interaction effects on the higher-frequency equipment items. The energy dissipation capacity of the connecting element also helps to reduce the interaction effect.

As reported in Chapter 4, nonlinear random vibration analyses of equipment items connected by RB-FSC demonstrate that the nonlinear behavior of the FSC tends to considerably reduce the interaction effect. The benefits of the nonlinear behavior are due to two factors: (a) loss of stiffness of the FSC due to plastic deformation, and (b) energy dissipation of the FSC during its cyclic inelastic deformation. However, as confirmed by the results in Chapter 4, the amount of reduction in the interaction effect depends on the intensity of ground motion, which is intrinsically random. Furthermore, inelastic deformation in an FSC may require retooling or replacement after an earthquake event, which may cause significant restoration cost or delay of service.

An FSC that is highly flexible would tend to experience little inelastic deformation during an earthquake motion, thus avoiding nonlinear or inelastic behavior. Such an FSC can significantly reduce the adverse interaction effect, independently of the intensity of ground motion. Furthermore, no retooling or replacement after an earthquake would be necessary for such an FSC, since the FSC would not experience a significant plastic deformation. It is of course possible to think of installing a special device in the rigid bus or the FSC for energy dissipation. How-

ever, in general it would be less costly to design an FSC with a higher flexibility than to acquire expensive energy dissipation devices.

In the analysis and testing of U-shaped FSC's, it has been observed that contacts between the two legs of the FSC may occur during the earthquake excitation, if the distance between the two legs is not sufficiently large. In the event of such a contact, the FSC instantly loses its flexibility in the longitudinal direction of the rigid bus, and the interaction effect is likely to sharply increase in consequence. Therefore, an FSC also needs to have sufficient displacement capacity in order to maintain the flexibility of the RB-FSC assembly during the motion. Hereafter we denote this type of displacement capacity as the *stroke* of the FSC.

In summary, it is desirable to design a highly flexible FSC with a large stroke, which can reduce the interaction effect without experiencing inelastic deformation. Consideration should also be given to electrical requirements, such as the capacity to carry a certain electrical load and clearance requirements. Experience gained from nonlinear FE analyses of the existing FSC's, leads us to modify the shape of the existing FSC's in order to achieve the above desirable characteristics and satisfy the electrical requirements.

In order to gain a better insight, we first examine the mechanical behaviors of the existing FSC designs, PG&E 30-2021, 30-2022 and 30-2023, under cyclic loading. Figures 3.13, 3.14 and 3.15 show the original configurations and extreme deformed shapes in compression and tension, which are produced by detailed FE analyses employing a 1-dimensional elasto-plastic model for each strap.

In order to make a comparative study of the existing FSC's with the FSC to be proposed, Table 3.2 lists some key characteristics of each FSC obtained from FE analysis. The first three rows of this table list the initial stiffnesses of the FSC's in the longitudinal, transverse and vertical directions of the rigid bus, respectively. The stiffness in the longitudinal direction is defined as the tip-to-tip equivalent stiffness when the FSC experiences a cyclic displacement of amplitude 2.54 cm in each longitudinal direction. The stiffnesses in the transverse and vertical directions are defined for small displacements, so they essentially represent the stiffnesses under linear behavior. Numbers in parenthesis in each row represent the equivalent stiffnesses for an RB-FSC assembly, where the RB is a 3.05 meter aluminum pipe of inner radius 5.11 cm and outer radius 5.72 cm. The elastic modulus of aluminum is assumed to be  $E = 68.9$  GPa for this analy-

sis. In order to quantify the energy dissipation capacity of each FSC, the energy dissipated during a common cycle of displacement loading shown as the cycle ABCDE in Figure 3.16 is computed for each FSC and is listed in the fourth row of Table 3.2. The fifth row of the table shows the maximum stroke of each FSC. This is computed by FE analysis as the maximum inward (compressive) displacement until contact by straps on opposite legs is made. The next two rows in the table compare the maximum vertical displacement experienced by the RB-FSC as the FSC is deformed into its extreme compressive (C) and elongated (E) shapes. Finally, the last two rows in the table list the dimensions of each FSC.

The deformed shapes predicted by FE analysis in Figure 3.13 and 3.14 show that the the FSC designs PG&E 30-2021 and 30-2022 mainly rely on the opening-closing motions of the main bends to accommodate the horizontal displacement. These motions induce large deformations around the bends, which consequently lead to inelastic material behavior at these points. In the case of PG&E 30-2021 in Figure 3.13, the asymmetric configuration transforms the horizontal displacement also to the axial extension of the vertical leg, thus further amplifying the large deformation around the bend. This FSC requires a larger force for the same amount of displacement. As a result, the tip-to-tip equivalent stiffness of this FSC under  $\pm 2.54$  cm cyclic longitudinal displacement is 49.2 kN/m, whereas that for PG&E 30-2022 is 35.6 kN/m. The asymmetric shape of PG&E 30-2021 also results in a large deformation in the vertical direction when the FSC is compressed. The FE analyses show that the maximum strokes (inward displacement capacity before contact between the straps on opposite legs occurs) for the two FSC's are 12.7 cm and 13.0 cm, respectively. Furthermore, the energies dissipated during a common cycle of displacement loading (ABCDE in Figure 3.16) are computed as 701 N-m for PG&E 30-2021 and 637 N-m for PG&E 30-2022. It is observed that the asymmetric model (30-2021) experiences more inelastic behavior, as expected from its deformation behavior.

The FSC PG&E 30-2023 (Figure 3.15), which is a special design for connecting attachment points at different vertical levels, allows horizontal displacements of the two ends mainly through the rotation of the long vertical leg. This motion needs smaller forces for the same horizontal displacement than the previous opening-closing motion and thus induces less deformation around the bends. The tip-to-tip equivalent stiffness ( $\pm 2.54$  cm) measured in the FE analysis is as low as 10.6 kN/m. Thus, FSC PG&E 30-2023 is much more flexible than PG&E 30-2021 and 30-2022. The dissipated energy during the one-cycle in Figure 3.16 amounts to 116 N-m, which

is much less than those for PG&E 30-2021 and PG&E 30-2022. These numerical results confirm that the FSC design PG&E 30-2023 is more flexible than the previous designs and it responds to displacement loading by much smaller inelasticity. Obviously, the longer the vertical leg becomes, the more flexible the FSC will be. However, the length of the vertical leg of the FSC PG&E 30-2023 is designed according to the difference in the levels of the two attachment points.

Based on the above observations regarding the desirable characteristics of an FSC and the behaviors of existing FSC's, a new FSC design with an *S* shape is proposed (Figure 3.17). This FSC, named *S*-FSC, is made of the same material and has the same detail as the existing FSC's, i.e., it is made of three parallel straps, each strap consisting of a pair of copper bars 7.62 cm wide and 0.318 cm thick. Thus, it satisfies electrical requirements as a conductor. The behavior of the *S*-FSC under large deformation, as predicted by FE analysis, is depicted in Figure 3.18. This analysis shows that, due to its anti-symmetric shape, the *S*-FSC responds to the horizontal displacement mainly through the rotation of the long vertical leg. The difference with FSC PG&E 30-2023 is that the *S* shape allows the rotation to occur while the two attachment points are at the same level, a condition that applies to most practical situations. The *S*-FSC shown in Figure 3.17, *S*-FSC (1), has the equivalent stiffness 7.13 kN/m in the longitudinal direction, which is significantly smaller than that of any of the three existing FSC's. As noted in Table 3.2, *S*-FSC also has consistently smaller stiffness than the previous FSC's in the transverse and vertical directions. This is advantageous in reducing the interaction effect between the connected equipment items for motions in the transverse and vertical directions.

Another advantage of *S*-FSC is that one can control the stiffness of the FSC by adjusting the length of the vertical leg. For example, the *S*-FSC (2) gains further flexibility in each direction by lengthening the vertical leg of *S*-FSC (1) by 50%. The dissipated energy during the one-cycle loading in Figure 3.16 is 27.5 N-m for *S*-FSC (1) and 1.01 N-m for *S*-FSC (2). These small amounts of energy dissipation imply that the *S*-FSC's behave almost elastically for the same displacement for which the existing FSC's experience significant inelasticity. The strokes for *S*-FSC's are about 25.4 cm, which is much larger than those of PG&E 30-2021 and PG&E 30-2022.

A possible concern for the *S*-FSC might be that its lower extension may violate electrical clearance requirements. If that is the case, then *S*-FSC can be positioned in the horizontal plane. In that case, stiffnesses listed in the second and third rows of Table 3.2 will have to be exchanged.

### 3.4.2 Bouc-Wen Hysteresis Model for *S*-FSC

In order to confirm the expected benefits of *S*-FSC, quasi-static and shake table tests were performed by Stearns & Filiatrault (2003) for two specimens specifically manufactured for this purpose on order from PG&E. Unfortunately, the first specimen was mistakenly manufactured in the form shown in Figure 3.18 (b). This specimen was stretched out to deform into the initial shape of the proposed design. This process induced yielding in the straps, thus affecting the hysteretic behavior of the specimen. Moreover, the re-shape process made the straps pinch together, creating friction between them. Due to these differences from the original design, the first specimen was used only for quasi-static tests within the range  $\pm 10.2$  cm. The second *S*-FSC specimen was manufactured in the correct shape. Quasi-static tests for this specimen were performed within the restricted range  $\pm 5.08$  cm in order to avoid yielding. This specimen was subsequently used in shake table tests, as described later in Chapter 4.

Figure 3.19 compares the experimental hysteresis loops of the two specimens with the FE prediction. The loops of the first specimen are much wider than those predicted by FE analysis. The specimen produces 50% lower resisting force at  $\pm 10.2$  cm displacement. It is believed that these differences are due to the pinching effect and yielding caused by the re-shaping process. Although restricted within the shorter range of  $\pm 5.08$  cm, the hysteresis loops of the second specimen show a close agreement with the FE prediction.






As an analytical model of the *S*-FSC for use in time history and nonlinear random vibration analysis, the original Bouc-Wen model in (3.1) and (3.3) is used. Figure 3.20 compares the experimental hysteresis loops of the two specimens with those by fitted Bouc-Wen models. The model parameters are  $k_0 = 7.81$  kN/m,  $\alpha = 0.0568$ ,  $A = 1$ ,  $n = 1$ ,  $\beta = 0.288$  and  $\gamma = 0.275$  for the first specimen, and  $k_0 = 8.58$  kN/m,  $\alpha = 0.206$ ,  $A = 1$ ,  $n = 1$ ,  $\beta = 0.175$  and  $\gamma = 0.176$  for the second specimen. It is seen that the Bouc-Wen model is able to describe the hysteresis behavior of the *S*-FSC with a close agreement. The Bouc-Wen model fitted to the second specimen is used for time history and nonlinear random vibration analysis by use of ELM in the remainder of this study.

Table 3.1 Values of the shape-control function for the generalized Bouc-Wen model

Phase	$x$	$\dot{x}$	$z$	$\psi(x, \dot{x}, z)$
1	+	+	+	$\psi_1 = \beta_1 + \beta_2 + \beta_3 + \beta_4 + \beta_5 + \beta_6$
2	+	-	+	$\psi_2 = -\beta_1 - \beta_2 + \beta_3 - \beta_4 + \beta_5 + \beta_6$
3	+	-	-	$\psi_3 = \beta_1 - \beta_2 - \beta_3 - \beta_4 - \beta_5 + \beta_6$
4	-	-	-	$\psi_4 = \beta_1 + \beta_2 + \beta_3 - \beta_4 - \beta_5 - \beta_6$
5	-	+	-	$\psi_5 = -\beta_1 - \beta_2 + \beta_3 + \beta_4 - \beta_5 - \beta_6$
6	-	+	+	$\psi_6 = \beta_1 - \beta_2 - \beta_3 + \beta_4 + \beta_5 - \beta_6$



Table 3.2 Comparison of FSC characteristics

FSC		PG&E 30-2021	PG&E 30-2022	PG&E 30-2023	S-FSC (1)	S-FSC (2)
Profile						
Initial Stiffness (kN/m)	Longi.	49.2 (49.2)	35.6 (35.6)	10.6 (10.6)	7.13 (7.13)	2.61 (2.61)
	Trans.	58.5 (16.0)	46.8 (15.0)	18.4 (10.0)	9.05 (6.41)	4.89 (3.99)
	Vert.	62.9 (16.3)	39.1 (14.1)	40.6 (14.3)	15.4 (9.07)	12.3 (7.90)
Dissipated Energy (N-m)		701	637	116	27.5	1.01
Maximum Stroke (cm)		12.7	13.0	27.9	25.9	25.4
Vertical Displ. (cm)	(C)	-5.21	-0.635	0.787	-2.87	-1.78
	(E)	0.914	-1.04	-4.29	2.84	1.65
Dimen- sions (cm)	Horiz.	33.8	40.6	40.6	54.0	54.0
	Vert.	27.7	23.8	45.7	52.7	74.3

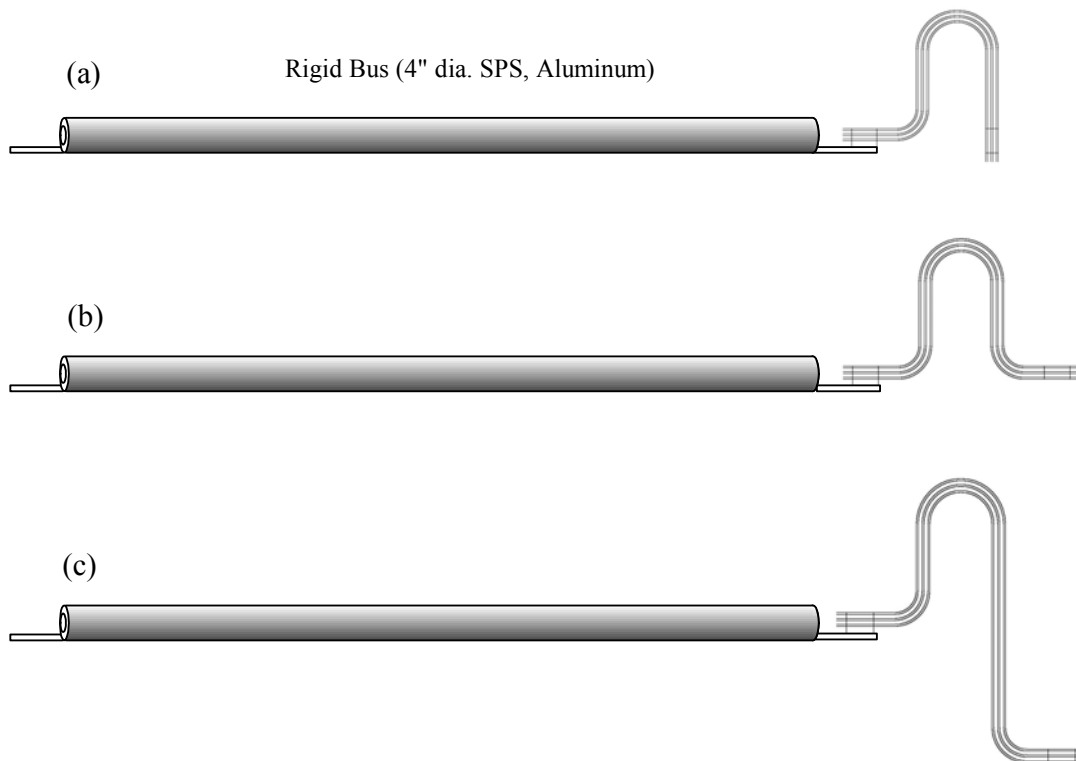


Figure 3.1 Rigid bus conductors fitted with flexible strap connectors: (a) asymmetric FSC (PG&E No. 30-2021), (b) symmetric FSC (PG&E No. 30-2022), (c) FSC with long leg (PG&E No. 30-2023)

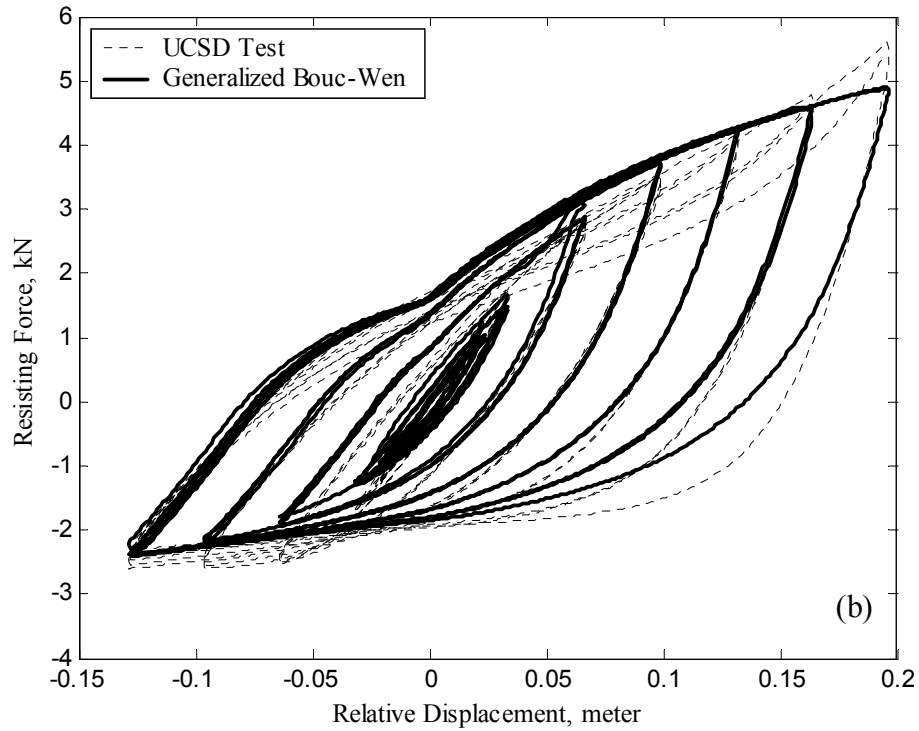
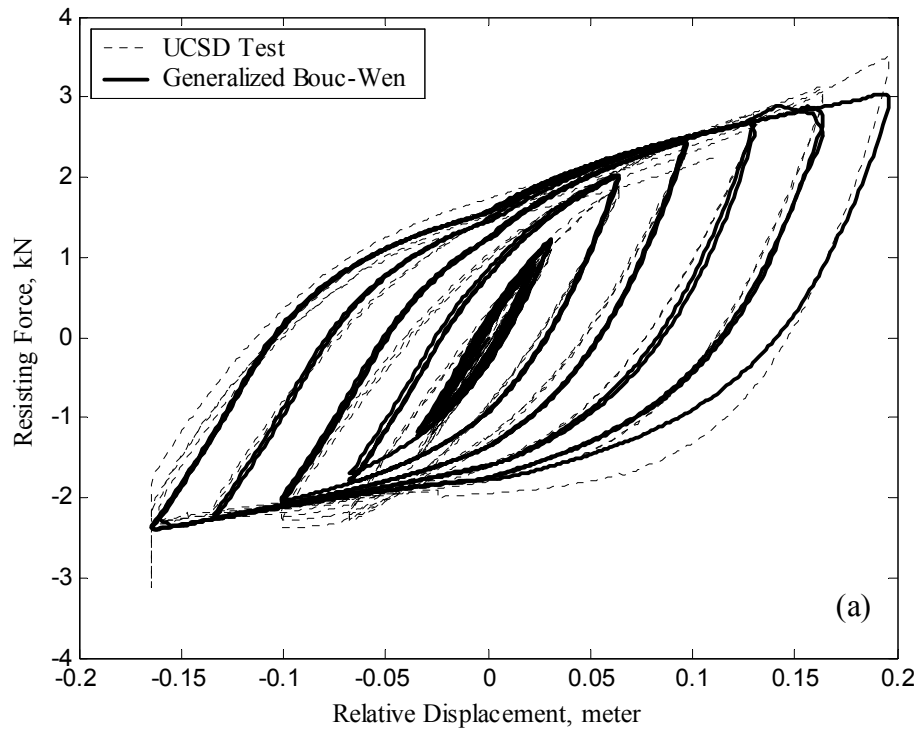


Figure 3.2 Hysteretic behavior of RB-FSC as observed in UCSD tests and as predicted by the fitted generalized Bouc-Wen model: (a) symmetric FSC (30-2022) and (b) asymmetric FSC (30-2021)

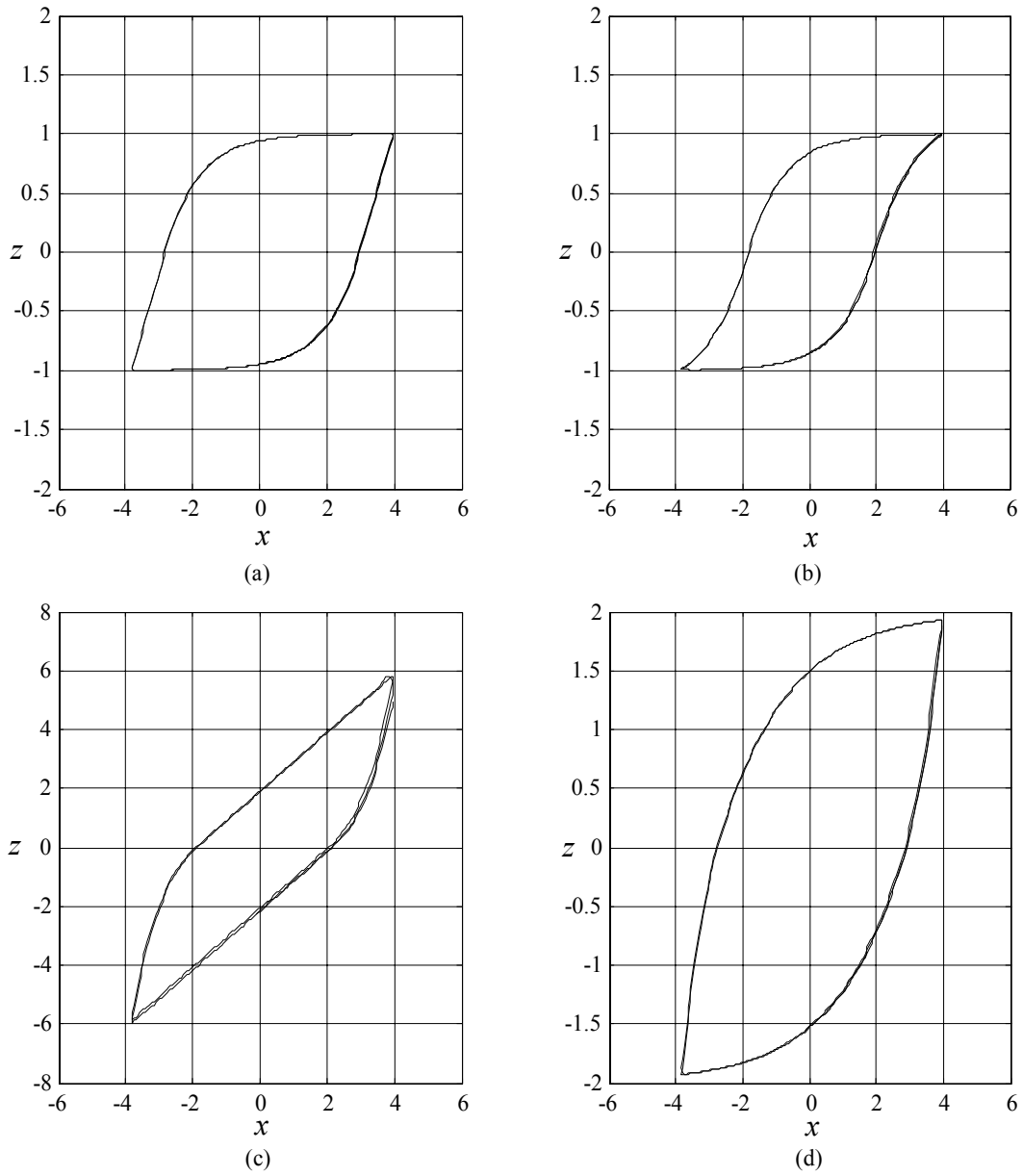


Figure 3.3 Hysteresis loops by Bouc-Wen model ( $A=1, n=1$ ) (a)  $\gamma=0.5$ ,  $\beta=0.5$ , (b)  $\gamma=0.1$ ,  $\beta=0.9$ , (c)  $\gamma=0.5$ ,  $\beta=-0.5$  and (d)  $\gamma=0.75$ ,  $\beta=-0.25$

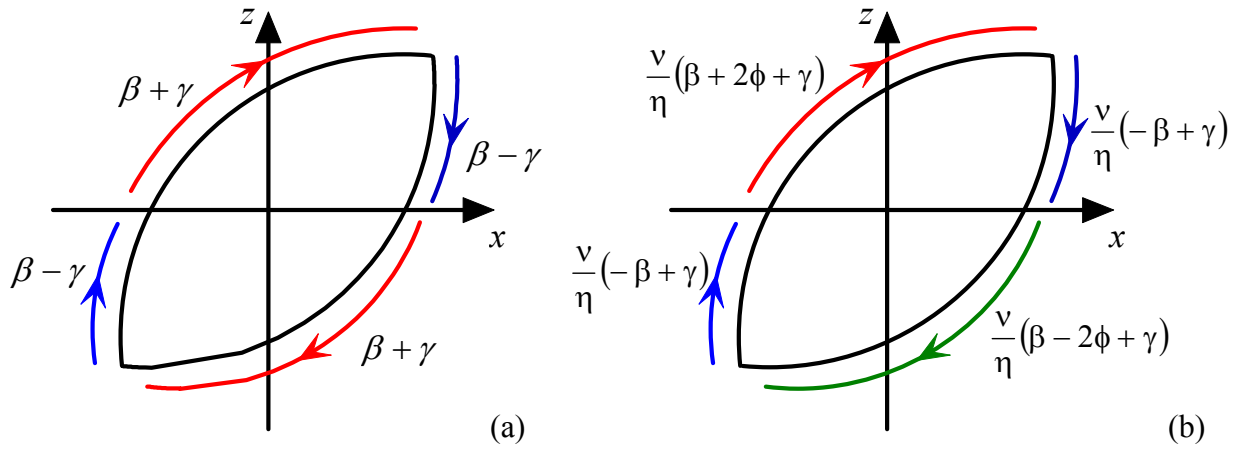


Figure 3.4 Values of shape-control functions for (a) original Bouc-Wen model, (b) model by Wang & Wen

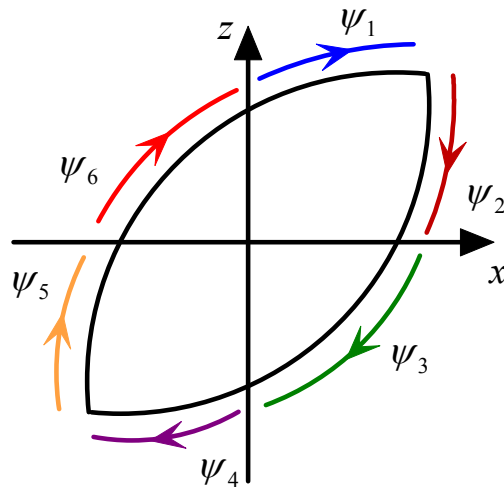


Figure 3.5 Values of the shape-control function for the generalized Bouc-Wen model

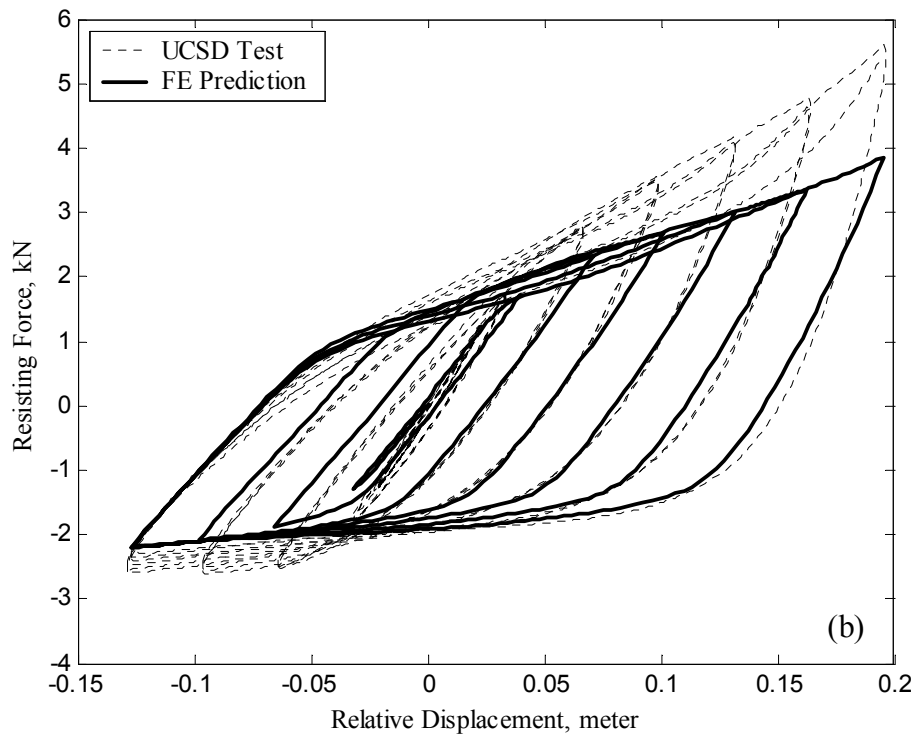
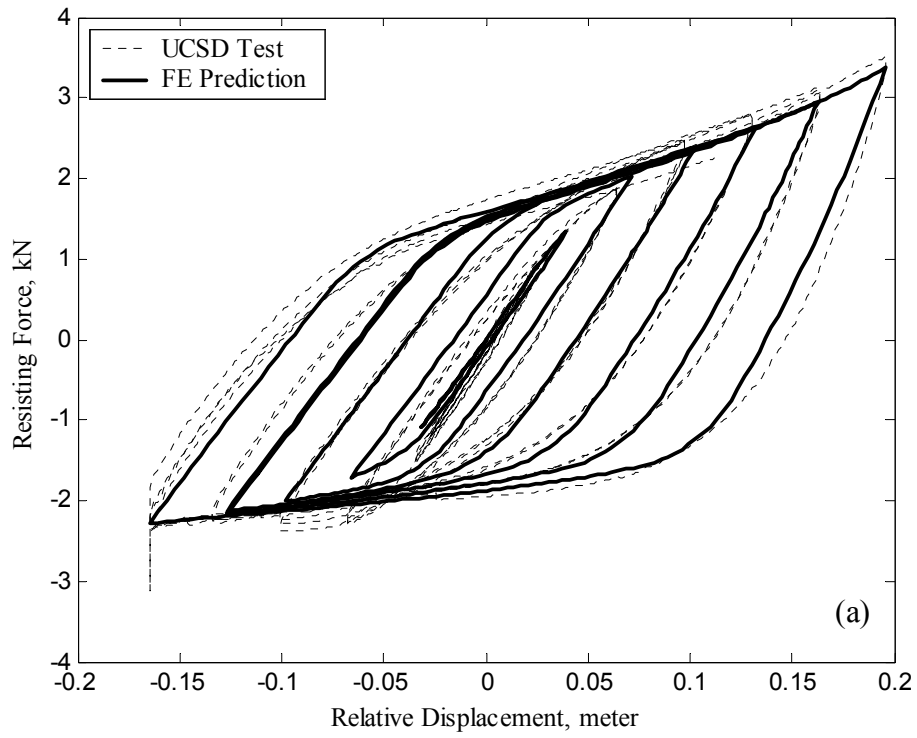


Figure 3.6 Hysteretic behavior of RB-FSC as observed in UCSD test and as predicted by the FE model: (a) symmetric FSC (30-2022), (b) asymmetric FSC (30-2021)

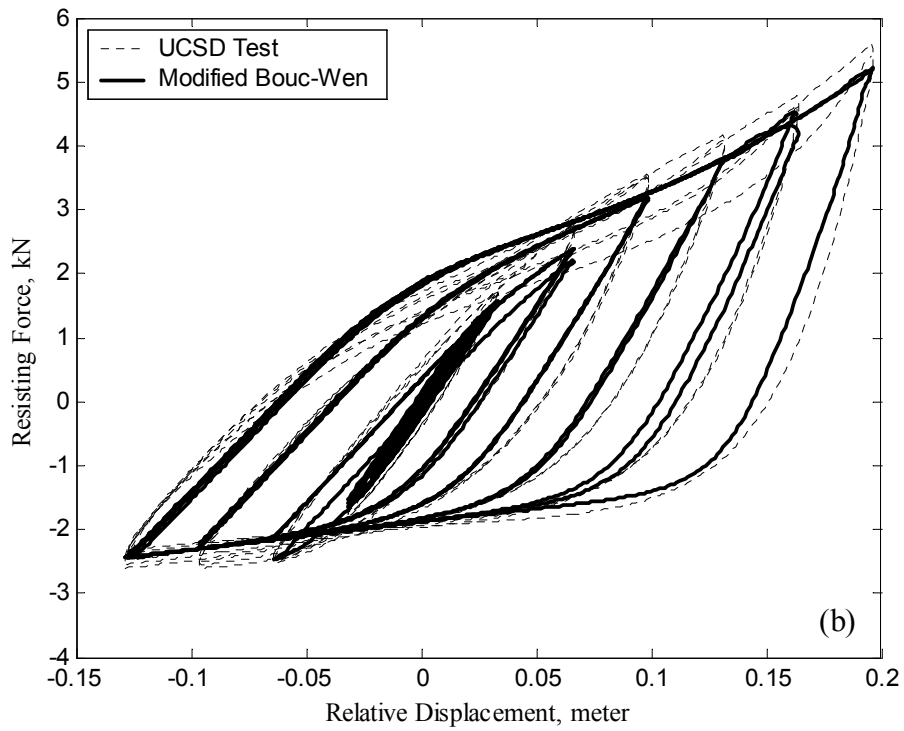
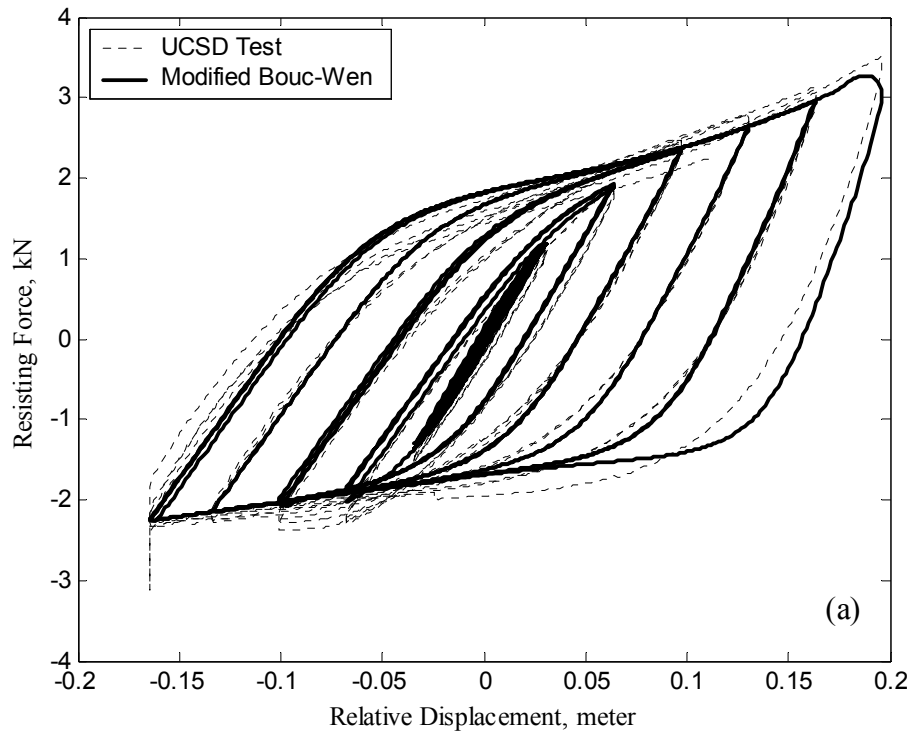


Figure 3.7 Hysteretic behavior of RB-FSC as observed by UCSD tests and as predicted by the fitted modified Bouc-Wen model: (a) symmetric FSC (30-2022), (b) asymmetric FSC (30-2021)

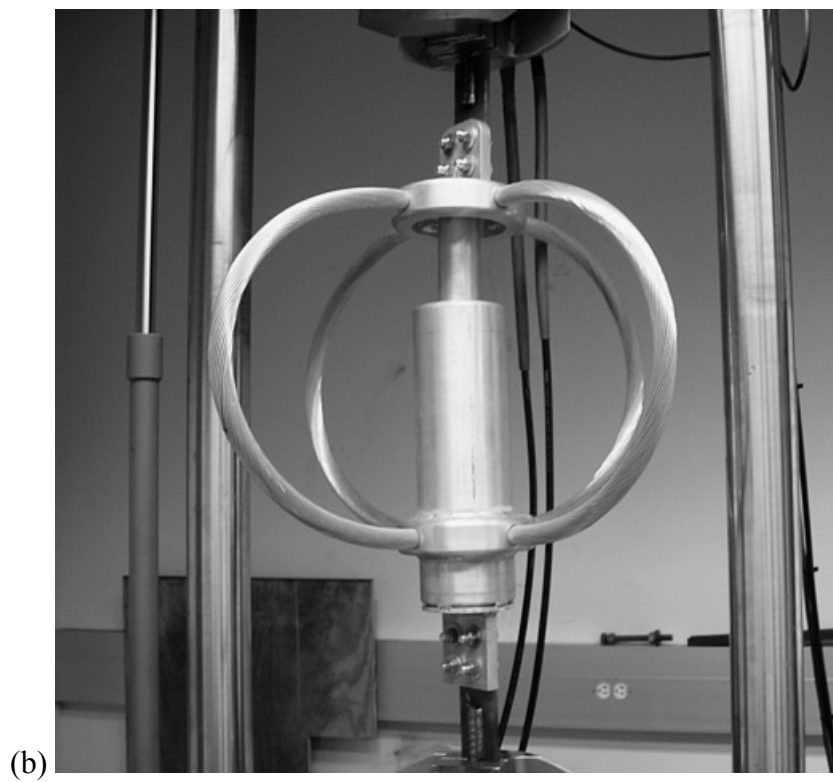
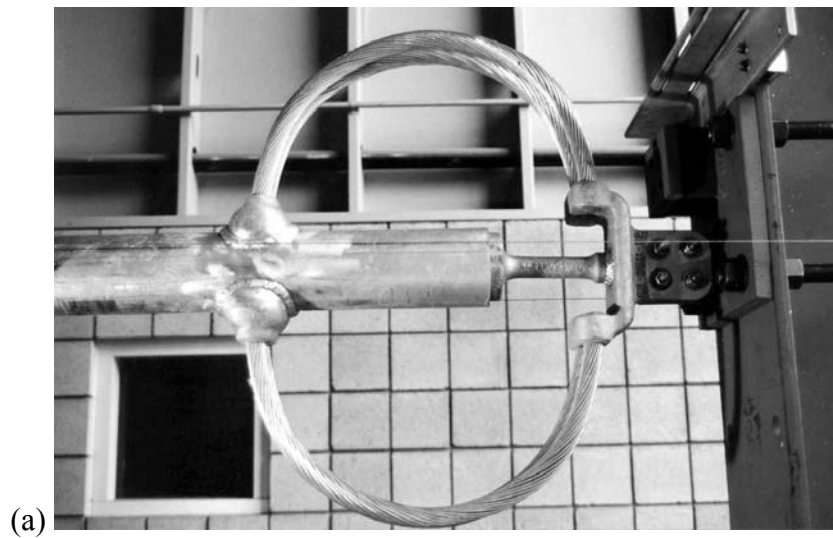


Figure 3.8 Slider connector specimens: (a) PG&E Type 221A, 30-4462, (b) improved model (Photo courtesy: UCSD)



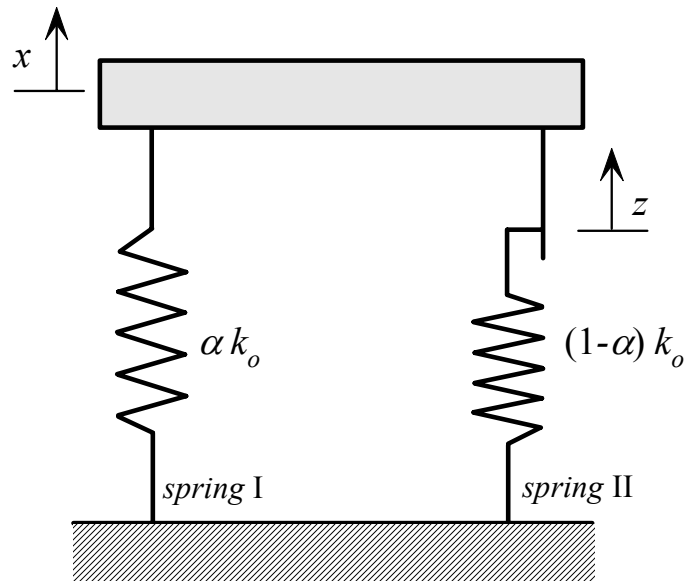


Figure 3.9 Coulomb slider-spring representation of slider connector

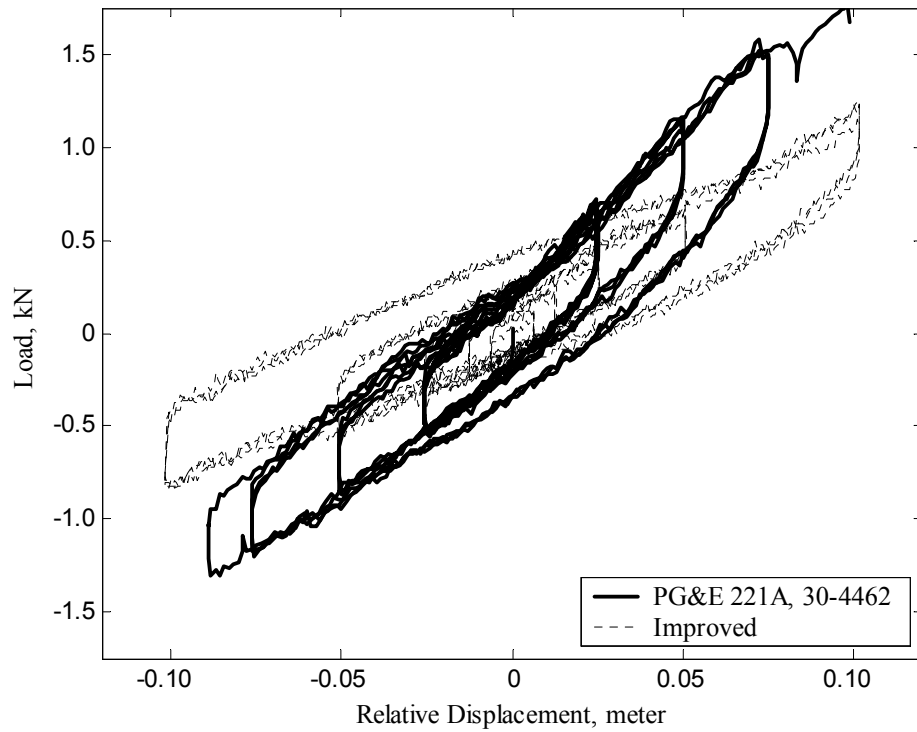


Figure 3.10 Experimental hysteresis loops of slider connectors (Filiatrault *et al.* 1999 and Stearns & Filiatrault 2003)

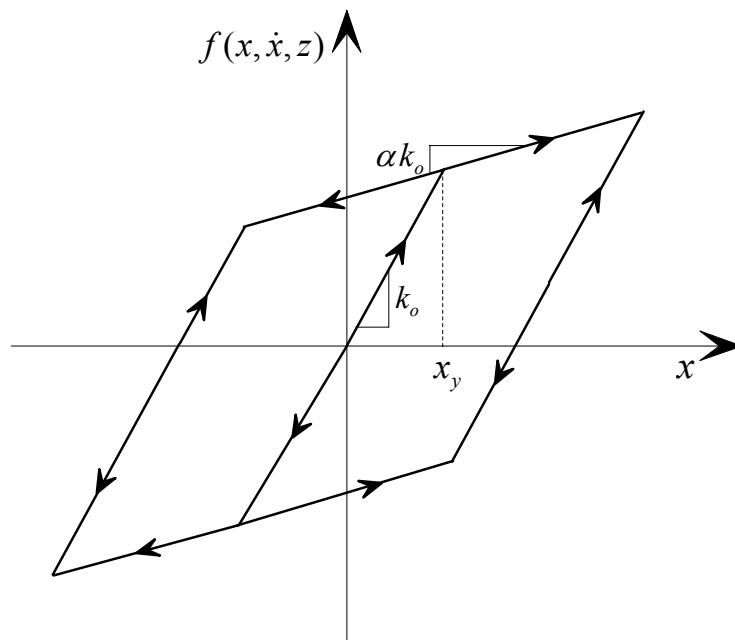
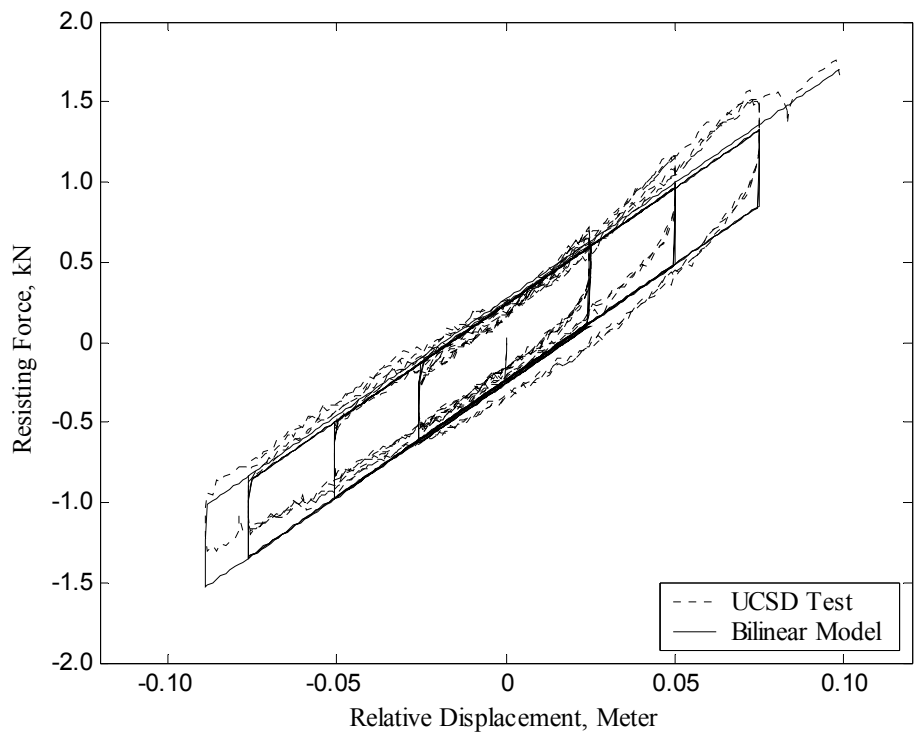
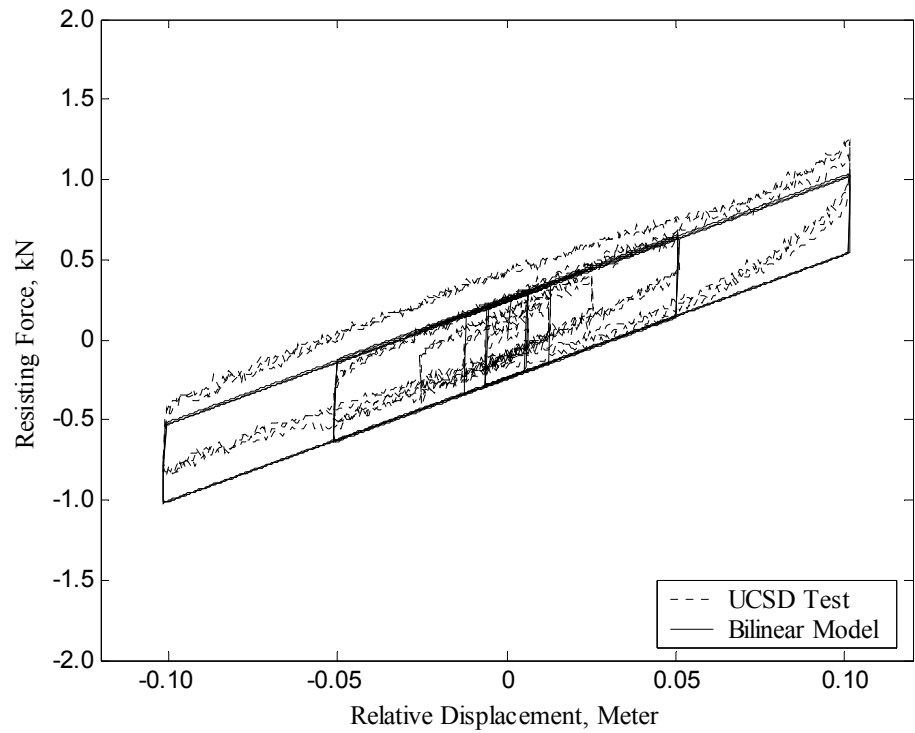


Figure 3.11 Ideal bi-linear hysteresis loop

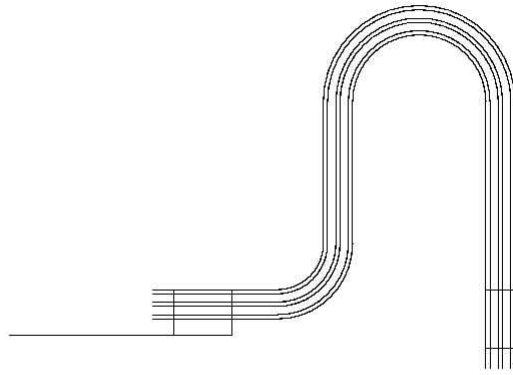


(a)

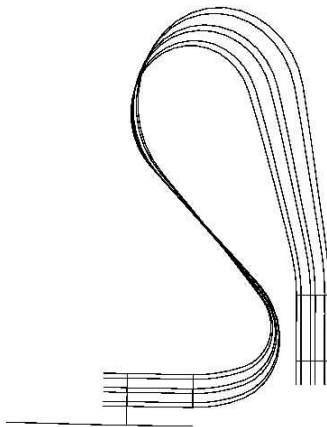


(b)

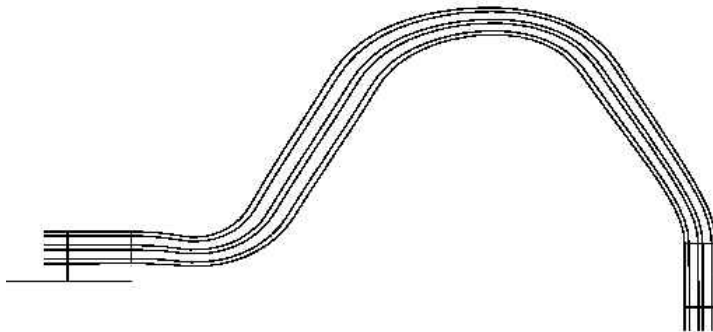
Figure 3.12 Bi-linear hysteresis as observed in UCSD tests and as predicted by the differential equation model: (a) PG&E Type 221A, 30-4462 and (b) improved slider connector



(a)

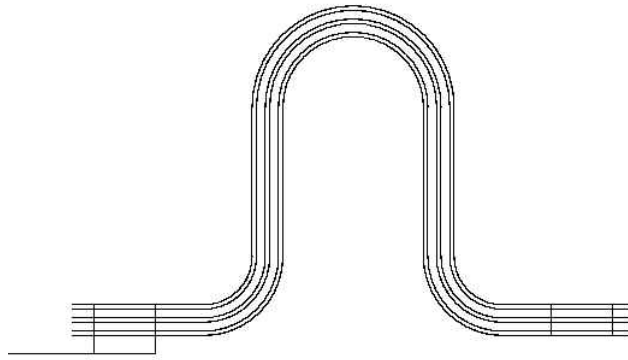


(b)

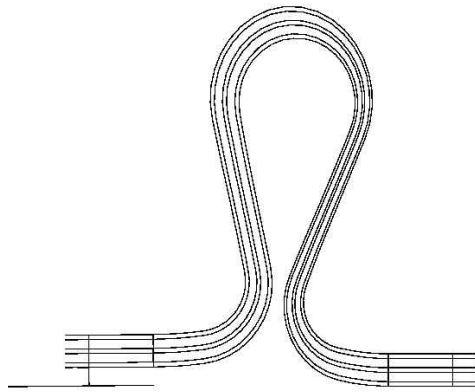


(c)

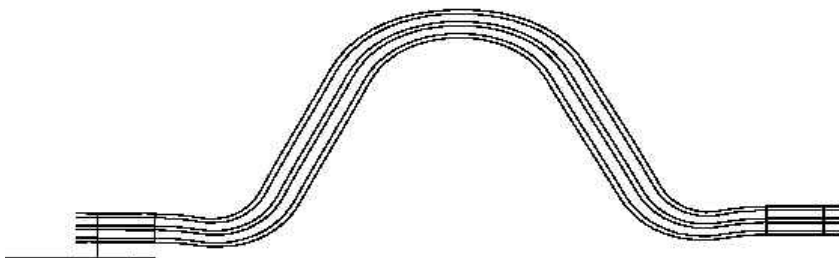
Figure 3.13 PG&E 30-2021: (a) undeformed shape, (b) extreme compressed shape and (c) extreme elongated shape



(a)

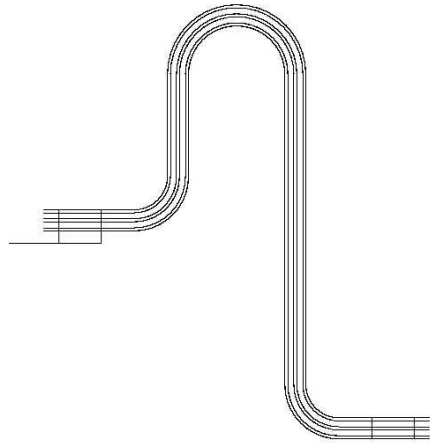


(b)

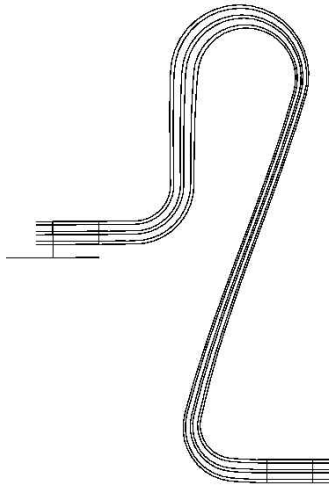


(c)

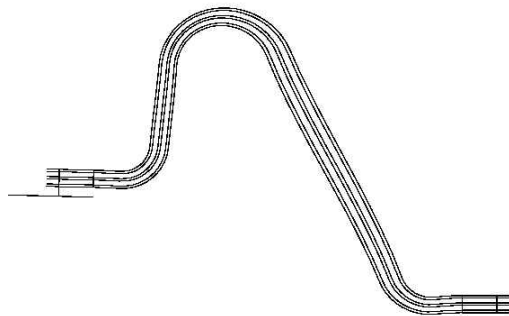
Figure 3.14 PG&E 30-2022: (a) undeformed shape, (b) extreme compressed shape and (c) extreme elongated shape



(a)



(b)



(c)

Figure 3.15 PG&E 30-2023: (a) undeformed shape, (b) extreme compressed shape and (c) extreme elongated shape

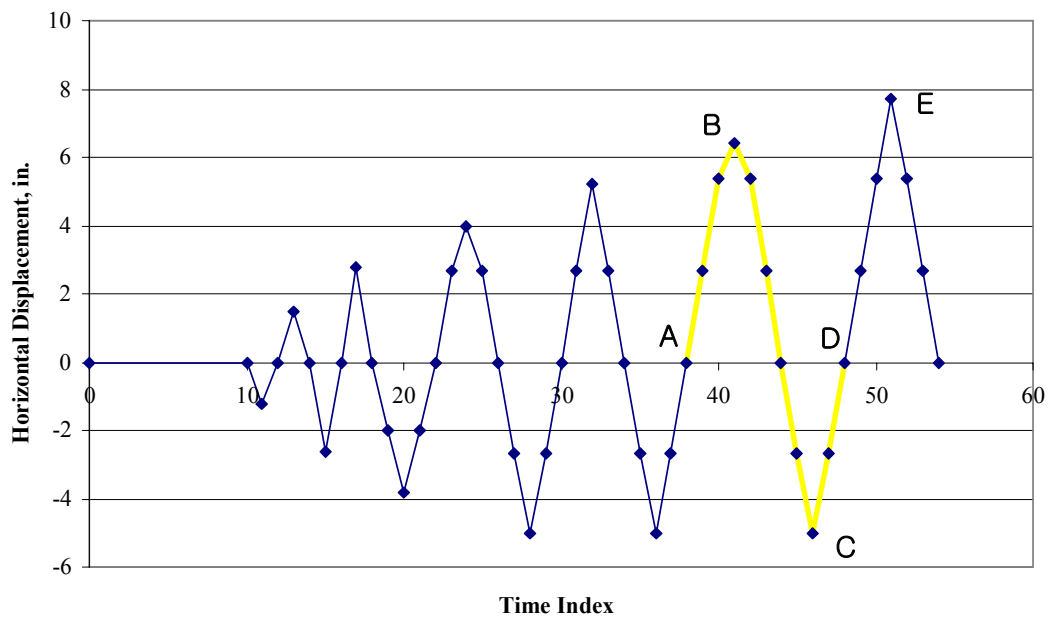


Figure 3.16 Displacement load cycles used for RB-FSC

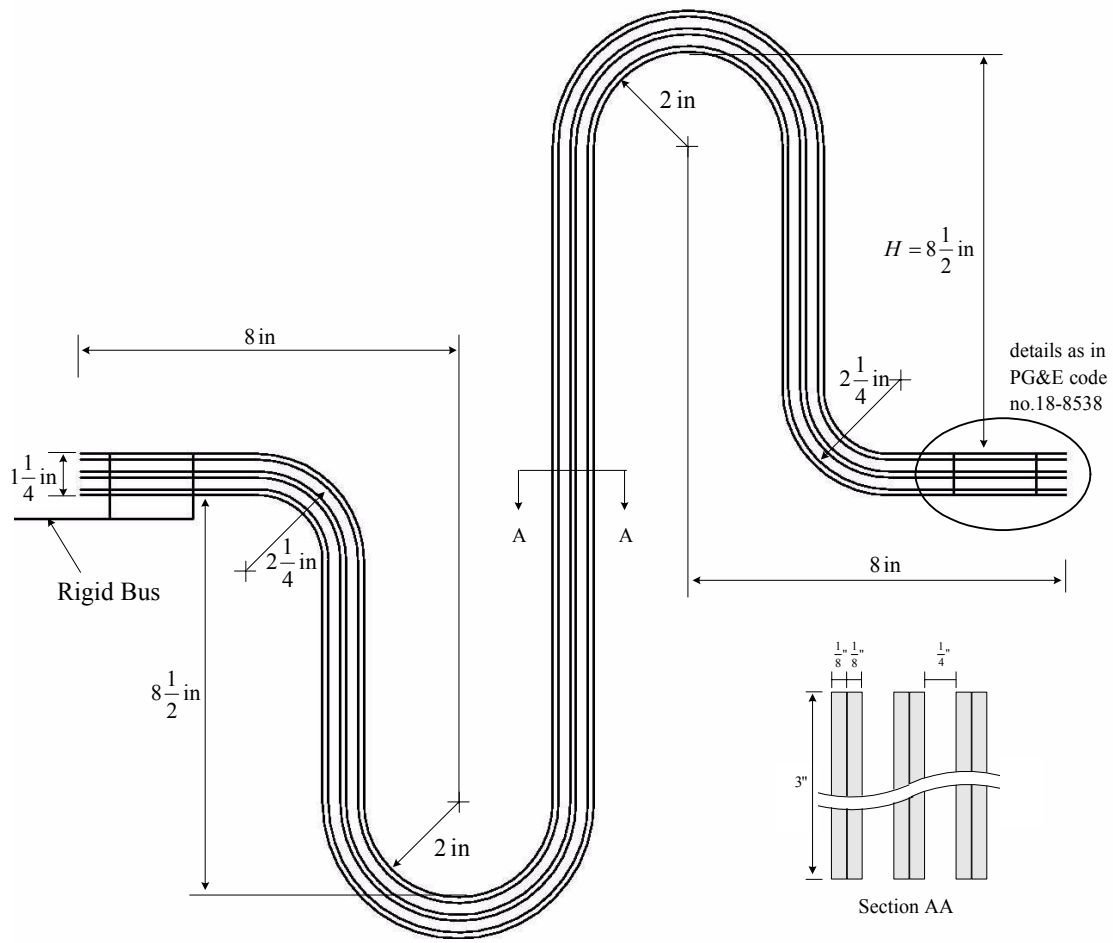
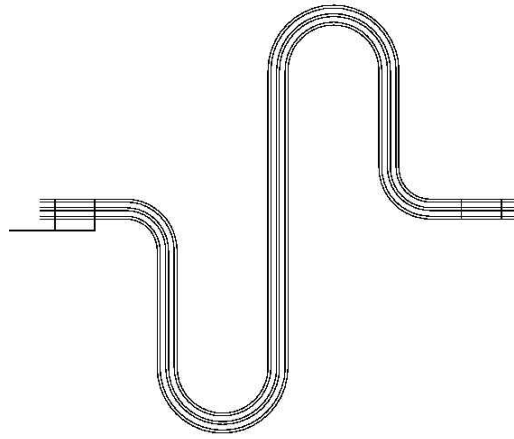
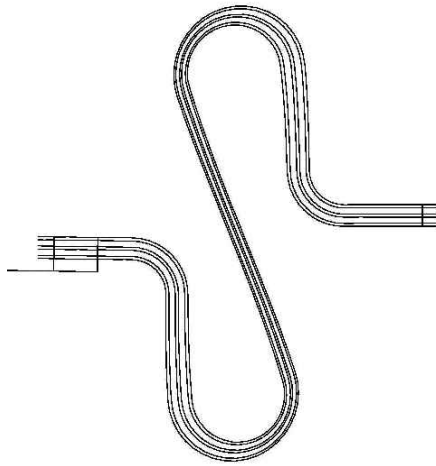


Figure 3.17 S-FSC (1)

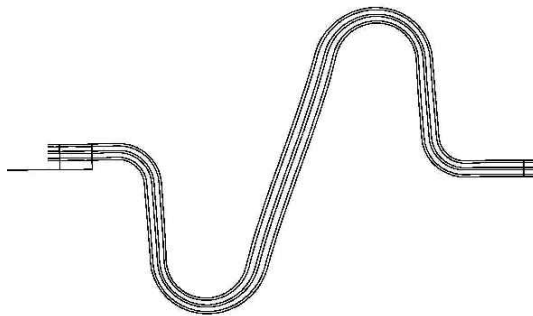




(a)



(b)



(c)

Figure 3.18 *S*-FSC (1): (a) undeformed shape, (b) extreme compressed shape and (c) extreme elongated shape

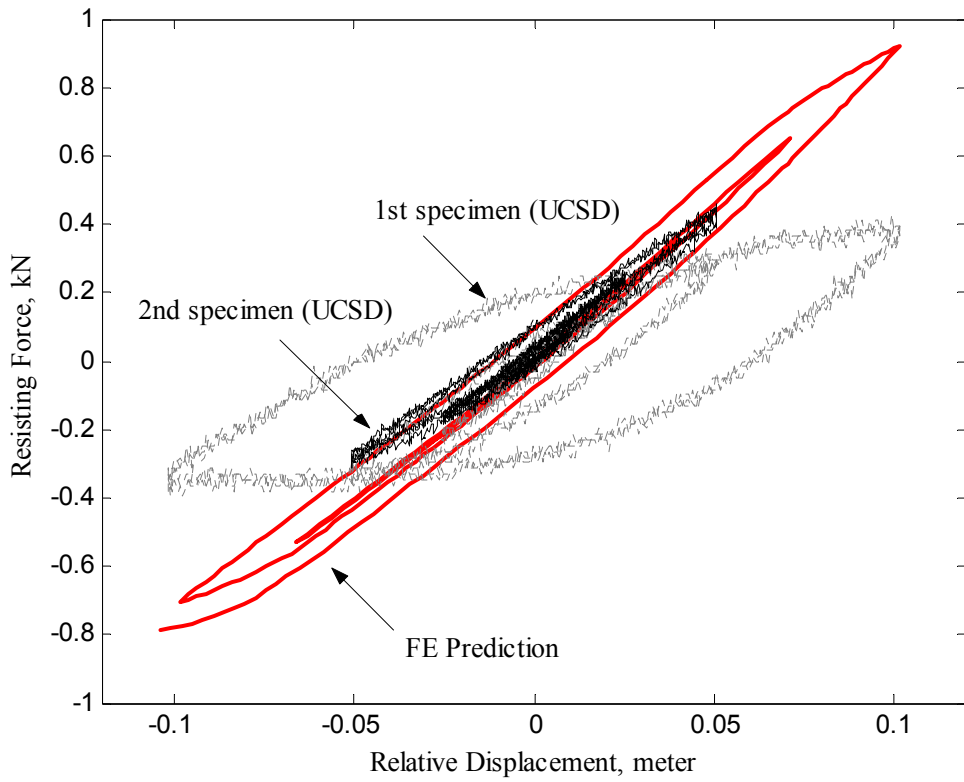


Figure 3.19 Hysteresis loops of *S*-FSC

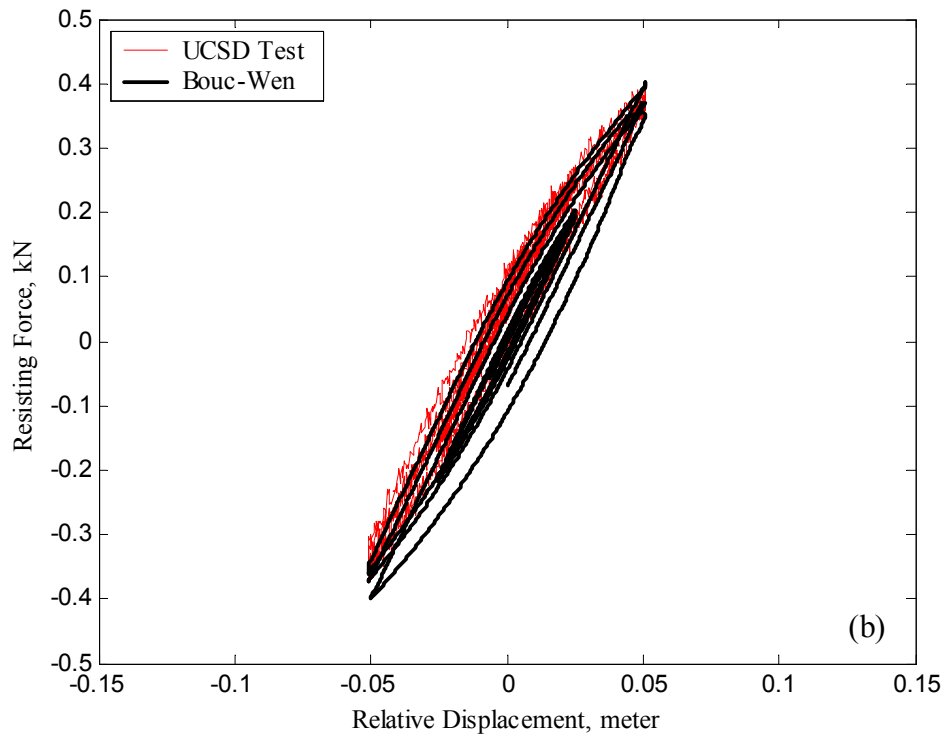
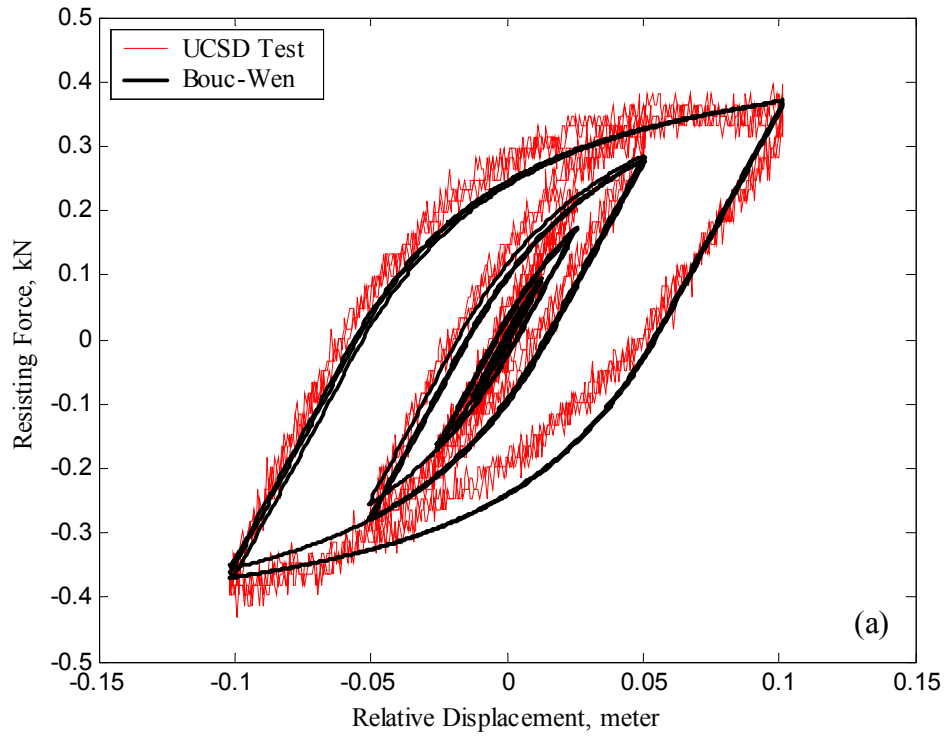


Figure 3.20 Hysteretic behavior of *S*-FSC as observed in UCSD tests and as predicted by the fitted Bouc-Wen model: (a) first specimen, (b) second specimen



## 4 Seismic Response of Equipment Items Connected by Rigid Bus Conductors

### 4.1 INTRODUCTION

This chapter deals with analysis methods for estimating the seismic response of equipment items connected by rigid bus (RB) conductors. Both deterministic and stochastic descriptions of the ground motion are considered. The analysis methods use the single-degree-of-freedom (SDOF) models for equipment items described in Chapter 2 and the differential-equation models for the cyclic behavior of the rigid bus connectors described in Chapter 3. Due to the nonlinear behavior of the connector, the combined system requires a nonlinear dynamic analysis method for either type of ground motion description. For the deterministic analysis, the adaptive Runge-Kutta-Fehlberg algorithm is used to solve the equations of the dynamical system. For the random vibration analysis, the equivalent linearization method (ELM) is used. For this purpose, closed-form relations are derived for the coefficients of the equivalent linear system in terms of the second moments of the response for the generalized Bouc-Wen model, the bi-linear model, and the original Bouc-Wen model, which are all described in Chapter 3. Numerical examples verify the accuracy of the analysis methods and models proposed in the previous chapters.

### 4.2 DYNAMIC ANALYSIS OF EQUIPMENT ITEMS CONNECTED BY RIGID BUS CONDUCTORS

The equations of motion for two interconnected electrical substation equipment items modeled as SDOF oscillators is given by (2.8)-(2.10). Analogous to (3.1), the resisting force of the rigid bus connector in (2.10),  $q(\Delta u, \Delta \dot{u}, z)$ , can be written as

$$q(\Delta u, \Delta \dot{u}, z) = \alpha k_0 \Delta u + (1 - \alpha) k_0 z \quad (4.1)$$

where  $\alpha$  is a parameter controlling the degree of nonlinearity,  $k_0$  is the initial stiffness,

$\Delta u(t) = u_2(t) - u_1(t)$  is the relative displacement between the two equipment items, and  $z$  is the auxiliary variable for describing the hysteretic behavior of the connecting element. The auxiliary variable  $z$  is subject to the differential equations (3.5) and (3.9) for the existing flexible strap connectors (FSC), (3.12) for the bus slider, and (3.3) for the  $S$ -FSC, where  $x$  and  $\dot{x}$  should be replaced by  $\Delta u$  and  $\Delta \dot{u}$ , respectively.

Among various methods available for solving the system of nonlinear equations of motion of the RB-connected system, one convenient method is to reduce the second-order differential equation to first order and then use the Runge-Kutta algorithm (Cheney & Kincaid 1999). Consider a first-order differential equation

$$\frac{dy}{dt} = \tilde{\mathbf{g}}(t, \mathbf{y}) \quad (4.2)$$

where  $\mathbf{y} = \{y_1, y_2, \dots, y_n\}^T$  is a vector with  $n$  components,  $t$  is time, and  $\tilde{\mathbf{g}} : R^{n+1} \rightarrow R^n$  is a general vector function. The fourth-order Runge-Kutta algorithm computes the solution of  $\mathbf{y}(t+h)$  from  $\mathbf{y}(t)$  and five evaluations of  $\tilde{\mathbf{g}}(\cdot)$  as follows:

$$\mathbf{y}(t+h) = \mathbf{y}(t) + \frac{25}{216} \mathbf{K}_1 + \frac{1408}{2565} \mathbf{K}_3 + \frac{2197}{4104} \mathbf{K}_4 - \frac{1}{5} \mathbf{K}_5 \quad (4.3)$$

where

$$\mathbf{K}_1 = h \tilde{\mathbf{g}}(t, \mathbf{y}) \quad (4.4a)$$

$$\mathbf{K}_2 = h \tilde{\mathbf{g}}\left(t + \frac{1}{4}h, \mathbf{y} + \frac{1}{4}\mathbf{K}_1\right) \quad (4.4b)$$

$$\mathbf{K}_3 = h \tilde{\mathbf{g}}\left(t + \frac{3}{8}h, \mathbf{y} + \frac{3}{32}\mathbf{K}_1 + \frac{9}{32}\mathbf{K}_2\right) \quad (4.4c)$$

$$\mathbf{K}_4 = h \tilde{\mathbf{g}}\left(t + \frac{12}{13}h, \mathbf{y} + \frac{1932}{2197}\mathbf{K}_1 - \frac{7200}{2197}\mathbf{K}_2 + \frac{7296}{2197}\mathbf{K}_3\right) \quad (4.4d)$$

$$\mathbf{K}_5 = h \tilde{\mathbf{g}}\left(t + h, \mathbf{y} + \frac{439}{216}\mathbf{K}_1 - 8\mathbf{K}_2 + \frac{3680}{513}\mathbf{K}_3 - \frac{845}{4104}\mathbf{K}_4\right) \quad (4.4e)$$

A fifth-order Runge-Kutta solution is obtained by just one additional function evaluation:

$$\mathbf{y}(t+h) = \mathbf{y}(t) + \frac{16}{135} \mathbf{K}_1 + \frac{6656}{12825} \mathbf{K}_3 + \frac{28561}{56430} \mathbf{K}_4 - \frac{9}{50} \mathbf{K}_5 + \frac{2}{55} \mathbf{K}_6 \quad (4.5)$$

$$\mathbf{K}_6 = h \tilde{\mathbf{g}} \left( t + \frac{1}{2}h, \mathbf{y} - \frac{8}{27} \mathbf{K}_1 + 2\mathbf{K}_2 - \frac{3544}{2565} \mathbf{K}_3 + \frac{1859}{4104} \mathbf{K}_4 - \frac{11}{40} \mathbf{K}_5 \right) \quad (4.6)$$

The difference between the values of  $\mathbf{y}(t+h)$  by the fourth-order (Eq. 4.3) and the fifth-order (Eq. 4.5) Runge-Kutta algorithms is an approximate estimate of the local truncation error in the fourth-order algorithm. The step size  $h$  is reduced until this error estimate is less than a given tolerance. This is known as the adaptive Runge-Kutta-Fehlberg (RKF) algorithm (Fehlberg 1969). In this study, the fourth-order adaptive RKF algorithm with a relative tolerance of  $10^{-6}$  is used for nonlinear time history analysis of the connected and stand-alone equipment items, subjected to recorded or simulated ground motions.

The equations of motion of the connected system in (2.8)-(2.10) can be reduced to a first-order system as in (4.2) by defining the state-space vector  $\mathbf{y}$  as

$$\mathbf{y} = \{u_1 \quad \dot{u}_1 \quad u_2 \quad \dot{u}_2 \quad z\}^T \quad (4.7)$$

The state-space equation corresponding to (4.2) then is

$$\dot{\mathbf{y}} = \mathbf{g}(\mathbf{y}) + \mathbf{f} \quad (4.8)$$

where

$$\mathbf{g}(\mathbf{y}) = \left\{ \begin{array}{c} \dot{u}_1 \\ -\left(\frac{k_1 + \alpha k_o}{m_1}\right)u_1 - \left(\frac{c_1 + c_o}{m_1}\right)\dot{u}_1 + \frac{\alpha k_o}{m_1}u_2 + \frac{c_o}{m_1}\dot{u}_2 + \frac{(1-\alpha)k_o}{m_1}z \\ \dot{u}_2 \\ \frac{\alpha k_o}{m_2}u_1 + \frac{c_o}{m_2}\dot{u}_1 - \left(\frac{k_2 + \alpha k_o}{m_2}\right)u_2 - \left(\frac{c_2 + c_o}{m_2}\right)\dot{u}_2 - \frac{(1-\alpha)k_o}{m_2}z \\ \dot{z}(\Delta u, \Delta \dot{u}, z) \end{array} \right\} \quad (4.9)$$

$$\mathbf{f} = \left\{ 0 \quad -\frac{l_1}{m_1} \ddot{x}_g \quad 0 \quad -\frac{l_2}{m_2} \ddot{x}_g \quad 0 \right\}^T \quad (4.10)$$

where  $\dot{z}(\cdot)$  denotes the nonlinear function in (3.5) or (3.12).

In evaluating the response ratios defined in (2.11), one also needs an analytical model for the equipment items in their stand-alone configurations. The equation of motion for a stand-alone equipment item, modeled as a SDOF oscillator, can be transformed into the state-space form (4.8) as well. In that case, the expressions corresponding to (4.7), (4.9) and (4.10), respectively, are

$$\mathbf{y} = \{u \quad \dot{u}\}^T \quad (4.11)$$

$$\mathbf{g}(\mathbf{y}) = \begin{bmatrix} 0 & 1 \\ -\frac{k_1}{m_1} & -\frac{c_1}{m_1} \end{bmatrix} \begin{Bmatrix} u \\ \dot{u} \end{Bmatrix} \quad (4.12)$$

$$\mathbf{f} = \left\{ 0 \quad -\frac{l}{m} \ddot{x}_g \right\}^T \quad (4.13)$$

### 4.3 EVALUATION OF ANALYTICAL MODELS FOR CONNECTED EQUIPMENT SYSTEM

This section examines the analytical models developed for the connected equipment system. The nonlinear differential equations employing the SDOF models for the equipment items and the analytical hysteresis models for the connectors are solved by the adaptive RKF algorithm. The accuracy of the models and the dynamic analysis method is demonstrated through comparison with shake-table test results or analysis results by use of other hysteresis models.

#### 4.3.1 Generalized Bouc-Wen Model for RB-FSC

As described in Chapter 3, Der Kiureghian *et al.* (2000) developed a modified Bouc-Wen model to describe the asymmetric hysteresis behavior of the RB-FSC. As shown in Figure 3.7 of Chapter 3, this model closely matches the cyclic test results of Filiatrault *et al.* (1999). However, since



the coefficients in the model are dependent on the response, this model is not convenient for random vibration analysis by use of the ELM. In contrast, the generalized Bouc-Wen model developed in Chapter 3 is convenient for ELM analysis, but it is not in as close an agreement with the test results as the modified Bouc-Wen model (compare Figures 3.2 and 3.7 of Chapter 3). This section examines the accuracy of the generalized Bouc-Wen model for the existing RB-FSC by comparing response predictions by this model with those obtained with the modified Bouc-Wen model. Shake-table test results for systems connected by RB-FSC are available (Filiatrault *et al.* 1999). However, comparison with the test results would entail other modeling approximations, e.g., in describing the equipment items, that would mask the error due to the modeling of the hysteresis loop of the RB-FSC. For the following analysis, the analytical models of the RB-FSC-connected system in (4.7)-(4.10) and the RKF algorithm in (4.3)-(4.6) are used.

Consider a RB-FSC-connected system having the stand-alone equipment frequencies  $f_1 = 2$  Hz and  $f_2 = 5$  Hz, the equipment mass ratio  $m_1/m_2 = 2.0$ , initial RB-FSC stiffness  $k_0 = 35.6$  kN/m (PG&E No. 30-2022), ratio of stiffnesses  $k_0/(k_1 + k_2) = 0.05$ , where  $k_1$  and  $k_2$  are the equipment stiffnesses, equipment damping ratios  $\zeta_i = c_i/(4\pi f_i m_i) = 0.02$ ,  $i = 1, 2$ , and external inertia force coefficients  $l_1/m_1 = l_2/m_2 = 1.0$  (see definitions in Chapter 2). This connected system is assumed to be subject to the longitudinal record of Tabas (1978) earthquake (TabasLN) shown in Figure 2.9.

Figures 4.1 and 4.2 respectively show the displacement time histories of the lower- and higher-frequency equipment items as computed for the modified and generalized Bouc-Wen models. It is seen that the proposed generalized Bouc-Wen model predicts equipment response time histories that are practically identical to those obtained by the modified Bouc-Wen model. The maximum relative displacement between the two equipment items predicted by both models is 9.80 cm, which shows that the RB-FSC experiences significant nonlinear deformation. This is confirmed by the hysteresis loops shown in Figure 4.3.

Der Kiureghian *et al.* (2000) compared the response time histories predicted by the modified Bouc-Wen model and the shaking test results. The general features are alike despite the errors due to other modeling approximations. Since the generalized Bouc-Wen model essentially gives results identical to those by the modified Bouc-Wen model, one can say that the generalized Bouc-Wen model provides a sufficiently accurate characterization of the hysteretic behavior

of the RB-FSC under cyclic loading. This model is used in all subsequent nonlinear random vibration analyses of equipment items connected by existing RB-FSC's in this study.

### 4.3.2 Bi-linear Model for SC

Next, the analytical bi-linear model of the bus slider described in Chapter 3 is examined by comparing analytical predictions with shake-table test results by Filiatrault *et al.* (1999). Tests RB-79 and RB-112 are selected for this purpose. The “equipment” items used in the tests were typical steel tubular columns with steel weights attached at their tops. The equipment natural frequencies and viscous damping ratios were measured during the testing. The effective mass,  $m_i$ , and the effective external inertia force coefficient,  $l_i$ , for each equipment item are computed employing the shape function  $\psi(y) = 1 - \cos(\pi y/2L)$  together with (2.1) and (2.4), respectively, assuming the steel columns have uniform mass distribution. In test RB-79, the lower-frequency equipment item had measured frequency  $f_1 = 1.99$  Hz and damping ratio  $\zeta_1 = 0.0042$ . The effective mass is computed as  $m_1 = 359$  kg and the effective external inertia force coefficient is computed as  $l_1 = 372$  kg. The corresponding values for the higher-frequency equipment item are  $f_2 = 4.11$  Hz,  $\zeta_2 = 0.0041$ ,  $m_2 = 67.1$  kg and  $l_2 = 82.0$  kg. This system was subjected to a modified version of the Tabas (1979, Iran) earthquake (LN) ground acceleration. The acceleration time history of the shake table during the actual test is shown in Figure 4.4a. Test RB-112 used the same lower-frequency equipment item, but the higher-frequency equipment item had the properties  $f_2 = 5.47$  Hz,  $\zeta_2 = 0.0039$ ,  $m_2 = 71.7$  kg and  $l_2 = 107$  kg. This system was subjected to a modified version of the N-S component of the Newhall (1994, Northridge) earthquake ground motion. Figure 4.4b shows the acceleration time history of the shake table during the actual test.

Figures 4.5 and 4.6 compare the predicted displacement time histories computed using the bi-linear model in (4.1) and (3.12), which is fitted to the experimental hysteresis loops by Filiatrault *et al.* (1999) (see Chapter 3). The close agreement between the analytical predictions and test measurements observed in these figures clearly indicates that the adopted bi-linear model accurately characterizes the hysteresis behavior of the bus slider for dynamic analyses. Figure 4.7 compares the predicted force-deformation hysteresis loops for the bus slider with the experimental measurements in tests RB-79 and RB-112. The experimental results include significant noise in the measurement of forces and are affected by rotations at the equipment ends.

Nevertheless, the analytical results appear to accurately capture the overall hysteretic behavior of the bus slider under the cyclic motion. Although not shown here, similar results were obtained for the tests RB-15, RB-18, RB-47, RB-49 and RB-78 reported in Filiatrault *et al.* (1999).

### 4.3.3 Bouc-Wen Model for S-FSC

Chapter 3 proposed the use of the original Bouc-Wen model for S-FSC based on its close agreement with experimental hysteresis loops (see Figure 3.20). Here, the accuracy of this model for dynamic analysis is examined by comparing analytical predictions with the results of shake-table tests conducted by Stearns & Filiatrault (2003). Tests RC-86 and RC-88B are selected for this purpose (see Stearns & Filiatrault (2003)). The “equipment” items used in the tests were steel tubular columns with steel weights attached at their tops. The equipment natural frequencies and viscous damping ratios were measured during the tests. The effective mass,  $m_i$ , and the effective external inertia force coefficient,  $l_i$ , for each equipment item are computed employing the shape function  $\psi(y) = 1 - \cos(\pi y / 2L)$  together with (2.1) and (2.4), respectively, assuming a uniform mass distribution for the steel columns. Tests RC-86 and RC-88B use the same equipment items and S-FSC, but different excitations. The lower-frequency equipment item had the measured frequency  $f_1 = 1.88$  Hz and damping ratio  $\zeta_1 = 0.0040$ . The effective mass is computed as  $m_1 = 94.8$  kg and the effective external inertia force coefficient is computed as  $l_1 = 111$  kg. The corresponding values for the higher-frequency equipment item are  $f_2 = 5.47$  Hz,  $\zeta_2 = 0.0038$ ,  $m_2 = 109$  kg and  $l_2 = 149$  kg. This system was subjected to modified versions of the Newhall (Test RC-86) and Tabas (Test RC-88B) earthquake ground motions. Figure 4.8 shows the acceleration time histories of the shake-table motions recorded during the two tests.

The displacement time histories of the RB-S-FSC-connected equipment items were predicted based on the natural frequencies reported by Stearns & Filiatrault (2003), as mentioned above. The computed results (not shown here) indicated significant differences from the shake-table test results. In order to identify errors in equipment modeling, dynamic analyses of the SDOF equipment items in their stand-alone configurations were performed and the analytical predictions were compared to the corresponding test results. For example, in Test RC-64, the lower-frequency equipment item used in Test RC-86 and Test RC-88B was subjected to shake-table motions in its stand-alone configuration. Figure 4.9a compares the displacement time his-

tory obtained by Test RC-64 with the displacement predicted by the dynamic analysis based on the reported equipment frequency of  $f_1 = 1.88$  Hz. Even though the equipment item was tested in its stand-alone configuration, that is, without connection to any other equipment, the predicted response is significantly different from the test measurement. The equipment natural frequency is adjusted in order to achieve a better agreement with test results. Figure 4.9b shows the comparison when the equipment frequency is adjusted to  $f_1 = 1.81$  Hz. A similar approach is used to adjust the frequency of equipment 2 to  $f_2 = 5.39$  Hz. Although these adjustments are small, the effect on response predictions is quite significant. The following numerical examples use these adjusted frequencies.

Figures 4.10 and 4.11 compare the displacement time histories computed using the Bouc-Wen model in (4.1) and (3.3), which is fitted with the experimental hysteresis loops of the second specimen of *S*-FSC (See Figure 3.20b). The fairly close agreement between the analytical and test results observed in these figures indicates that the adopted Bouc-Wen model accurately characterizes the hysteresis behavior of the *S*-FSC in dynamic analyses. Figure 4.12 compares the predicted force-deformation hysteresis loops for the *S*-FSC with the measured hysteresis loops of tests RC-86 and RC-88B. Although the experimental results include significant noise in the measurement of forces and are affected by rotations at the equipment ends, the analytical results appear to capture the overall hysteretic behavior of the *S*-FSC under cyclic loading. Although not shown here, similar level of accuracy was obtained for the tests RC-11, RC-51, RC-53, RC-54, RC-73 and RC-74 reported in Stearns & Filiatrault (2003).

#### **4.4 NONLINEAR RANDOM VIBRATION ANALYSIS OF CONNECTED EQUIPMENT BY THE EQUIVALENT LINEARIZATION METHOD**

One of the objectives of this study is to develop design guidelines for interconnected electrical substation equipment so as to reduce the adverse effect of dynamic interaction during earthquakes. Since the characteristics of future earthquakes are highly uncertain, it is important to develop a method for the assessment of the interaction effect, which is based on a stochastic model of the ground motion and properly accounts for the attendant uncertainty. As we have seen above, the behavior of the connecting element in general is nonlinear and hysteretic in nature. These two factors give rise to a need for a method for nonlinear random vibration analysis.

The ELM is considered as a random vibration approach with the highest potential for practical use in estimating nonlinear dynamic response of structures excited by stochastic inputs (Pradlwarter & Schuëller 1991). This is because the ELM procedure can be applied to nonstationary excitations and to any type of nonlinear structure described as a multi-degree-of-freedom system, or through a general finite element model. Moreover, the required computational effort is significantly less than that of simulation methods. Significant experience in using ELM for earthquake applications has been gained in recent years (Schuëller *et al.* 1994, Kimura *et al.* 1994, Hurtado & Barbat 2000)

Consider a nonlinear structural system, whose equation of motion can be reduced to a nonlinear first-order differential equation of the form (4.8). The corresponding equivalent linear system is defined as

$$\dot{\mathbf{y}} = \mathbf{A}\mathbf{y} + \mathbf{f} \quad (4.14)$$

where  $\mathbf{A}$  is the equivalent linear coefficient matrix.  $\mathbf{A}$  is obtained by minimizing the mean-square error of the responses of the equivalent system, which results in the best linear estimator (Kozin 1987)

$$\mathbf{A} = \frac{E[\mathbf{g}(\mathbf{y})\mathbf{y}^T]}{E[\mathbf{y}\mathbf{y}^T]} \quad (4.15)$$

where  $E[\cdot]$  denotes the statistical expectation. However, the ELM based on (4.14) and (4.15) is often impractical due to the unknown probability distribution of the exact solution  $\mathbf{y}$  of the nonlinear system and the difficulty in numerically computing the required expectations.

When the input excitation  $\mathbf{f}(t)$  is a vector of zero-mean stationary Gaussian processes and the response  $\mathbf{y}(t)$  is nearly Gaussian, the coefficients of the equivalent linear system can be computed more easily. Suppose we have a nonlinear differential system of equations of the form

$$\mathbf{q}(\ddot{\mathbf{u}}, \dot{\mathbf{u}}, \mathbf{u}) = \tilde{\mathbf{f}} \quad (4.16)$$

where  $\tilde{\mathbf{f}}$  is a zero-mean, stationary Gaussian input vector and  $\mathbf{u}$  is the response vector, which is assumed to be nearly Gaussian. Let the equivalent linearized differential system of equations be

$$\mathbf{M}^e \ddot{\mathbf{u}} + \mathbf{C}^e \dot{\mathbf{u}} + \mathbf{K}^e \mathbf{u} = \tilde{\mathbf{f}} \quad (4.17)$$

Then, the components of the equivalent linear coefficient matrices  $\mathbf{M}^e$ ,  $\mathbf{C}^e$  and  $\mathbf{K}^e$ , obtained by minimizing the mean-square error, are given as (Atalik and Utku 1976)

$$M_{ij}^e = E \left[ \frac{\partial q_i}{\partial \ddot{u}_j} \right], \quad C_{ij}^e = E \left[ \frac{\partial q_i}{\partial \dot{u}_j} \right], \quad K_{ij}^e = E \left[ \frac{\partial q_i}{\partial u_j} \right] \quad (4.18)$$

These relations are used to derive algebraic expressions for the equivalent linear coefficients in terms of the second moments of the Gaussian responses. By defining  $\mathbf{y}$  as a state-space vector including the components of  $\mathbf{u}$  and  $\dot{\mathbf{u}}$ , for example, as in (4.7), the second-order equivalent linear system of equations (4.17) can be reduced to a first-order form

$$\dot{\mathbf{y}} = \mathbf{G}\mathbf{y} + \mathbf{f} \quad (4.19)$$

where  $\mathbf{G}$  denotes the equivalent linear coefficient matrix computed by (4.17) and (4.18) based on the Gaussian assumption, and  $\mathbf{f}$  is obtained by scaling the Gaussian input vector  $\tilde{\mathbf{f}}$  by mass terms.

Let  $\mathbf{S}$  denote the covariance matrix of the zero-mean state vector  $\mathbf{y}$  in the above formulation, i.e.,  $\mathbf{S} = E[\mathbf{y}\mathbf{y}^T]$ . When the excitation vector  $\mathbf{f}$  is a delta-correlated process (including white noise), the differential equation that  $\mathbf{S}$  must satisfy can be simplified into (Lin 1967)

$$\frac{d}{dt}\mathbf{S} = \mathbf{G}\mathbf{S} + \mathbf{S}\mathbf{G}^T + \mathbf{B} \quad (4.20)$$

where  $B_{ij} = 0$  except  $B_{ii} = 2\pi\Phi_0^i(t)$ , where  $\Phi_0^i(t)$  is the evolutionary power spectral density of the delta-correlated process,  $f_i(t)$ . In the case of stationary response, the covariance matrix is constant in time and the preceding equation reduces to the Lyapunov (Lin 1967) equation

$$\mathbf{G}\mathbf{S} + \mathbf{S}\mathbf{G}^T + \mathbf{B} = \mathbf{0} \quad (4.21)$$

where  $B_{ij} = 0$  except  $B_{ii} = 2\pi\Phi_0^i$  where  $\Phi_0^i$  is the power spectral density of the stationary delta-correlated process,  $f_i(t)$ . This equation can be solved by transforming the matrices  $\mathbf{G}$  and  $\mathbf{G}^T$  into complex Schur form and computing the solution of the resulting system (Bartels & Stewart 1972). It is noted that the solution of (4.20) or (4.21) requires an iterative scheme, since the matrix  $\mathbf{G}$  involves the coefficients in (4.18), which are the functions of the second moments in the covariance matrix  $\mathbf{S}$ .

The equations of the form (4.20) or (4.21) can be derived also for filtered white-noise input processes. Suppose the absolute ground acceleration  $\ddot{x}_g(t)$  is a stationary, filtered white-noise process defined by the Kanai-Tajimi power spectral density function (Clough & Penzien 1993)

$$\Phi_{\ddot{x}_g\ddot{x}_g}(\omega) = \frac{\omega_g^4 + 4\zeta_g^2\omega_g^2\omega^2}{(\omega_g^2 - \omega^2)^2 + 4\zeta_g^2\omega_g^2\omega^2} \Phi_0 \quad (4.22)$$

where  $\omega_g$ ,  $\zeta_g$  and  $\Phi_0$  are parameters defining the predominant frequency, the bandwidth and the intensity of the process, respectively. In that case, the ground displacement relative to the base,  $x_g^r(t)$ , is the solution of the differential equation

$$\ddot{x}_g^r + 2\zeta_g\omega_g\dot{x}_g^r + \omega_g^2x_g^r = w(t) \quad (4.23)$$

where  $w(t)$  is a white noise with power spectral density  $\Phi_0(t)$ . The absolute ground acceleration  $\ddot{x}_g$  can be described in terms of the relative ground displacement and velocity

$$\ddot{x}_g = \ddot{x}_g^r - w = -2\zeta_g\omega_g\dot{x}_g^r - \omega_g^2x_g^r \quad (4.24)$$

The equivalent linear system in (4.19) can be used with the filtered white-noise process by adding two new variables  $x_g^r$  and  $\dot{x}_g^r$  to the state space vector  $\mathbf{y}$  and augmenting the matrix  $\mathbf{G}$  for (4.23) and (4.24). All elements of  $\mathbf{f}$  are zero except for  $w(t)$  at the element corresponding to  $\dot{x}_g$  in vector  $\mathbf{y}$ . The corresponding  $\mathbf{B}$  matrix has only one non-zero term,  $B_{ii} = 2\pi\Phi_0(t)$ , where  $i$  is the element index for the position of  $\dot{x}_g^r$  in  $\mathbf{y}$ . The details of this procedure are shown in the example that follows.

#### 4.5 APPLICATION OF ELM TO INVESTIGATION OF INTERACTION EFFECT IN EQUIPMENT ITEMS CONNECTED BY RIGID BUS

The ELM has been applied to hysteretic systems described by the bi-linear model (Kaul & Penzien 1974), the original Bouc-Wen model (Wen 1980), the extended Bouc-Wen models (Baber & Wen 1979, Wang & Wen 1998), and others. For each model, the coefficients of the equivalent linear model must be derived as algebraic functions of the response statistics so they can be used in the iterative procedure. The first sub-section below, applies the ELM to the generalized Bouc-

Wen Model, which was developed in Chapter 3. The necessary expressions for the coefficients of the equivalent linear system are derived. The next two sub-sections deal with the application of ELM to connected equipment items described by the bi-linear model and the original Bouc-Wen model. In each case, example systems connected by three rigid buses in parallel (as in Figure 2.8) are investigated. In order to verify the accuracy of the proposed ELM method, the values of the equipment parameters are selected such that the higher-frequency equipment items experience significant amount of amplification. The performances of the connectors in the same configurations of equipment items are compared later in Chapter 5.

#### 4.5.1 Generalized Bouc-Wen Model for RB-FSC

Electrical substation equipment items connected by the RB-FSC are modeled by the system of differential of equations (2.8)-(2.10), (4.1) and (3.5) with (3.9). When the response is nearly Gaussian, according to (4.18), the nonlinear auxiliary equations (3.5) and (3.9) of the generalized Bouc-Wen model are linearized in the form

$$\dot{z} + C_1 \Delta \dot{u} + C_2 \Delta u + C_3 z = 0 \quad (4.25)$$

where

$$C_1 = E \left[ \frac{\partial q}{\partial \Delta \dot{u}} \right], \quad C_2 = E \left[ \frac{\partial q}{\partial \Delta u} \right], \quad C_3 = E \left[ \frac{\partial q}{\partial z} \right] \quad (4.26)$$

in which

$$q = \dot{z} - \Delta \dot{u} [A - |z|^n \psi(\Delta u, \Delta \dot{u}, z)] \quad (4.27)$$

Algebraic expressions for the coefficients  $C_1$ ,  $C_2$  and  $C_3$  in (4.25)-(4.26) are obtained by use of the following well known relation for a zero-mean, Gaussian vector  $\mathbf{y}$  (Atalik and Utku 1976):

$$E[\mathbf{y}h(\mathbf{y})] = E[\mathbf{y}\mathbf{y}^T]E[\nabla h(\mathbf{y})] \quad (4.28)$$

In the above,  $h(\cdot)$  is a general nonlinear scalar function. In addition, the following properties of zero-mean, Gaussian random variables  $X_1$ ,  $X_2$  and  $X_3$  are utilized:



$$f_3(x_1, x_2, 0) = \frac{1}{\sqrt{2\pi}\sigma_3} f_2(x_1^*, x_2^*) \quad (4.29)$$

$$f_2(x_1, 0) = \frac{1}{\sqrt{2\pi}\sigma_2} f(x_1^*) \quad (4.30)$$

$$\int_0^\infty \int_0^\infty f_2(x_1, x_2) dx_1 dx_2 = \frac{1}{4} + \frac{1}{2\pi} \sin^{-1} \rho_{12} \quad (4.31)$$

In the above,  $f(\cdot)$ ,  $f_2(\cdot)$  and  $f_3(\cdot)$  denote the uni-, bi- and tri-variate normal probability density functions with zero means, respectively,  $\sigma_i$  denotes the standard deviation of  $X_i$ , and  $\rho_{ij}$  is the correlation coefficient between  $X_i$  and  $X_j$ . The jointly normal random variable set  $(x_1^*, x_2^*)$  in (4.29) has zero means, the standard deviations  $\sigma_1^* = \sigma_1 \sqrt{1 - \rho_{13}^2}$  and  $\sigma_2^* = \sigma_2 \sqrt{1 - \rho_{23}^2}$ , and the correlation coefficient  $\rho_{12}^* = (\rho_{12} - \rho_{13}\rho_{23}) / \sqrt{1 - \rho_{13}^2} / \sqrt{1 - \rho_{23}^2}$ . The normal random variable  $x_1^*$  in (4.30) has a zero mean and the standard deviation  $\sigma_1^* = \sigma_1 \sqrt{1 - \rho_{12}^2}$ . The last expression above is due to Sheppard (1899).

Using the above relations, the coefficients  $C_1$ ,  $C_2$  and  $C_3$  of the linearized equation (4.25) are obtained as algebraic functions of the second moments of  $\Delta u$ ,  $\Delta \dot{u}$  and  $z$  for the case  $n = 1$  and the shape function in (3.9). The results can be summarized in the form

$$C_1 = -A + \beta_1 E_1 + \beta_2 E_2 + \beta_3 E_3 \quad (4.32)$$

$$C_2 = \beta_2 E_4 + \beta_3 E_5 \quad (4.33)$$

$$C_3 = \beta_1 E_6 + \beta_2 E_7 + \beta_3 E_8 \quad (4.34)$$

where the expressions for  $E_i$ ,  $i = 1, \dots, 8$ , are derived in terms of the response second moments and are listed Table 4.1.

Replacing the nonlinear differential equation (3.5)&(3.9) with the linear equation (4.25), the linearized system of equations for the connected system can be written as a system of first-order equations of the form (4.19), where  $\mathbf{y}$  is the state-space vector defined in (4.7),  $\mathbf{f}$  is the force vector defined in (4.10), and

$$\mathbf{G} = \begin{bmatrix} 0 & 1 & 0 & 0 & 0 \\ -\left(\frac{k_1 + \alpha k_o}{m_1}\right) & -\left(\frac{c_1 + c_o}{m_1}\right) & \frac{\alpha k_o}{m_1} & \frac{c_o}{m_1} & \frac{(1-\alpha)k_o}{m_1} \\ 0 & 0 & 0 & 1 & 0 \\ \frac{\alpha k_o}{m_2} & \frac{c_o}{m_2} & -\left(\frac{k_2 + \alpha k_o}{m_2}\right) & -\left(\frac{c_2 + c_o}{m_2}\right) & -\frac{(1-\alpha)k_o}{m_2} \\ C_2 & C_1 & -C_2 & -C_1 & -C_3 \end{bmatrix} \quad (4.35)$$

where  $C_1$ ,  $C_2$  and  $C_3$  are as defined in (4.32)-(4.34) and Table 4.1. Note that these coefficients depend on the second moments of the response quantities  $\Delta u$ ,  $\Delta \dot{u}$  and  $z$ . It is noted that, for a zero-mean excitation, the response of the linearized system has a zero mean.

In case the ground acceleration  $\ddot{x}_g$  is a modulated Gaussian white noise with power spectral density  $\Phi_0(t)$ , one can solve the equations of (4.20) or (4.21) with  $\mathbf{y}$  and  $\mathbf{G}$  as given above and with a  $5 \times 5$  matrix  $\mathbf{B}$  such that  $B_{ij} = 0$  for  $i, j = 1, \dots, 5$ , except

$$B_{22} = 2\pi\Phi_0(t)(l_1/m_1)^2 \text{ and } B_{44} = 2\pi\Phi_0(t)(l_2/m_2)^2 \quad (4.36)$$

When the ground acceleration is a zero-mean Gaussian, filtered white-noise process defined by the Kanai-Tajimi power spectral density in (4.22), the corresponding state-space system of equations is also in the form of (4.19) but with different definition of  $\mathbf{y}$ ,  $\mathbf{G}$  and  $\mathbf{f}$ . Based on (4.23) and (4.24),

$$\mathbf{y} = \{u_1 \quad \dot{u}_1 \quad u_2 \quad \dot{u}_2 \quad z \quad x_g^r \quad \dot{x}_g^r\}^T \quad (4.37)$$

$$\mathbf{G} = \begin{bmatrix} 0 & 1 & 0 & 0 & 0 & 0 & 0 \\ -\left(\frac{k_1 + \alpha k_o}{m_1}\right) & -\left(\frac{c_1 + c_o}{m_1}\right) & \frac{\alpha k_o}{m_1} & \frac{c_o}{m_1} & \frac{(1-\alpha)k_o}{m_1} & \left(\frac{l_1}{m_1}\right)\omega_g^2 & \left(\frac{l_1}{m_1}\right)(2\zeta_g\omega_g) \\ 0 & 0 & 0 & 1 & 0 & 0 & 0 \\ \frac{\alpha k_o}{m_2} & \frac{c_o}{m_2} & -\left(\frac{k_2 + \alpha k_o}{m_2}\right) & -\left(\frac{c_2 + c_o}{m_2}\right) & -\frac{(1-\alpha)k_o}{m_2} & \left(\frac{l_2}{m_2}\right)\omega_g^2 & \left(\frac{l_2}{m_2}\right)(2\zeta_g\omega_g) \\ C_2 & C_1 & -C_2 & -C_1 & -C_3 & 0 & 0 \\ 0 & 0 & 0 & 0 & 0 & 0 & 1 \\ 0 & 0 & 0 & 0 & 0 & -\omega_g^2 & -2\zeta_g\omega_g \end{bmatrix} \quad (4.38)$$

$$\mathbf{f} = \{0 \quad 0 \quad 0 \quad 0 \quad 0 \quad 0 \quad w(t)\}^T \quad (4.39)$$

where  $w(t)$  is a white-noise process with the power spectral density  $\Phi_0(t)$  (Wen 1980). Recall again that  $C_1$ ,  $C_2$  and  $C_3$  depend on the second moments of the response quantities  $\Delta u$ ,  $\Delta \dot{u}$

and  $z$ . The corresponding  $7 \times 7$   $\mathbf{B}$  matrix for the Lyapunov equation (4.20) or (4.21) has the elements  $B_{ij} = 0$  for  $i, j = 1, \dots, 7$ , except

$$B_{77} = 2\pi\Phi_0(t) \quad (4.40)$$

Since the nonlinear random vibration analysis by use of the ELM provides the rms (root-mean-square) responses of the connected and stand-alone equipment systems, it is convenient to define the response ratios in terms of the rms values instead of peak values, as in (2.11). Based on the fact that the mean of the extreme peak of a stationary process is approximately proportional to its rms value (Der Kiureghian 1980), the response ratios for the case of stochastic input are defined as

$$R_i = \frac{\text{rms}[u_i(t)]}{\text{rms}[u_{i0}(t)]}, i = 1, 2 \quad (4.41)$$

where  $\text{rms}[\cdot]$  denotes the rms value and  $u_i(t)$  and  $u_{i0}(t)$  respectively denote the displacements of equipment  $i$  in the connected and stand-alone configurations at time  $t$ . By use of the generalized Bouc-Wen model for the RB-FSC and the derived algebraic expressions for the coefficients of the equivalent linearized system, one can now estimate the rms response ratios of the RB-FSC-connected equipment system. This method allows one to account for the influences of the energy dissipation capacity and the material and geometric nonlinearity of the RB-FSC on the interaction effect. As expected, these influences are significantly affected by the intensity of the seismic motion. This effect cannot be captured by linear random vibration analysis.

As an example, consider two equipment items connected by three RB-FSC's. The system parameters have the values  $f_1 = 1 \text{ Hz}$ ,  $f_2 = 5 \text{ Hz}$ ,  $m_1 / m_2 = 2.0$ ,  $k_0 = 3 \times 35.6 = 106.8 \text{ kN/m}$ ,  $k_0 / (k_1 + k_2) = 0.5$ ,  $\zeta_i = 0.02$ ,  $i = 1, 2$ ,  $c_0 = 0$  and  $l_1 / m_1 = l_2 / m_2 = 1.0$ . The RB is a 3.05 m long aluminum pipe having a diameter of 10.2 cm and a thickness of 1.2 cm. The selected FSC is consistent with the PG&E No. 30-2022 (Figure 3.1). The parameters of the fitted generalized Bouc-Wen model are  $\alpha = 0.1$ ,  $A = 1.0$ ,  $n = 1$ ,  $\beta_1 = 0.419$ ,  $\beta_2 = -0.193$ ,  $\beta_3 = 0.174$ ,  $\beta_4 = 0.0901$ ,  $\beta_5 = -0.116$  and  $\beta_6 = -0.0564$ . Note that  $\alpha = 1.0$  corresponds to the case when the equipment items are connected by a linear connecting element having the initial stiffness  $k_0$  of the RB-FSC. For the ground acceleration, we consider a zero-mean, stationary Gaussian filtered white-noise process defined by the Kanai-Tajimi power spectral density of (4.22). The present analysis uses

$\omega_g = 5\pi$  rad/sec and  $\zeta_g = 0.6$  as the frequency and damping ratio of the filter. The amplitude of the process,  $\Phi_0$ , is varied to examine the variation in the nonlinearity of the system with increasing intensity of the ground motion, as measured in terms of the rms acceleration in units of gravity acceleration. We note that, roughly speaking, the rms intensity is a factor 1/2 to 1/3 of the peak ground motion.

The rms response ratios are evaluated by three different approaches: 1) nonlinear random vibration analysis by use of the ELM based on (4.21), (4.38) and (4.40) for the system with the proposed generalized Bouc-Wen model for the RB-FSC, 2) linear random vibration analysis by use of the initial stiffness of the RB-FSC, obtained by setting  $\alpha = 1.0$  in the nonlinear random vibration analysis, and 3) nonlinear time history analyses by use of five simulated ground motions based on the specified power spectral density. In the latter case, assuming ergodicity of the response process, the rms values are computed by time averaging the response samples over a sufficiently long interval of time.

Figure 4.13a shows a plot of the response ratio of the lower-frequency equipment item,  $R_1$ , versus the rms value of the ground acceleration. Figure 4.13b shows a similar plot for the response ratio  $R_2$  of the higher-frequency equipment item. It is seen that the estimate based on the linear random vibration analysis is a constant response ratio, independent of the intensity of the ground motion. This is because the responses of the linear systems representing the stand-alone and connected configurations are amplified by the same ratio when the seismic intensity is increased. As earlier observed by Der Kiureghian *et al.* (2001), the interaction between the two connected equipment items results in de-amplification of the response of the lower-frequency equipment and amplification of the response of the higher-frequency equipment relative to their stand-alone responses. We note that the de-amplification in the lower frequency item is a factor of 0.5, whereas the amplification in the higher-frequency equipment item is a factor of 3.7. The estimates by ELM using the hysteretic model of the RB-FSC show a significant reduction in the response ratios of both equipment items, which depends on the intensity of the ground motion. Two factors contribute to this reduction: (a) energy dissipation by the RB-FSC, which tends to reduce all responses of the connected system relative to those of the linear system, and (b) softening of the RB-FSC, which tends to reduce the interaction effect between the two connected equipment items. The reduction in the interaction effect tends to increase the response ratio for the lower-frequency equipment item and reduce the response ratio of the higher-frequency

equipment item. The overall result is a reduction in the response ratio of both equipment items with increasing intensity of ground motion.

To examine the accuracy of the response predictions by the ELM, time-history analyses are carried out for five sample functions of the ground motion, which are simulated in accordance to the specified power spectral density. The results in Figure 4.13 show reductions in the response ratios with increasing intensity of the ground motion, which are in close agreement with the ELM predictions. The ELM is able to provide a fairly good prediction of the response ratios.

It is also worthwhile to note in Figure 4.13 that the time history results show significant dispersion, even though the five sample ground motions are consistent with a single power spectral density. This indicates the high sensitivity of the interaction effect and the response ratios on the details of the ground motion. Under these conditions, clearly a stochastic analysis method is essential. In spite of its approximate nature, the ELM offers a viable and fairly accurate alternative for this purpose.

#### 4.5.2 Bi-linear Model for SC

In this section, the ELM is used to investigate equipment items connected by a bus slider having a bi-linear hysteretic behavior, as described in Chapter 3. The bi-linear model by Kaul & Penzien (1974) is described by the nonlinear auxiliary differential equation (3.12). When the responses are assumed to be zero-mean, Gaussian processes, according to (4.18), the auxiliary differential equation is linearized as

$$\dot{z} \cong a_0 + a_1 \Delta u + a_2 \Delta \dot{u} + a_3 z \quad (4.42)$$

where

$$a_0 = E[\dot{z}(t)] = 0 \quad (4.43a)$$

$$a_1 = E \left[ \frac{\partial \dot{z}(t)}{\partial \Delta u(t)} \right] = 0 \quad (4.43b)$$

$$\begin{aligned}
a_2 &= \mathbb{E} \left[ \frac{\partial \dot{z}(t)}{\partial \Delta \dot{u}(t)} \right] = 1 - 2 \int_{x_y}^{\infty} \int_0^{\infty} f_{\Delta \dot{u}(t), Z(t)}(v, w) dv dw \\
&= 1 - 2 \int_{x_y / \sigma_z}^{\infty} \frac{e^{-r^2/2}}{\sqrt{2\pi}} \Phi \left( \frac{\rho_{\Delta \dot{u}z} r}{\sqrt{1 - \rho_{\Delta \dot{u}z}^2}} \right) dr
\end{aligned} \tag{4.43c}$$

$$\begin{aligned}
a_3 &= \mathbb{E} \left[ \frac{\partial \dot{z}(t)}{\partial z(t)} \right] \\
&= -2 \int_0^{\infty} v f_{\Delta \dot{u}(t), Z(t)}(v, x_y) dv \\
&= -2 \frac{\sigma_{\Delta \dot{u}}}{\sigma_z} \left\{ \frac{\rho_{\Delta \dot{u}z} x_y}{\sqrt{2\pi} \sigma_z} \exp \left( -\frac{x_y^2}{2\sigma_z^2} \right) \Phi \left( \frac{\rho_{\Delta \dot{u}z} x_y}{\sigma_z \sqrt{1 - \rho_{\Delta \dot{u}z}^2}} \right) + \frac{1}{2\pi} \sqrt{1 - \rho_{\Delta \dot{u}z}^2} \exp \left[ -\frac{x_y^2}{2\sigma_z^2 (1 - \rho_{\Delta \dot{u}z}^2)} \right] \right\}
\end{aligned} \tag{4.43d}$$

where  $f_{\Delta \dot{u}(t), Z(t)}(\cdot, \cdot)$  is the joint probability density function of the Gaussian random variables  $\Delta \dot{u}(t)$  and  $z(t)$ , and  $\Phi(\cdot)$  denotes the cumulative distribution function of the standard Gaussian random variable.

All other steps of the ELM analysis are the same as those for the generalized Bouc-Wen model described in the previous section. When the state-space vector  $\mathbf{y}$  in the first-order equivalent system of (4.19) is defined as (4.7), the corresponding  $\mathbf{G}$  matrix in case of a white-noise input is

$$\mathbf{G} = \begin{bmatrix} 0 & 1 & 0 & 0 & 0 \\ -\left( \frac{k_1 + \alpha k_o}{m_1} \right) & -\left( \frac{c_1 + c_o}{m_1} \right) & \frac{\alpha k_o}{m_1} & \frac{c_o}{m_1} & \frac{(1 - \alpha)k_o}{m_1} \\ 0 & 0 & 0 & 1 & 0 \\ \frac{\alpha k_o}{m_2} & \frac{c_o}{m_2} & -\left( \frac{k_2 + \alpha k_o}{m_2} \right) & -\left( \frac{c_2 + c_o}{m_2} \right) & -\frac{(1 - \alpha)k_o}{m_2} \\ 0 & -a_2 & 0 & a_2 & a_3 \end{bmatrix} \tag{4.44}$$

The Lyapunov analysis utilizes the  $\mathbf{B}$  matrix in (4.36), as used for the generalized Bouc-Wen model. The formulation is expanded for the case of a filtered white-noise input excitation in the same manner as done for the generalized Bouc-Wen model.

As an example, consider two equipment items connected by three identical bus sliders, with the parameter values  $f_1 = 1$  Hz,  $f_2 = 5$  Hz,  $m_1 / m_2 = 2.0$ ,  $k_o = 3 \times 1,163 = 3,489$  kN/m,  $k_o / (k_1 + k_2) = 16.3$ ,  $\zeta_i = 0.02$ ,  $i = 1, 2$ ,  $c_o = 0$  and  $l_1 / m_1 = l_2 / m_2 = 1.0$ . The analytical model

for the bus slider is fitted to the measurement of the old bus slider model by Filiatrault *et al.* (1999). The parameters used for the bi-linear model are  $x_y = 0.0203$  cm. and  $\alpha = 0.0125$ . The ground acceleration is considered as a stationary, filtered white-noise process defined by the Kanai-Tajimi power spectral density of (4.22) with  $\omega_g = 5\pi$  rad/sec and  $\zeta_g = 0.6$ . The amplitude of the process,  $\Phi_0$ , is varied to examine the variation in the nonlinearity of the system with increasing intensity of the ground motion, as measured in terms of the rms acceleration in units of gravity acceleration. As in the case of the generalized Bouc-Wen model, the rms response ratios are evaluated by three different approaches: linear random vibration analysis, ELM, and deterministic time-history analysis using five samples of the ground motion that are simulated according to the specified power spectral density.

Figure 4.14 shows the response ratios  $R_1$  and  $R_2$  for the lower- and higher-frequency equipment items, respectively, plotted as functions of the ground motion intensity, as measured in terms of the rms acceleration. The results based on the ELM, which are in close agreement with the simulated time-history results, show a significant reduction in the response ratio of the higher-frequency equipment item, when compared with the linear system. At a low intensity level, the response ratio for this equipment item is much greater than unity, indicating strong amplification of the response due to the interaction. As the intensity increases and the shaft starts to slide, the interaction effect is quickly reduced due to the softening and energy dissipation of the sliding connector.

### 4.5.3 Bouc-Wen Model for S-FSC

Electrical substation equipment items connected by the RB-S-FSC are modeled by the differential system of equations (2.8)-(2.10), (4.1) and (3.3). When the response is nearly Gaussian, according to (4.18), the nonlinear auxiliary equation (3.3) for the original Bouc-Wen model is linearized as (Wen 1980)

$$\dot{z} + b_1 \Delta \dot{u} + b_2 z = 0 \quad (4.45)$$

where

$$b_1 = E \left[ \frac{\partial q}{\partial \Delta \dot{u}} \right], \quad b_2 = E \left[ \frac{\partial q}{\partial z} \right] \quad (4.46)$$

in which

$$q = \dot{z} - \Delta\dot{u} \left\{ A - |z|^n [\beta + \gamma \operatorname{sgn}(\Delta\dot{u}z)] \right\} \quad (4.47)$$

By use of (4.28), the coefficients  $b_1$  and  $b_2$  are obtained as algebraic expressions of the second moments of  $\Delta\dot{u}$  and  $z$ ,

$$b_1 = \sqrt{\frac{2}{\pi}} \left[ \gamma \frac{E[\Delta\dot{U}Z]}{\sigma_{\Delta\dot{U}}} + \beta \sigma_Z \right] - A \quad (4.48a)$$

$$b_2 = \sqrt{\frac{2}{\pi}} \left[ \gamma \sigma_{\Delta\dot{U}} + \beta \frac{E[\Delta\dot{U}Z]}{\sigma_Z} \right] \quad (4.48b)$$

All the other steps of the ELM analysis are the same as those for the generalized Bouc-Wen model. When the state-space vector  $\mathbf{y}$  in the first-order equivalent equation (4.19) is defined as (4.7), the corresponding  $\mathbf{G}$  matrix in the case of a white-noise input process is obtained as

$$\mathbf{G} = \begin{bmatrix} 0 & 1 & 0 & 0 & 0 \\ -\left(\frac{k_1 + \alpha k_o}{m_1}\right) & -\left(\frac{c_1 + c_o}{m_1}\right) & \frac{\alpha k_o}{m_1} & \frac{c_o}{m_1} & \frac{(1-\alpha)k_o}{m_1} \\ 0 & 0 & 0 & 1 & 0 \\ \frac{\alpha k_o}{m_2} & \frac{c_o}{m_2} & -\left(\frac{k_2 + \alpha k_o}{m_2}\right) & -\left(\frac{c_2 + c_o}{m_2}\right) & -\frac{(1-\alpha)k_o}{m_2} \\ 0 & b_1 & 0 & -b_1 & -b_2 \end{bmatrix} \quad (4.49)$$

The Lyapunov analysis utilizes the same  $\mathbf{B}$  matrix in (4.36) as used for the generalized Bouc-Wen model. The formulation can be expanded for the case of a filtered white-noise input in the same manner as for the generalized Bouc-Wen model.

As an example, consider two equipment items connected by three RB-S-FSC's. The parameters have the values  $f_1 = 1$  Hz,  $f_2 = 5$  Hz,  $m_1/m_2 = 2.0$ ,  $k_0 = 3 \times 8.58 = 25.7$  kN/m,  $k_0/(k_1 + k_2) = 0.5$ ,  $\zeta_i = 0.02$  for  $i = 1, 2$ ,  $c_0 = 0$  and  $l_1/m_1 = l_2/m_2 = 1.0$ . The analytical model for the S-FSC is fitted to the second S-FSC specimen tested by Stearns & Filiatrault (2003). The parameters used for the Bouc-Wen model are  $\alpha = 0.206$ ,  $A = 1$ ,  $n = 1$ ,  $\beta = 0.175$  and  $\gamma = 0.176$ . The ground acceleration is considered as a zero-mean, stationary Gaussian filtered white-noise process defined by the Kanai-Tajimi power spectral density of (4.22) with  $\omega_g = 5\pi$



rad/sec and  $\zeta_g = 0.6$ . The amplitude of the process,  $\Phi_0$ , is varied to examine the variation in the nonlinearity of the system with increasing intensity of the ground motion. The rms response ratios are evaluated by three different approaches as used in the example for the generalized Bouc-Wen model.

Figure 4.15 shows plots of the response ratios  $R_1$  and  $R_2$  for the lower- and higher-frequency equipment items versus the rms of the ground acceleration. The ELM results, which are in close agreement with the simulated time-history results, show significant reductions in the response ratios with increasing intensity of the ground motion. These are due to the softening and energy dissipation of the  $S$ -FSC.

Table 4.1 Expressions for  $E_i$ ,  $i = 1, \dots, 8$ , in (4.32)-(4.34), for computing the coefficients of the linearized equations for the generalized Bouc-Wen model for  $n = 1$

$E_i$	Expression
$E_1$	$\sqrt{\frac{2}{\pi}} \frac{E[\Delta \dot{u}z]}{\sigma_{\Delta \dot{u}}}$
$E_2$	$\left(\frac{2}{\pi}\right)^{3/2} \left[ \frac{E[\Delta uz]}{\sigma_{\Delta u}} \sin^{-1}(\tilde{\rho}_{\Delta \dot{u}z}) + \frac{E[\Delta \dot{u}z]}{\sigma_{\Delta \dot{u}}} \sin^{-1}(\tilde{\rho}_{\Delta uz}) + \sigma_z \sin^{-1}(\tilde{\rho}_{\Delta u \Delta \dot{u}}) \right]$
$E_3$	$\sqrt{\frac{2}{\pi}} \frac{E[\Delta uz]}{\sigma_{\Delta u}}$
$E_4$	$\left(\frac{2}{\pi}\right)^{3/2} \frac{\sigma_{\Delta \dot{u}} \sigma_z}{\sigma_{\Delta u}} \sqrt{1 - \rho_{\Delta u \Delta \dot{u}}^2} \sqrt{1 - \rho_{\Delta uz}^2} \left( \sqrt{1 - \tilde{\rho}_{\Delta \dot{u}z}^2} + \tilde{\rho}_{\Delta \dot{u}z} \sin^{-1} \tilde{\rho}_{\Delta \dot{u}z} \right)$
$E_5$	$\sqrt{\frac{2}{\pi}} \frac{\sigma_{\Delta \dot{u}} \sigma_z}{\sigma_{\Delta u}} (\rho_{\Delta \dot{u}z} - \rho_{\Delta u \Delta \dot{u}} \rho_{\Delta uz})$
$E_6$	$\sqrt{\frac{2}{\pi}} \sigma_{\Delta \dot{u}}$
$E_7$	$\left(\frac{2}{\pi}\right)^{3/2} \left[ \frac{E[\Delta u \Delta \dot{u}]}{\sigma_{\Delta u}} \sin^{-1}(\tilde{\rho}_{\Delta \dot{u}z}) + \sigma_{\Delta \dot{u}} \sin^{-1}(\tilde{\rho}_{\Delta uz}) + \frac{E[\Delta \dot{u}z]}{\sigma_z} \sin^{-1}(\tilde{\rho}_{\Delta u \Delta \dot{u}}) \right]$
$E_8$	$\sqrt{\frac{2}{\pi}} \frac{E[\Delta u \Delta \dot{u}]}{\sigma_{\Delta u}}$

where  $\sigma$  denotes the standard deviation,  $\rho$  stands for the correlation coefficient, and

$$\tilde{\rho}_{\Delta \dot{u}z} = \frac{\rho_{\Delta \dot{u}z} - \rho_{\Delta u \Delta \dot{u}} \rho_{\Delta uz}}{\sqrt{1 - \rho_{\Delta u \Delta \dot{u}}^2} \sqrt{1 - \rho_{\Delta uz}^2}}, \quad \tilde{\rho}_{\Delta uz} = \frac{\rho_{\Delta uz} - \rho_{\Delta u \Delta \dot{u}} \rho_{\Delta \dot{u}z}}{\sqrt{1 - \rho_{\Delta u \Delta \dot{u}}^2} \sqrt{1 - \rho_{\Delta \dot{u}z}^2}},$$

$$\tilde{\rho}_{\Delta u \Delta \dot{u}} = \frac{\rho_{\Delta u \Delta \dot{u}} - \rho_{\Delta uz} \rho_{\Delta \dot{u}z}}{\sqrt{1 - \rho_{\Delta uz}^2} \sqrt{1 - \rho_{\Delta \dot{u}z}^2}}$$

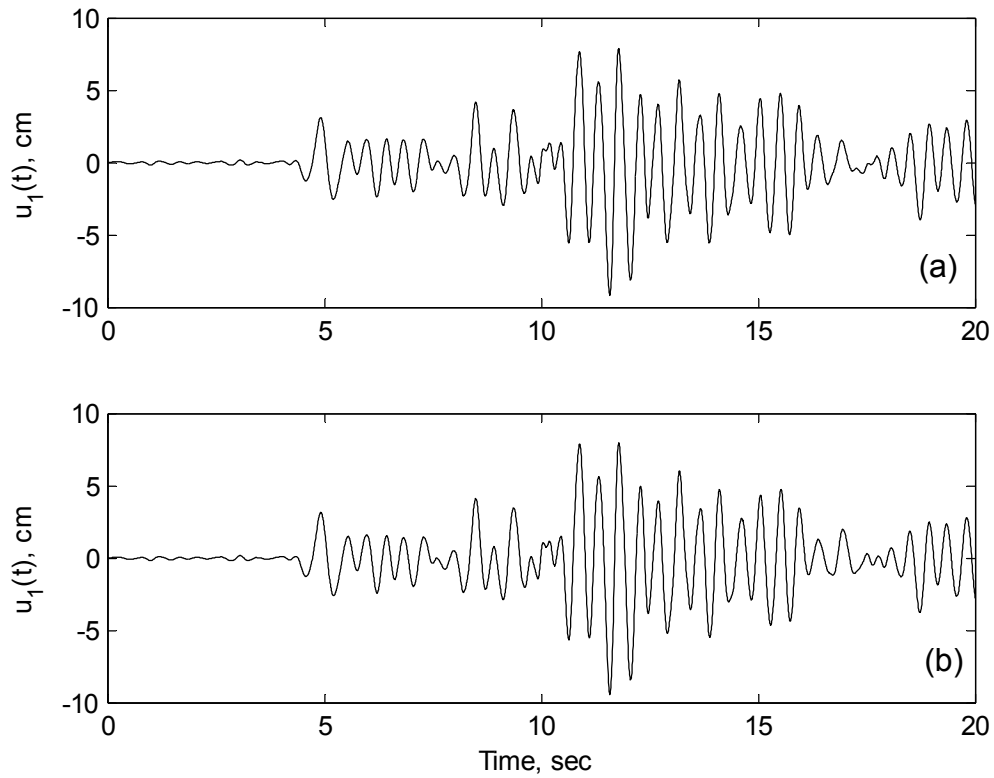


Figure 4.1 Displacement time histories of the lower-frequency equipment item in the RB-FSC (symmetric, 30-2022)-connected system for the TabasLN record: (a) modified Bouc-Wen model; (b) generalized Bouc-Wen model

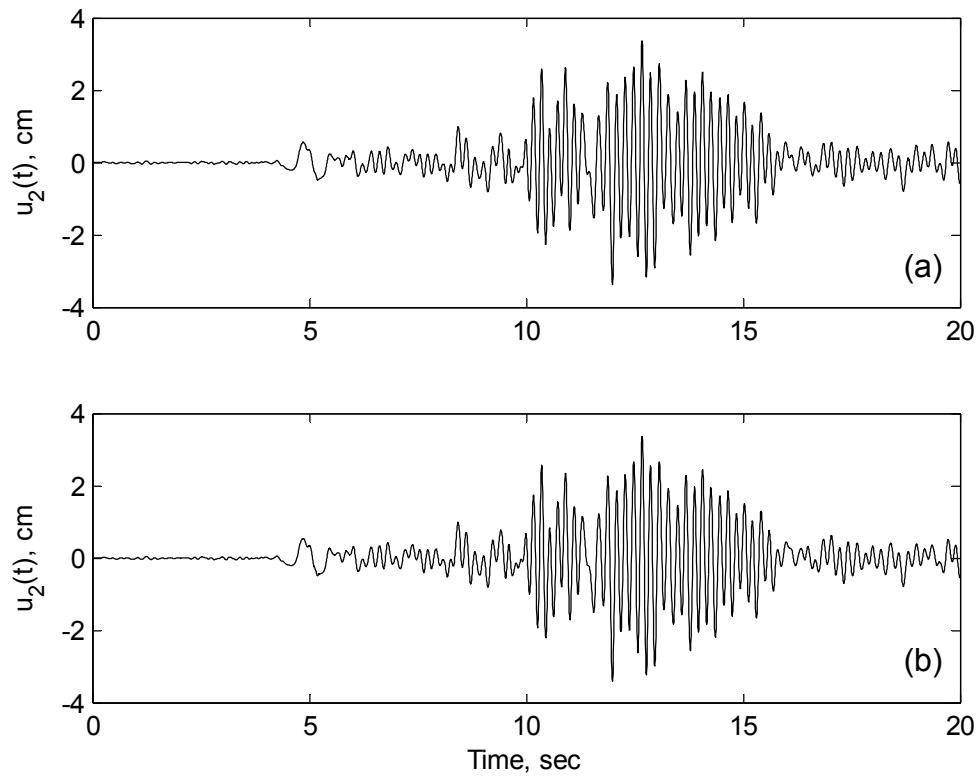


Figure 4.2 Displacement time histories of the higher-frequency equipment item in the RB-FSC (symmetric, 30-2022)-connected system for the TabasLN record: (a) modified Bouc-Wen model; (b) generalized Bouc-Wen model

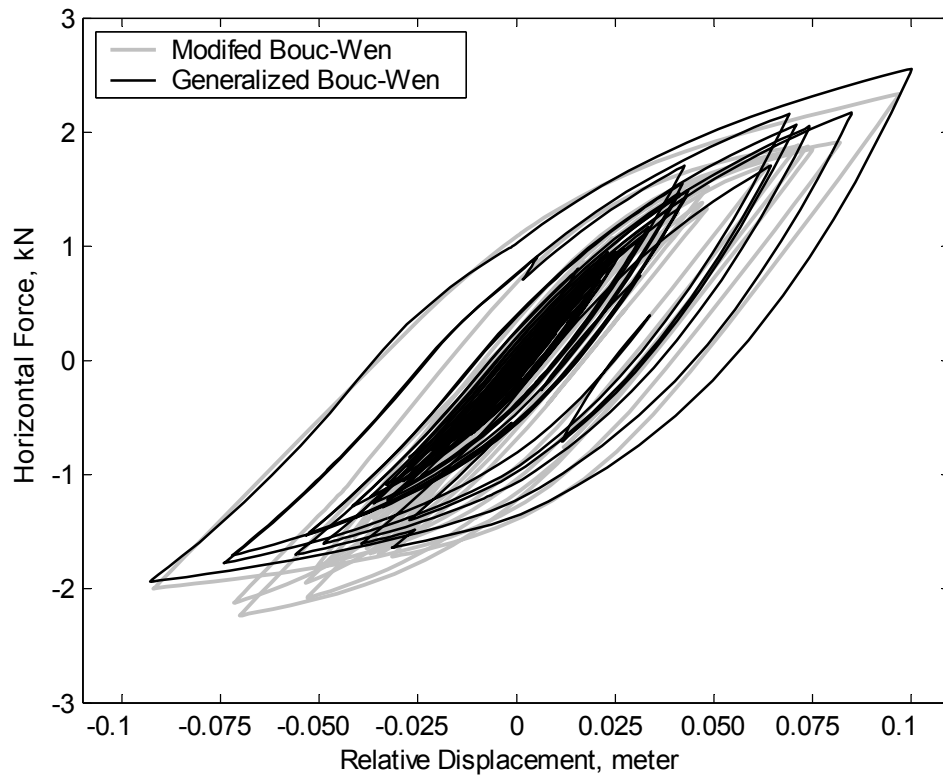


Figure 4.3 Force-elongation hysteresis loops of the RB-FSC (symmetric, 30-2022) in the interconnected system subjected to the Tabas LN record

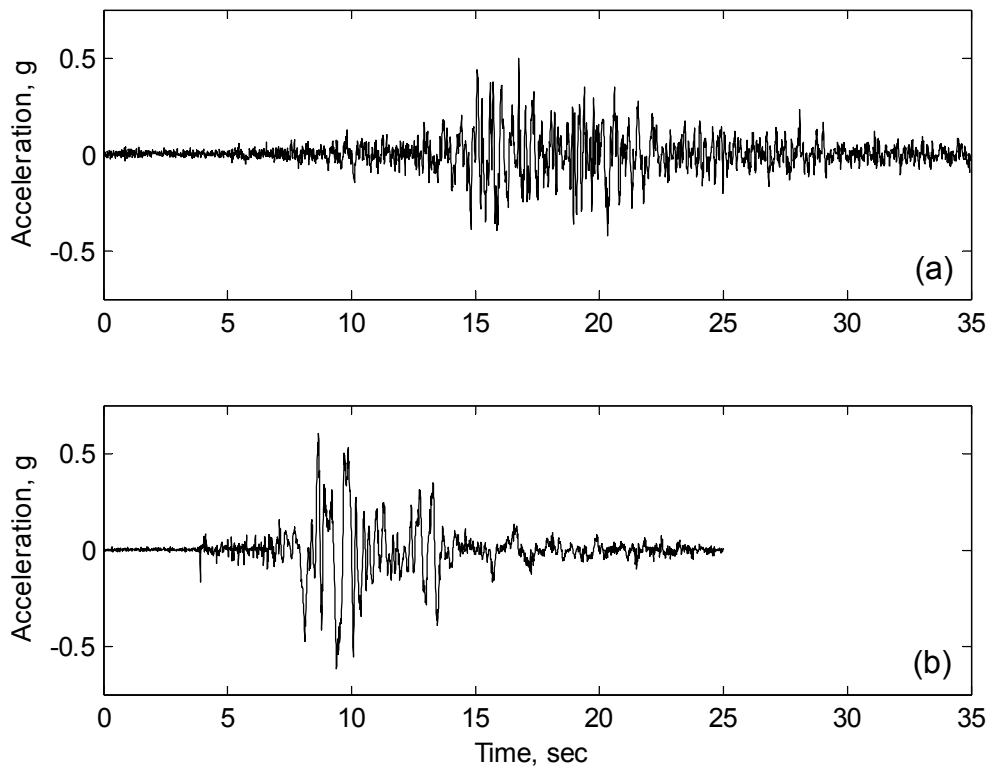


Figure 4.4 Acceleration time histories of shake-table motions for (a) Test RB-79 (Tabas 50%); (b) Test RB-112 (Newhall 100%)

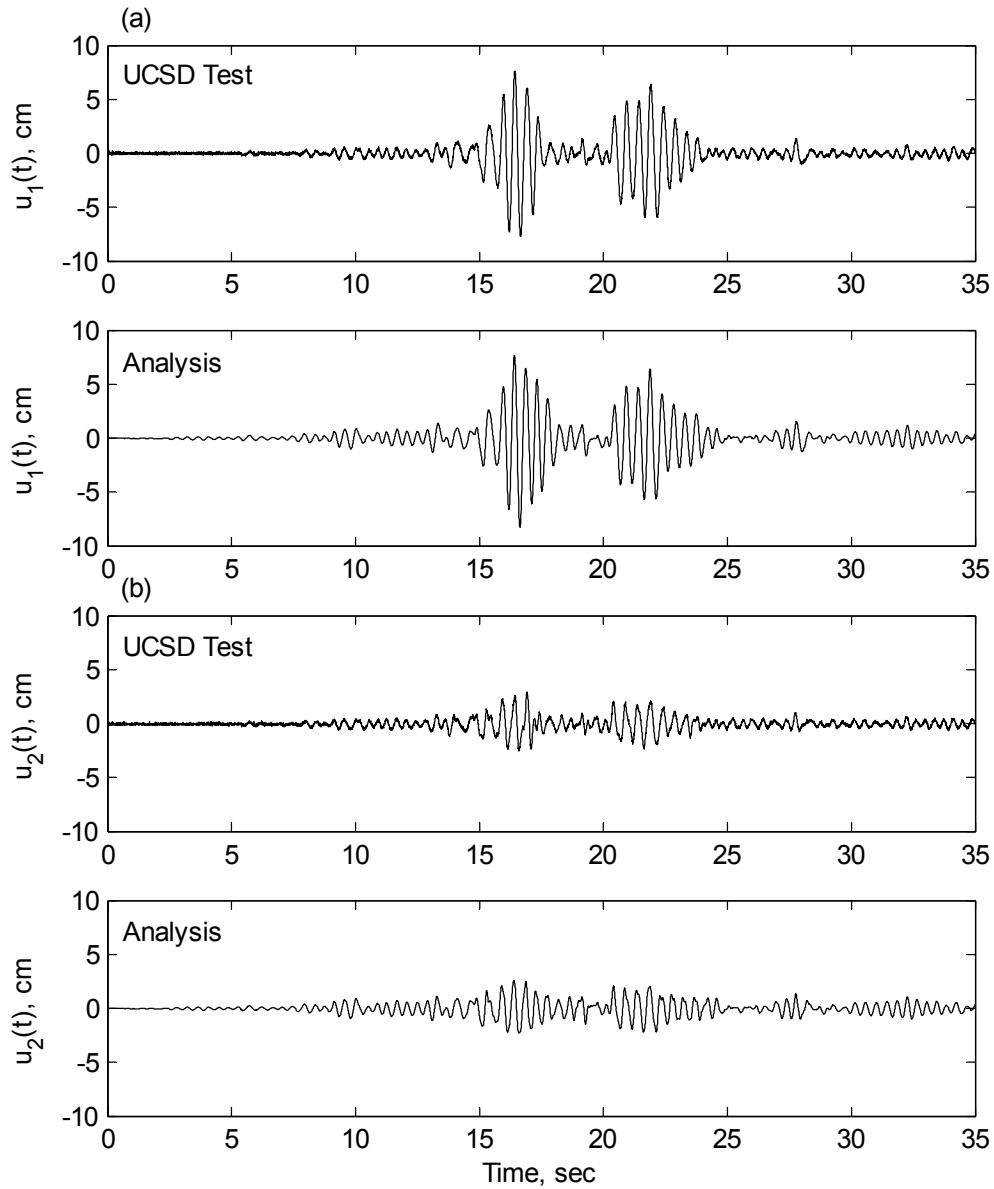


Figure 4.5 Displacement time histories of equipment items in the bus-slider-connected system for the table motion of Test RB-79: (a) lower frequency equipment item; (b) higher-frequency equipment item

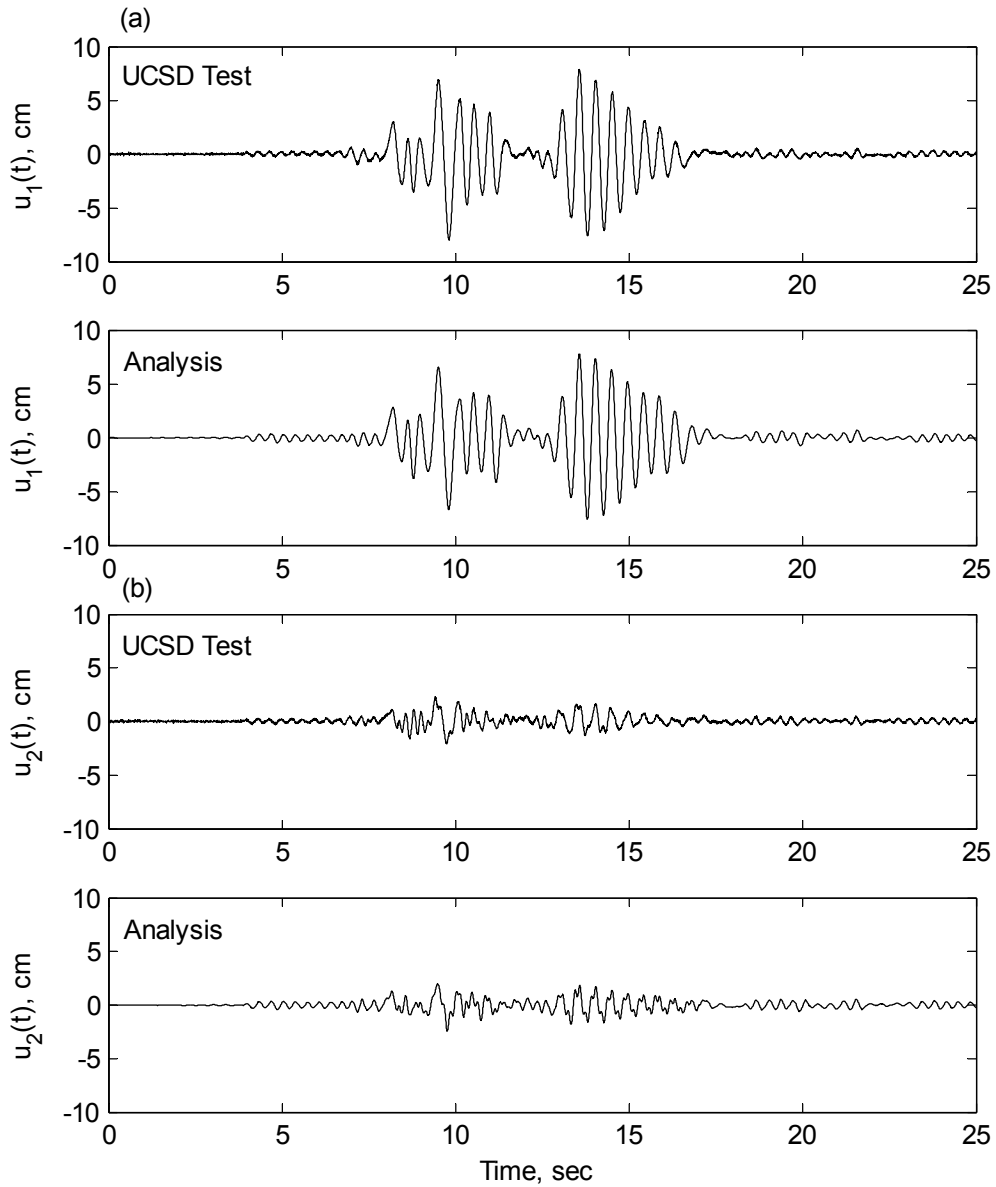


Figure 4.6 Displacement time histories of equipment items in the bus-slider-connected system for the table motion of Test RB-112: (a) lower-frequency equipment item; (b) higher-frequency equipment item



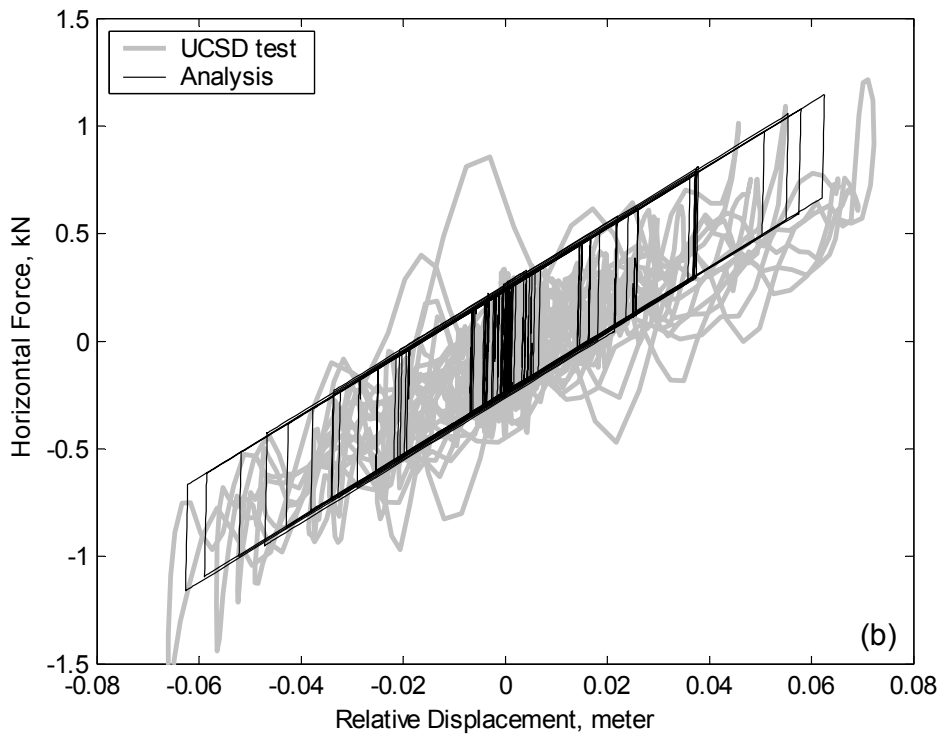
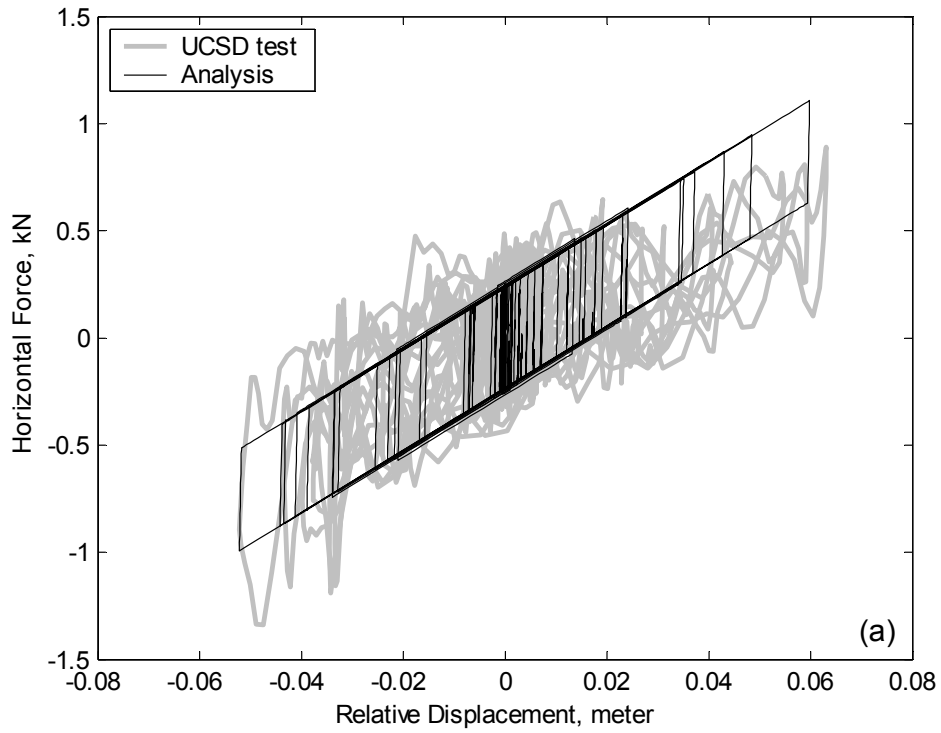


Figure 4.7 Force-elongation hysteresis loops of the bus slider in the connected system: (a) Test RB-79; (b) Test RB-112

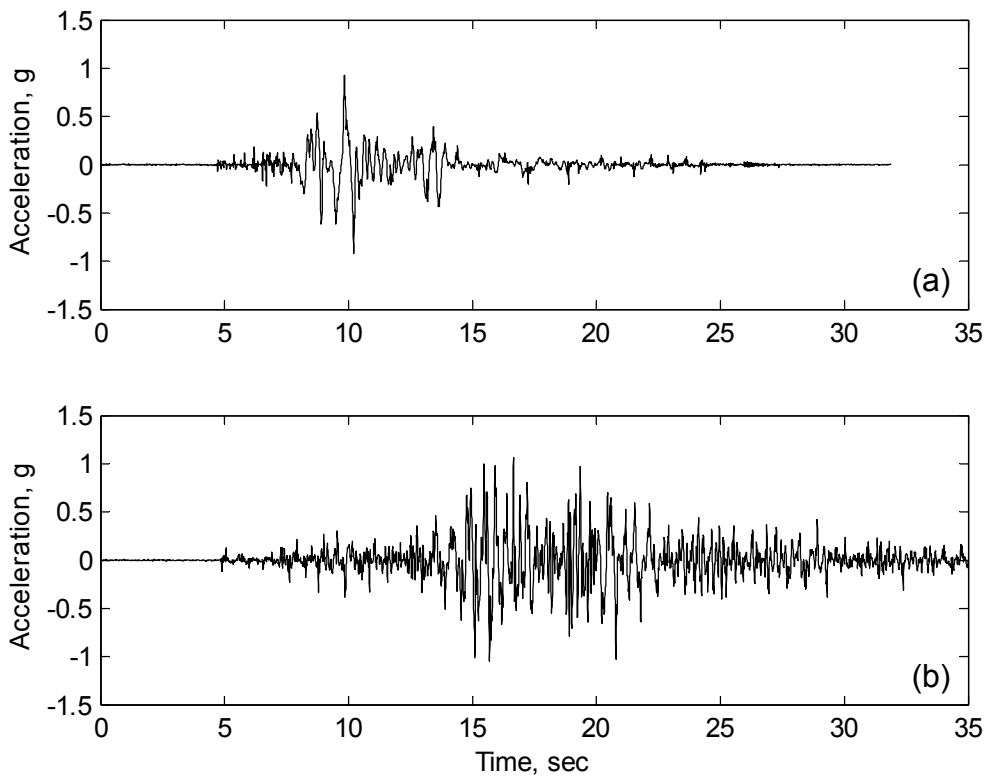


Figure 4.8 Acceleration time histories for shake table motions of (a) Test RC-86 (Newhall 100%); (b) Test RC-88B (Tabas 100%)

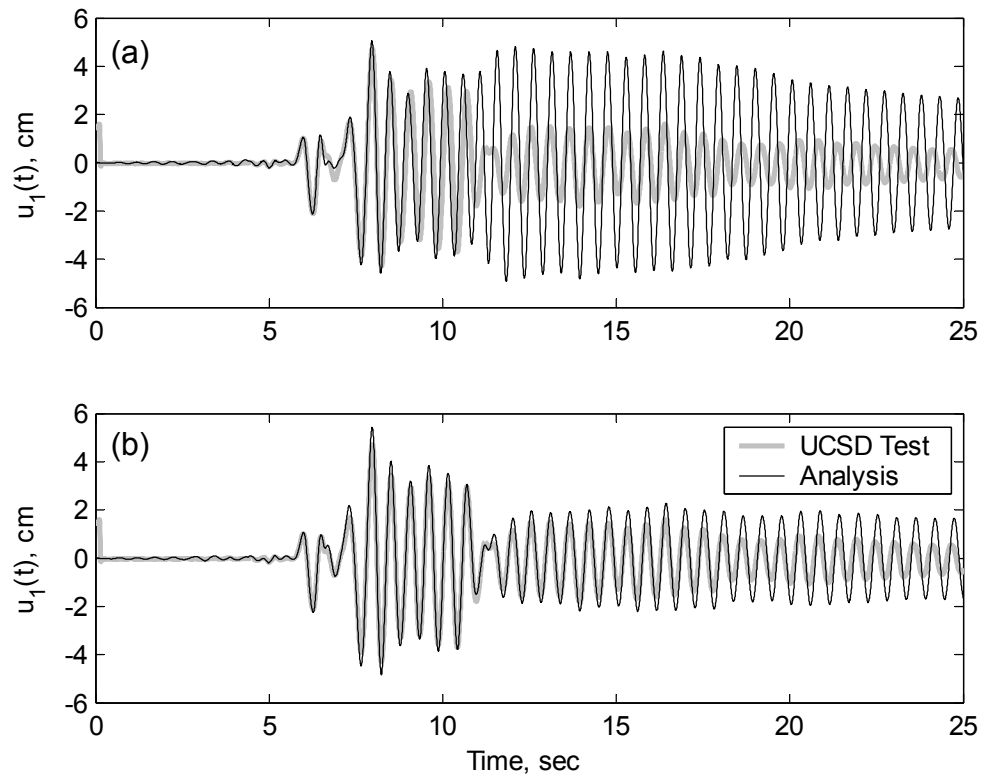


Figure 4.9 Displacement time histories of the lower-frequency equipment item of Test RC-86 and RC-88B when excited in its stand-alone configuration (Test RC-64): (a) analysis based on the reported equipment frequency  $f_1 = 1.88$  Hz; (b) analysis based on the adjusted frequency  $f_1 = 1.81$  Hz

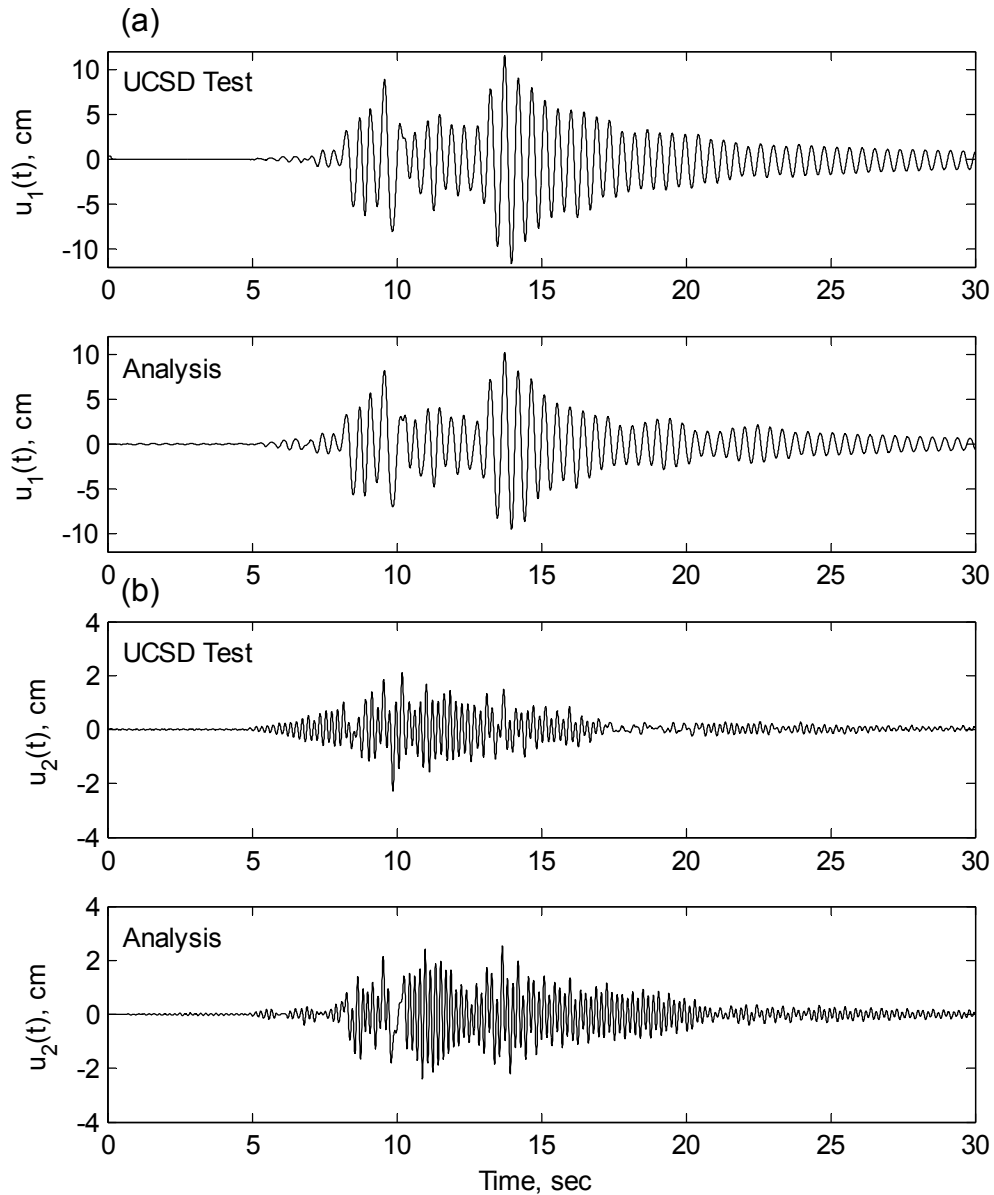


Figure 4.10 Displacement time histories of equipment items in the *S*-FSC-connected system for the table motion of Test RC-86: (a) lower-frequency equipment item; (b) higher-frequency equipment item

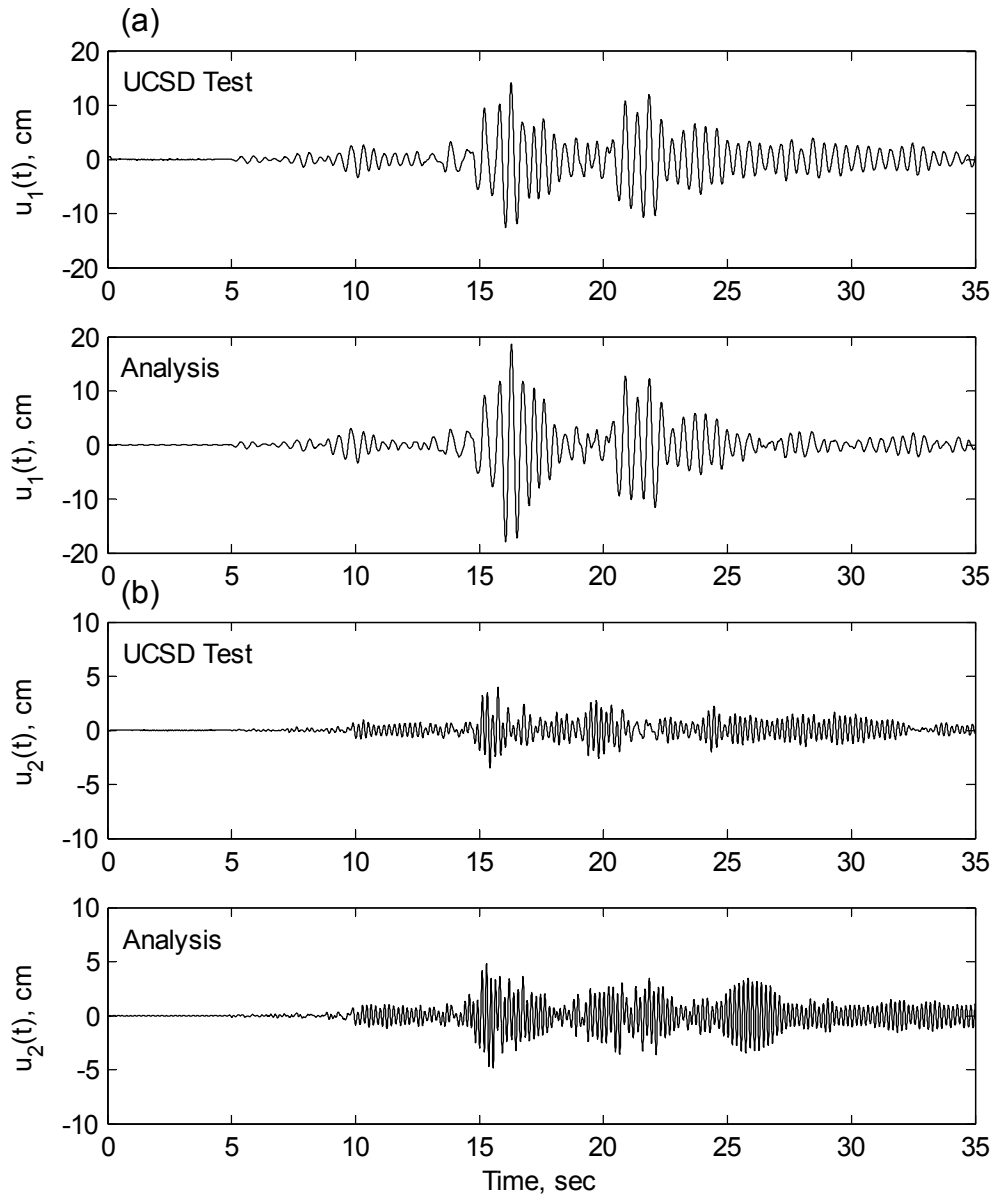


Figure 4.11 Displacement time histories of equipment items in the *S*-FSC-connected system for the table motion of Test RC-88B: (a) lower-frequency equipment item; (b) higher-frequency equipment item

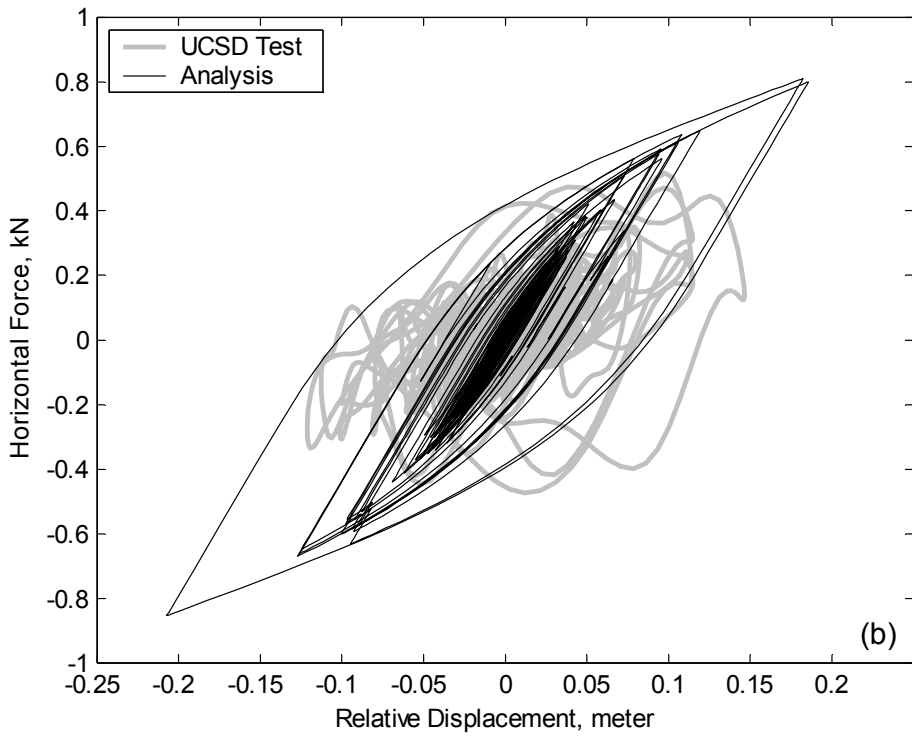
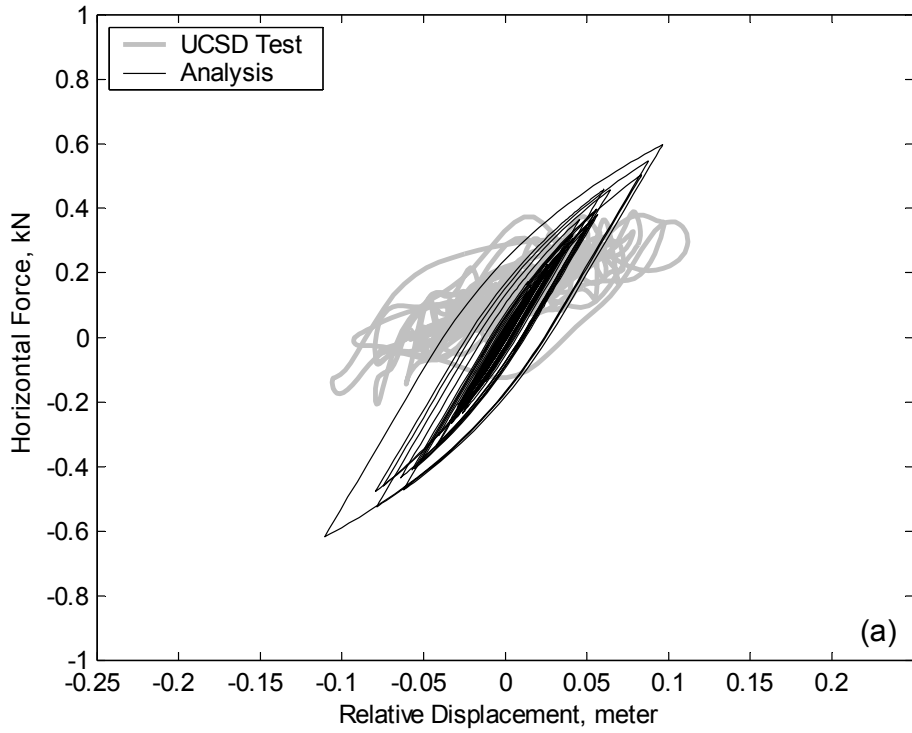


Figure 4.12 Force-elongation hysteresis loops of the *S*-FSC in the connected system: (a) Test RC-86; (b) Test RC-88B

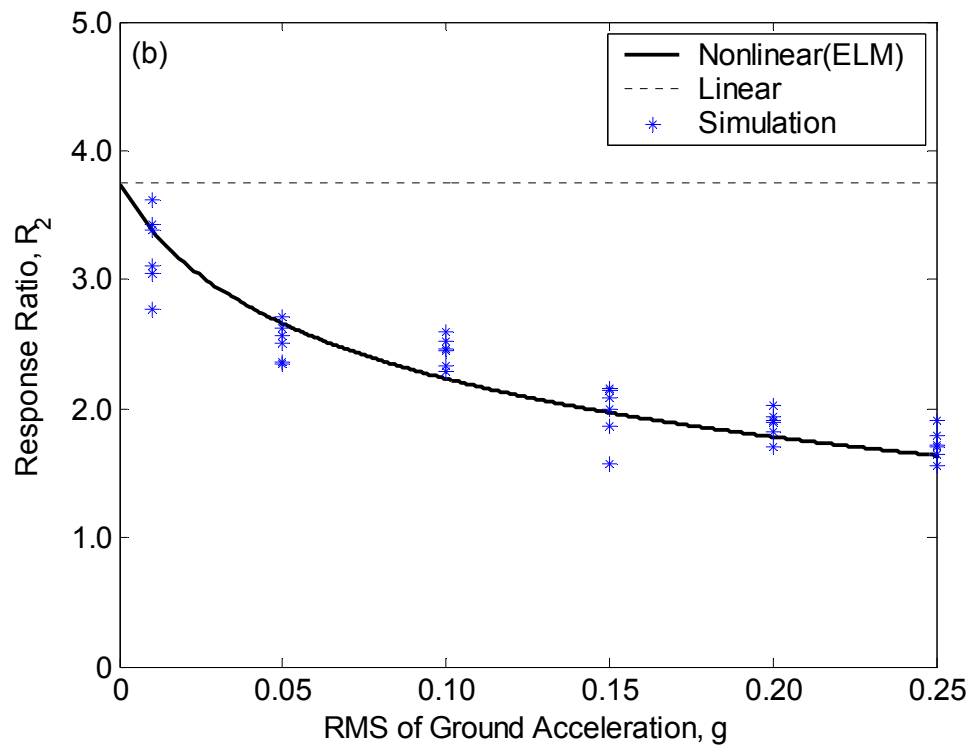
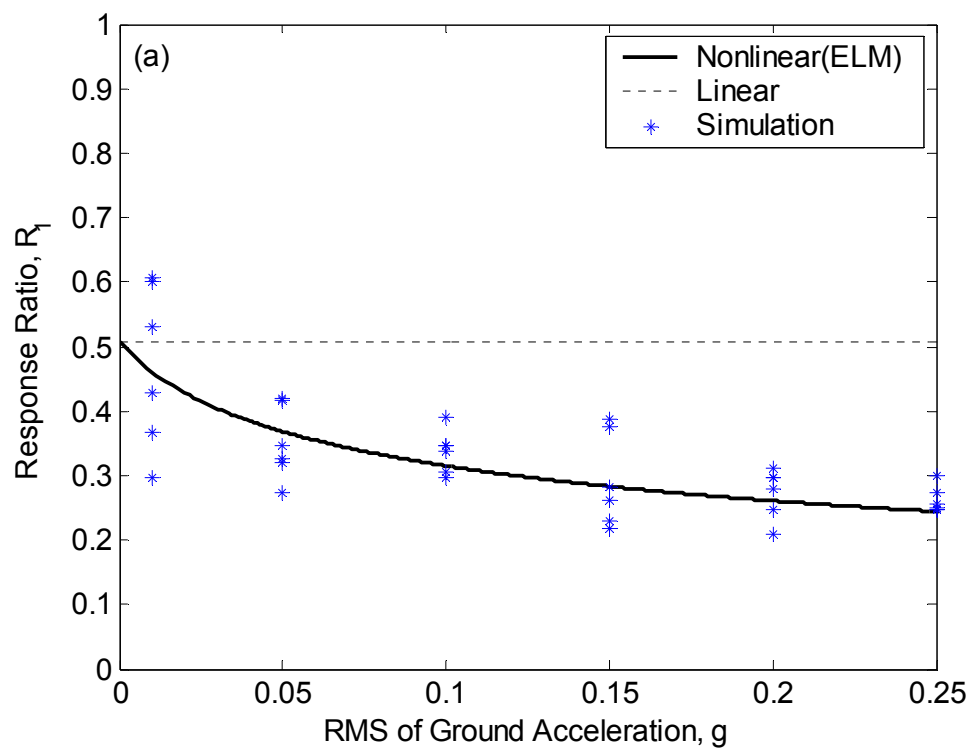


Figure 4.13 Response ratios for equipment items connected by RB-FSC 30-2022: (a) lower-frequency equipment item; (b) higher-frequency equipment item

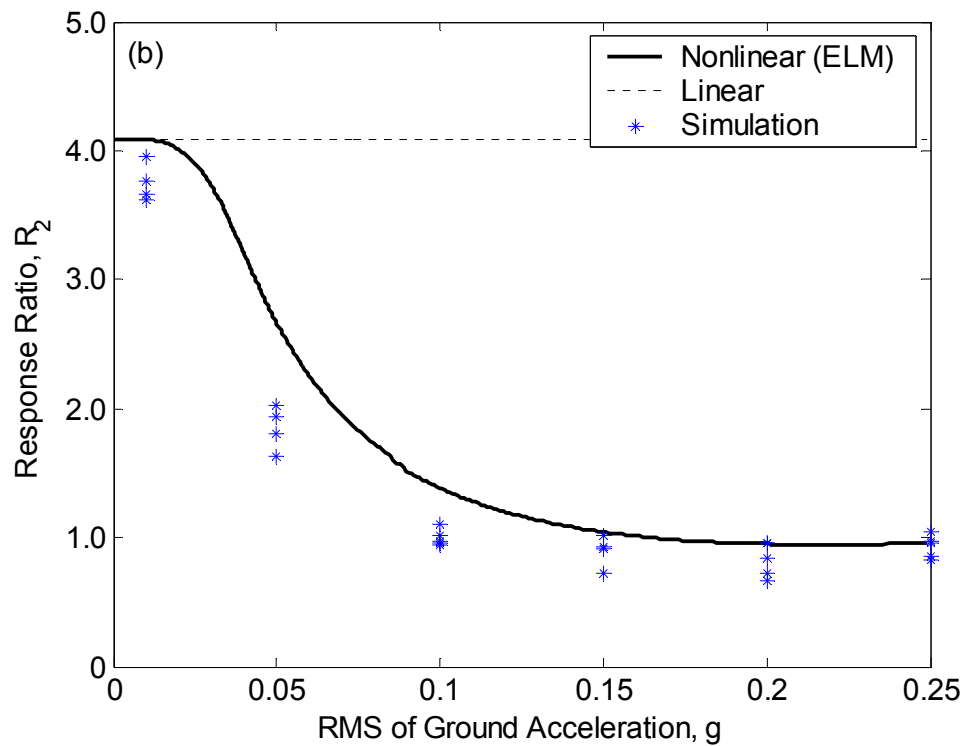
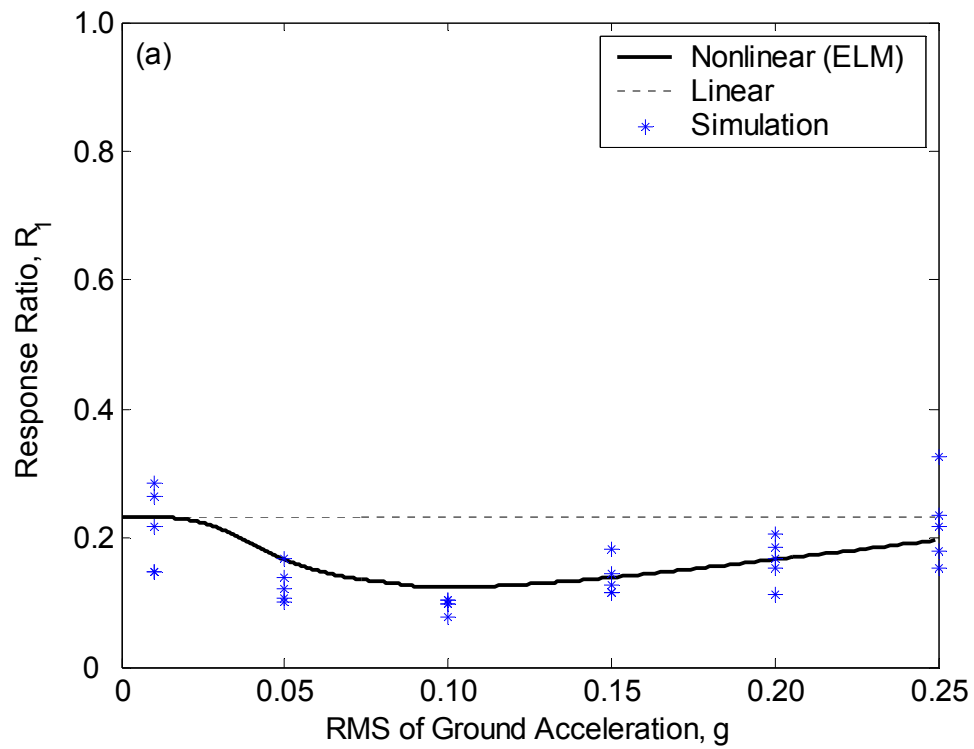


Figure 4.14 Response ratios for equipment items connected by bus slider: (a) lower-frequency equipment item; (b) higher-frequency equipment item



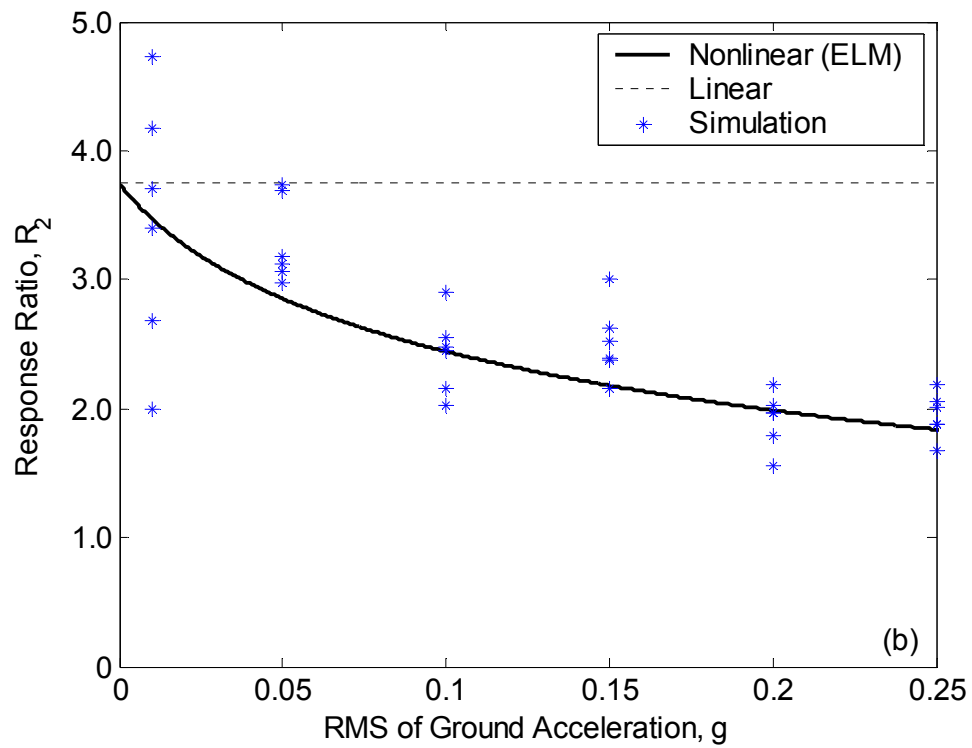
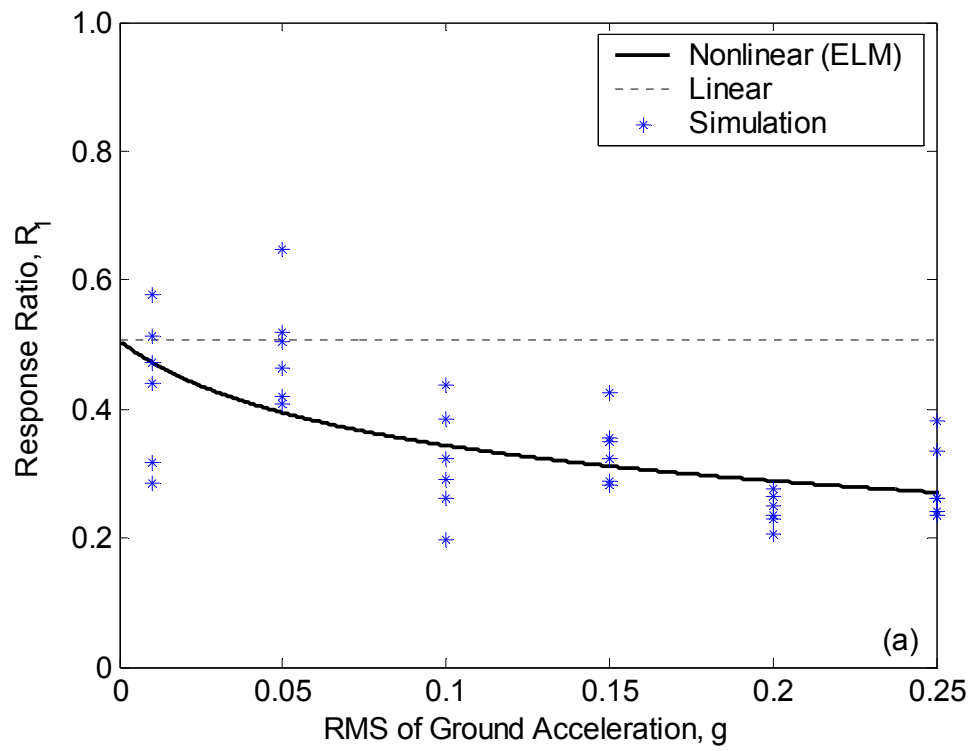


Figure 4.15 Response ratios for equipment items connected by  $S$ -FSC: (a) lower-frequency equipment item; (b) higher-frequency equipment item



# 5 Effect of Interaction on Connected Electrical Equipment

## 5.1 INTRODUCTION

In the previous chapters, analytical models and methods were developed for estimating the responses of connected electrical substation equipment subjected to deterministic and stochastic ground motions. In this chapter, the effect of interaction in the connected equipment system is investigated through extensive parametric studies, using nonlinear random vibration analysis employing the models and methods developed in Chapters 2-4. The influences of various system parameters and connector types on the interaction effect are examined in terms of the estimated response ratios. Based on these results, simple guidelines are suggested for reducing the hazardous effect of seismic interaction in practice.

Section 5.2 examines the interaction effect in two equipment items connected by a linear element and subjected to a stochastic ground motion. The equipment items are modeled as single-degree-of-freedom (SDOF) oscillators, as described in Chapter 2. The rms response ratios are estimated by linear random vibration analysis to examine the influences of various system parameters on the interaction effect.

Section 5.3 investigates the interaction effect in equipment items connected by nonlinear rigid-bus connectors. The hysteretic behavior of the connectors is described by the differential equation models developed in Chapter 3. The rms response ratios are computed by nonlinear random vibration analysis by use of the equivalent linearization method (ELM), as described in Chapter 4. For each connector, parametric charts of the response ratio  $R_2$  for the higher-frequency equipment item are developed, which describe the influences of a wide range of system parameters. The performances of the various connectors under the same conditions are then compared in terms of the response ratios for the higher-frequency equipment item, which is the

equipment that is adversely affected by the interaction.

Based on the results of the parametric investigation, Section 5.4 provides guidelines for the seismic design of interconnected electrical substation equipment. The design guidelines utilize the parametric charts in Section 5.3 for easy estimate of the interaction effect in practice.

## 5.2 EFFECT OF INTERACTION IN LINEARLY CONNECTED EQUIPMENT ITEMS

The last three numerical examples of Chapter 4 compare the rms response ratios of connected equipment items, evaluated by linear and nonlinear random vibration analyses. As demonstrated in Figures 4.13-4.15, the nonlinear behavior of the connectors, specifically the energy dissipation and softening characteristics, help to reduce the responses of the connected equipment items in most cases. Therefore, modeling the rigid bus connector as a linear spring having the initial stiffness of the connector will lead to conservative estimates of the response ratios. Moreover, the linear analysis cannot account for the influence of the intensity of the ground motions on the response ratios. Nevertheless, the simplicity of the linear random vibration analysis makes it easy to perform extensive parametric investigations for understanding the basic nature of the interaction effect and for identifying the key parameters that influence it.

Der Kiureghian *et al.* (1999, 2001) carried out the extensive parametric studies for the system described by linear SDOF equipment models and a linear connecting element. The peak response ratios (2.11) were computed by the response spectrum method with the CQC modal combination rule (Der Kiureghian 1981) in order to identify the influences of the equipment frequencies, the ratio of equipment masses, the stiffness and mass of the connecting element, and the attachment configuration on the interaction effect. For investigating the influence of the damping of the connecting element, linear random vibration analysis was used because the conventional response spectrum method is not applicable to systems with general, non-classical damping.

To be consistent with the method of analysis used later for the nonlinear connectors, the parametric study of the linear connector is carried out by use of linear random vibration analysis instead of the response spectrum method. This approach requires the frequency response functions of the equipment displacements. These functions are obtained from the equations of motion (2.8)-(2.10) with the resisting force of the connector modeled as  $q = k_0 \Delta u$ . The steady-state solu-

tion of the equation under a harmonic ground acceleration with frequency  $\omega$ , i.e.,  $\ddot{x}_g(t) = \exp(i\omega t)$ ,  $i = \sqrt{-1}$ , is

$$\mathbf{u}_{\text{steady state}}(\omega) = -\mathbf{H}(\omega)\mathbf{L} \exp(i\omega t) \quad (5.1)$$

where

$$\begin{aligned} \mathbf{H}(\omega) &= (-\omega^2\mathbf{M} + i\omega\mathbf{C} + \mathbf{K})^{-1} \\ &= \begin{bmatrix} -\omega^2 m_1 + i\omega(c_0 + c_1) + k_0 + k_1 & -i\omega c_0 - k_0 \\ -i\omega c_0 - k_0 & -\omega^2 m_2 + i\omega(c_0 + c_2) + k_0 + k_2 \end{bmatrix}^{-1} \\ &= \frac{1}{\Delta} \begin{bmatrix} -\omega^2 m_2 + i\omega(c_0 + c_2) + k_0 + k_2 & i\omega c_0 + k_0 \\ i\omega c_0 + k_0 & -\omega^2 m_1 + i\omega(c_0 + c_1) + k_0 + k_1 \end{bmatrix} \end{aligned} \quad (5.2a)$$

$$\Delta = [-\omega^2 m_1 + i\omega(c_0 + c_1) + k_0 + k_1][-\omega^2 m_2 + i\omega(c_0 + c_2) + k_0 + k_2] - (i\omega c_0 + k_0)^2 \quad (5.2b)$$

where  $\mathbf{L}$  is the vector of coefficients of the external inertia force,  $l_i$ ,  $i = 1, 2$ . The components of the vector  $\mathbf{H}(\omega)\mathbf{L}$ ,  $H_{u_1}(\omega)$  and  $H_{u_2}(\omega)$ , are the frequency response functions of the displacements  $u_1(t)$  and  $u_2(t)$ , respectively. The frequency response function for the relative displacement  $\Delta u$  is given as  $H_{u_2-u_1}(\omega) = H_{u_2}(\omega) - H_{u_1}(\omega)$ .

In the stand-alone configuration, the motion of each equipment, which is modeled as a SDOF oscillator, is governed by the linear differential equation

$$m_i \ddot{u}_{i0} + c_i \dot{u}_{i0} + k_i u_{i0} = -l_i \ddot{x}_g, \quad i = 1, 2 \quad (5.3)$$

The frequency response function of the displacement  $u_{i0}(t)$ , denoted  $H_{u_{i0}}(\omega)$ , is determined from the steady-state solution of (5.3):

$$H_{u_{i0}}(\omega) = -\frac{l_i}{m_i} \frac{1}{(k_i/m_i) - \omega^2 + 2i\zeta_i \sqrt{k_i/m_i} \omega}, \quad i = 1, 2 \quad (5.4)$$

The frequency response function of the relative displacement  $u_{20}(t) - u_{10}(t)$  is obtained as  $H_{u_{20}-u_{10}}(\omega) = H_{u_{20}}(\omega) - H_{u_{10}}(\omega)$ .

When a linear system is subjected to a stationary ground motion  $\ddot{x}_g(t)$  with power spectral density  $\Phi_{\ddot{x}_g \ddot{x}_g}(\omega)$ , the rms value of a generic response  $u(t)$  is

$$\text{rms}[u(t)] = \sqrt{\int_{-\infty}^{\infty} |H_u(\omega)|^2 \Phi_{\ddot{x}_g \ddot{x}_g}(\omega) d\omega} \quad (5.5)$$

where  $H_u(\omega)$  is the frequency response function of  $u(t)$ . Substituting the frequency response functions (5.2) or (5.4) and the power spectral density of the input ground motion in (5.5), one can compute the rms values of the equipment displacements in the connected and stand-alone configurations, respectively.

The rms response ratios for equipment items were defined in (4.41). Following Der Kiureghian *et al.* (1999), for the connecting element, an rms response ratio is defined as

$$R_0 = \frac{\text{rms}|u_2(t) - u_1(t)|}{\text{rms}|u_{20}(t) - u_{10}(t)|} \quad (5.6)$$

This ratio describes the change in the relative displacement between the two equipment items as a result of the interconnection. Since the equipment items are modeled as linear SDOF oscillators, the above response ratios also describe the amounts of de-amplification or amplification in the equipment responses.

A set of parametric studies are carried out to investigate the effect of the equipment frequencies, the mass ratio and the stiffness of the connecting element. The rms response ratios  $R_1$ ,  $R_2$  and  $R_0$  are evaluated according to (4.41) and (5.6) from the rms responses computed by substituting the frequency response functions of (5.2) into (5.5). The input ground acceleration is assumed to be a zero-mean, stationary, filtered white-noise process, defined by the Kanai-Tajimi power spectral density of (4.22). The parameter values  $\omega_g = 5\pi$  rad/sec and  $\zeta_g = 0.6$ , which are appropriate for a firm ground, are used. The intensity parameter  $\Phi_0$  does not affect the response ratios when the system is linear. As we have seen in Chapter 4, this is not the case when the nonlinearity in the connecting element is taken into account.

Figure 5.1 shows the response ratios as functions of the ratio of frequencies  $f_1/f_2$  for the ratio of stiffnesses  $\kappa = k_0/(k_1 + k_2) = 0.2, 1$  and  $\infty$ , and ratio of masses  $m_1/m_2 = 0.5$  and  $5$ . The damping values are set to  $\zeta_1 = \zeta_2 = 0.02$  and  $c_0 = 0$ , and the higher frequency item has the frequency  $f_2 = 5$  Hz. The attachment configuration is assumed to be such that  $l_1/m_1 = l_2/m_2$ . The most important observation in this figure is that, for all values of  $\kappa$ ,  $m_1/m_2$  and  $f_1/f_2 < 1$ , the interaction amplifies the response of the higher-frequency equipment item, i.e.,  $R_2 > 1$ , while

the response of the lower frequency item is de-amplified, i.e.,  $R_1 < 1$ . This means that the interaction between the two equipment items generally has an adverse effect on the equipment item with the higher frequency. This effect intensifies as  $\kappa$  increases, i.e., as the connecting element becomes stiffer. This observation motivated the development of the *S*-FSC, which is a highly flexible rigid bus connector. As the mass ratio  $m_1/m_2$  increases, the response ratios of both items tend to increase. The separation between the frequencies of the equipment items also generally enhances the interaction effects.

Next, a different value of  $f_2$  is selected to examine the effect of a change in the absolute values of the equipment frequencies. By shifting the frequencies of the equipment items relative to a fixed input power spectral density shape, the influence of the frequency content of the ground motion is also examined. Figure 5.2 shows the response ratios for the case of  $f_2 = 10$  Hz. Comparing the results in Figures 5.1 and 5.2, it is observed that the response ratios at most moderately depend on the absolute values of the equipment frequencies. This is because the ratios are of concern rather than absolute responses. It is also due to the fact that a wide-band power spectral density model is used for the input ground motion.

To investigate the influence of the bandwidth of the input ground motion on the interaction effect, a different set of values is selected for the parameters of the Kanai-Tajimi power spectral density function. Figure 5.3 shows the response ratios when  $\omega_g = \pi$  rad/sec and  $\zeta_g = 0.3$ , with all the system parameters similar to those of Figure 5.1. This case corresponds to a strongly narrow-band ground motion, which may occur in places with a lake bed, such as Mexico City. Although the plots show trends similar to those in Figure 5.1, the estimated response ratios are significantly different. This suggests that response ratios estimated for ground motions with a certain bandwidth are not directly applicable to ground motions with overly different bandwidths.

Next, the response ratios of systems with damping ratios  $\zeta_1 = \zeta_2 = 0.02$  and those with damping ratios  $\zeta_1 = \zeta_2 = 0.05$  are compared to investigate the effect of the equipment damping on the interaction effect. Figure 5.4 shows that there is practically no influence of equipment damping ratios on the interaction effects.

The energy dissipation capacity of a connecting element has considerable influence on the interaction effect. The energy dissipation in the connecting element may arise from its hys-

teretic behavior, viscosity of the material, friction at the connections, etc. To investigate the effects of the damping in the linear model, it is assumed that the equivalent viscous damping coefficients  $c_0$ ,  $c_1$  and  $c_2$  approximately describe the energy dissipation characteristics of the connecting element and the two equipment items. For a parametric study, the ratio of damping coefficients  $\chi = c_0 / (c_1 + c_2)$  is introduced. Figure 5.5 shows the rms response ratios as functions of the ratio of equipment frequencies  $f_1 / f_2$ , for the parameter values  $m_1 / m_2 = 2$ ,  $f_2 = 10$  Hz,  $\zeta_1 = \zeta_2 = 0.02$ ,  $\kappa = 0.05$ , and  $\chi = 0, 1$  and  $10$ . It is evident that increasing the damping of the connecting element reduces the amplification of the higher frequency item by a significant amount, especially when the equipment frequencies are well separated from each other.

The influence of the mass of the connecting element and attachment configurations were also examined by Der Kiureghian *et al.* (1999) by use of the response spectrum method. The investigation revealed that increasing the mass of the connecting element causes relatively modest amplifications in both equipment responses, as long as the mass remains small compared to those of the equipment items. It was also observed that attaching the connecting element near the base of the higher frequency equipment item would produce the most adverse interaction effect.

### **5.3 EFFECT OF INTERACTION IN EQUIPMENT ITEMS CONNECTED BY NONLINEAR RIGID BUS CONDUCTORS**

The nonlinear behavior of rigid bus conductors has significant influence over the interaction effect in connected electrical substation equipment. In particular, the softening and the hysteretic damping of the conductor can significantly reduce the amplification of the response of the higher-frequency equipment. This was confirmed by the parametric study of the linear system in the preceding section, where the softening can be thought of as a reduction in the ratio of stiffnesses  $\kappa$  and the hysteretic damping can be thought of as an increase in the ratio of damping coefficients  $\chi$ .

As shown in Chapter 3, each rigid bus connector has a unique hysteretic behavior in terms of the shape of the hysteresis loop, the post-yielding stiffness, and the energy dissipation capacity. Since this nonlinear behavior strongly depends on the amplitude of the response, it is not appropriate to describe a rigid bus connector as a linear element with equivalent stiffness and damping values independent of the intensity of the ground motion. In order to examine the inter-



action effect accurately, therefore, it is necessary to use analytical models and methods which can properly account for the nonlinear behavior of the connector. One can perform nonlinear time-history analysis employing selected ground motions. However, this approach is not appropriate for the purpose of a parametric investigation, because it allows us to evaluate the interaction effect only for the selected time histories, not for a class of ground motions. A Monte Carlo approach employing artificially simulated ground motions and nonlinear time history analysis is a valid alternative, but not a practical one because it would require an enormous amount of computations to obtain meaningful results.

Nonlinear random vibration analysis employing the ELM provides an accurate and efficient method to obtain the rms responses of the connected equipment system for a class of ground motions without costly computations. For a wide range of the system parameter values, the rms response ratios are computed by ELM for two equipment items connected by the six rigid bus conductors introduced in Chapter 3. These are: 1) PG&E 30-2021, 2) PG&E 30-2022, 3) PG&E 30-2023, 4) Slider Connector (old), 5) Slider Connector (new) and 6) *S*-FSC. The equipment items are modeled as SDOF oscillators and the nonlinear behaviors of the connectors are described by the differential equation models in Chapter 3. It is assumed that the viscous damping of each connector is negligible compared to its hysteretic damping, i.e.,  $c_0 = 0$  is assumed. Based on the finding from the above linear analysis that the equipment damping has almost no influence over the interaction effect, the equipment damping ratios are fixed at  $\zeta_1 = \zeta_2 = 0.02$  for all cases. The input ground motion is represented by a zero-mean, stationary Gaussian, filtered white-noise process defined by the Kanai-Tajimi power spectral density in (4.22). The filter parameter values  $\omega_g = 5\pi$  rad/s and  $\zeta_g = 0.6$ , which are appropriate for a firm ground, are used. The intensity parameter  $\Phi_0$  is adjusted such that the rms of the ground acceleration varies from 0.1g to 0.3g. This range roughly corresponds to the peak ground acceleration range 0.25g-0.75g, representing ground motions with moderate to severe intensities. Consideration is given only to the higher-frequency equipment item, for which the interaction effect results in an amplification relative to the stand-alone response. For each connector, the response ratio  $R_2$  is computed as a function of the ratio of equipment frequencies,  $f_1/f_2$ , for a total of 27 cases determined by the following set of parameters:  $f_2 = 1, 5$  and  $10$  Hz,  $m_2 = 100, 500$  and  $1000$  kg, and  $m_1/m_2 = 0.5, 1.0$  and  $5.0$ . Figures 5.6-5.11 show the minimum and maximum values of the computed response ratios obtained over the considered range of the ground motion

intensities for each connector. In general, for each set of parameters, the minimum value of  $R_2$  corresponds to the higher intensity of the ground motion, i.e., an rms value of 0.3g or a peak ground acceleration of 0.75g, while the maximum value corresponds to the moderate intensity of ground motion, i.e., an rms intensity of 0.1g or a peak ground acceleration of 0.25g.

The following observations in Figures 5.6-5.11 are noteworthy: (a) Similar to the linear case, the response ratio  $R_2$  increases with decreasing ratio of equipment frequencies, i.e., with further separation of the equipment frequencies. (b) In most cases, the response ratio  $R_2$  is greater than 1, indicating amplification of the higher-frequency equipment response relative to its stand-alone response. A notable exception is in Figures 5.9 and 5.10 for the slider connector, where the response ratio for certain parameter values is seen to fall below 1. This reduction in the response is due to the energy dissipation of the slider connector. (c) For a fixed value of  $f_2$  and the frequency ratio  $f_1/f_2$  (i.e., for fixed equipment frequencies), the response ratio  $R_2$  tends to increase with increasing  $m_1$  and with decreasing  $m_2$ . With the equipment frequencies fixed, these changes in the equipment masses imply similar changes in the equipment stiffnesses  $k_1$  and  $k_2$ . Therefore, for fixed equipment frequencies,  $R_2$  tends to increase with increasing  $m_1$  and  $k_1$  (a “bigger” lower-frequency equipment item) and with decreasing  $m_2$  and  $k_2$  (a “smaller” higher-frequency equipment item). (d) The influence of the nonlinear behavior of the connecting element on  $R_2$  is reflected in the gap between the minimum and maximum values of the response ratio for each set of the parameters. As mentioned earlier, the maximum value of  $R_2$  corresponds to the case of a moderate-intensity ground motion, whereas the minimum value corresponds to the case of a severe-intensity ground motion. For intensity values in between these two extremes, we recommend a simple linear interpolation of  $R_2$  between the values in the chart for peak ground accelerations 0.25g and 0.75g. It is evident that the amount of reduction in  $R_2$  due to the nonlinear behavior of the connector depends on the combination of the system parameters.

To compare the relative performances of the six types of rigid bus connectors, the response ratio  $R_2$  is computed for a series of connected systems having identical equipment and ground motion characteristics but different connectors. Among the cases shown in Figures 5.6-5.11, two with significant interaction effects are selected for this purpose. Figure 5.12 compares the response ratios  $R_2$  for the six connectors for the set of parameters  $f_1 = 1$  Hz,  $f_2 = 5$  Hz,  $m_1 = 500$  kg,  $m_2 = 100$  kg,  $\zeta_1 = \zeta_2 = 0.02$ ,  $l_1/m_1 = l_2/m_2 = 1.0$  and  $c_0 = 0$ . Figure 5.13 shows similar results for  $f_2 = 10$  Hz and  $m_1 = 100$  kg, with all other parameters remaining unchanged.

The input ground motion in both cases is modeled by the Kanai-Tajimi power spectral density with  $\omega_g = 5\pi$  rad/s and  $\zeta_g = 0.6$ . The following noteworthy observations can be made in these figures: (a) The three existing PG&E FSC's produce moderate reductions of the interaction effect by their nonlinear behavior. These reductions are mainly due to the loss of stiffness of these FSC's by localized yielding. Among the three FSC's, the long-leg FSC PG&E 30-2023 produces the smallest interaction effect. Note, however, that this FSC can only be used when the connection points of the two equipment items are at different vertical levels (See Figure 3.1c). (b) With the slider connectors, the response ratio  $R_2$  is initially large for low-intensity ground motions. As the intensity increases and the shaft starts to slide, the interaction effect quickly diminishes. Interestingly, the old and new slider connectors provide almost identical results, even though they have significantly different configurations. Overall, for high-intensity ground motions, the slider connector provides a significant advantage by sharply reducing the adverse interaction effect on the high-frequency equipment item. (c) Due to its high flexibility, the *S*-FSC reduces the interaction effect to levels similar to that of the slider connector, but independent of the intensity of the ground motion. This FSC does not experience much inelastic deformation. Therefore, it will not be necessary to replace it even after a severe earthquake.

From the above study, it is clear that among the six connectors, the slider connector and the *S*-FSC have the most effective designs. Other considerations, such as manufacturing cost or electrical requirements, may affect the choice of the best connector for each application.

## 5.4 DESIGN GUIDELINES

Based on the results reported above and in Chapters 2-4, in this section we summarize a number of guiding principles for consideration when assessing the effect of interaction on connected electrical substation equipment, or when making design decisions in practice. These include considerations for modeling equipment items, rigid bus connectors and the ground motion, methods for assessing the resulting amplification in the response of the higher-frequency equipment item, and design considerations for reducing this adverse effect.

### 5.4.1 Characterization of Equipment Items as SDOF Oscillators

Each equipment item in its stand-alone configuration is characterized as a SDOF oscillator having the equivalent mass  $m_i$ , stiffness  $k_i$ , damping ratio  $\zeta_i$ , and external inertial load coefficient  $l_i$ . As demonstrated in Chapter 2, an appropriate displacement shape function should be selected to compute these effective properties. If available, the displacement shape under self-weight in the direction of the ground motion is expected to produce the best estimates of the parameters  $m_i$ ,  $k_i$  and  $l_i$ . Assume an equivalent damping ratio  $\zeta_i$  characterizing the expected energy dissipation capacity of the equipment. These parameters can also be obtained through laboratory or field tests, as conducted by Filiatrault *et al.* (1999). In many practical situations, it may be difficult to carry out the SDOF idealization either by shape functions or tests due to the complexity of the equipment item or lack of information. The design engineer must exercise engineering judgment in selecting these parameters of the idealized SDOF model of the equipment. If necessary, the interaction effect may be assessed for a range of parameter values in order to account for the uncertainty in the parameters.

### 5.4.2 Modeling of the Rigid-Bus Connector

The rigid-bus connectors are characterized by selecting an appropriate differential equation model and finding the values of the parameters in the selected model. For the six rigid-bus connectors investigated in this study, complete models are developed and fitted to test measurements in Chapter 3. For a new connector, it will be necessary to first obtain the hysteresis loop under cyclic loading, either by a physical test or a virtual experiment employing a detailed finite element model of the connector. A differential equation model may then be selected based on the shape of the obtained hysteresis loop. The parameters of the selected model are found by fitting the analytical hysteresis loop to the experimental result.

### 5.4.3 Characterization of Input Ground Motion

In order to account for the nonlinear behavior of the rigid bus connector, this study employs nonlinear random vibration analysis in conjunction with ELM and a stochastic representation of the ground motion in terms of a power spectral density function. The parameters of the power

spectral density function should be selected in accordance with the dominant frequency and bandwidth expected of the ground motion at the site of interest. The intensity of the ground acceleration should be selected on the basis of the seismic zone of the site or based on seismic hazard analysis. Alternatively, nonlinear time-history analysis may be carried out if the response of the connected system to a specific ground motion is of interest. It is noted that the interaction effect is strongly sensitive to the details of the ground motion and general conclusions should not be derived from the analysis for a single ground motion.

#### 5.4.4 Evaluation of the Effect of Interaction on the Higher-Frequency Equipment

Parametric studies reported in this chapter showed that the interaction effect tends to de-amplify the response of the lower-frequency equipment item and amplify the response of the higher-frequency equipment item. For the purpose of design, it is not advisable to take advantage of the de-amplification in the response of the lower-frequency equipment item in the connected system, in order to ensure safety in its stand-alone configuration. The amplification in the response of the higher-frequency equipment item, however, should be accurately estimated so that adequate capacity to resist earthquake forces in the connected configuration are provided.

The response ratio  $R_2$  of the higher-frequency equipment in a system of two connected equipment items can be estimated by use of the charts in Figures 5.6-5.11. For a given connector, each figure shows a total of 27 response ratio curves as functions of the ratio of equipment frequencies  $f_1 / f_2$ . These correspond to combinations of three discrete values of three parameters: 1, 5 and 10 Hz for  $f_2$ ; 100, 500 and 1000 kg for  $m_2$ ; and 0.5, 1.0 and 5.0 for the ratio of masses  $r \equiv m_1 / m_2$ . For an arbitrary set of these parameters, an interpolation or extrapolation scheme can be used to approximately estimate  $R_2$  by reading bounding values from the appropriate chart. For this purpose, one needs to find two adjacent values for each parameter. We denote these as  $f_2^{(1)}$  and  $f_2^{(2)}$  for the parameter  $f_2$ ;  $m_2^{(1)}$  and  $m_2^{(2)}$  for the parameters  $m_2$ ; and  $r^{(1)}$  and  $r^{(2)}$  for the parameter  $r$ . We adopt the convention that  $x^{(1)} < x^{(2)}$ , where  $x$  stands for any of the three parameters  $f_2$ ,  $m_2$  or  $r$ . By extending a linear interpolation/extrapolation into three variables, the response ratio  $R_2$  for the values  $f_2$ ,  $m_2$  and  $r$  is approximated as

$$R_2(f_2, m_2, r) = \frac{1}{V} \left[ \begin{array}{l} (f_2^{(2)} - f_2)(m_2^{(2)} - m_2)(r^{(2)} - r)R_2(f_2^{(1)}, m_2^{(1)}, r^{(1)}) + \\ (f_2 - f_2^{(1)})(m_2^{(2)} - m_2)(r^{(2)} - r)R_2(f_2^{(2)}, m_2^{(1)}, r^{(1)}) + \\ (f_2^{(2)} - f_2)(m_2 - m_2^{(1)})(r^{(2)} - r)R_2(f_2^{(1)}, m_2^{(2)}, r^{(1)}) + \\ (f_2 - f_2^{(1)})(m_2 - m_2^{(1)})(r^{(2)} - r)R_2(f_2^{(2)}, m_2^{(2)}, r^{(1)}) + \\ (f_2^{(2)} - f_2)(m_2^{(2)} - m_2)(r - r^{(1)})R_2(f_2^{(1)}, m_2^{(1)}, r^{(2)}) + \\ (f_2 - f_2^{(1)})(m_2^{(2)} - m_2)(r - r^{(1)})R_2(f_2^{(2)}, m_2^{(1)}, r^{(2)}) + \\ (f_2^{(2)} - f_2)(m_2 - m_2^{(1)})(r - r^{(1)})R_2(f_2^{(1)}, m_2^{(2)}, r^{(2)}) + \\ (f_2 - f_2^{(1)})(m_2 - m_2^{(1)})(r - r^{(1)})R_2(f_2^{(2)}, m_2^{(2)}, r^{(2)}) \end{array} \right] \quad (5.7)$$

where  $V = (f_2^{(2)} - f_2^{(1)})(m_2^{(2)} - m_2^{(1)})(r^{(2)} - r^{(1)})$  and  $R_2(f_2^{(i)}, m_2^{(j)}, r^{(k)})$ ,  $i, j, k = 1, 2$ , is the response ratio for the specified parameter values. The minimum and maximum response ratios can be approximated separately. After determining  $R_2$  for the specified parameters, the seismic demand on the higher-frequency equipment item in the connected system is determined by multiplying the demand for the stand-alone configuration of the equipment by the response ratio  $R_2(f_2, m_2, r)$ .

As an example, suppose we wish to estimate the maximum response ratio  $R_2$  of an equipment system connected by the RB-FSC PG&E 30-2022. Suppose the given values of the system parameters are  $f_1/f_2 = 0.1$ ,  $f_2 = 4$  Hz,  $m_2 = 200$  kg and  $r = 3.0$ . The two adjacent values for  $f_2$ ,  $m_2$  and  $r$  are  $(f_2^{(1)}, f_2^{(2)}) = (1, 5)$  Hz,  $(m_2^{(1)}, m_2^{(2)}) = (100, 500)$  kg and  $(r^{(1)}, r^{(2)}) = (1, 5)$ . The response ratios needed in (5.7) are read from the curves in Figure 5.7 at  $f_1/f_2 = 0.1$  as follows:  $R_2(f_2^{(1)}, m_2^{(1)}, r^{(1)}) = 1.78$ ,  $R_2(f_2^{(2)}, m_2^{(1)}, r^{(1)}) = 3.21$ ,  $R_2(f_2^{(1)}, m_2^{(2)}, r^{(1)}) = 1.80$ ,  $R_2(f_2^{(2)}, m_2^{(2)}, r^{(1)}) = 1.63$ ,  $R_2(f_2^{(1)}, m_2^{(1)}, r^{(2)}) = 4.17$ ,  $R_2(f_2^{(2)}, m_2^{(1)}, r^{(2)}) = 5.50$ ,  $R_2(f_2^{(1)}, m_2^{(2)}, r^{(2)}) = 3.96$  and  $R_2(f_2^{(2)}, m_2^{(2)}, r^{(2)}) = 2.15$ . Substituting these response ratios and the given parameter values into (5.7), the approximate estimate  $R_2 \cong 3.54$  for the maximum value of the response ratio for the higher-frequency equipment is obtained. The “exact” solution obtained by ELM analysis with the above set of parameters yields  $R_2 = 3.35$ .

#### 5.4.5 Reducing the Effect of Interaction on the Higher-Frequency Equipment Item

When the seismic demand on the higher-frequency equipment item exceeds its capacity, the design engineer has two alternative recourses: increase the capacity of the equipment, or reduce the amplification due to the interaction. The following measures can be employed to reduce the interaction effect on the higher-frequency equipment item.

- Reduce the separation between the stand-alone equipment frequencies. This can be done by increasing the stiffness or reducing the mass of the lower frequency equipment item. In this case, a re-qualification of the modified lower-frequency equipment item may be necessary.
- Select a more flexible rigid-bus connector. The *S*-FSC or the slider connector can be effective choices. If the existing connector is one of the PG&E FSC models, then replacement by an *S*-FSC will require minimal alteration of the connecting system.
- Select a connector that has a large energy dissipation capacity. The slider connector is an effective option for this purpose. Another possibility is to install a special damper on the connecting element or, more practically, provide an expansion connector that dissipates energy through plastic deformation. These options, however, are likely to be much more expensive than the *S*-FSC.

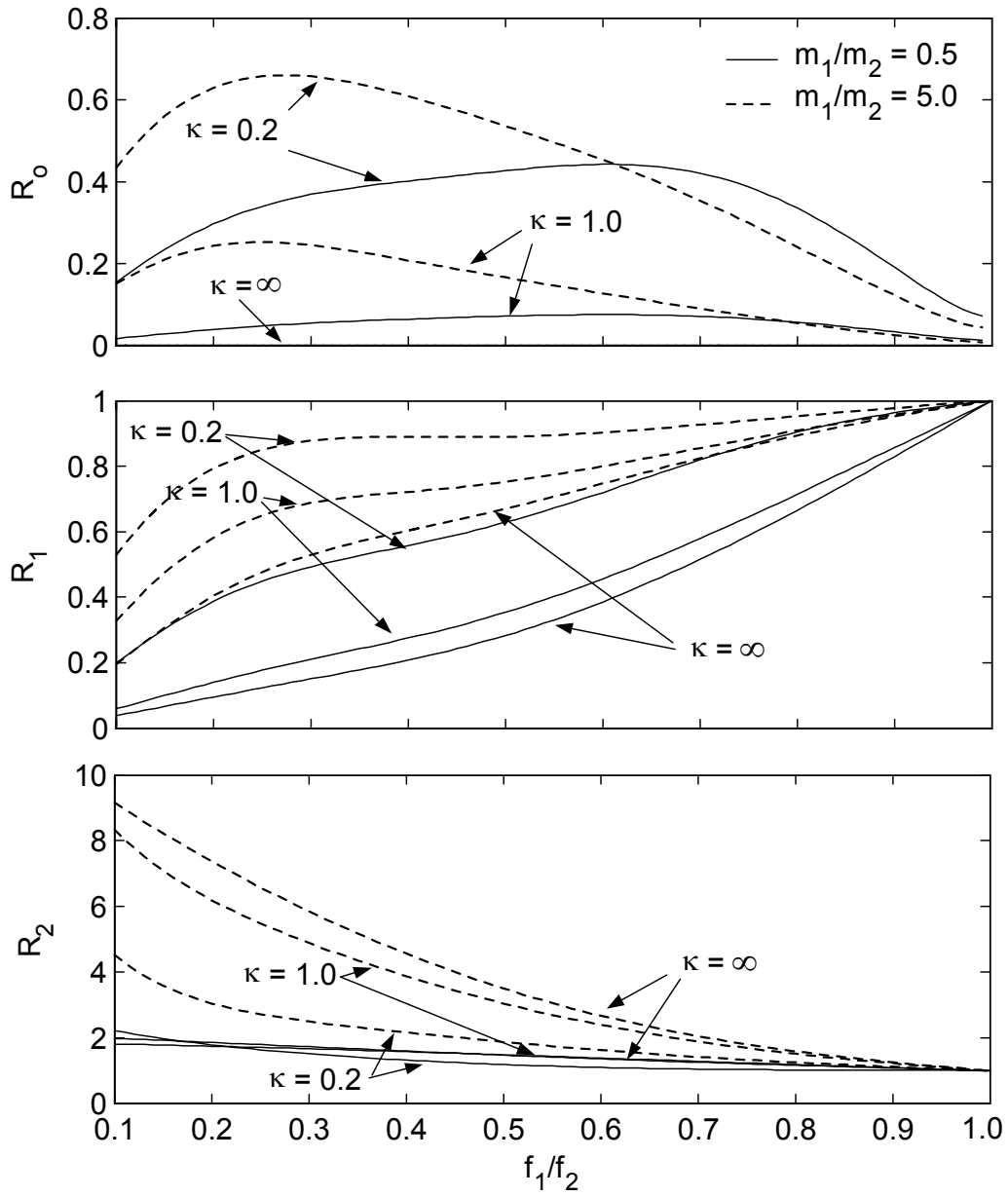


Figure 5.1 Response ratios for  $l_1/m_1 = l_2/m_2$ ,  $f_2 = 5$  Hz,  $\zeta_1 = \zeta_2 = 0.02$  and  $c_0 = 0$  based on the Kanai-Tajimi power spectral density with  $\omega_g = 5\pi$  rad/s and  $\zeta_g = 0.6$



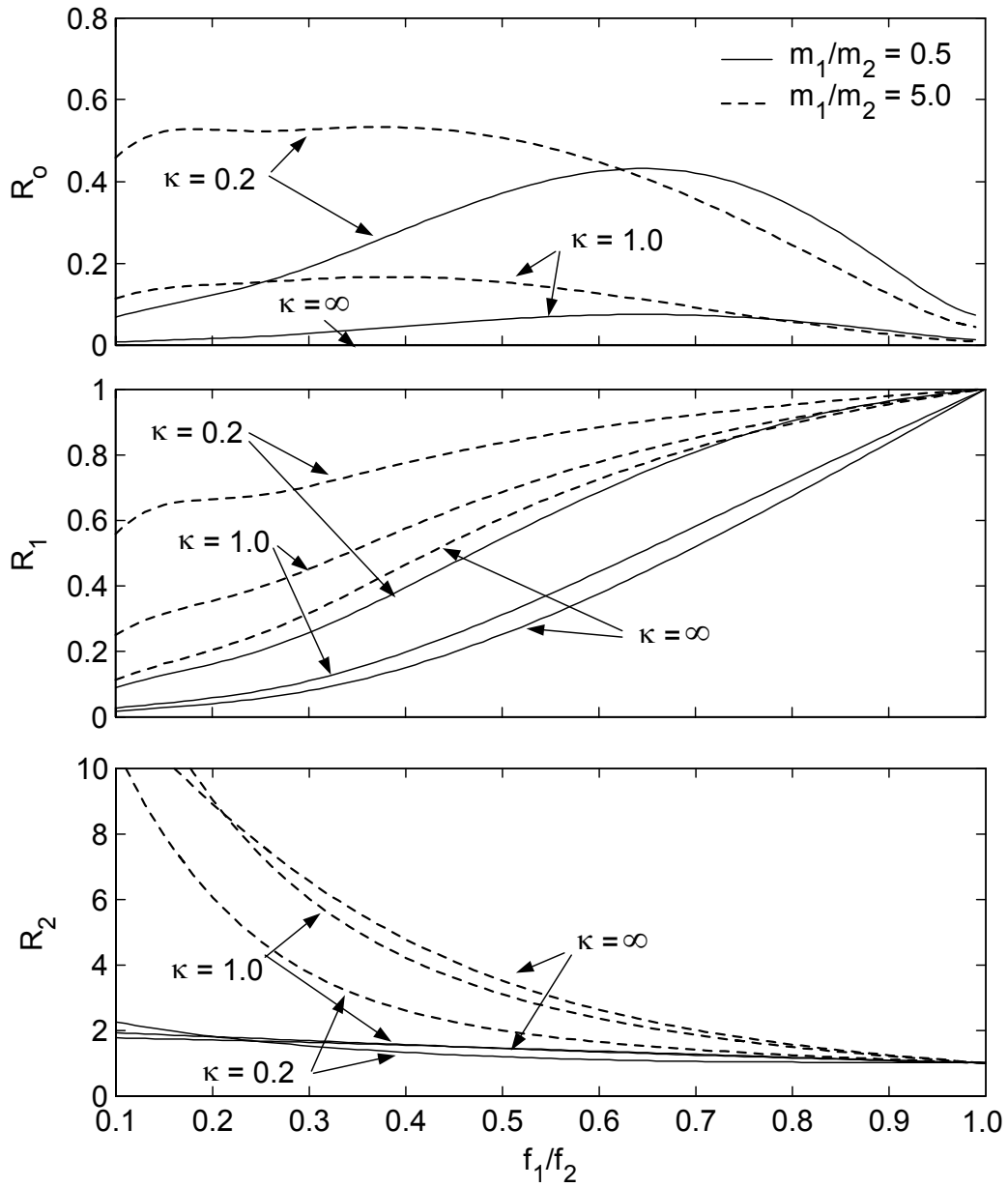


Figure 5.2 Response ratios for  $l_1/m_1 = l_2/m_2$ ,  $f_2 = 10$  Hz,  $\zeta_1 = \zeta_2 = 0.02$  and  $c_0 = 0$  based on the Kanai-Tajimi power spectral density with  $\omega_g = 5\pi$  rad/s and  $\zeta_g = 0.6$

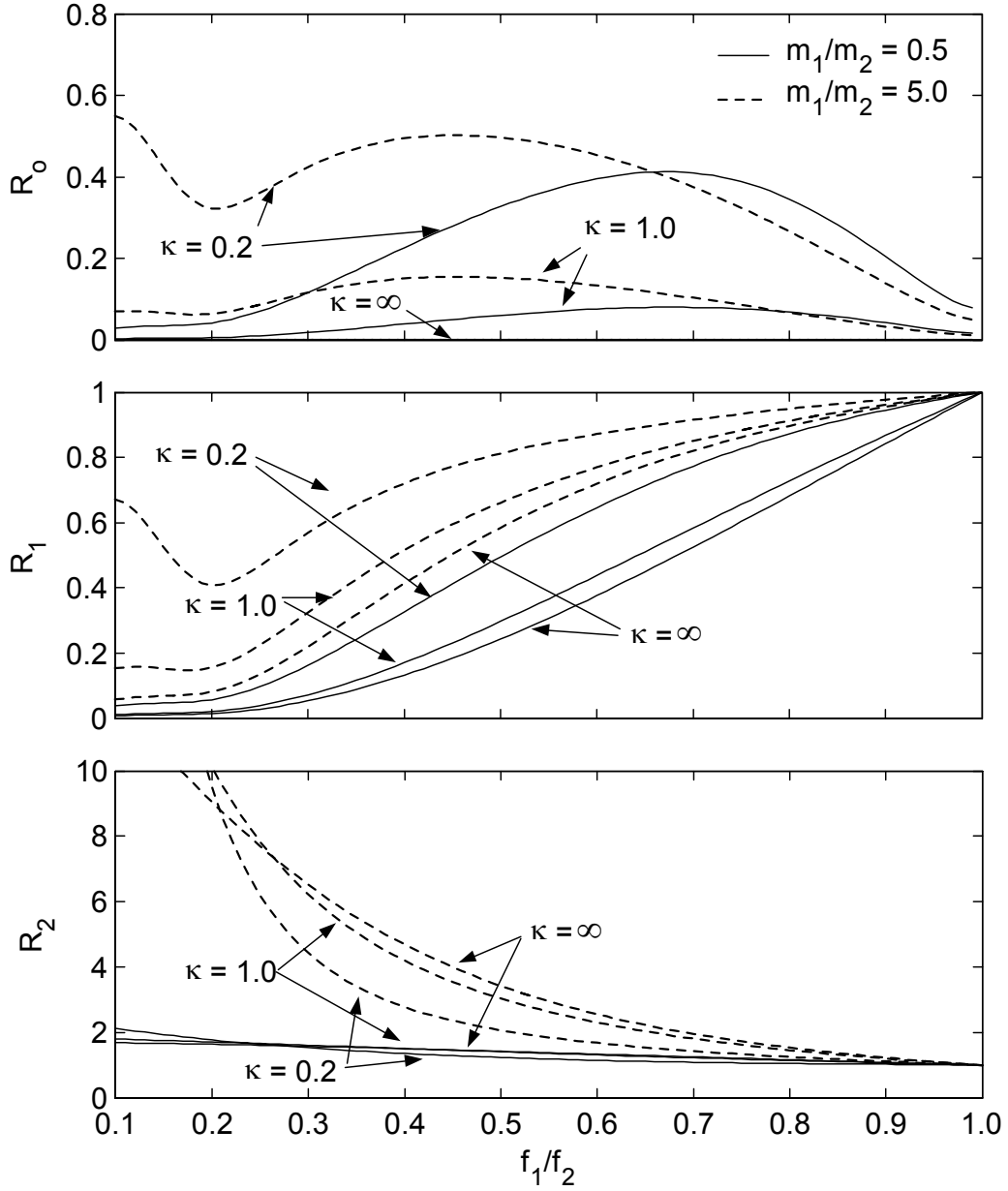


Figure 5.3 Response ratios for  $l_1/m_1 = l_2/m_2$ ,  $f_2 = 5$  Hz,  $\zeta_1 = \zeta_2 = 0.02$  and  $c_0 = 0$  based on the Kanai-Tajimi power spectral density with  $\omega_g = \pi$  rad/s and  $\zeta_g = 0.3$

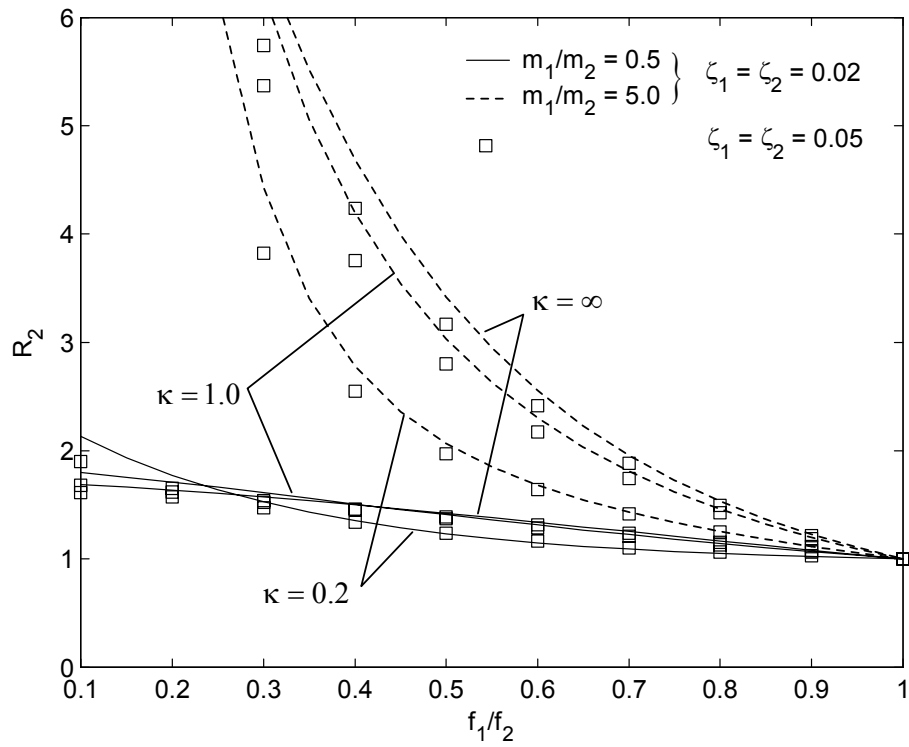


Figure 5.4 Effect of equipment damping on the response ratio  $R_2$  for  $l_1/m_1 = l_2/m_2$ ,  $f_2 = 10\text{Hz}$  and  $c_o = 0$ , based on the Kanai-Tajimi power spectral density with  $\omega_g = 5\pi \text{ rad/s}$  and  $\zeta_g = 0.6$

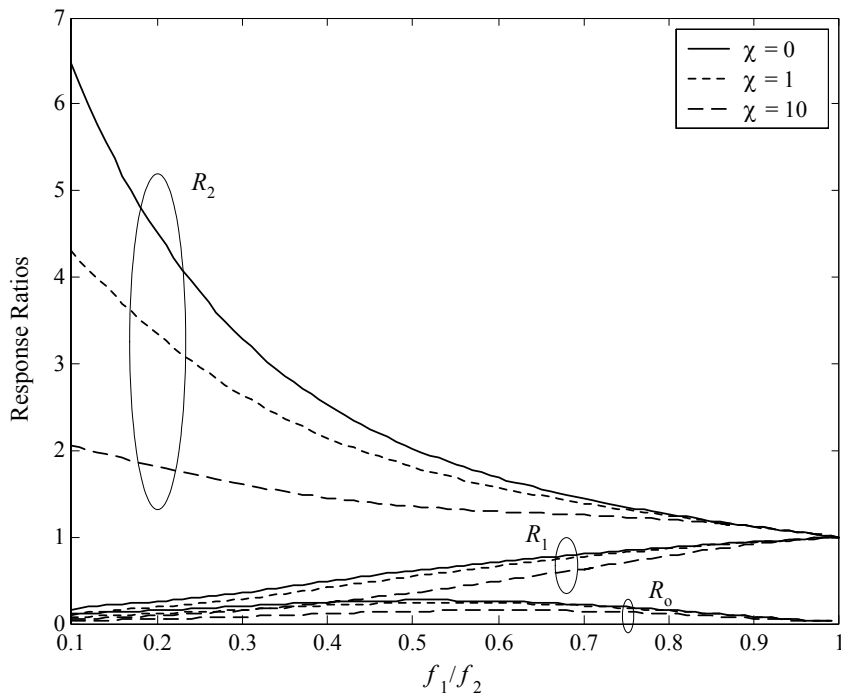


Figure 5.5 Effect of energy dissipation of the connecting element on response ratios for  $m_1/m_2 = 2$ ,  $l_1/m_1 = l_2/m_2$ ,  $f_2 = 10$  Hz,  $\kappa = 0.5$  and  $\zeta_1 = \zeta_2 = 0.02$ , based on the Kanai-Tajimi power spectral density with  $\omega_g = 5\pi$  rad/s and  $\zeta_g = 0.6$

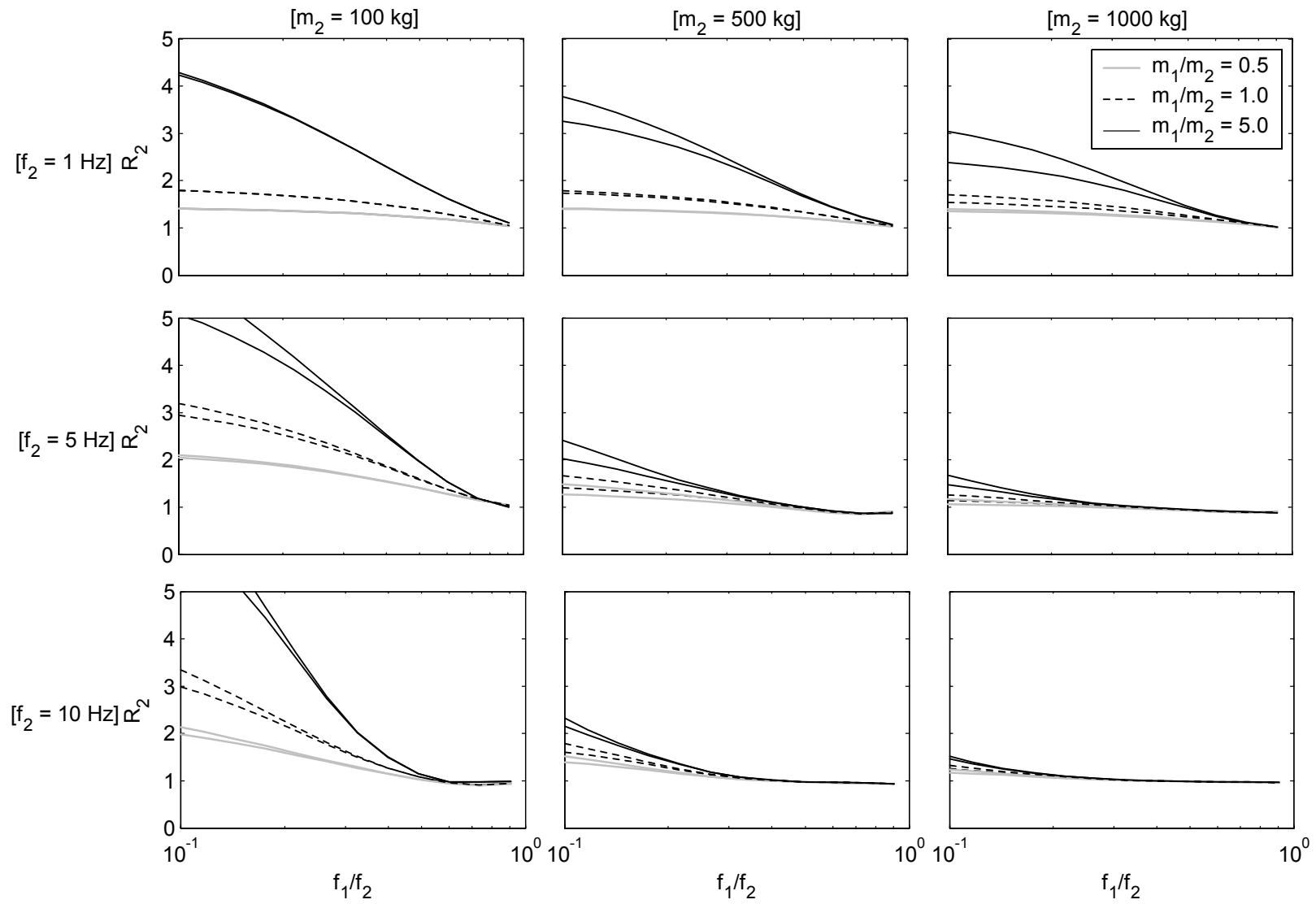


Figure 5.6 Range of response ratios of higher-frequency equipment item connected by PG&E: 30-2021

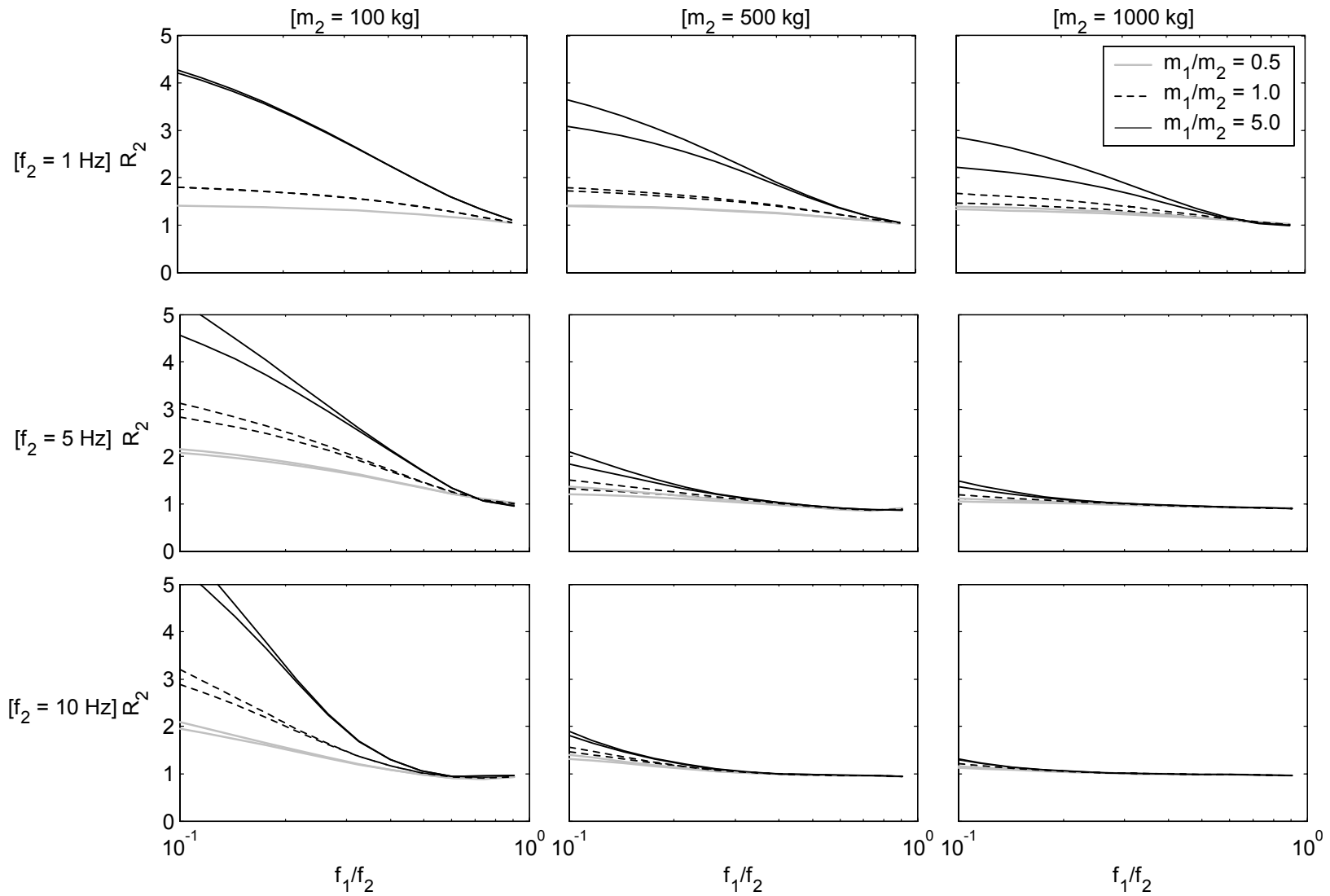


Figure 5.7 Range of response ratios of higher-frequency equipment item connected by PG&E: 30-2022

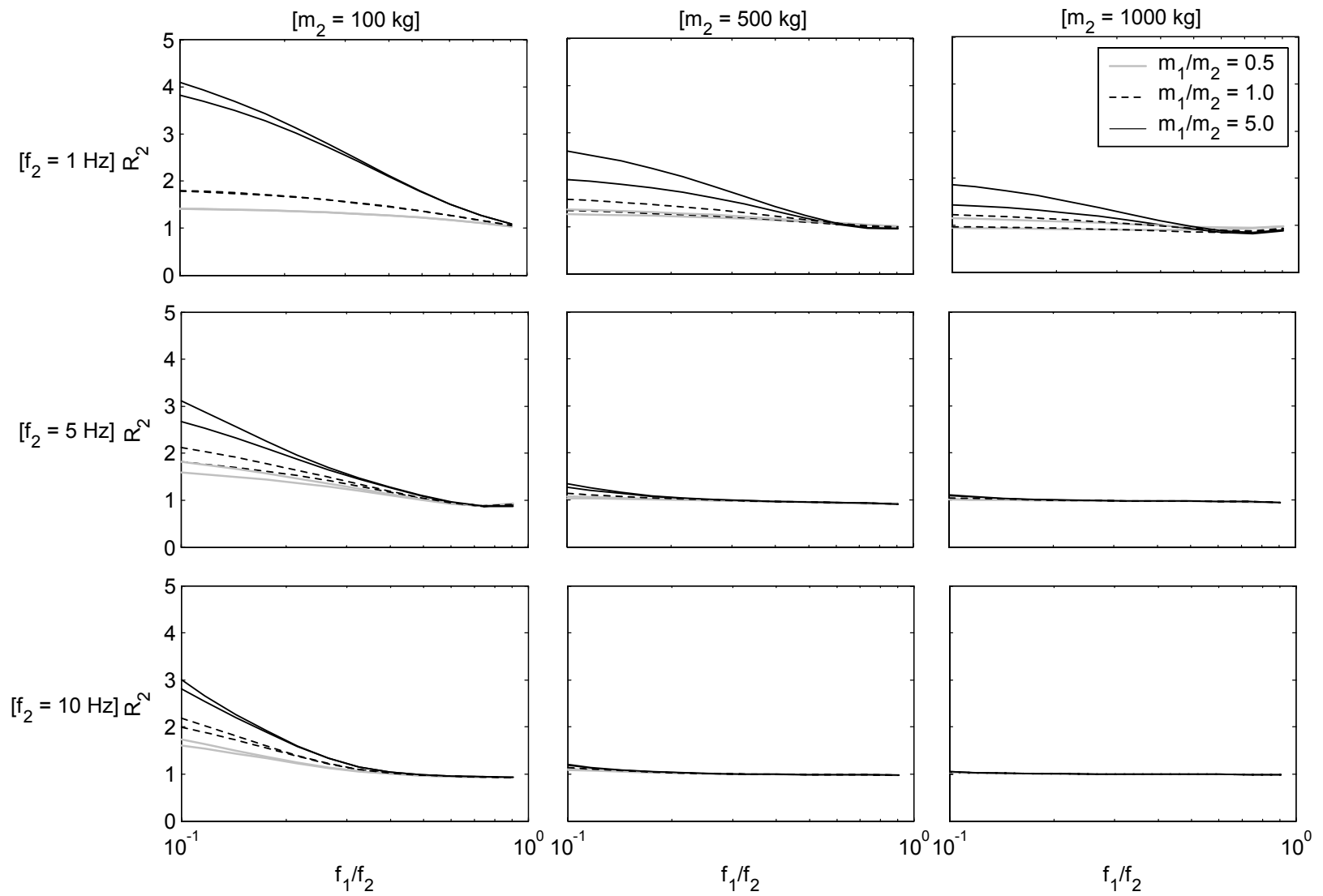


Figure 5.8 Range of response ratios of higher-frequency equipment item connected by PG&E: 30-2023

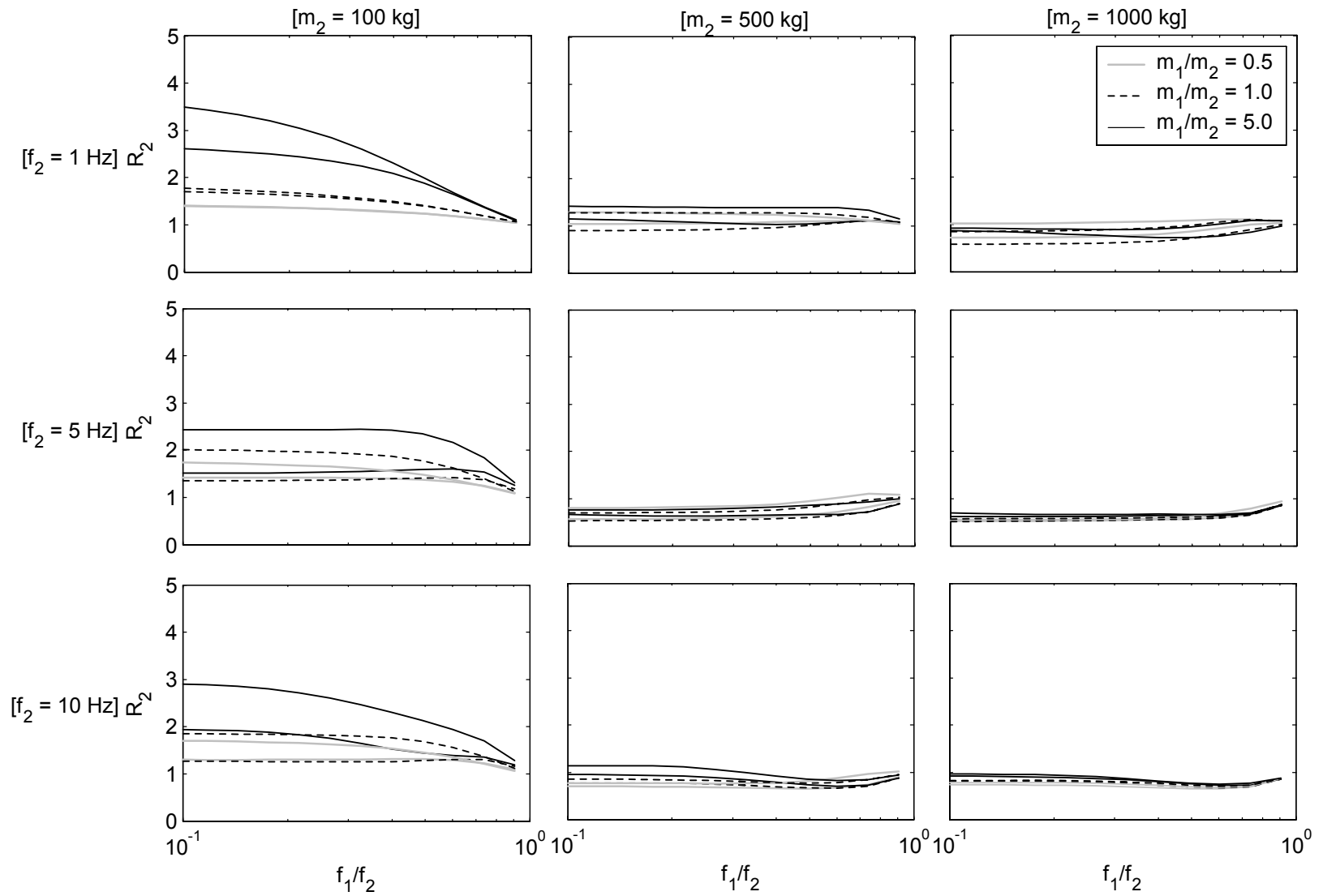


Figure 5.9 Range of response ratios of higher-frequency equipment item connected by Slider Connector (old)



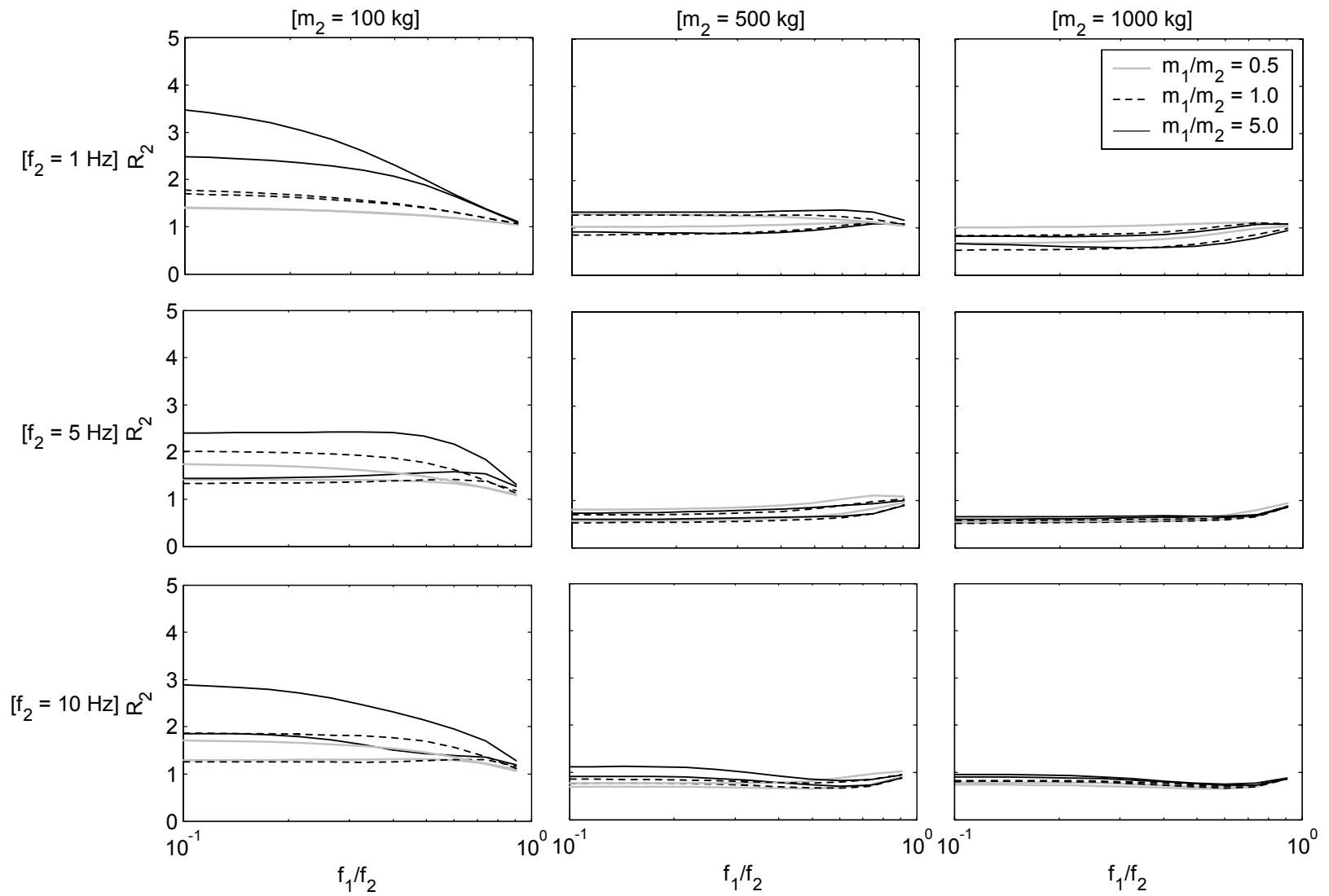


Figure 5.10 Range of response ratios of higher-frequency equipment item connected by Slider Connector (new)

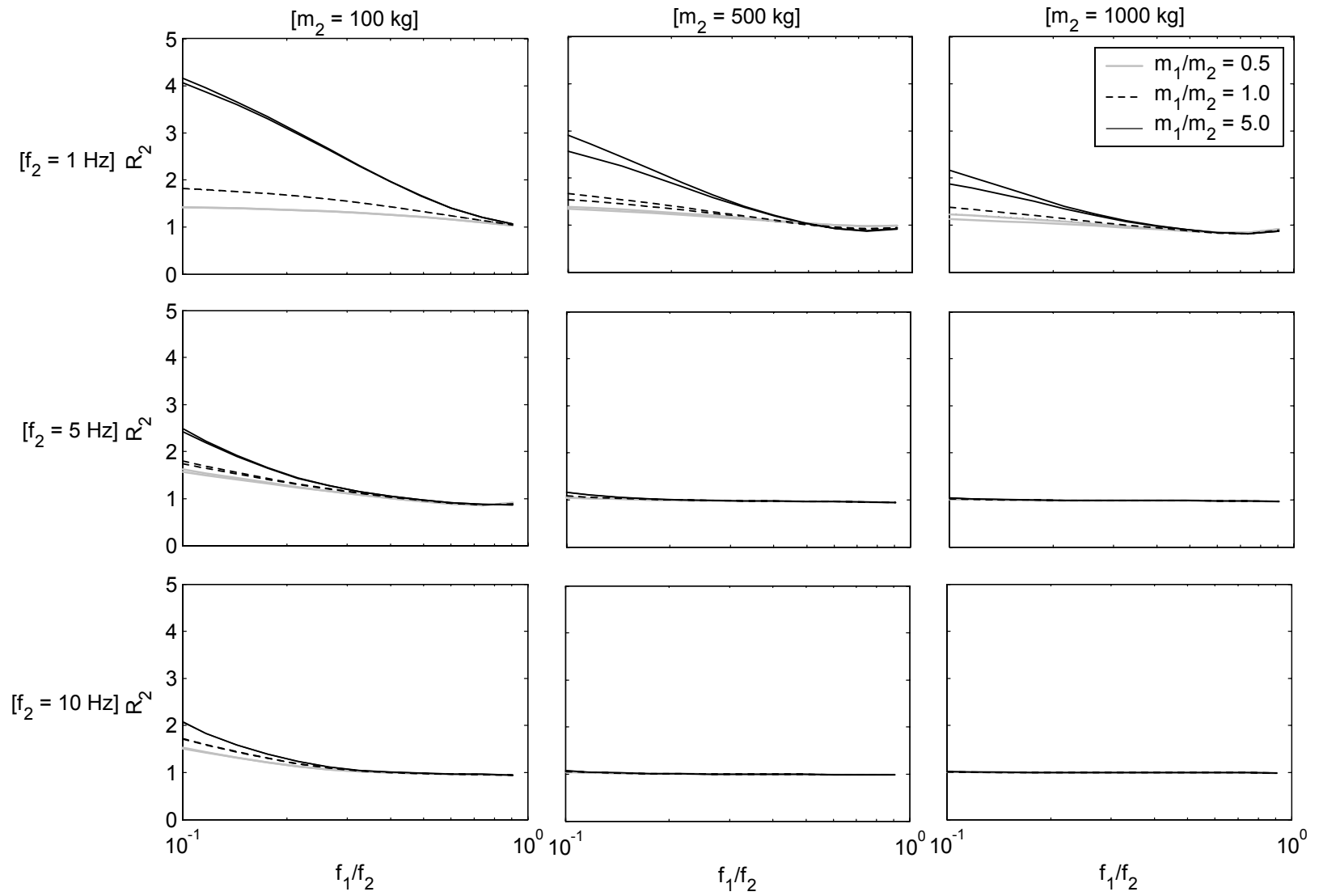


Figure 5.11 Range of response ratios of higher-frequency equipment item connected by S-FSC

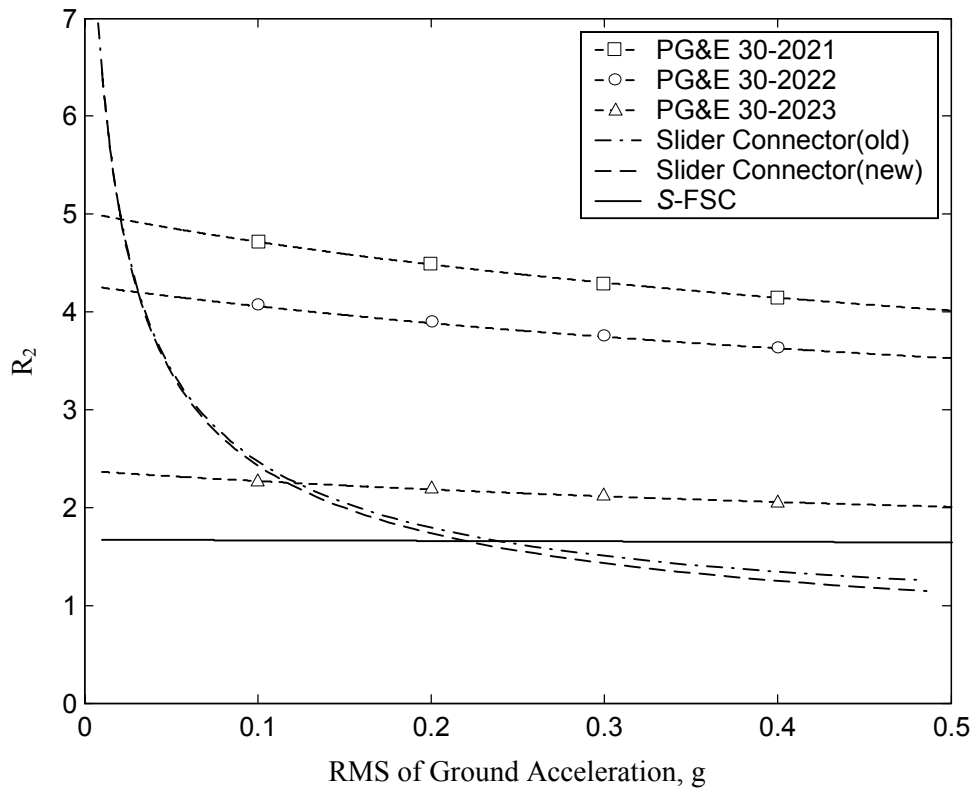


Figure 5.12 Response ratios for  $l_1/m_1 = l_2/m_2 = 1.0$ ,  $f_1 = 1$  Hz,  $f_2 = 5$  Hz,  $m_1 = 500$  kg,  $m_2 = 100$  kg,  $\zeta_1 = \zeta_2 = 0.02$ ,  $c_0 = 0$  based on the Kanai-Tajimi power spectral density with  $\omega_g = 5\pi$  rad/s and  $\zeta_g = 0.6$

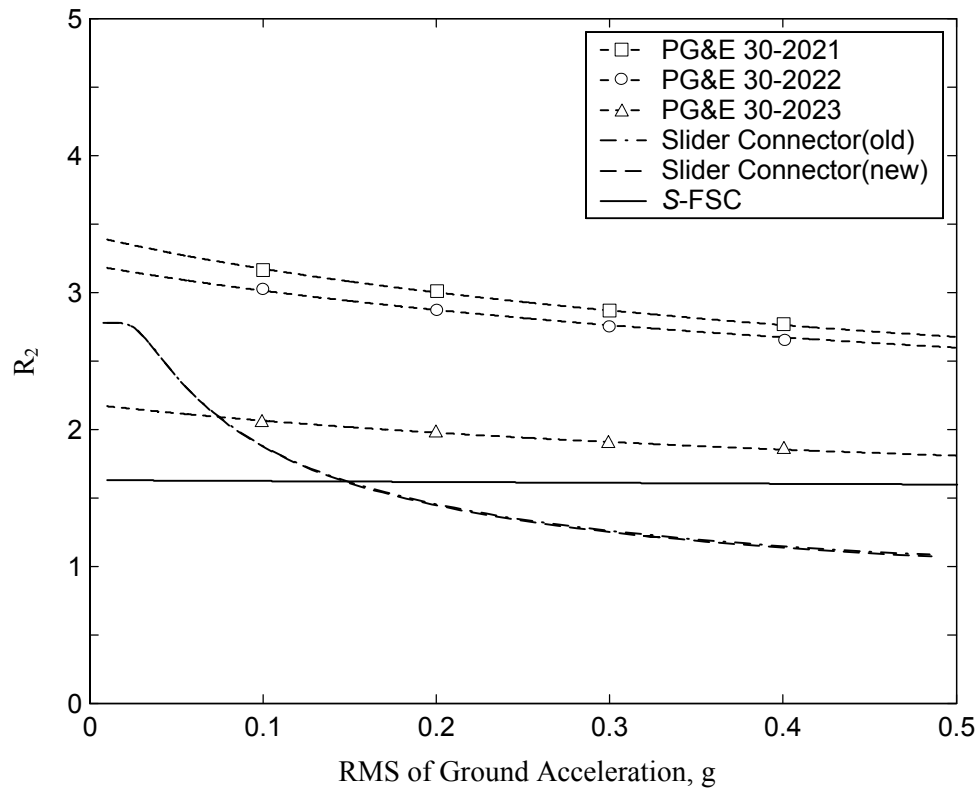


Figure 5.13 Response ratios for  $l_1/m_1 = l_2/m_2 = 1.0$ ,  $f_1 = 1$  Hz,  $f_2 = 10$  Hz,  $m_1 = 100$  kg,  $m_2 = 100$  kg,  $\zeta_1 = \zeta_2 = 0.02$ ,  $c_0 = 0$  based on the Kanai-Tajimi power spectral density with  $\omega_g = 5\pi$  rad/s and  $\zeta_g = 0.6$

# 6 Reliability of Electrical Substation Systems

## 6.1 INTRODUCTION

An electrical substation system consists of a complex set of interconnected equipment items, such as circuit breakers, transformers, disconnect switches, surge arresters, etc. At any given time, the performance of the substation depends on the states of its constituent equipment items – the components of the system – as well as the nature of the redundancies present in the system. The loss of function of an electrical substation system after a major earthquake could hamper emergency services and severely enhance the magnitude of losses sustained by a community. As a result, there is great interest in methods for assessing the seismic reliability of electrical substation systems and in developing efficient methods for upgrading their reliability, where necessary.

The reliability of a system, in general, is a complex function of the reliabilities of its components. When component failure events are dependent, evaluation of the system reliability is a monumental task. For this reason, methods to derive bounds on the system reliability in terms of marginal or joint component failure probabilities have been of interest. Currently, bounding formulas employing individual (uni-) component probabilities are available for series and parallel systems, and formulas employing bi- and higher-order joint component probabilities are available for series systems. No theoretical formulas exist for general systems typical of electrical substations. In Section 6.2, we present a recently developed method (Song & Der Kiureghian 2003) for computing reliability bounds on general systems by use of Linear Programming (LP). It is shown that LP can be used to compute bounds for any system for any level of information available on the component probabilities. For series systems, unlike the theoretical bi- and higher-order component bounds, the LP bounds are independent of the ordering of the components and are guaranteed to produce the narrowest possible bounds for any given information on component probabilities. Furthermore, the LP bounds can incorporate any type of information, including an incomplete set of component probabilities or inequality constraints on com-

ponent probabilities. Song & Der Kiureghian (2003) demonstrates the methodology using numerical examples involving series, parallel and general structural systems.

The LP bounds are useful for assessing the reliability of electrical substations, because these systems are usually too complex to be analyzed analytically and the probability information on equipment items is often incomplete. Section 6.3 demonstrates the use of LP bounds for estimating and improving the seismic reliability of example electrical substation systems. The first example is a single-transmission-line substation, which is modeled as a series system. The influence of the reliability of a critical component on the system reliability is investigated. The second example explores the effectiveness of adding redundancy to the weakest component of the series system in order to enhance its reliability. The third example deals with a two-transmission-line substation, designed to provide more redundancy. This is a general system and is formulated by use of cut sets. For this example, the case of incomplete probability information is explored. In each case, the LP bounds are computed assuming knowledge of up to uni-, bi- and tri-component probabilities. These results are compared with Monte Carlo simulation results assuming complete probability information to demonstrate the accuracy of the LP bounds.

In order to improve the reliability of engineering systems against deterioration and natural and man-made hazards, it is important to identify their critical components and cut sets. System components are defined as critical when they make significant contributions to the system failure probability for a specified performance criterion and load hazard. A similar definition applies to critical cut sets. Section 6.4 shows that the proposed LP formulation provides a convenient framework for a systematic identification of critical components and cut sets. Once the bounds on the system failure probability are obtained by LP, simple calculations yield well-known importance measures, which provide the order of importance of the components or cut sets in terms of their contributions to the system failure probability. Numerical examples with the two-transmission-line substation system demonstrate the proposed method.

## **6.2 BOUNDS ON SYSTEM RELIABILITY BY LINEAR PROGRAMMING**

A system is a set of possibly interdependent components, such that the state of the system depends on the states of its constituent components. For many systems, the system state can be expressed as a Boolean or logical function (consisting of unions and intersections) of the compo-

nent states. The system reliability, i.e., the probability that the system is in a particular functioning state, or its complement, the system failure probability, can then be expressed as the probability of the Boolean function of the component states that produce that system state. Computation of this probability, however, is extremely difficult for many systems, particularly when there is dependence between the component states. Because of this difficulty, attempts have been made to derive bounds on the system failure probability by use of individual component probabilities or joint probabilities of small sets of the components. Available formulas for such bounds are primarily restricted to series and parallel systems.

This section proposes a method for computing bounds on the system failure probability by use of Linear Programming (LP) that was recently developed (Song & Der Kiureghian 2003). The idea of using LP to compute bounds on system reliability was first explored by Hailperin (1965). Kounias and Marin (1976) used the approach to examine the accuracy of some theoretical bounds. Since the number of variables in the LP problem increases exponentially with the number of system components, these early attempts were abandoned as they were computationally too demanding for the computers existing of the time. Later, specialized versions of this approach were employed in fields such as operations research (Prékopa 1988). However, it appears that this approach has never been used in the field of structural reliability, which is the application focus of the present study. With the enormous increase in the speed and capacity of computers in recent years, the LP approach is believed to be viable and worthy of a reconsideration for many system reliability problems.

### 6.2.1 Formulation and Estimation of System Reliability

Consider a system having  $n$  components. Let  $E_{\text{system}}$  denote a particular system state of interest (e.g., the state of failure relative to a prescribed performance criterion) and  $\mathbf{E}_i = (E_{i1}, E_{i2}, \dots)$ ,  $i = 1, \dots, n$ , denote vectors of the component states such that  $E_{im}$  = the event that component  $i$  is in its  $m$ -th state. In general one can write

$$E_{\text{system}} = L(\mathbf{E}_1, \dots, \mathbf{E}_n) \quad (6.1)$$

where  $L(\cdot)$  denotes a logical function involving unions and intersections of the component events or their complements. Specific cases of this function are described below. For the sake of

simplicity of the notation, and without loss of generality, in the following we consider two-state components, where  $\mathbf{E}_i$  can be written as  $\mathbf{E}_i = (E_i, \bar{E}_i)$ , where the superposed bar indicates the complement of an event. In that case, (6.1) simplifies to

$$E_{\text{system}} = L(E_1, \bar{E}_1, \dots, E_n, \bar{E}_n) \quad (6.2)$$

For easy visualization, it is useful to think of  $E_i$  ( $\bar{E}_i$ ) as the state of failure (survival) of component  $i$  and  $E_{\text{system}}$  as the state of failure of the system.

Mathematically speaking, a series system is one in which  $L(\cdot)$  includes only union operations (over all or a subset of the component events), i.e.,

$$E_{\text{series system}} = \bigcup_i E_i \quad (6.3)$$

In this case, the system fails if any of its components fail. A parallel system is characterized by intersection operations, i.e.,

$$E_{\text{parallel system}} = \bigcap_i E_i \quad (6.4)$$

In this case, the system fails if all its components fail. More generally, the system function  $L(\cdot)$  may include both union and intersection operations. In that case, two alternative formulations are possible:

$$E_{\text{system}} = \bigcup_k \bigcap_{i \in C_k} E_i \quad (6.5)$$

$$E_{\text{system}} = \bigcap_l \bigcup_{i \in L_l} E_i \quad (6.6)$$

The formulation in (6.5) is in terms of *cut sets*, i.e., sets of component states  $E_i$ ,  $i \in C_k$ , whose joint realizations constitute realizations of the system state  $E_{\text{system}}$ . In this expression,  $C_k$  denotes the set of component state indices that constitute the  $k$ -th cut set. The system in this case is represented by a series of parallel subsystems. The formulation in (6.6) is in terms of *link sets*, i.e., sets of complementary component states  $\bar{E}_i$ ,  $i \in L_l$ , whose joint realizations constitute realizations of the complementary system state  $\bar{E}_{\text{system}}$ . In this expression  $L_l$  denotes the set of component state indices that constitute the  $l$ -th link set. The system in this case is represented by a par-



allel of series subsystems. The form in (6.6) is obtained by use of De Morgan's rule. For later use, it is useful to introduce the notions of *minimum cut sets* and *minimum link sets*. These are cut sets and link sets, which are minimal in the sense that the removal of any component from the set renders a set that is not a cut set or a link set.

Computing the probability for any of the system events given above is a daunting task when the component events are statistically dependent. One in general needs to know the probabilities of intersections of all combinations of component states. For example, for the series system, using the inclusion-exclusion rule, one can write

$$P(E_{\text{series system}}) = P\left(\bigcup_i E_i\right) = \sum_i P(E_i) - \sum_{i < j} P(E_i E_j) + \sum_{i < j < k} P(E_i E_j E_k) - \dots \quad (6.7)$$

Similar expressions can be developed for the general system formulations in (6.5) and (6.6). When the component events are statistically dependent, computation of the probabilities of event intersections is difficult for large number of components. Because of this, there has been continued interest in developing bounds on the system probability that employ the marginal component probabilities,  $P_i = P(E_i)$ , and joint probabilities of small sets of component events, i.e., bi-component probabilities,  $P_{ij} = P(E_i E_j)$ ,  $i < j$ , tri-component probabilities,  $P_{ijk} = P(E_i E_j E_k)$ ,  $i < j < k$ , etc.

For series structural systems, probability bounds using uni-component probabilities were derived by Boole (1854):

$$\max_i P_i \leq P\left(\bigcup_{i=1}^n E_i\right) \leq \min\left(1, \sum_{i=1}^n P_i\right) \quad (6.8)$$

These are the narrowest possible bounds when only the uni-component probabilities are known (Fréchet 1935). However, these bounds are often too wide to be of practical use. Efforts made by Kounias (1968), Hunter (1976) and Ditlevsen (1979) led to the following widely used bounds for series systems that involve the uni- and bi-component probabilities:

$$P_1 + \sum_{i=2}^n \max\left(0, P_i - \sum_{j=1}^{i-1} P_{ij}\right) \leq P\left(\bigcup_{i=1}^n E_i\right) \leq P_1 + \sum_{i=2}^n (P_i - \max_{j < i} P_{ij}) \quad (6.9)$$

These bounds depend on the ordering of the component events, and the order that maximizes the

lower bound and the order that minimizes the upper bound are not necessarily the same. In order to obtain the narrowest bounds, one must consider all the possible  $n!$  ordering alternatives, since there does not exist an ordering rule that guarantees this result. Furthermore, the narrowest bounds obtained from this formula are not necessarily the narrowest possible bounds (see Song and Der Kiureghian 2003 for example cases). In the remainder of this report, the above bounds are referred to as “KHD bounds.”

Hohenbichler and Rackwitz (1983) and Zhang (1993) generalized the concept of the KHD bounds for series systems by including joint probabilities of larger sets of component events, i.e., tri-component probabilities,  $P_{ijk}$ , quadri-component probabilities,  $P_{ijkl}$ , etc. The bounding formulas for up to tri-component probabilities are

$$P\left(\bigcup_{i=1}^n E_i\right) \geq P_1 + P_2 - P_{12} + \sum_{i=3}^n \max\left(0, P_i - \sum_{j=1}^{i-1} P_{ij} + \max_{k \in \{1, 2, \dots, i-1\}} \sum_{\substack{j=1 \\ j \neq k}}^{i-1} P_{ijk}\right) \quad (6.10a)$$

$$P\left(\bigcup_{i=1}^n E_i\right) \leq P_1 + P_2 - P_{12} + \sum_{i=3}^n \left[ P_i - \max_{\substack{k \in \{2, 3, \dots, i-1\} \\ j < k}} (P_{ik} + P_{ij} - P_{ijk}) \right] \quad (6.10b)$$

These bounds inherit the order-dependency problem of KHD bounds. In the remainder of this report, these bounds are referred to as “Zhang bounds.”

For parallel systems, bounds based on uni-component probabilities derived by Boole (1854) are:

$$\max\left(0, \sum_{i=1}^n P_i - (n-1)\right) \leq P\left(\bigcap_{i=1}^n E_i\right) \leq \min_i P_i \quad (6.11)$$

Fréchet (1935) has shown that these are the narrowest possible bounds based on the uni-component probabilities alone. Unfortunately, these bounds are too wide to be of practical use for most systems. Theoretical bounds using bi- or tri-component probabilities do not exist for parallel systems. However, one can use the De Morgan’s rule  $\overline{\bigcap E_i} = \bigcup \overline{E_i}$  to convert the complement of the parallel system to a series system involving the complementary component events, and then use (6.9) or (6.10).

For general systems, no theoretical bounding formulas exist. One can of course represent

the system as a series system of parallel subsystems, and then combine (6.9) or (6.10) with (6.11) to develop relaxed uni-component bounds, or represent the system as a parallel system of series subsystems, and then combine (6.11) with (6.9) or (6.10) to develop relaxed bi- or tri-component bounds. However, these usually lead to unacceptably wide bounds.

## 6.2.2 Bounds on System Reliability by Linear Programming

Linear programming (LP) solves the problem of minimizing (maximizing) a linear function, whose variables are subject to linear equality or inequality constraints. The first appearance of LP goes back to J.B. Fourier's work in 1824, but it became practical after G. B. Dantzig developed the simplex method in 1947 (Dantzig 1951). Since then, together with dramatic improvements in computing technology, many powerful algorithms have been developed and a profound mathematical understanding of the problem has been gained. The compact formulation of LP appropriate for our analysis has the form

$$\text{minimize (maximize) } \mathbf{c}^T \mathbf{p} \tag{6.12a}$$

$$\text{subject to } \mathbf{a}_1 \mathbf{p} = \mathbf{b}_1 \tag{6.12b}$$

$$\mathbf{a}_2 \mathbf{p} \geq \mathbf{b}_2 \tag{6.12c}$$

In the above,  $\mathbf{p} = (p_1, p_2, \dots)$  is the vector of “decision” or “design” variables,  $\mathbf{c}^T \mathbf{p}$ , where  $\mathbf{c}$  is a vector of coefficients, is the linear “objective” or “cost” function, and  $\mathbf{a}_1$ ,  $\mathbf{b}_1$ ,  $\mathbf{a}_2$ , and  $\mathbf{b}_2$  are coefficient matrices and vectors that respectively define equality and inequality constraints. In (6.12c), the inequality between the vectors must be interpreted component-wise. A vector  $\mathbf{p}$  is called feasible if it satisfies all the constraints. The solution of the LP problem is a feasible  $\mathbf{p}$  that minimizes (maximizes) the objective function.

The following theorem plays a key role in understanding LP. The detailed proof can be found in Bertsimas & Tsitsiklis (1997).

**Theorem 6.1.** Consider the linear programming problem of minimizing (maximizing)  $\mathbf{c}^T \mathbf{p}$  over a polyhedron  $P$  defined by the imposed constraints. Suppose that  $P$  has at least one extreme point (vertex). Then, either the optimal cost is equal to  $-\infty$  ( $\infty$ ), or there exists an extreme point which is optimal.

The theorem implies that the optimal solution of LP, if it exists, is located at one of the extreme points (vertices) of the polyhedron defined by the given linear constraints. This fact led to the development of the simplex algorithm (Dantzig 1951), which moves from one vertex to another under a certain pivoting rule, until the requirements for the optimal solution are met. Since the simplex algorithm appeared, LP has flourished and numerous algorithms (interior point method, ellipsoid method, etc.) have been developed, dramatically increasing our ability to solve large-scale problems. Useful information and on-line LP solvers can be found at the Internet web site <http://www-neos.mcs.anl.gov>.

Hailperin (1965) divided the sample space of the component events into  $2^n$  mutually exclusive and collectively exhaustive (MECE) events, each consisting of a distinct intersection of the component events  $E_i$  and their complements  $\bar{E}_i$ ,  $i=1, \dots, n$ . Let us call these the basic MECE events and denote them by  $e_i$ ,  $i=1, \dots, 2^n$ . For example, in the case of  $n=3$  component events, one finds the  $2^3=8$  basic MECE events to be  $\{e_1 = E_1E_2E_3, e_2 = \bar{E}_1E_2E_3, e_3 = E_1\bar{E}_2E_3, e_4 = E_1E_2\bar{E}_3, e_5 = \bar{E}_1\bar{E}_2E_3, e_6 = \bar{E}_1E_2\bar{E}_3, e_7 = E_1\bar{E}_2\bar{E}_3, \text{ and } e_8 = \bar{E}_1\bar{E}_2\bar{E}_3\}$  (see Figure 6.1). Let  $p_i = P(e_i)$ ,  $i=1, \dots, 2^n$ , denote the probabilities of the basic MECE events. These probabilities serve as the design variables in the LP problem to be formulated.

According to the basic axioms of probability, the probabilities  $\mathbf{p} = (p_1, \dots, p_{2^n})$  are subject to the following linear constraints:

$$\sum_{i=1}^{2^n} p_i = 1 \quad (6.13a)$$

$$p_i \geq 0, \forall i \quad (6.13b)$$

The constraint (6.13a) is analogous to (6.12b) with  $\mathbf{a}_1$  being a row vector of 1's and  $\mathbf{b}_1 = 1$ , whereas (6.13b) is analogous to (6.12c) with  $\mathbf{a}_2$  being an identity matrix of size  $2^n$  and  $\mathbf{b}_2$  a  $2^n$ -vector of 0's.

Due to mutual exclusivity of the basic MECE events, the probability of any subset made of these events is the sum of the corresponding probabilities. In particular, the probability of any component event  $E_i$  is the sum of the probabilities of the basic MECE events that constitute that component event. For example, for the system with 3 components mentioned above,

$$\begin{aligned}
P(E_1) &= P_1 = p_1 + p_3 + p_4 + p_7 \\
P(E_2) &= P_2 = p_1 + p_2 + p_4 + p_6 \\
P(E_3) &= P_3 = p_1 + p_2 + p_3 + p_5
\end{aligned} \tag{6.14}$$

Similarly, the probability of any intersection of the component events is given as the sum of the probabilities of the basic MECE events that constitute the intersection event. For example, the bi-component probabilities of the three component example are given by

$$\begin{aligned}
P(E_1E_2) &= P_{12} = p_1 + p_4 \\
P(E_1E_3) &= P_{13} = p_1 + p_3 \\
P(E_2E_3) &= P_{23} = p_1 + p_2
\end{aligned} \tag{6.15}$$

More generally, one can write

$$P(E_i) = P_i = \sum_{r: e_r \subseteq E_i} p_r \tag{6.16a}$$

$$P(E_iE_j) = P_{ij} = \sum_{r: e_r \subseteq E_iE_j} p_r \tag{6.16b}$$

$$P(E_iE_jE_k) = P_{ijk} = \sum_{r: e_r \subseteq E_iE_jE_k} p_r \tag{6.16c}$$

$$\text{etc.} \tag{6.16d}$$

In most system reliability problems, the uni-, bi- and sometimes tri-component probabilities are known or can be computed. In that case, the above expressions provide linear equality constraints on the variables  $\mathbf{p}$  in the form of (6.12b) with  $\mathbf{a}_1$  a matrix having elements of 0 or 1 and  $\mathbf{b}_1$  a vector listing the known component probabilities. If, instead, inequality constraints on component probabilities are given, such as  $P_i \leq 0.1$ ,  $0.01 \leq P_{ij} \leq 0.02$ , or  $P_i \leq P_j$ , then the above expressions provide linear inequality constraints on the variables  $\mathbf{p}$  in the form of (6.12c).

Any Boolean function of the component events can also be considered as being composed of a subset of the basic MECE events. It follows that the probability of the system event  $E_{\text{system}}$  can be written in the form  $P(E_{\text{system}}) = \mathbf{c}^T \mathbf{p}$ , where  $\mathbf{c}$  is a vector whose elements are either 0 or 1. Table 6.1 lists the elements of the vector  $\mathbf{c}$  for example systems with  $n = 3$  components. Included are series, parallel and general systems, the latter represented by both cut-set and link-set formulations. It is seen that in all cases the system probability is a linear function of  $\mathbf{p}$ .

It is clear from the above analysis that the system reliability problem can be cast in the form of an LP problem. The probabilities of the basic MECE events represent the design variables, the system probability defines the linear objective function, and information given in terms of the individual or joint component probabilities define the linear equality or inequality constraints. Additional linear constraints are imposed by the axioms of probability. The lower bound of the system probability is obtained as the minimum of the objective function, and the upper bound is obtained as the maximum of the objective function. For a system with  $n$  component events, the number of design variables is  $2^n$ ; one equality and  $2^n$  inequality constraints result from the probability axioms (6.13a) and (6.13b), respectively (note that (6.13b) is automatically satisfied by only searching in the non-negative domain of the design variable space),  $n$  equality or inequality constraints result from knowledge of uni-component probabilities or bounds thereof as in (6.16a),  $n!/2!(n-2)!$  equality or inequality constraints result from knowledge of bi-component probabilities or bounds thereof as in (6.16b), and so on. Obviously the size of the LP problem quickly grows with the number of component events. This issue is further discussed below.

Hailperin (1965) has shown that the LP problem described above gives the best (narrowest) possible bounds on the system probability for any given information on the individual or joint component probabilities, as long as the given constraints are feasible, i.e., such that the polyhedron defined by the constraints is not empty. This is also evident from the following argument: If the polyhedron is not empty, i.e., the given constraints are feasible, the polyhedron will have at least one extreme point. Then, according to Theorem 6.1, the optimal cost is either equal to  $-\infty$  ( $\infty$ ), or there exists an extreme point which is optimal. In our LP problem, the design variables  $p_i$  are bounded between 0 and 1 and vector  $\mathbf{c}$  in the objective function contains only 0's and 1's. It follows that for any feasible  $\mathbf{p}$  the cost is finite and, therefore, there must exist an optimal solution, i.e., a global minimum (maximum) value, under the given constraints. Thus, the bounds obtained by LP are not only true bounds but also the narrowest bounds that one can obtain by use of the given information (constraints).

The bounds by LP have a number of advantages over the existing theoretical bounds. First, LP is guaranteed to provide the narrowest possible bounds, if a feasible solution exists for the given constraints. This is not the case for the theoretical bounds for series systems based on the bi- or tri-component probabilities, even for the best ordering of the component events. (Note

that the LP formulation is independent of the ordering of the component events.) Second, the LP formulation is uniformly applicable to all systems, including general systems characterized by unions and intersections of component events. As mentioned earlier, existing formulas for bounds based on bi- and tri-component probabilities are primarily restricted to series systems. Third, the LP formulation can incorporate general forms of information about the component probabilities. Specifically, any linear equality or inequality expression involving uni- or multi-component probabilities can be used. For example, information conveyed in the form of equality expressions such as  $P_i = 0.01$ ,  $P_i + P_k = 0.02$  and  $P_{kl} = 0.001$ , or inequality expressions such as  $0.01 \leq P_i \leq 0.02$ ,  $P_i \leq P_j$  or  $P_{ij} \leq P_{kl}$  are easily incorporated. Note that with the LP approach it is not necessary to have the complete set of probabilities for all components at a particular, e.g., uni-, bi- or tri-, level. Any partial set of the component probabilities can be used.

The main drawback of the LP approach is that the size of the problem increases exponentially with the number of component events. This drawback may have been the main reason for not pursuing this approach when it was first suggested by Hailperin in 1965. However, with the enormous speed and memory capacity of today's computers, this purely computational problem is not as acute. The size of the LP problem is usually determined by the number of design variables and the number of constraints. For the LP problem in this study, the number of constraints, which depends on the available information on component probabilities, is usually not critical. However, the number of design variables, which is  $2^n$  for a system with  $n$  components, exponentially grows with the number of components. The fact that, for the formulation of this study, the design variables are all bounded within the interval (0,1) and all coefficients in the objective function or the constraint equations are either 0 or 1 provides considerable advantage. Problems with  $n \leq 17$  (about 100,000 design variables) can be solved with ordinary LP solvers on a PC. For larger problems, computers with larger memory and/or parallel computing may be necessary. There are a number of advanced LP algorithms for such large problems (see Chapter 6 in Bertsimas & Tsitsiklis 1997). The discussion of these algorithms is beyond the scope of the report. With rapidly advancing speed and capacity of computers, these purely computational issues may not be a major hindrance in application of the approach to many systems reliability problems, even with large  $n$ . We note, in passing, that for  $n = 17$  the number of orderings of the component events is  $17! = 3.56 \times 10^{14}$ . In using the KHD or the higher order bounds for series systems, obviously it will not be possible to check all the possible orderings of the component events. In

that case, bounds computed by these theoretical formulas can potentially be far from the narrowest possible bounds.

It is possible to conceive of ways to reduce the size of the LP problem at the expense of relaxing the bounds. One way to do this is to define selected subsets of components in a large system as “super-components.” Using the LP approach, one computes bounds on the probability of each “super-component” as well as on the joint probabilities of pairs, triples, etc., of the “super-components.” The system bounds are then computed by LP in terms of the computed bounds on the “super-component” probabilities. Since the number of “super-components” can be much smaller than the number of components in the system, a drastic reduction in the problem size can be achieved. In effect, one solves several LP problems of smaller size in place of an impractically large LP problem. It is likely that in this process of decomposition some information will be lost and the resulting bounds on the system probability will be wider than those obtained if the large problem were solved directly. It would be desirable to develop a method of system decomposition, which achieves the objective of problem size reduction, while minimizing the information loss.

In summary, while the LP approach may become computationally demanding for systems with large number of component events (say greater than 17), it has the following important advantages: (a) it provides the narrowest possible bounds for any given level of information on component probabilities, (b) it is independent of the ordering of the component events, (c) it can incorporate general forms of information about component events, (d) it is uniformly applicable to all types of systems, and (e) general-purpose software is widely available for solving the problem. Furthermore, computational limitations of the approach will diminish with increasing speed and memory capacity of computers.

### **6.3 APPLICATION TO ELECTRICAL SUBSTATION SYSTEMS**

In this section, three numerical examples are used to demonstrate the application of the LP bounds to estimating the seismic reliability of electrical substation systems. The first example deals with a single-transmission-line system with 5 equipment items, which is modeled as a series system with  $n = 5$  components. The system is subjected to an earthquake ground motion with random intensity and local soil effects. Each component is assumed to have an uncertain



capacity to base acceleration. For this system, the uni-, bi- and tri-component bounds are estimated by LP and are compared with simulation results. The effect of varying the capacity of a critical component on the system reliability is investigated.

The second example deals with the same system with the critical component replaced with a parallel sub-system, hence introducing redundancy with respect to the state of the critical component. Systems with different number of redundant components are investigated by use of a cut-set formulation. The results by LP bounds based on uni-, bi- and tri-component probabilities are compared with simulation results.

The final example deals with a two-transmission-line system, which is a variation of the first example with system redundancy. The system is modeled through a cut-set formulation and uni-, bi- and tri-component bounds are estimated by LP and compared with simulation results. The simplex algorithm and the primal-dual algorithm implemented in Matlab<sup>®</sup> Optimization Toolbox are used to solve all the LP problems.

For all the examples in this paper, let  $A$  denote the bed-rock peak ground acceleration (PGA) in the vicinity of the substation and  $S_i$  denote a factor representing the local site response for equipment  $i$ , such that  $AS_i$  is the actual PGA experienced by the  $i$ -th equipment item. Assume  $A$  is a lognormal random variable with mean  $0.15g$  (in units of gravity acceleration,  $g$ ) and coefficient of variation (C.O.V.,  $\delta$ )  $0.5$ , and  $S_i$ ,  $i = 1, \dots, n$ , are independent lognormal random variables, also independent of  $A$ , with means  $1.0$  and C.O.V.  $0.2$ . Also let  $R_i$  denote the capacity of the  $i$ -th equipment item with respect to base acceleration in units of  $g$ , and assume it has the lognormal distribution. The means and C.O.V.'s of the equipment capacities are assumed as follows: disconnect switch (DS)  $\sim (0.4g, 0.3)$ , circuit breaker (CB)  $\sim (0.3g, 0.3)$ , power transformer (PT)  $\sim (0.5g, 0.5)$ , drawout breaker (DB)  $\sim (0.4g, 0.3)$ , feeder breaker (FB)  $\sim (1.0g, 0.3)$  and tie breaker (TB)  $\sim (1.0g, 0.3)$ . The capacities of equipment items within each category are assumed to be equally correlated with a correlation coefficient of  $0.3$  except  $0.5$  for PT's. Equipment capacities in different categories are assumed to be statistically independent. The above assumed statistics are rough approximations based on Bayesian analyses of observed data on the performance of electrical substation equipment in past earthquakes (Der Kiureghian 2002).

### 6.3.1 Single-Transmission-Line Substation

Consider the single-transmission-line substation system in Figure 6.2, which is adopted from Brown (2002). The failure of any equipment item constitutes failure of the substation. Therefore, the single-transmission-line substation is a series system with its equipment items representing the components.

The failure events of the individual equipment items are formulated as

$$E_i = \{\ln R_i - \ln A - \ln S_i \leq 0\} \quad i = 1, \dots, 5 \quad (6.17)$$

Since the logarithm of a lognormal random variable is normal,  $v_i = \ln R_i - \ln A - \ln S_i$  has the normal distribution. Therefore, the uni-component probabilities are given by

$$P_i = \Phi\left(-\frac{\mu_i}{\sigma_i}\right) \quad i = 1, \dots, 5 \quad (6.18)$$

where  $\mu_i$  and  $\sigma_i$  are the mean and standard deviation of  $v_i$ , respectively, which are easily computed in terms of the statistics of  $A$ ,  $S_i$  and  $R_i$  given above. Furthermore, for any pair of components  $i$  and  $j$ , the random variables  $v_i$  and  $v_j$  are jointly normal and the bi-component joint probabilities can be computed from (Ditlevsen & Madsen 1996)

$$P_{ij} = \Phi(u_i)\Phi(u_j) + \int_0^{\rho_{ij}} \varphi_2(u_i, u_j, \rho) d\rho \quad (6.19)$$

where  $u_i = -\mu_i/\sigma_i$ ,  $\rho_{ij}$  denotes the correlation coefficient between  $v_i$  and  $v_j$ , and  $\varphi_2(\cdot, \cdot, \rho)$  represents the bi-normal probability density function with zero means, unit standard deviations and correlation coefficient  $\rho$ . The tri-component joint probabilities of component  $i, j$  and  $k$  can be computed by the following double-fold numerical integration by use of conditional normal probabilities and (6.19).

$$P_{ijk} = \int_{-\infty}^{u_k} \varphi(z) [\Phi(u'_i)\Phi(u'_j) + \int_0^{\rho'} \varphi_2(u'_i, u'_j, \rho) d\rho] dz \quad (6.20)$$

where  $\varphi(\cdot)$  represents the probability density function with zero-mean and unit standard deviation, and  $u'_i, u'_j$  and  $\rho'$  are respectively defined as

$$u'_i = \frac{u_i - \rho_{ik}z}{\sqrt{1 - \rho_{ik}^2}} \quad (6.21a)$$

$$u'_j = \frac{u_j - \rho_{jk}z}{\sqrt{1 - \rho_{jk}^2}} \quad (6.21b)$$

$$\rho' = \frac{\rho_{ij} - \rho_{jk}\rho_{ik}}{\sqrt{1 - \rho_{ik}^2}\sqrt{1 - \rho_{jk}^2}} \quad (6.21c)$$

The above uni-, bi- and tri-component probabilities are used to compute the bounds on the series-system probability by use of LP. The LP formulation involves  $2^5 = 32$  design variables, 5 equality constraints for the uni-component probabilities, 10 for bi-component, and 10 for tri-component probabilities. The uni-component bounds on the system failure probability are 0.0925 and 0.202. The bi-component bounds are 0.122 and 0.147. The tri-component bounds are 0.139 and 0.142. To check the accuracy of these results, Monte Carlo simulation is performed and the system failure probability is estimated as 0.138 with a 1% coefficient of variation. Considering the expected variation in this estimate, one can say that this result is bracketed by the uni-, bi- and tri-component LP bounds.

One may ask the need for LP bounds when Monte Carlo simulation can be performed. The point is that the Monte Carlo simulation method can be impractical when the failure probability is small, whereas LP bounds are not affected by the magnitude of the failure probability. In this application, by the nature of the problem and the specified fragilities of the equipment items, the probability of failure is high. This, however, is not the case with all systems, including all electrical substations.

An important observation to be derived from the above result is that the seismic reliability of a single-transmission-line substation is quite low, i.e., the failure probability is high. This is partly due to the vulnerability of the circuit breaker, which is a top-heavy item with tendency to fail by fracture of its ceramic bushings or oil leakage through its gaskets. In order to investigate the influence of the capacity of the circuit breaker on the reliability of the system, the failure probability of the single-transmission-line substation is computed for a range of mean values of its capacity, while maintaining a constant C.O.V. Table 6.2 shows the assumed mean values of the capacity of circuit breaker and the corresponding component and system failure probabilities.

Uni-, bi- and tri-component LP bounds as well as Monte Carlo simulation results are listed. Figure 6.3 presents the same results in a graphical form. It is seen that a reduced capacity for the circuit breaker<sup>1</sup> drastically increases the failure probability of the system, whereas increasing the mean capacity of the circuit breaker to 0.4g significantly enhances the reliability of the system. Further increases in the mean capacity of the circuit breaker, however, have little influence on the reliability of the system. This is because another component in the series system becomes the “weakest link.”

### 6.3.2 Single-Transmission-Line with a Parallel Sub-system of Circuit Breakers

An alternative way to enhance the reliability of the single-transmission-line substation is to install several circuit breakers in parallel. This provides redundancy to the system, such that one or more circuit breakers can be taken out of service without affecting the operation of the substation (ASCE 1999).

As shown in Figure 6.4, this example replaces the single circuit breaker in the previous example with a parallel sub-system of  $k$  circuit breakers. As mentioned earlier, the capacities of the circuit breakers are equally correlated with a coefficient of variation of 0.3. Numbering the components from left to right in Figure 6.4, the system failure event is described by the following cut-set formulation:

$$E_{\text{system}} = E_1 \cup (E_2 E_3 \cdots E_{k+1}) \cup E_{k+2} \cup E_{k+3} \cup E_{k+4} \quad (6.22)$$

For a system with  $k$  circuit breakers in parallel, the LP formulation has  $2^{k+4}$  design variables,  $k + 4$  equality constraints for the uni-component probabilities,  $(k + 3)(k + 4)/2$  equalities for the bi-component probabilities, and  $(k + 2)(k + 3)(k + 4)/6$  for the tri-component probabilities. Table 6.3 lists the uni-, bi- and tri-component LP bounds as well as Monte Carlo simulation results for the selected numbers,  $k$ , of the circuit breakers in parallel. It can be seen that adding a second circuit breaker in parallel to the first one significantly enhances the reliability of the single-transmission-line system. However, the addition of further circuit breakers in parallel does not provide significantly more improvement in the reliability of the system.

In the above example, the circuit breakers were assumed to be positively correlated. Such

---

<sup>1</sup> Many circuit breakers in operation actually have mean capacities around 0.2g.

correlation is present when circuit breakers are of the same model or from the same manufacturer. One can increase the reliability of a parallel sub-system by reducing positive correlation between the components. To investigate this effect, the above example is repeated, while assuming the circuit breaker capacities are uncorrelated. In practice, such a case might be achieved by assembling circuit breakers of different make or model. The results in Table 6.4 show that this modification improves the reliability of the system, but only by a small amount. The reason is that the common random variable  $A$  still causes strong correlation between the component failure events.

### 6.3.3 Two-Transmission-Line Substation

A further alternative to increase the redundancy of the substation system is to add one or more transmission lines, such that the system has alternative paths for electric flow. Consider the two-transmission-line substation system shown in Figure 6.5. As before, we assume a correlation coefficient of 0.3 between equipment capacities within each category (except 0.5 for PT's), and statistical independence between equipment capacities in different categories.

Using the component identification numbers shown in parentheses in Figure 6.5, the 25 minimum cut sets of the system are identified as follows: (1,2), (4,5), (4,7), (4,9), (5,6), (6,7), (6,9), (5,8), (7,8), (8,9), (11,12), (1,3,5), (1,3,7), (1,3,9), (2,3,4), (2,3,6), (2,3,8), (4,10,12), (6,10,12), (8,10,12), (5,10,11), (7,10,11), (9,10,11), (1,3,10,12), (2,3,10,11). The LP problem has  $2^{12} = 4,096$  design variables. The uni-component probabilities introduce 12 equality constraints, and the bi- and tri-component probabilities introduce additional 66 and 220 equality constraints, respectively.

The uni-, bi- and tri-component bounds obtained by LP, as well as the Monte Carlo simulation results are listed in Table 6.5 as *Case 1*. Compared to the single-transmission-line substation, we observe a significant reduction in the tri-component LP bounds. The simulation result also confirms the improvement in reliability in account of the added system redundancy.

To further demonstrate the usefulness of the LP bounds, suppose no information is available on one of the equipment items in the substation, say the tie breaker TB (component 10). In that case, the uni-component probability and all the joint-component probabilities involving this equipment item are not available. With the LP bounds, we only need to remove the equality constraints corresponding to these unknown probabilities. For the present example, the result ob-

tained by removing the equality constraints involving the tie breaker TB is shown in Table 6.5 as *Case 2*. No appreciable change in the bi- or tri-component bounds of the system is observed for this case. This implies that the TB may not have a critical role in the system reliability. Note that with incomplete probability information, Monte Carlo simulation cannot be performed and, for that reason, “NA” (not applicable) is indicated in the last column of Table 6.5. If, instead of TB, the equipment item  $CB_1$  is assumed to lack probability information, the result for *Case 3* in Table 6.5 is obtained. The tri-component LP bounds for this case are significantly wider than the corresponding bounds for *Case 1*.

Now suppose that the equipment item  $CB_1$  (component 4 in the system), which has a marginal failure probability of 0.0925 (See Table 6.2, third row), is strengthened and it is estimated that its marginal probability of failure after strengthening is less than 0.01. Suppose no information on joint-component probabilities between this and other equipment items is available. The LP solution for this case, denoted *Case 4* in Table 6.5, is obtained by removing all equality constraints involving this component and adding an inequality constraint of the form  $P_4 \leq 0.01$ . The result in Table 6.5 indicates a reduction in the upper bound, but no change in the lower bound.

#### **6.4 IDENTIFICATION OF CRITICAL COMPONENTS AND CUT SETS**

An important objective in system reliability assessment is the identification of critical components and cut sets. These are defined as components or cut sets which make significant contributions to the system failure probability for a specified system performance criterion and load hazard. When upgrading the system reliability is an objective, the identified critical components and cut sets should be considered as prime candidates for reinforcement and strengthening on a preferential basis, especially when the system upgrade is subject to cost or other constraints.

Various importance measures (IM) have been defined for evaluating and ranking the contributions of components and cut sets to the failure probability of a system. The most widely used measures are Fussell-Vesely (FV; Fussell 1973), Risk Achievement Worth (RAW; Boronovo & Apostolakis 2001), Risk Reduction Worth (RRW; Vinod *et al.* 2003), Boundary Probability (BP; Anders 1990), Fussell-Vesely Cut-set IM (Fussell 1973), etc. When the component failure events are statistically independent of each other, these measures can be easily computed

by use of the marginal component failure probabilities (Henley & Kumamoto 1981, Anders 1990). However, when there is dependence between the component states, it is a daunting task to compute the probabilities required for these measures, including the system failure probability. An incomplete set of component probabilities or inequality type information on component probabilities would make the task even more difficult.

The proposed LP formulation provides a convenient framework for a systematic identification of critical components and cut sets. Suppose the bounds on the failure probability of a system are obtained by solving the LP problem in (6.12) for a given information on component probabilities. Let  $\hat{\mathbf{p}}$  denote the solution of  $\mathbf{p}$  at the upper bound of the system failure probability. The vector  $\hat{\mathbf{p}}$  stores the probabilities of all the basic MECE events that contribute to the upper bound of the system failure probability. Therefore, the contribution of any event of interest to the upper bound system failure probability can be determined by simply adding the components of  $\hat{\mathbf{p}}$  for the basic MECE events that are contained within the specified event. This can be done by simple algebraic manipulation of vectors and matrices. The same can be done with the solution of  $\mathbf{p}$  for the lower bound of the system failure probability. In general, the set of critical components and cut sets and the corresponding importance measures obtained based on the two system bounds may be different. However, as the probability information increases and the two bounds approach each other, the ordering of the critical components and cut sets and the corresponding importance measures based on the two bounds also tend to approach each other. In the following, we describe the formulas in general terms, where either bound can be used.

The proposed method allows us to easily compute various importance measures for components and cut sets, even when there is statistical dependence between the component failure events. Inheriting all the advantages of the LP bounding methodology, this method is fairly flexible in gathering information such that it can incorporate incomplete sets of probabilities or inequality-type constraints.

#### **6.4.1 Importance Measures by LP Bounds**

This section introduces several well-known component and cut set importance measures and shows how they can be easily determined by use of the LP bounds formulation. For the sake of simplicity of the notation, and without loss of generality, in the following we only consider the

general system formulation by cut sets in (6.5). Series and parallel systems are then special cases: For a series system, each component is a cut set; and a parallel system has only one cut set containing all the components. Unless defined otherwise, the term ‘cut set’ in the following discussion means ‘minimum cut set’. A cut set is called minimum when the removal of any component renders the remainder not a cut set.

#### 6.4.1.1 Fussell-Vesely Importance Measure

The Fussell-Vesely (FV) importance measure for a component evaluates the fraction of the system failure probability, which is contributed by cut sets containing the component of interest (Fussell 1973). For component  $i$ , the FV IM is defined as

$$FV_i = \frac{P(\bigcup_{k:E_i \subseteq C_k} C_k)}{P(E_{\text{system}})} \quad (6.23)$$

This measure quantifies the contribution of each component to the system failure probability. In the case of statistically independent component events, both the numerator and denominator in (6.23) can be computed in terms of marginal component probabilities employing the elementary rules of probability.

In the LP formulation (6.12), the system failure probability in the denominator is computed in terms of its lower or upper bound. With the solution  $\hat{\mathbf{p}}$  available, the corresponding probability in the numerator is computed as the vector product

$$P(\bigcup_{k:E_i \subseteq C_k} C_k) \cong \mathbf{a}_i^{FV} \hat{\mathbf{p}} \quad (6.24)$$

where  $\mathbf{a}_i^{FV}$  is a row vector whose  $j$ -th element is

$$[\mathbf{a}_i^{FV}]_j = \begin{cases} 1 & \text{if } e_j \subset \bigcup_{k:E_i \subseteq C_k} C_k \\ 0 & \text{otherwise} \end{cases} \quad (6.25)$$

where  $e_j$  denotes the  $j$ -th basic MECE event in the sample space. The vector  $\mathbf{a}_i^{FV}$  is easily obtained by simple logical operations.



It is noteworthy that the proposed method computes the FV IM for general systems, regardless of whether statistical dependence between the component events exists or not. Furthermore, these measures can be computed for the lower and upper bounds of the system failure probability, even when the available information on component probabilities is incomplete or is in terms of inequalities.

#### 6.4.1.2 Risk Achievement Worth

The failure of important components tends to increase the failure probability of the system. The Risk Achievement Worth (RAW) IM measures the importance of a component by the increase in the system failure probability when the component is removed from the system (Borgonovo & Apostolakis 2001), i.e., it is assumed to be perfectly unreliable. The RAW of the  $i$ -th component is defined as

$$RAW_i = \frac{P(E_{\text{system}}^{(i)})}{P(E_{\text{system}})} \quad (6.26)$$

where  $P(E_{\text{system}}^{(i)})$  denotes the failure probability of the system with component  $i$  removed.

The system failure probability in the denominator of (6.26) is obtained from the original LP problem in (6.12). The probability in the numerator is obtained by solving a new LP problem formulated for the system with the  $i$ -th component removed. This requires the following changes in the original LP problem: (1) Remove  $E_i$  from any cut set that contains it. (2) When  $E_i$  itself is a cut set, set  $P(E_{\text{system}}^{(i)}) = 1.0$ . (3) If a cut set contains  $\bar{E}_i$ , remove the cut set from the system event. (4) Remove all LP constraints related to  $E_i$ . For example, consider the system event  $E_{\text{system}} = E_1 E_2 \cup \bar{E}_2 E_3 \cup E_4$ . According to the above rules, the new system events are

$$E_{\text{system}}^{(1)} = E_2 \cup \bar{E}_2 E_3 \cup E_4 \quad (6.27a)$$

$$E_{\text{system}}^{(2)} = E_1 \cup E_4 \quad (6.27b)$$

$$E_{\text{system}}^{(3)} = E_1 E_2 \cup \bar{E}_2 \cup E_4 \quad (6.27c)$$

and for component 4

$$P(E_{\text{system}}^{(4)}) = 1 \quad (6.27d)$$

Thus, a new LP problem should be solved to obtain the RAW IM of each component. As described above, the new LP problem is formulated from the original problem through a set of simple logical rules.

When the component events are statistically independent of each other,  $P(E_{\text{system}}^{(i)})$  is equivalent to the conditional probability of the system failure given the failure of component  $i$ , i.e.,  $P(E_{\text{system}} | E_i)$ . This can be proven as follows: The conditional probability is defined as

$$P(E_{\text{system}} | E_i) = \frac{P(E_{\text{system}} \cap E_i)}{P(E_i)} \quad (6.28)$$

By the distributive rule of probability, the numerator is

$$P(E_{\text{system}} \cap E_i) = P(C_1 E_i \cup C_2 E_i \cup \dots \cup C_K E_i) \quad (6.29)$$

where  $K$  denotes the total number of cut sets of the system. Due to the assumed statistical independence between the component events,  $P(E_i)$  can be factored out such that

$$P(E_{\text{system}} \cap E_i) = P(E_i) P(X) \quad (6.30)$$

where  $X$  is the remainder event after removal of  $E_i$  from the event in the right-hand side of (6.29). We now show that  $X = E_{\text{system}}^{(i)}$ . This is evident by noting that the formation of  $X$  follows the same rules as described above for forming  $E_{\text{system}}^{(i)}$ . Specifically,  $E_i$  should be removed from any cut set that contains it;  $P(X) = 1$  if  $E_i$  itself is a cut set; and any cut set containing  $\bar{E}_i$  is removed due to the intersection with  $E_i$ . Thus,  $P(X) = P(E_{\text{system}}^{(i)})$ . Substituting (6.30) into (6.28) completes the proof. Therefore, for a system with statistically independent component events, the RAW IM for component  $i$  is

$$RAW_i = \frac{P(E_{\text{system}} \cap E_i)}{P(E_i) P(E_{\text{system}})} \quad (\text{stat. indep. comp. events}) \quad (6.31)$$

In this case, the probability in the numerator can be computed by algebraic manipulation of  $\hat{\mathbf{p}}$  without solving an additional LP problem. Specifically,

$$P(E_{\text{system}} \cap E_i) = \mathbf{a}_i^{\text{comp}} \mathbf{C} \hat{\mathbf{p}} \quad (6.32)$$

where  $\mathbf{C}$  is the diagonal matrix of the vector  $\mathbf{c}$  and  $\mathbf{a}_i^{\text{comp}}$  is a row vector with elements

$$\left[ \mathbf{a}_i^{\text{comp}} \right]_j = \begin{cases} 1 & \text{if } e_j \subset E_i \\ 0 & \text{otherwise} \end{cases} \quad (6.33)$$

As described earlier, in the case of statistically dependent component events, a new LP problem should be solved for determining RAW IM for each component.

#### 6.4.1.3 Risk Reduction Worth

The Risk Reduction Worth (RRW) IM measures the decrease in the system failure probability when the component of interest is replaced by a perfectly reliable component, i.e., a component have zero probability of failure (Vinod *et al.* 2003). Thus, the RRW of the  $i$ -th component is

$$RRW_i = \frac{P(E_{\text{system}})}{P(\overline{E_{\text{system}}^{(i)}})} \quad (6.34)$$

where  $P(\overline{E_{\text{system}}^{(i)}})$  denotes the failure probability of the system when the  $i$ -th component is replaced with a perfectly reliable component. This probability is placed in the denominator so that a higher value of RRW indicates higher importance of the corresponding component.

The system failure probability in the numerator of (6.34) is obtained from the original LP problem in (6.12). For the probability in the denominator, one needs to solve another LP problem formulated for the system with the  $i$ -th component replaced with a perfectly reliable component. This is accomplished by making the following changes to the original LP problem: (1) If a cut set contains  $E_i$ , remove the cut set (including when  $E_i$  itself is a cut set). (2) Remove  $\overline{E}_i$  from any cut set that contains it. (3) Remove all constraints containing  $E_i$ . According to the above rules, for example, the new system events for the system event  $E_{\text{system}} = E_1 E_2 \cup \overline{E}_2 E_3 \cup E_4$  are

$$E_{\text{system}}^{(1)} = \overline{E}_2 E_3 \cup E_4 \quad (6.35a)$$

$$E_{\text{system}}^{(2)} = E_3 \cup E_4 \quad (6.35b)$$

$$E_{\text{system}}^{(3)} = E_1 E_2 \cup E_4 \quad (6.35c)$$

and for component 4

$$P(E_{\text{system}}^{(4)}) = E_1 E_2 \cup \bar{E}_2 E_3 \quad (6.35d)$$

Clearly, a new LP problem should be solved to obtain the RRW IM of each component.

When the component events are statistically independent of each other,  $P(E_{\text{system}}^{(i)})$  is identical to the conditional probability of failure of the system given survival of component  $i$ , i.e.,  $P(E_{\text{system}} | \bar{E}_i)$ . This can be proven with a derivation analogous to that used for  $P(E_{\text{system}}^{(i)})$ . Therefore, for a system with statistically independent component events, the RRW IM is

$$RRW_i = \frac{P(E_{\text{system}} \cap \bar{E}_i)}{P(\bar{E}_i)P(E_{\text{system}})} \quad (\text{stat. indep. comp. events}) \quad (6.36)$$

The probability in the numerator can be computed by algebraic manipulation of  $\hat{\mathbf{p}}$  without solving a new LP problem. Specifically,

$$P(E_{\text{system}} \cap \bar{E}_i) = (\mathbf{1} - \mathbf{a}_i^{\text{comp}}) \mathbf{C} \hat{\mathbf{p}} \quad (6.37)$$

where  $\mathbf{1}$  is a row vector of 1's.

#### 6.4.1.4 Boundary Probability

The Boundary Probability (BP) of a component measures the change in the probability of failure of the system that is solely due to a change in the state of the component (Anders 1990). To determine the BP IM for the  $i$ -th component, consider the following two events defined earlier:  $E_{\text{system}}^{(i)}$  = the failure event of the system when the  $i$ -th component has been removed;  $E_{\text{system}}^{\bar{(i)}}$  = the failure event of the system when the  $i$ -th component has been replaced with a perfectly reliable component. The difference  $P(E_{\text{system}}^{(i)}) - P(E_{\text{system}})$  describes the increase in the failure probability due to removal of component  $i$ , whereas  $P(E_{\text{system}}) - P(E_{\text{system}}^{\bar{(i)}})$  describes the gain in reliability by replacing the component with a perfectly reliable component. The net change is the BP IM, i.e.,

$$BP_i = P(E_{\text{system}}^{(i)}) - P(E_{\text{system}}^{\bar{(i)}}) \quad (6.38)$$

It can be seen that the BP is the probability of two events near the boundary of the component

and system failure events. As shown for RAW and RRW, the probabilities  $P(E_{\text{system}}^{(i)})$  and  $P(\overline{E_{\text{system}}^{(i)}})$  can be obtained by solving LP problems for systems derived from the original system by removing or replacing component  $i$ .

#### 6.4.1.5 Fussell-Vesely Cut-set Importance Measure

The critical cut sets can be identified by measuring the contributions of the individual cut sets to the system failure probability. For this purpose, the Fussell-Vesely Cut set (FVC) IM for the  $k$ -th cut set is defined as (Fussell 1973)

$$FVC_k = \frac{P(C_k)}{P(E_{\text{system}})} \quad (6.39)$$

The probability in the numerator is computed in terms of the LP solution:

$$P(C_i) \cong \mathbf{a}_i^{\text{cut}} \hat{\mathbf{p}} \quad (6.40)$$

where  $\mathbf{a}_i^{\text{cut}}$  is a row vector with its  $j$ -th element given by

$$[\mathbf{a}_i^{\text{cut}}]_j = \begin{cases} 1 & \text{if } e_j \subset C_i \\ 0 & \text{otherwise} \end{cases} \quad (6.41)$$

### 6.4.2 Applications to Electrical Substation Systems

As a numerical example, consider the two-transmission-line substation system described in Section 6.3.3 and Figure 6.5. This is a general system composed of 12 components and having 25 minimum cut sets. Due to the correlation between the equipment capacities within the same category and the presence of  $A$  in the limit-state functions of all components, significant statistical dependence between the component failure events is present. Under the uni-, bi- and tri-component probability constraints, the upper LP bound is estimated as 0.0942. In the following, IM's are computed with respect to this bound.

Simple post-processing of the upper-bound LP solution yields the vectors  $\hat{\mathbf{p}}$  and  $\mathbf{a}_i^{FV}$ . The FV IM is obtained by substituting these results together with the upper bound probability estimate (0.0942) into (6.23) with (6.24). For the probabilities  $P(E_{\text{system}}^{(i)})$  and  $P(\overline{E_{\text{system}}^{(i)}})$ , a total

of  $2 \times 12 = 24$  additional LP problems are solved according to the rules described above. Substituting these probabilities and the upper bound LP solution in (6.26), (6.34) and (6.38), the RAW, RRW and BP importance measures are, respectively, obtained for each component.

Table 6.6 lists the various importance measures of the components in the substation system. According to the FV, RRW and BP measures, the importance ranking of the components is in the order  $(CB_{1,2}) \rightarrow (PT_{1,2}) \rightarrow (DB_{1,2}) \rightarrow (DS_{1,2}) \rightarrow (DS_3) \rightarrow (FB_{1,2}, TB)$ . The ranking according to RAW is  $(CB_{1,2}, PT_{1,2}, DB_{1,2}) \rightarrow (DS_{1,2}) \rightarrow (DS_3) \rightarrow (FB_{1,2}, TB)$ , which is identical to the order by the other measures, except that CB, PT and DB have the same order of importance. As a result, one can say that the two circuit breakers ( $CB_{1,2}$ ) are the most critical components in the system, followed by the other equipment items as listed above.

To identify the critical minimum cut sets, the FVC importance measure is computed by (6.39) with (6.40) using the upper bound LP solution. The cut sets are sorted in the descending order of FVC and the first 12 cut sets are listed in Table 6.7. The joint failure of the two circuit breakers is the most critical cut set. The joint failures of the drawout breaker and circuit breaker on different lines are ranked next. It is noteworthy that the top five most critical cut sets all include at least one circuit breaker. This further reinforces the importance of these components for the system.

Once the importance order of components within a system has been determined, measures can be taken to strengthen the critical components, if upgrading the system reliability is desired. Usually, the decision to strengthen a component also involves costs and other constraints. A decision framework that incorporates all these considerations is recommended as a topic of future study.

Table 6.1 Coefficients  $c_i$  of the object functions  $\mathbf{c}^T \mathbf{p}$  for three-component systems

System event	Basic MECE events							
	$E_1E_2E_3$	$\bar{E}_1E_2E_3$	$E_1\bar{E}_2E_3$	$E_1E_2\bar{E}_3$	$\bar{E}_1\bar{E}_2E_3$	$\bar{E}_1E_2\bar{E}_3$	$E_1\bar{E}_2\bar{E}_3$	$\bar{E}_1\bar{E}_2\bar{E}_3$
	Design variables							
	$p_1$	$p_2$	$p_3$	$p_4$	$p_5$	$p_6$	$p_7$	$p_8$
$E_1 \cup E_2 \cup E_3$	1	1	1	1	1	1	1	0
$E_1E_2E_3$	1	0	0	0	0	0	0	0
$E_1E_2 \cup E_3$	1	1	1	1	1	0	0	0
$(E_1 \cup E_2)(\bar{E}_2 \cup E_3)$	1	1	1	0	0	0	1	0

Table 6.2 Failure probabilities of circuit breaker and corresponding system failure probabilities

$E[R_{CB}]$	$P_{CB}$	Uni-comp. LP	Bi-comp. LP	Tri-comp. LP	M.C. $\delta = 0.01$
0.1	0.704	0.704~0.813	0.7048~0.7053	0.7052~0.7052	0.701
0.2	0.261	0.261~0.371	0.272~0.284	0.2818~0.2824	0.280
0.3	0.0925	0.0925~0.202	0.122~0.147	0.139~0.142	0.138
0.4	0.0349	0.0393~0.144	0.0853~0.114	0.0989~0.103	0.0997
0.5	0.0142	0.0393~0.124	0.0805~0.0980	0.0886~0.0908	0.0901
0.6	0.00621	0.0393~0.116	0.0805~0.0927	0.0858~0.0868	0.0869
0.7	0.00288	0.0393~0.112	0.0805~0.0908	0.0850~0.0855	0.0858

Table 6.3 Failure probabilities of single-transmission-line substation with parallel sub-system of  $k$  correlated circuit breakers

$k$	Uni-comp. LP	Bi-comp. LP	Tri-comp. LP	M.C. $\delta = 0.01$
1	0.0925~0.202	0.122~0.147	0.139~0.142	0.138
2	0.0393~0.202	0.0805~0.130	0.0992~0.109	0.104
3	0.0393~0.202	0.0805~0.122	0.0874~0.104	0.0950
4	0.0393~0.202	0.0805~0.120	0.0847~0.100	0.0892

Table 6.4 Failure probabilities of single-transmission-line substation with parallel sub-system of  $k$  uncorrelated circuit breakers

$k$	Uni-comp. LP	Bi-comp. LP	Tri-comp. LP	M.C. $\delta = 0.01$
1	0.0925~0.202	0.122~0.147	0.139~0.142	0.138
2	0.0393~0.202	0.0805~0.125	0.0957~0.105	0.100
3	0.0393~0.202	0.0805~0.116	0.0847~0.100	0.0916
4	0.0393~0.202	0.0805~0.114	0.0847~0.0961	0.0864

Table 6.5 Failure probabilities of two-transmission-line substation system

Case	Uni-comp. LP	Bi-comp. LP	Tri-comp. LP	M.C. $\delta = 0.01$
1	$1.13 \times 10^{-12}$ ~0.202	0.0436~0.146	0.0616~0.0942	0.0752
2	$1.82 \times 10^{-11}$ ~0.202	0.0436~0.146	0.0615~0.0943	NA
3	$1.26 \times 10^{-9}$ ~0.202	0.0267~0.147	0.0395~0.136	NA
4	$5.19 \times 10^{-9}$ ~0.120	0.0267~0.0995	0.0395~0.0701	NA



Table 6.6 Component importance measures for the two-transmission-line substation system (maximum IM's are highlighted)

$i$	$P(\bigcup_{k:E_i \subseteq C_k} C_k)$	$P(E_{\text{system}}^{(i)})$	$P(\overline{E_{\text{system}}^{(i)}})$	$FV_i$	$RAW_i$	$RRW_i$	$BP_i$
1 (DS <sub>1</sub> )	0.0172	0.112	0.0848	0.183	1.18	1.11	0.0264
2 (DS <sub>2</sub> )	0.0172	0.112	0.0848	0.183	1.18	1.11	0.0264
3 (DS <sub>3</sub> )	0.0158	0.103	0.0887	0.168	1.09	1.06	0.0142
4 (CB <sub>1</sub> )	0.0566	0.136	0.0601	0.601	1.44	1.57	0.0760
5 (CB <sub>2</sub> )	0.0566	0.136	0.0601	0.601	1.44	1.57	0.0760
6 (PT <sub>1</sub> )	0.0267	0.136	0.0795	0.283	1.44	1.18	0.0565
7 (PT <sub>2</sub> )	0.0267	0.136	0.0795	0.283	1.44	1.18	0.0565
8 (DB <sub>1</sub> )	0.0264	0.136	0.0822	0.280	1.44	1.15	0.0539
9 (DB <sub>2</sub> )	0.0264	0.136	0.0822	0.280	1.44	1.15	0.0539
10 (TB)	$5.77 \times 10^{-5}$	0.0943	0.0943	$6.12 \times 10^{-4}$	1.00	1.00	$3.90 \times 10^{-5}$
11 (FB <sub>1</sub> )	$7.72 \times 10^{-5}$	0.0943	0.0943	$8.19 \times 10^{-4}$	1.00	1.00	$5.20 \times 10^{-5}$
12 (FB <sub>2</sub> )	$7.72 \times 10^{-5}$	0.0943	0.0943	$8.19 \times 10^{-4}$	1.00	1.00	$5.20 \times 10^{-5}$

Table 6.7 Fussell-Vesely cut-set importance measures for the two-transmission-line substation system

Order	Cut Set	$FVC_i$
1	(4, 5)	0.463
2	(5, 8)	0.200
3	(4, 9)	0.200
4	(5, 6)	0.179
5	(4, 7)	0.179
6	(6, 7)	0.155
7	(1, 2)	0.138
8	(8, 9)	0.138
9	(2, 3, 4)	0.0976
10	(1, 3, 5)	0.0976
11	(7, 8)	0.0951
12	(6, 9)	0.0951

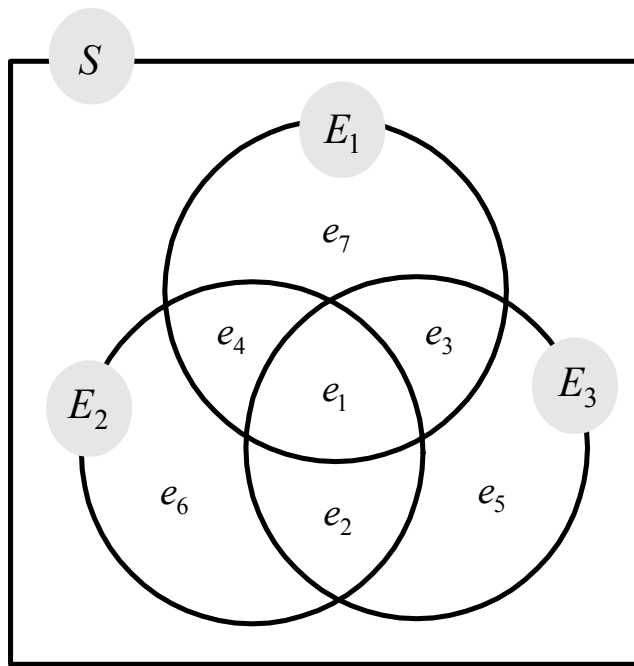


Figure 6.1 Basic MECE events  $e_i$  for a three-event sample space

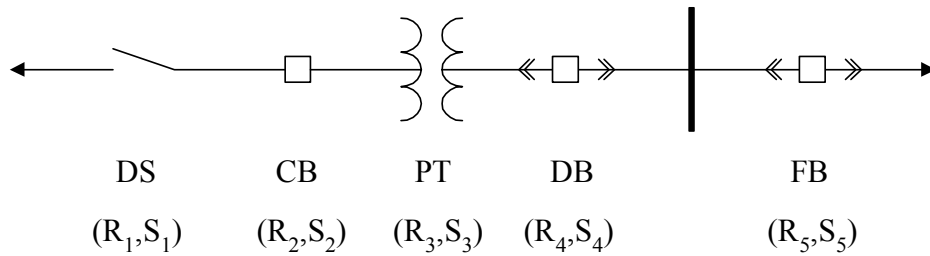


Figure 6.2 Example single-transmission-line substation system

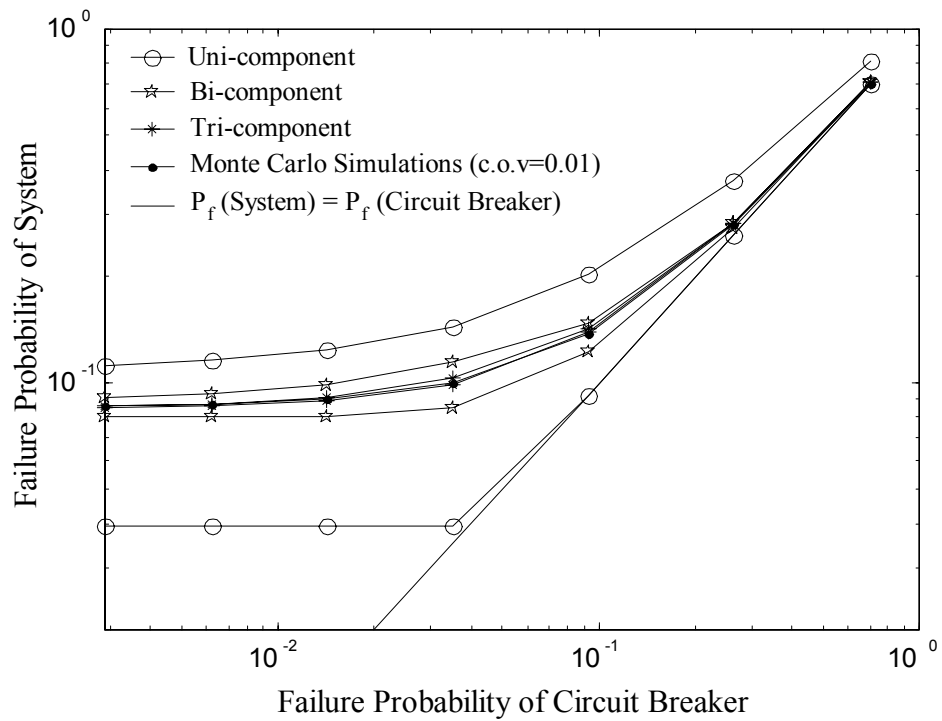


Figure 6.3 System versus circuit-breaker failure probabilities

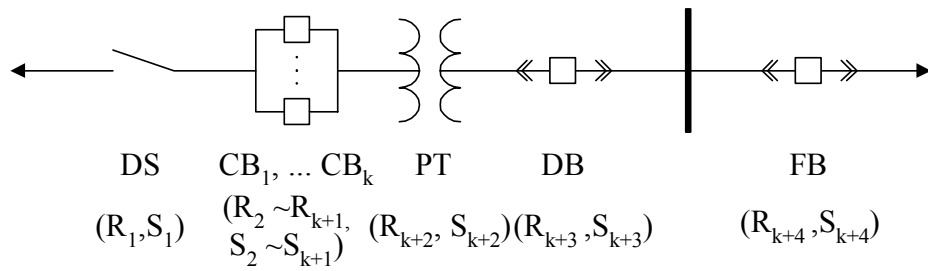


Figure 6.4 Example single-transmission-line substation with a parallel sub-system of circuit breakers

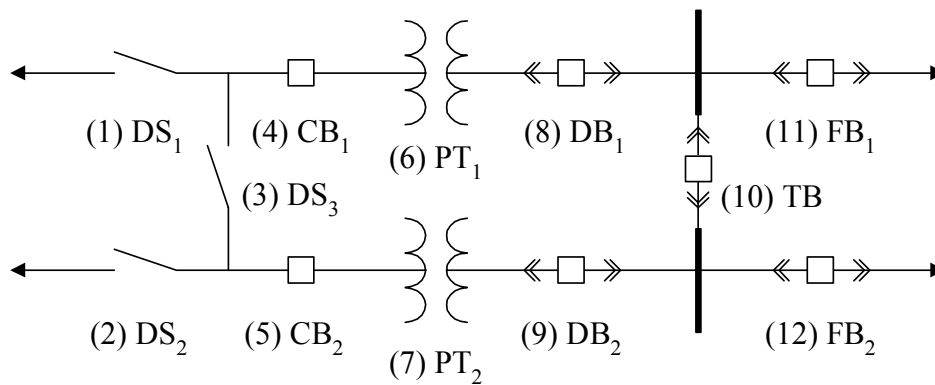


Figure 6.5 Example two-transmission-line substation system

# 7 First-Passage Probability of Systems and Application to Electrical Substations

## 7.1 INTRODUCTION

Engineering systems consisting of multiple structural components, e.g., electrical substations, highway transportation networks, water, gas and power distribution systems, and marine structural systems, are often subject to stochastic loads, such as earthquakes, wind or sea waves. Under these conditions, the response of each structural component is a stochastic process and its reliability can be estimated in terms of the first-passage probability, i.e., the probability that the stochastic response process exceeds a prescribed threshold during a given interval of time. Section 7.2 deals with the marginal first-passage probability and introduces several well-known approximate formulas.

The reliability of a complex system, however, cannot be directly deduced from the marginal first-passage probabilities of its components when the component failure events are statistically dependent. Such dependence is often present in systems composed of structural components, particularly when the components are subject to a common source of excitation. For such systems, bounds on the system failure probability can be obtained from analytical bounding formulas (Ditlevsen 1979; Hohenbichler & Rackwitz 1983; Zhang 1993) or linear programming (LP) (Song & Der Kiureghian 2003) as described in Chapter 6. However, in order to achieve narrow bounds, it is necessary to have information on the joint failure probabilities of pairs, triplets or, in general, subsets of the components. For systems under stochastic loading, the joint probability of interest is the probability that the response of each component in the subset exceeds its respective safe threshold during the given period of time. We denote this as a *joint first-passage probability*. It is not straightforward to estimate this probability because the joint failure event is not represented by a single out-crossing of the vector response process. Section 7.3 proposes ap-

proximate formulas for the joint first-passage probability of a vector process. By applying the inclusion-exclusion rule of probability, the joint first-passage probability is derived in terms of the marginal first-passage probability of the individual scalar processes and the out-crossing (union event) probability of the vector process. The latter probability is approximated by use of the mean crossing rate of the vector process out of a safe domain, which is the sum of the crossing rates of the processes over their respective double-barriers with finite dimensions. Dependence between the crossing events is approximately accounted for by considering the clumping of their occurrences.

Section 7.4 verifies the proposed formulas by comparing the analytical estimates with Monte Carlo simulation results. For the simulation, the joint first-passage probabilities are computed for stationary responses of two or three single-degree-of-freedom (SDOF) oscillators under simulated zero-mean, Gaussian, white noise processes. Also investigated in this section is the effect of the correlation between the response processes and the influence of the bandwidths of the processes on the accuracy of the formulas.

Section 7.5 develops a methodology for estimating the reliability of an interconnected equipment system subjected to a stochastic excitation. The methodology is a synthesis of the analytical models and methods developed in this study: (1) the connected equipment items are represented by SDOF linear models; (2) the nonlinear hysteretic behavior of the rigid bus connector is described by differential-equation-type analytical models; (3) the second moments of the responses of the connected system are computed by nonlinear random vibration analysis employing the equivalent linearization method (ELM); (4) marginal and joint fragilities of equipment items are obtained by use of approximate first-passage probability functions; and (5) the fragility of the entire substation system is approximated by system reliability bounds employing marginal and joint component fragilities together with the LP algorithm. The methodology is demonstrated through an application to an example electrical substation system.

## 7.2 MARGINAL FIRST-PASSAGE PROBABILITY

Let  $P_i(a_i, \tau)$  denote the first-passage probability of a stochastic process  $X_i(t)$  over a prescribed double-sided threshold  $|x_i| = a_i$  during an interval of time  $t \in (0, \tau)$ . This probability is usually described by use of an exponential function

$$P_i(a_i, \tau) = 1 - A_i \exp\left[-\int_0^\tau \alpha_i(a_i, t) dt\right] \quad (7.1)$$

where  $A_i$  is the probability that the process is in the safe domain at  $t = 0$  and  $\alpha_i(a_i, t)$  is the conditional mean crossing rate at time  $t$ , given no crossings prior to that time. In most cases, this conditional crossing rate is impossible to obtain because the necessary conditional joint density function of the process and its rate is unknown (Lutes & Sarkani 1997).

A well-known approximation is to replace  $\alpha_i(a_i, t)$  of (7.1) with the unconditional mean crossing rate of  $X_i(t)$  over  $|x_i| = a_i$ , i.e.,  $v_i(a_i, t)$ . Since this assumption neglects the statistical dependence between the crossing events, it is often called the *Poisson approximation* (Rice 1944 & 1945). With this approximation,

$$P_i(a_i, \tau) \cong 1 - A_i \exp\left[-\int_0^\tau v_i(a_i, t) dt\right] \quad (7.2a)$$

$$A_i = P[|X_i(0)| < a_i] = \int_{-a_i}^{a_i} f_{X_i}(x_i, 0) dx_i \quad (7.2b)$$

$$\begin{aligned} v_i(a_i, t) &= v_i^+(a_i, t) + v_i^-(-a_i, t) \\ &= \int_0^\infty \dot{x}_i f_{X_i, \dot{X}_i}(a_i, \dot{x}_i, t) d\dot{x}_i + \int_{-\infty}^0 \dot{x}_i f_{X_i, \dot{X}_i}(-a_i, \dot{x}_i, t) d\dot{x}_i \end{aligned} \quad (7.2c)$$

where  $f_{X_i}(x_i, t)$  is the marginal probability density function (PDF) of  $X_i(t)$  and  $v_i^+(a_i, t)$  and  $v_i^-(-a_i, t)$  denote the unconditional mean rates of up- and down-crossings of the process  $X_i(t)$ , respectively. These rates are computed by Rice's formula (Rice 1944 & 1945) in (7.2c), where  $f_{X_i, \dot{X}_i}(\cdot, \cdot, t)$  is the joint PDF of the process  $X_i(t)$  and its time rate,  $\dot{X}_i(t)$ , at the same instant of time.

For a stationary, zero-mean, Gaussian process, the first-passage probability based on the Poisson approximation is (Cramer & Leadbetter 1967; Crandall & Mark 1963)

$$P_i(a_i, \tau) = 1 - A_i \exp[-v_i(a_i) \tau] \quad (7.3a)$$

$$A_i = 1 - 2\Phi(-r_i) \quad (7.3b)$$

$$v_i(a_i) = \frac{1}{\pi} \frac{\sigma_{\dot{X}_i}}{\sigma_{X_i}} \exp(-r_i^2/2) \quad (7.3c)$$

where  $\Phi(\cdot)$  denotes the cumulative distribution function (CDF) of the standard normal distribution and  $r_i = a_i / \sigma_{X_i}$  is the prescribed threshold normalized by the standard deviation,  $\sigma_{X_i}$ , of the process.

Convenient as it is, the Poisson approximation can result in significant errors, depending on the bandwidth of the process and the time it spends in the unsafe domain. VanMarcke (1975) proposed an improved formula, accounting for the dependence between the crossing events. He employed the envelope process and considered the clumping of the process crossings associated with each crossing of the envelope. The conditional crossing rate in (7.1) is replaced by  $\eta_i(a_i, t)$ , the unconditional mean crossing rate of the envelope process, discounted by the probability that crossings by the process will indeed occur during a single envelope excursion. For consistency,  $A_i$  in (7.1) is replaced by  $B_i$ , the probability that the envelope process is in the safe domain at  $t = 0$ . The resulting approximation is

$$P_i(a_i, \tau) = 1 - B_i \exp\left[-\int_0^\tau \eta_i(a_i, t) dt\right] \quad (7.4a)$$

$$B_i = P[E_i(0) < a_i] = \int_0^{a_i} f_{E_i}(e_i, 0) de_i \quad (7.4b)$$

$$\eta_i(a_i, t) = \frac{P[E_i(t) > a_i] v_i(0, t)}{P[E_i(t) < a_i]} \left[ 1 - \exp\left(\frac{-v_{E_i}^+(a_i, t)}{P[E_i(t) > a_i] v_i(0, t)}\right) \right] \quad (7.4c)$$

where  $E_i(t)$  denotes the envelope process of  $X_i(t)$ ,  $f_{E_i}(e_i, t)$  is the marginal PDF of  $E_i(t)$ , and  $v_{E_i}^+(a_i, t)$  is the unconditional mean up-crossing rate of  $E_i(t)$ .

When  $X_i(t)$  is a stationary, zero-mean, Gaussian process and the envelope process defined by Cramer and Leadbetter (1967) is used, the corresponding formulas are

$$P_i(a_i, \tau) = 1 - B_i \exp[-\eta_i(a_i) \tau] \quad (7.5a)$$

$$B_i = 1 - \exp(-r_i^2/2) \quad (7.5b)$$



$$\eta_i(a_i) = v_i(a_i) \left[ \frac{1 - \exp(-\sqrt{\pi/2} \delta_i^{1.2} r_i)}{1 - \exp(-r_i^2/2)} \right] \quad (7.5c)$$

where  $\delta_i = (1 - \lambda_{1,i}^2 / \lambda_{0,i} \lambda_{2,i})^{1/2}$  is a shape factor that characterizes the bandwidth of the process, in which  $\lambda_{m,i}$  are the spectral moments of the process  $X_i(t)$  defined by

$$\lambda_{m,i} = \int_0^\infty \omega^m G_{X_i X_i}(\omega) d\omega \quad m = 0, 1, 2, \dots \quad (7.6)$$

where  $G_{X_i X_i}(\omega)$  is the one-sided power spectral density (PSD) function of the process  $X_i(t)$ .

Various analytical estimates have been examined through comparison with stationary responses of SDOF oscillators under simulated zero-mean, Gaussian, white noise processes (Lutes & Sarkani 1997). VanMarcke's formula (7.5) performs better than other available approximations, including the Poisson approximation in (7.3). VanMarcke's approximation provides accurate estimates, especially when the damping of the SDOF oscillator is not less than 5%.

### 7.3 JOINT FIRST-PASSAGE PROBABILITY

The joint first-passage probability of a vector process is defined as the probability that each member scalar process in the vector exceeds its respective safe threshold during the given period of time. Unlike the marginal first-passage probability, it is not straightforward to estimate this probability by use of crossing rates because the joint failure event is not represented by a single out-crossing of the vector process. However, using the inclusion-exclusion rule of probability, the joint probability can be represented by the sum of marginal and union probabilities of crossing events. For the union probabilities, the mean crossing rate of the vector process out of a safe domain is derived as the sum of the crossing rates of the processes over their respective double-barriers with finite dimensions. In order to account for dependence between the crossing events, the crossing rates of the envelope processes are employed. In the following, approximate formulas are derived for 2- and 3-dimensional vector processes. The proposed formulas can be generalized to vector processes with higher dimensions.

### 7.3.1 Joint First-Passage Probability of Two Processes

Consider a 2-dimensional vector process  $\mathbf{X}(t)$  with the scalar processes  $X_i(t)$  and  $X_j(t)$  as its elements. Its joint first-passage probability over the time interval  $t \in (0, \tau)$ , denoted,  $P_{ij}(a_i, a_j, \tau)$ , is defined as

$$P_{ij}(a_i, a_j, \tau) = P[(R_\tau^{(i)} > a_i) \cap (R_\tau^{(j)} > a_j)] \quad (7.7a)$$

$$R_\tau^{(i)} = \max_{0 \leq t \leq \tau} |X_i(t)| \quad \text{and} \quad R_\tau^{(j)} = \max_{0 \leq t \leq \tau} |X_j(t)| \quad (7.7b)$$

As illustrated in Figure 7.1, the joint first-passage event occurs when each process exceeds its own threshold at least once during the specified interval. In this case, the fact that the vector process enters a certain domain does not guarantee the occurrence of the joint failure event. Therefore, it is not straightforward to approximate the joint probability by mean crossing rates.

Applying the inclusion-exclusion rule in (6.7), (7.7a) can be written as

$$\begin{aligned} P_{ij}(a_i, a_j, \tau) &= P(R_\tau^{(i)} > a_i) + P(R_\tau^{(j)} > a_j) - P[(R_\tau^{(i)} > a_i) \cup (R_\tau^{(j)} > a_j)] \\ &= P_i(a_i, \tau) + P_j(a_j, \tau) - P_{i+j}(a_i, a_j, \tau) \end{aligned} \quad (7.8)$$

The probabilities  $P_i(a_i, \tau)$  and  $P_j(a_j, \tau)$  are approximated using (7.2) or (7.4).  $P_{i+j}(a_i, a_j, \tau)$  denotes the probability that the vector process out-crosses the rectangular domain  $\{(x_i, x_j) : |x_i| < a_i, |x_j| < a_j\}$  during the interval  $t \in (0, \tau)$ . In the following, two approximate formulas are developed for this probability by extending the formulas for the marginal first-passage probability described in the preceding section.

First, analogous to the Poisson assumption in (7.2),  $P_{i+j}$  is approximated by use of an unconditional mean out-crossing rate over the rectangle barrier. For a vector process  $\mathbf{X} = \{X_i(t), X_j(t)\}^T$ , this is given as

$$P_{i+j}(a_i, a_j, \tau) = 1 - A_{ij} \exp \left[ - \int_0^\tau v_{ij}(a_i, a_j, t) dt \right] \quad (7.9)$$

where  $A_{ij}$  is the probability that  $\mathbf{X}(t)$  is in the safe domain at  $t = 0$ . This is obtained from integration of the joint PDF of  $\mathbf{X}(0)$  in the safe domain.  $v_{ij}(a_i, a_j, t)$  is the unconditional mean out-

crossing rate of  $\mathbf{X}(t)$  over the rectangular domain shown in Figure 7.2a. This rate is written as the sum of two mean crossing rates of the scalar processes over their respective double-barriers with finite dimensions, as shown in Figure 7.2b and 7.2c. That is,

$$v_{ij}(a_i, a_j, t) = v_{i|j}(a_i, t | a_j) + v_{j|i}(a_j, t | a_i) \quad (7.10)$$

where  $v_{i|j}(a_i, t | a_j)$  and  $v_{j|i}(a_j, t | a_i)$  are the unconditional mean crossing rates of  $\mathbf{X}(t)$  over the finite edges defined by  $\{(x_i, x_j) : |x_i| = a_i, |x_j| < a_j\}$  and  $\{(x_i, x_j) : |x_i| < a_i, |x_j| = a_j\}$ , respectively. By applying the generalized Rice formula (Belyaev 1968), one can compute the crossing rate  $v_{i|j}(a_i, t | a_j)$  by the integration

$$v_{i|j}(a_i, t | a_j) = \int_{-a_j}^{a_j} \left[ - \int_{-\infty}^0 \dot{x}_i f_{X_i X_j \dot{X}_i}(-a_i, x_j, \dot{x}_i, t) d\dot{x}_i + \int_0^{\infty} \dot{x}_i f_{X_i X_j \dot{X}_i}(a_i, x_j, \dot{x}_i, t) d\dot{x}_i \right] dx_j \quad (7.11)$$

where  $f_{X_i X_j \dot{X}_i}(\cdot, \cdot, \cdot, t)$  denotes the joint PDF of  $X_i(t)$ ,  $X_j(t)$  and  $\dot{X}_i(t)$  at the same time instant. Using symmetry,  $v_{j|i}(a_j, t | a_i)$  is obtained by interchanging the indices  $i$  and  $j$  in (7.11). Substituting the first-passage probabilities from (7.2) and (7.9) into (7.8), one obtains the approximate joint first-passage probability. Hereafter we call this the *extended Poisson* approximation, since it neglects the dependence between the crossing events. Expressions for  $v_{i|j}(a_i | a_j)$  (independent of time) are derived in Appendix A for the case of a 2-dimensional stationary, zero-mean, Gaussian vector process. For this case,  $A_{ij}$  is given by

$$A_{ij} = \int_{-r_j}^{r_j} \int_{-r_i}^{r_i} \phi_2(u_i, u_j; \rho_{X_i X_j}) du_i du_j \quad (7.12)$$

where  $\phi_2$  denotes the bi-variate standard but correlated normal PDF and  $\rho_{X_i X_j}$  is the correlation coefficient between  $X_i(t)$  and  $X_j(t)$ .

An improved approximation is obtained by using (7.4) for  $P_i(a_i, \tau)$  and  $P_j(a_j, \tau)$ , and a similar approximation developed herein for  $P_{i+j}(a_i, a_j, \tau)$ . The latter approximation employs an exponential form analogous to (7.4),

$$P_{i+j}(a_i, a_j, \tau) = 1 - B_{ij} \exp \left[ - \int_0^\tau \eta_{ij}(a_i, a_j, t) dt \right] \quad (7.13)$$

where  $B_{ij}$  is the probability that the vector of envelope processes is inside the rectangular domain at  $t = 0$ . Appendix B derives expressions for the joint PDFs of the envelopes of two correlated zero-mean, stationary, Gaussian processes, which are used to compute  $B_{ij}$ .  $\eta_{ij}(a_i, a_j, t)$ , the crossing rate over a rectangle barrier that accounts for the clumping of the crossings, is approximated as

$$\eta_{ij}(a_i, a_j, t) = v_{ij}(a_i, t | a_j) \left[ \frac{\eta_i(a_i, t)}{v_i(a_i, t)} \right] + v_{ji}(a_j, t | a_i) \left[ \frac{\eta_j(a_j, t)}{v_j(a_j, t)} \right] \quad (7.14)$$

where the bracketed quotients are intended to account for the types of corrections that are inherent in VanMarcke's approximation of the marginal first-passage probabilities. Substituting the first-passage probabilities by (7.4) and (7.13) into (7.8), one obtains the joint first-passage probability, which approximately accounts for the dependence between the crossing events. Hereafter we call this the *extended VanMarcke* approximation.

### 7.3.2 Joint First-Passage Probability of Three Processes

For a 3-dimensional vector process  $\mathbf{X}(t) = \{X_i(t), X_j(t), X_k(t)\}$ , the joint first-passage probability over the time interval  $t \in (0, \tau)$ , denoted,  $P_{ijk}(a_i, a_j, a_k, \tau)$ , is defined as

$$P_{ijk}(a_i, a_j, a_k, \tau) = P[(R_\tau^{(i)} > a_i) \cap (R_\tau^{(j)} > a_j) \cap (R_\tau^{(k)} > a_k)] \quad (7.15)$$

Similar to the 2-dimensional case, this joint event is not represented by a single crossing event. Using the inclusion-exclusion rule in (6.7) for three events, the joint probability is written as

$$\begin{aligned} P_{ijk}(a_i, a_j, a_k, \tau) = & -P_i(a_i, \tau) - P_j(a_j, \tau) - P_k(a_k, \tau) \\ & + P_{ij}(a_i, a_j, \tau) + P_{ik}(a_i, a_k, \tau) + P_{jk}(a_j, a_k, \tau) \\ & + P_{i+j+k}(a_i, a_j, a_k, \tau) \end{aligned} \quad (7.16)$$

where  $P_{i+j+k}(a_i, a_j, a_k, \tau)$  denotes the probability that  $\mathbf{X}(t)$  out-crosses the cuboidal domain  $\{(x_i, x_j, x_k) : |x_i| < a_i, |x_j| < a_j, |x_k| < a_k\}$  during the interval  $t \in (0, \tau)$  and all other terms are as defined earlier. Substituting (7.8) into (7.16), one can describe the joint first-passage probability

in terms of the probabilities of crossing events in one-, two- and three-dimensional spaces as follows:

$$\begin{aligned}
P_{ijk}(a_i, a_j, a_k, \tau) &= P_i(a_i, \tau) + P_j(a_j, \tau) + P_k(a_k, \tau) \\
&\quad - P_{i+j}(a_i, a_j, \tau) - P_{i+k}(a_i, a_k, \tau) - P_{j+k}(a_j, a_k, \tau) \\
&\quad + P_{i+j+k}(a_i, a_j, a_k, \tau)
\end{aligned} \tag{7.17}$$

To obtain an *extended Poisson* approximation of  $P_{ijk}(a_i, a_j, a_k, \tau)$ ,  $P_i$ ,  $P_j$ ,  $P_k$  by (7.2) and  $P_{i+j}$ ,  $P_{i+k}$  and  $P_{j+k}$  by (7.9) are substituted into (7.17).  $P_{i+j+k}$  is approximated by use of an unconditional mean out-crossing rate over a cuboid-barrier. This is given as

$$P_{i+j+k}(a_i, a_j, a_k, \tau) = 1 - A_{ijk} \exp \left[ - \int_0^\tau v_{ijk}(a_i, a_j, a_k, t) dt \right] \tag{7.18}$$

where  $A_{ijk}$  is the probability that  $\mathbf{X}(t)$  is in the safe domain at  $t = 0$ . This is obtained from integration of the joint PDF of  $\mathbf{X}(0)$  inside the cuboidal domain.  $v_{ijk}(a_i, a_j, a_k, t)$  is the unconditional mean out-crossing rate of  $\mathbf{X}(t)$  over the cuboidal domain, shown in Figure 7.3a. This rate is written as the sum of three mean crossing rates of the individual processes over their respective double-barriers with finite dimensions, shown in Figure 7.3b, 7.3c and 7.3d. Specifically,

$$v_{ijk}(a_i, a_j, a_k, t) = v_{i|jk}(a_i, t | a_j, a_k) + v_{j|ik}(a_j, t | a_i, a_k) + v_{k|ij}(a_k, t | a_i, a_j) \tag{7.19}$$

where  $v_{i|jk}(a_i, t | a_j, a_k)$  denotes the unconditional mean crossing rate of  $X_i(t)$  over the finite edge defined by  $\{(x_i, x_j, x_k) : |x_i| = a_i, |x_j| < a_j, |x_k| < a_k\}$ . This is computed by the generalized Rice formula (Belyaev 1968)

$$\begin{aligned}
v_{i|jk}(a_i, t | a_j, a_k) &= \int_{-a_k}^{a_k} \int_{-a_j}^{a_j} \left[ - \int_{-\infty}^0 \dot{x}_i f_{X_i X_j X_k \dot{X}_i}(-a_i, x_j, x_k, \dot{x}_i, t) d\dot{x}_i \right. \\
&\quad \left. + \int_0^\infty \dot{x}_i f_{X_i X_j X_k \dot{X}_i}(a_i, x_j, x_k, \dot{x}_i, t) d\dot{x}_i \right] dx_j dx_k
\end{aligned} \tag{7.20}$$

where  $f_{X_i X_j X_k \dot{X}_i}(\cdot, \cdot, \cdot, \cdot, t)$  denotes the joint PDF of  $X_i(t)$ ,  $X_j(t)$ ,  $X_k(t)$  and  $\dot{X}_i(t)$ , all taken at the same time instant. Using symmetry,  $v_{j|ik}(a_j | a_i, a_k)$  and  $v_{k|ij}(a_k | a_i, a_j)$  are obtained by interchanging the indices in (7.20). The expression for  $v_{i|jk}(a_i | a_j, a_k)$  (independent of time) for the case of a 3-dimensional, stationary, zero-mean, Gaussian vector process are given in Appendix A.

In this case,  $A_{ijk}$  is obtained as the integral

$$A_{ijk} = \int_{-r_k}^{r_k} \int_{-r_j}^{r_j} \int_{-r_i}^{r_i} \varphi_3(u_i, u_j, u_k; \rho_{X_i X_j}, \rho_{X_i X_k}, \rho_{X_j X_k}) du_i du_j du_k \quad (7.21)$$

where  $\varphi_3$  denotes a tri-variate standard but correlated normal PDF.

To obtain an *extended VanMarcke* approximation of  $P_{ijk}(a_i, a_j, a_k, \tau)$ ,  $P_i$ ,  $P_j$ ,  $P_k$  by (7.4) and  $P_{i+j}$ ,  $P_{i+k}$  and  $P_{j+k}$  by (7.13) are substituted into (7.17). A similar approximation of  $P_{i+j+k}(a_i, a_j, a_k, \tau)$  employs the exponential form

$$P_{i+j+k}(a_i, a_j, a_k, \tau) = 1 - B_{ijk} \exp\left[-\int_0^\tau \eta_{ijk}(a_i, a_j, a_k, t) dt\right] \quad (7.22)$$

where  $B_{ijk}$  is the probability that the vector of envelope processes is inside the cuboidal domain at  $t=0$ , and  $\eta_{ijk}(a_i, a_j, a_k, t)$  is the crossing rate over the cuboidal barrier accounting for the clumping of the crossings. The latter is approximated as

$$\begin{aligned} \eta_{ijk}(a_i, a_j, a_k, t) = & v_{i|jk}(a_i, t | a_j, a_k) \left[ \frac{\eta_i(a_i, t)}{v_i(a_i, t)} \right] + v_{j|ik}(a_j, t | a_i, a_k) \left[ \frac{\eta_j(a_j, t)}{v_j(a_j, t)} \right] + \\ & v_{k|ij}(a_k, t | a_i, a_j) \left[ \frac{\eta_k(a_k, t)}{v_k(a_k, t)} \right] \end{aligned} \quad (7.23)$$

where the bracketed quotients account for the types of corrections inherent in VanMarcke's approximation. For application to a vector of more than two stationary, zero-mean, Gaussian processes, in Appendix C an approximate expression for the joint PDF of the envelopes of correlated stationary Gaussian processes is derived by use of the Nataf distribution.

#### 7.4 VERIFICATION BY MONTE CARLO SIMULATION

In this section, the proposed approximate formulas for the joint first passage probability of 2- and 3-dimensional vector processes are verified through comparisons with stationary responses of SDOF oscillators subjected to simulated stationary, zero-mean, Gaussian, white-noise processes.

### 7.4.1 Verification of Joint First-Passage Probability of Two Processes

Consider the displacement response processes  $X_i(t)$  and  $X_j(t)$  of two SDOF oscillators having natural frequencies  $f_i$  and  $f_j$ , respectively, and equal damping ratios  $\zeta_i = \zeta_j = \zeta$ . The oscillators are assumed to be subjected to a white-noise excitation having a one-sided power spectral density  $G_0 = 1$ . The expressions for the statistical moments of the displacement and velocity responses given in Appendix D are used to compute the approximate first-passage probability formulas. A total of 2,000 sample realizations of a white-noise process are generated, each having a duration of 60 seconds. For each sample, the displacements  $X_i(t)$  and  $X_j(t)$  of the two oscillators are numerically computed. The last 30 seconds of each displacement time history, where the response has effectively achieved full stationarity, is then used to observe the crossing events. Nine combinations of the frequencies and damping ratios are selected to investigate the effect of the bandwidth and the correlation between processes on the accuracy of the proposed formulas. Table 7.1 lists the parameter values and the statistical moments of the selected cases. As can be seen in this table, three categories of bandwidth (Narrow, Medium, Wide) and three categories of correlation coefficient between the processes (Low, Medium, High) are selected. The cases are named by their bandwidth and correlation categories. For example, ‘Narrow-Medium’ denotes the case with the narrow bandwidth  $\delta_i = \delta_j = 0.158$  and the medium correlation coefficient  $\rho_{X_i X_j} = 0.50$ .

Figure 7.4 compares the results based on the proposed approximations of the joint first-passage probability with the simulation results for the ‘Medium-Medium’ case. The shape factors of the displacement processes are  $\delta_i = \delta_j = 0.246$  and the correlation coefficient between the processes is  $\rho_{X_i X_j} = 0.5$ . All first-passage probabilities are computed with respect to three normalized levels:  $r_i = 1, 2$  and  $3$ . Figure 7.4a and 7.4b show the marginal first-passage probabilities  $P_i(a_i, \tau)$  and  $P_j(a_j, \tau)$ . It can be seen that the estimates based on VanMarcke’s formula are significantly more accurate than those based on the Poisson assumption. Figure 7.4c shows  $P_{i+j}(a_i, a_j, \tau)$ , the probability that the vector process out-crosses the rectangular domain. The accuracy of the extended VanMarcke formula in estimating this probability is similar to that of VanMarcke’s formula for the marginal probability estimates. Figure 7.4d compares the joint first-passage probabilities over the three levels. The extended Poisson formula leads to significant errors, whereas the extended VanMarcke formula provides excellent agreement with the

simulation results.

In order to examine the effects of the bandwidth and correlation on the accuracy of the proposed formulas, the natural frequencies and damping ratios of the two oscillators are varied. Figure 7.5a and 7.5b show the joint first-passage probabilities for ‘Medium-Low’ and ‘Medium-High’ cases, which are for correlation coefficient values  $\rho_{X_i X_j} = 0.1$  and  $0.9$ , respectively, with the medium shape factors  $\delta_i = \delta_j = 0.246$ . Comparing the results in Figure 7.4d, 7.5a and 7.5b, one concludes that the performance of the extended VanMarcke formula is not affected by this correlation coefficient between the processes. Next, Figure 7.5c and 7.5d show the joint first-passage probabilities for the ‘Narrow-Medium’ and ‘Wide-Medium’ cases, which are for the shape factors  $\delta_i = \delta_j = 0.158$  and  $0.339$  respectively, and the medium correlation coefficient  $\rho_{X_i X_j} = 0.5$ . Comparing the results in Figure 7.4d, 7.5c and 7.5d, one can see that the extended VanMarcke formula does not perform as well in the case of strongly narrow-band processes, but still leads to reasonably accurate estimates of the joint first-passage probability. The error in this case is inherited from the inaccuracy of VanMarcke’s formula for strongly narrow-band processes. As shown in Figure 7.6, the extended VanMarcke formula also provides reasonable accuracy for the ‘Narrow-Low’, ‘Narrow-High’, ‘Wide-Low’ and ‘Wide-High’ cases.

#### 7.4.2 Verification of Joint First-Passage Probability of Three Processes

We now consider three SDOF oscillators in order to examine the formulas proposed for a vector with three processes. An additional oscillator with frequency  $f_k$  and damping ratio  $\zeta_k$  is added to each case in Table 7.1 such that  $\rho_{X_i X_j} = \rho_{X_j X_k}$  and  $\zeta_i = \zeta_j = \zeta_k = \zeta$ . Table 7.2 lists the parameter values and the statistical moments for the selected cases.

Figure 7.7 compares the analytical estimates with the simulation results for the ‘Medium-Medium’ case. The shape factors of the displacement processes are  $\delta_i = \delta_j = \delta_k = 0.246$  and the correlation coefficients between the pairs of processes are  $\rho_{X_i X_j} = \rho_{X_j X_k} = 0.5$ . The marginal first-passage probabilities  $P_i(a_i, \tau)$  and  $P_j(a_j, \tau)$  are shown in Figure 7.4a and 7.4b. Although not shown here, the same level of accuracy is achieved for  $P_k(a_k, \tau)$ . Figures 7.7a and 7.7b show the comparisons for  $P_{i+k}(a_i, a_k, \tau)$  and  $P_{j+k}(a_j, a_k, \tau)$ , while  $P_{i+j}(a_i, a_j, \tau)$  can be seen in Figure 7.4c. Figure 7.7c shows  $P_{i+j+k}(a_i, a_j, a_k, \tau)$ , the probability that the vector process out-crosses the cuboidal domain. The accuracy of the extended VanMarcke formula in estimating this prob-



ability is similar to that of VanMarcke's formula for estimating marginal first-passage probabilities and the extended VanMarcke's formula for probabilities of out-crossings over a rectangular domain. Figure 7.7d compares the joint first-passage probabilities  $P_{ijk}(a_i, a_j, a_k, \tau)$  over the three levels. It is seen that the extended VanMarcke formula provides excellent agreement with the simulation results.

Similar to the case with two processes, the natural frequencies and damping ratios of the three oscillators are varied to examine the effects of the bandwidth and the correlation coefficient between the processes on the approximate formulas for the joint first-passage probability. Figures 7.8 and 7.9 show the eight cases for the different bandwidth and correlation coefficient categories. Careful examination of the results in these figures leads to the same observations as made for the case of two processes: (1) the extended VanMarcke approximation provides significantly improved accuracy when compared with the extended Poisson approximation; (2) the performance of the extended VanMarcke formula is not affected by the correlation coefficients between the pairs of processes; (3) the accuracy of the extended VanMarcke approximation deteriorates with decreasing bandwidth of the process, but it still leads to reasonably accurate estimates for the damping values considered.

## 7.5 APPLICATIONS TO ELECTRICAL SUBSTATION SYSTEMS

In chapter 6 of this report, linear programming (LP) was used to compute bounds on the reliability of a system for given marginal and joint component failure probabilities. Employing this approach, the proposed joint first-passage probability estimates can be used to compute narrow bounds on the failure probability of a system composed of structural components and subjected to stochastic excitation. In this section, this method is employed to compute the seismic reliability of an example electrical substation system.

Consider a simple electrical substation system consisting of five equipment items, as shown in Figure 7.10. Equipment items 1 and 2 and equipment items 3 and 4 are connected to each other by three identical assemblies of a rigid bus and an  $S$ -FSC. Other connections are assumed to be sufficiently flexible so as not to cause dynamic interaction. The ground acceleration is defined as a stationary process having the power spectral density in (4.22) with  $\omega_g = 5\pi$  rad/s and  $\zeta_g = 0.6$ ; the amplitude of the process,  $\Phi_0$ , is varied to compute the fragility of the system

as a function of the root-mean-square of the ground acceleration. The duration of the stationary response is assumed to be 20s. The equipment items have the parameter values (see Chapter 2 for the definition of these terms)  $m_1 = 438$  kg,  $m_2 = 210$  kg,  $m_3 = 403$  kg,  $m_4 = 193$  kg,  $m_5 = 200$  kg,  $l_i/m_i = 1.0$ ,  $\zeta_i = 0.02$  for  $i = 1, \dots, 5$ ,  $k_1 = k_3 = 158$  kN/m, and  $k_2 = k_4 = k_5 = 198$  kN/m. The S-FSC is described by a Bouc-Wen model having the parameters (see Chapter 3 for the definition of these terms)  $k_0 = 3 \times 8.58 = 25.7$  kN/m,  $\alpha = 0.206$ ,  $A = 1$ ,  $n = 1$ ,  $\beta = 0.175$  and  $\gamma = 0.176$ .

For each intensity level, the spectral moments  $\lambda_0$ ,  $\lambda_1$  and  $\lambda_2$  for each equipment item in the connected system are computed by nonlinear random vibration analysis using the ELM. The joint and marginal equipment failure probabilities,  $P_1, \dots, P_5, P_{12}, P_{13}, \dots, P_{45}$  are computed by the extended Poisson or the extended VanMarcke's formula. The prescribed safe displacement thresholds are  $\pm 7.62$  cm for equipment 1 and 3, and  $\pm 3.81$  cm for equipment 2, 4 and 5. By use of the LP methodology, probability bounds on the system failure event

$$E_{\text{system}} = E_1 E_3 \cup E_2 E_4 \cup E_1 E_4 E_5 \cup E_2 E_3 E_5 \quad (7.24)$$

are estimated employing only marginal and bi-component probabilities.

Figure 7.11 shows the fragility of each equipment item and the lower and upper bounds on the system fragility. For this example, the system probability bounds are practically coinciding.

Table 7.1 Parameters of two SDOF oscillators and statistical moments of the responses under white noise excitation ( $f_i = 2$  Hz)

Band-width ( $\delta / \zeta$ )	Narrow (0.158 / 0.02)			Medium (0.246 / 0.05)			Wide (0.339 / 0.10)		
	Low	Med	High	Low	Med	High	Low	Med	High
Correlation $\rho_{X_i X_j}$	0.10	0.50	0.90	0.10	0.50	0.90	0.10	0.50	0.90
$f_j$ (Hz)	2.25	2.08	2.03	2.69	2.21	2.07	3.57	2.44	2.14
$\sigma_{X_i}$	0.141	0.141	0.141	0.0890	0.0890	0.0890	0.0629	0.0629	0.0629
$\sigma_{X_j}$	0.118	0.133	0.138	0.0570	0.0766	0.0846	0.0264	0.0467	0.0569
$\sigma_{\dot{X}_i}$	1.77	1.77	1.77	1.12	1.12	1.12	0.791	0.791	0.791
$\sigma_{\dot{X}_j}$	1.67	1.73	1.76	0.964	1.06	1.10	0.592	0.716	0.765
$\rho_{\dot{X}_i X_j}$	0.319	0.510	0.302	0.347	0.525	0.305	0.392	0.550	0.309
$\rho_{X_i \dot{X}_j}$	-0.283	-0.490	-0.298	-0.258	-0.475	-0.295	-0.220	-0.450	-0.290

Table 7.2 Parameters of three SDOF oscillators and statistical moments of the responses under white noise excitation ( $f_i = 2$  Hz)

Bandwidth ( $\delta / \zeta$ )	Narrow (0.158 / 0.02)			Medium (0.246 / 0.05)			Wide (0.339 / 0.10)		
	Low (0.10)	Med (0.50)	High (0.90)	Low (0.10)	Med (0.50)	High (0.90)	Low (0.10)	Med (0.50)	High (0.90)
Correlation $\rho_{X_i X_j}$ , $\rho_{X_j X_k}$									
$f_j$ (Hz)	2.25	2.08	2.03	2.69	2.21	2.07	3.57	2.44	2.14
$f_k$ (Hz)	2.54	2.17	2.05	3.62	2.44	2.14	6.35	2.98	2.29
$\sigma_{X_i}$	0.141	0.141	0.141	0.0890	0.0890	0.0890	0.0629	0.0629	0.0629
$\sigma_{X_j}$	0.118	0.133	0.138	0.0570	0.0766	0.0846	0.0264	0.0467	0.0569
$\sigma_{X_k}$	0.0982	0.125	0.135	0.0365	0.0659	0.0805	0.0111	0.0347	0.0515
$\sigma_{\dot{X}_i}$	1.77	1.77	1.77	1.12	1.12	1.12	0.791	0.791	0.791
$\sigma_{\dot{X}_j}$	1.67	1.73	1.76	0.964	1.06	1.10	0.592	0.716	0.765
$\sigma_{\dot{X}_k}$	1.57	1.70	1.74	0.831	1.01	1.08	0.444	0.648	0.740
$\rho_{X_i X_k}$	0.0268	0.200	0.693	0.0257	0.199	0.693	0.0223	0.196	0.691
$\rho_{\dot{X}_i \dot{X}_j}$	0.319	0.510	0.302	0.347	0.525	0.305	0.392	0.550	0.309
$\rho_{\dot{X}_i \dot{X}_k}$	0.182	0.416	0.468	0.208	0.440	0.476	0.243	0.478	0.492
$\rho_{X_i \dot{X}_j}$	-0.283	-0.490	-0.298	-0.258	-0.475	-0.295	-0.220	-0.450	-0.290
$\rho_{\dot{X}_j X_k}$	0.318	0.510	0.302	0.346	0.525	0.304	0.392	0.550	0.310
$\rho_{X_i \dot{X}_k}$	-0.143	-0.384	-0.455	-0.115	-0.360	-0.446	-0.076	-0.321	-0.431
$\rho_{X_j \dot{X}_k}$	-0.282	-0.490	-0.298	-0.257	-0.475	-0.294	-0.220	-0.451	-0.290

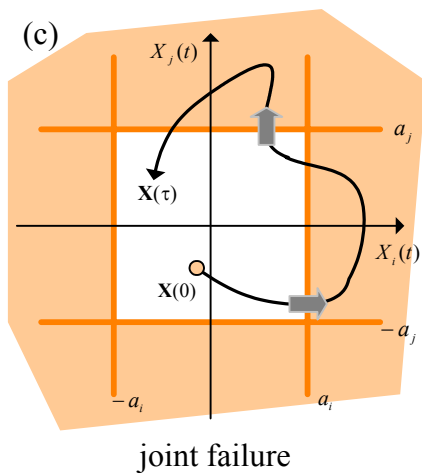
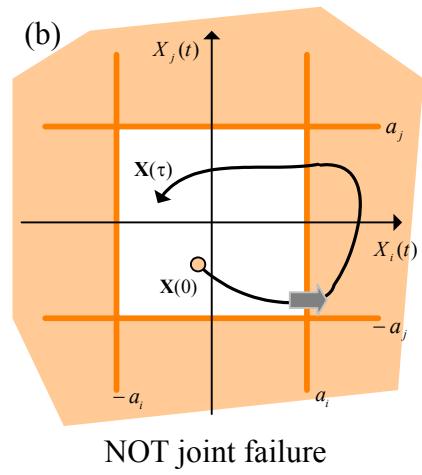
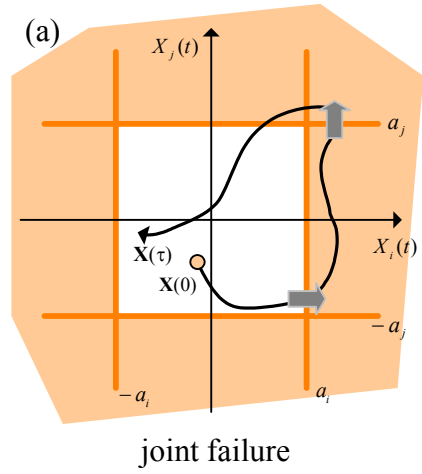


Figure 7.1 Trajectories of a vector process and relation to the joint failure event

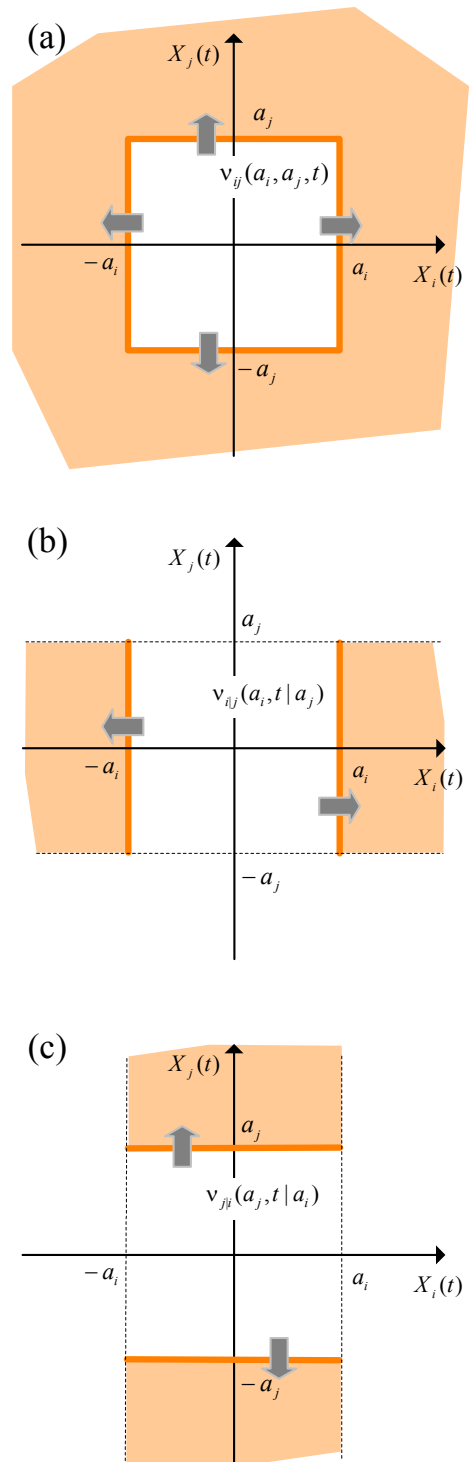


Figure 7.2 Unconditional mean crossing rates and corresponding thresholds for a 2-dimensional vector process

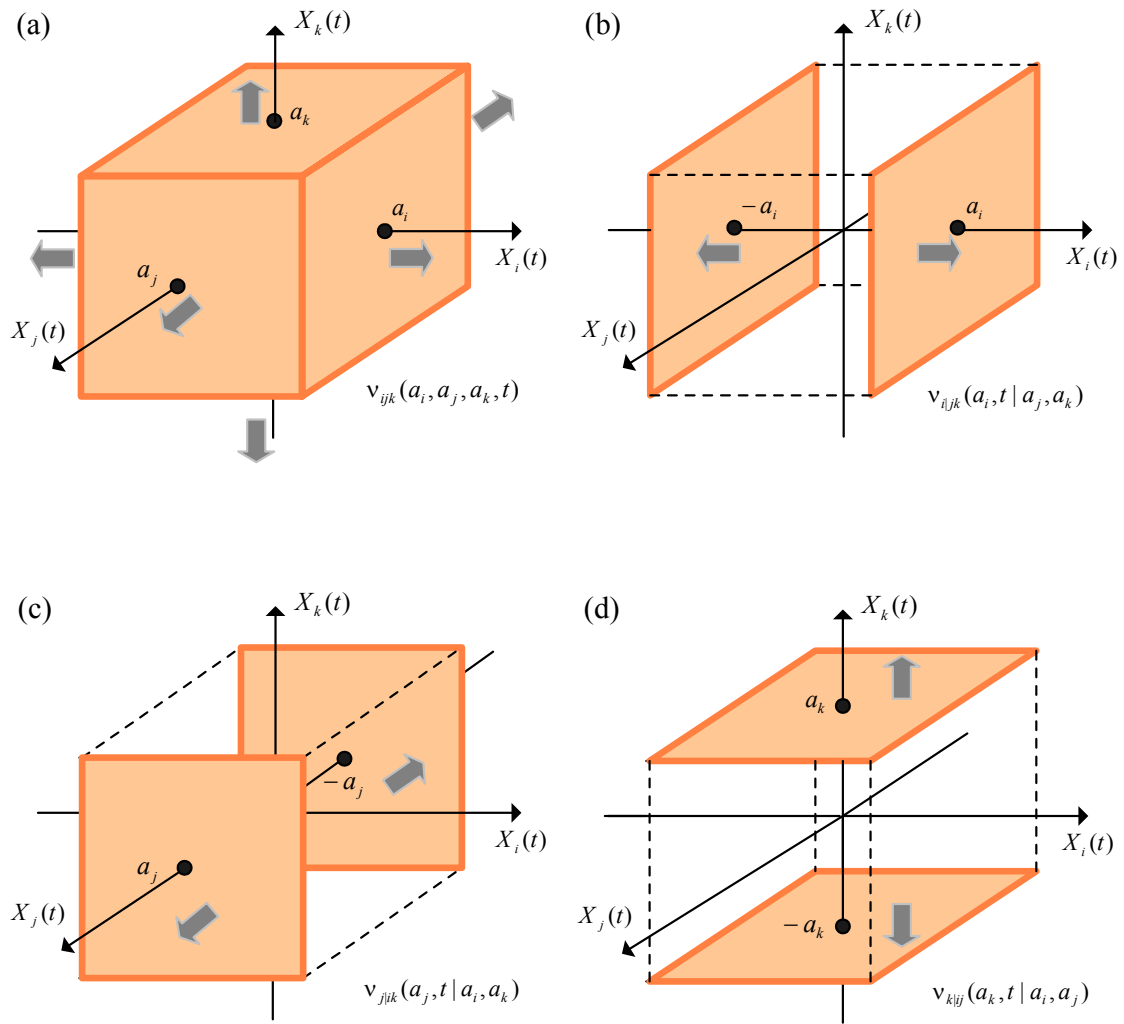


Figure 7.3 Unconditional mean crossing rates and corresponding thresholds for a 3-dimensional vector process

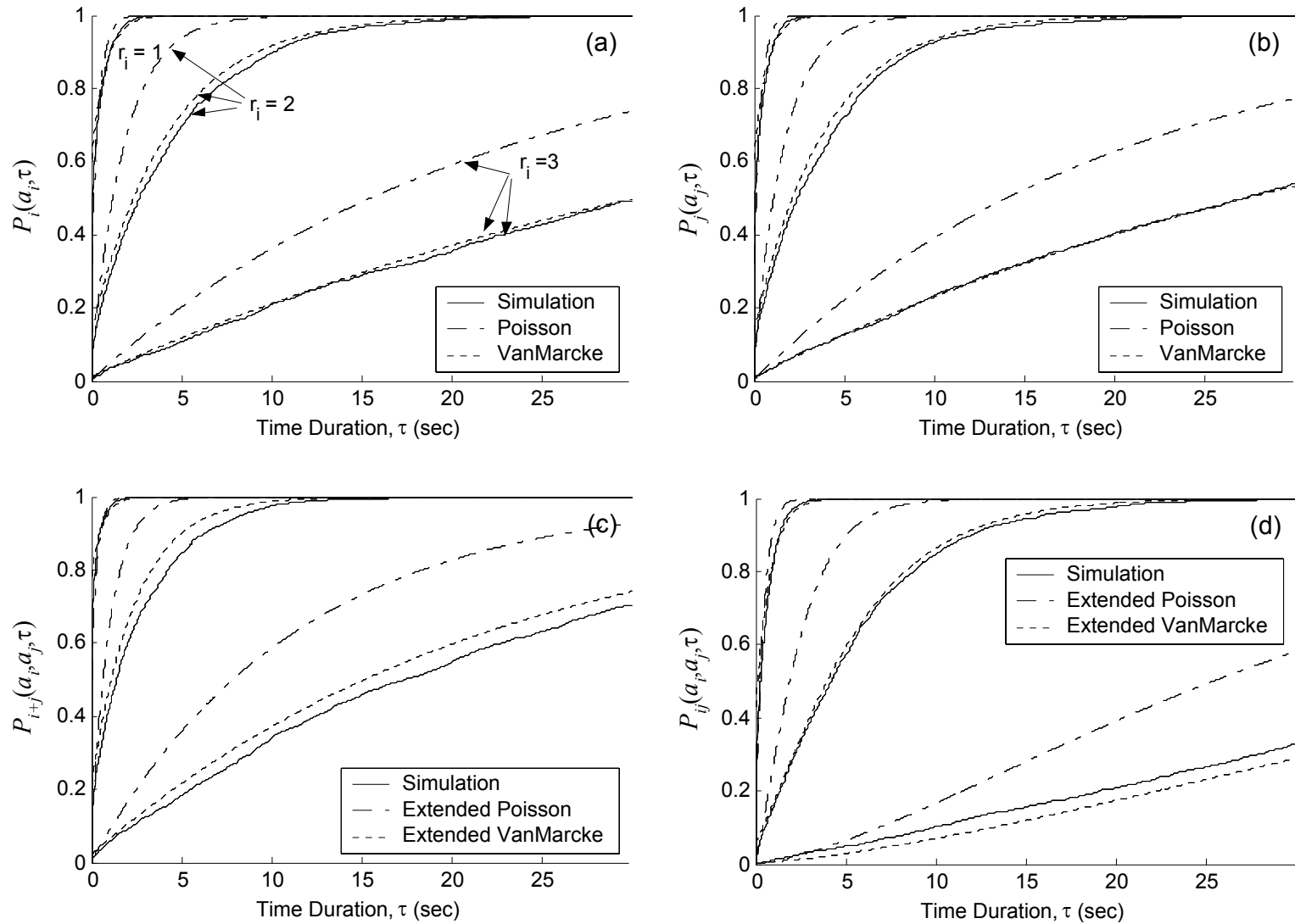


Figure 7.4 Comparison between analytical estimates and Monte Carlo simulation for the 'Medium-Medium' category of: (a)  $P_i(a_i, \tau)$ , (b)  $P_j(a_j, \tau)$ , (c)  $P_{i+j}(a_i, a_j, \tau)$ , (d)  $P_{ij}(a_i, a_j, \tau)$



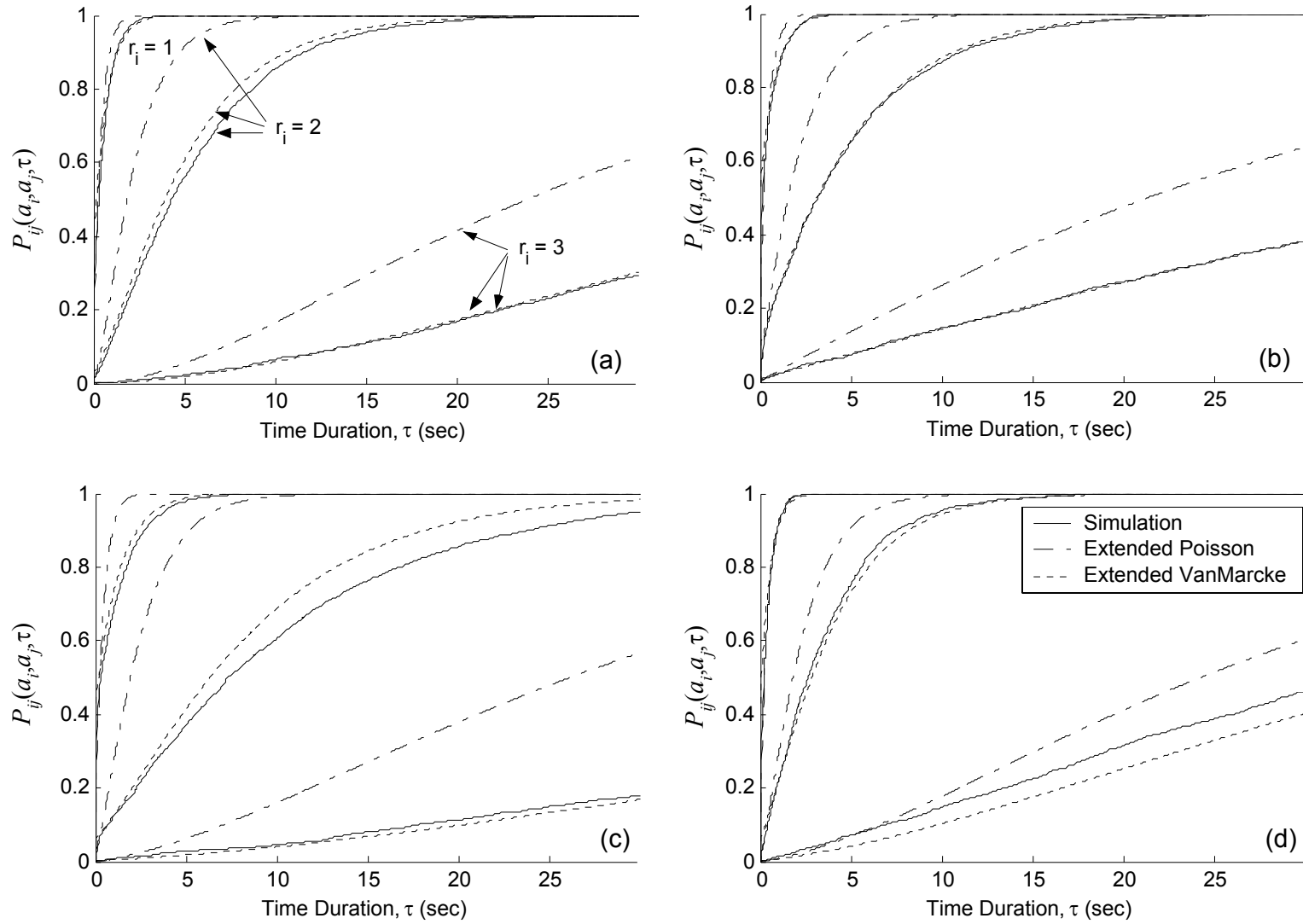


Figure 7.5 Joint first-passage probability  $P_{ij}(a_i, a_j, \tau)$  for (a) 'Medium-Low', (b) 'Medium-High', (c) 'Narrow-Medium', (d) 'Wide-Medium' categories

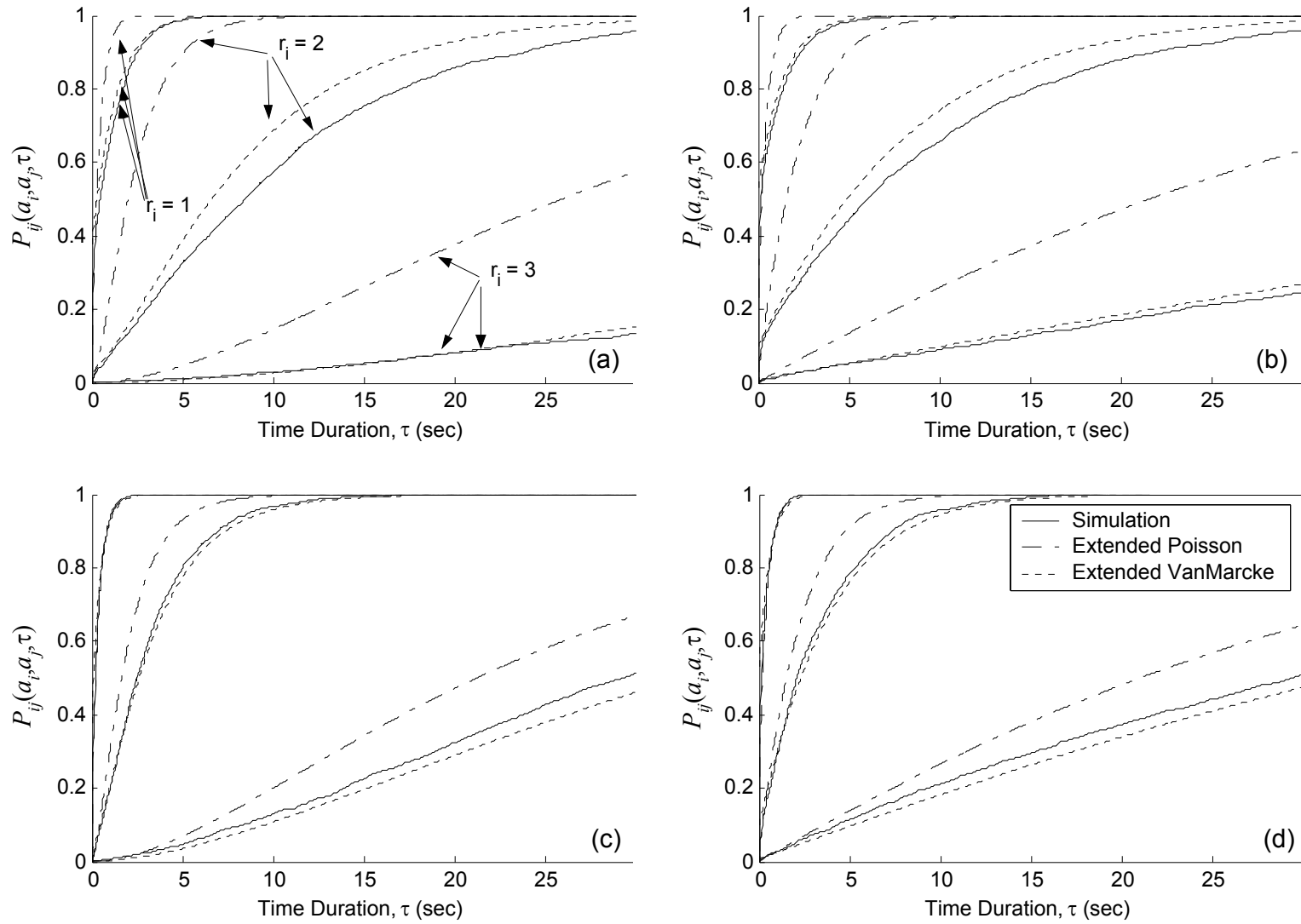


Figure 7.6 Joint first-passage probability  $P_{ij}(a_i, a_j, \tau)$  for (a) 'Narrow-Low', (b) 'Narrow-High', (c) 'Wide-Low', (d) 'Wide-High' categories

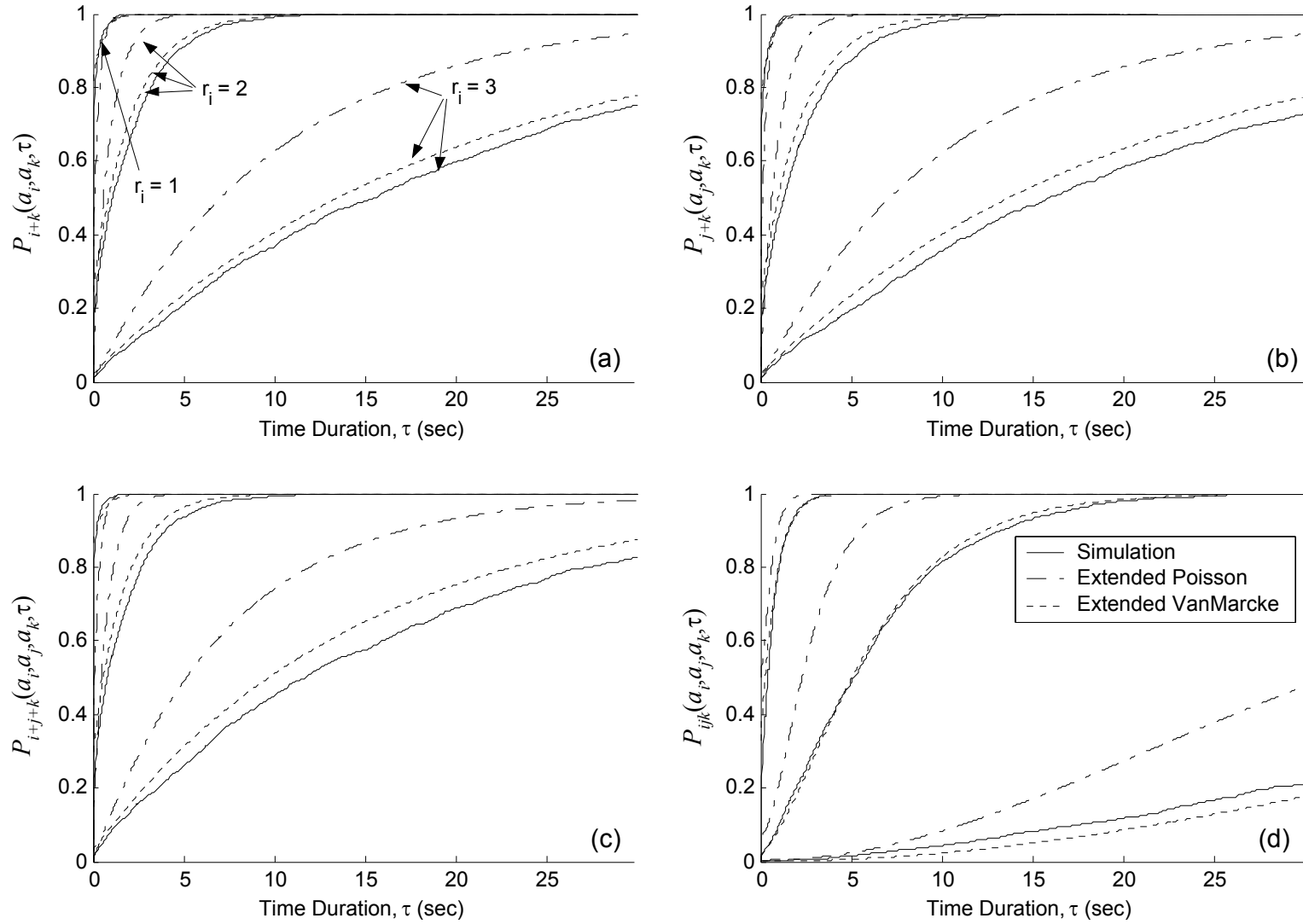


Figure 7.7 Comparison between analytical estimates and Monte Carlo simulation for the 'Medium-Medium' category: (a)  $P_{i+k}(a_i, a_k, \tau)$ , (b)  $P_{j+k}(a_j, a_k, \tau)$ , (c)  $P_{i+j+k}(a_i, a_j, a_k, \tau)$ , (d)  $P_{ijk}(a_i, a_j, a_k, \tau)$

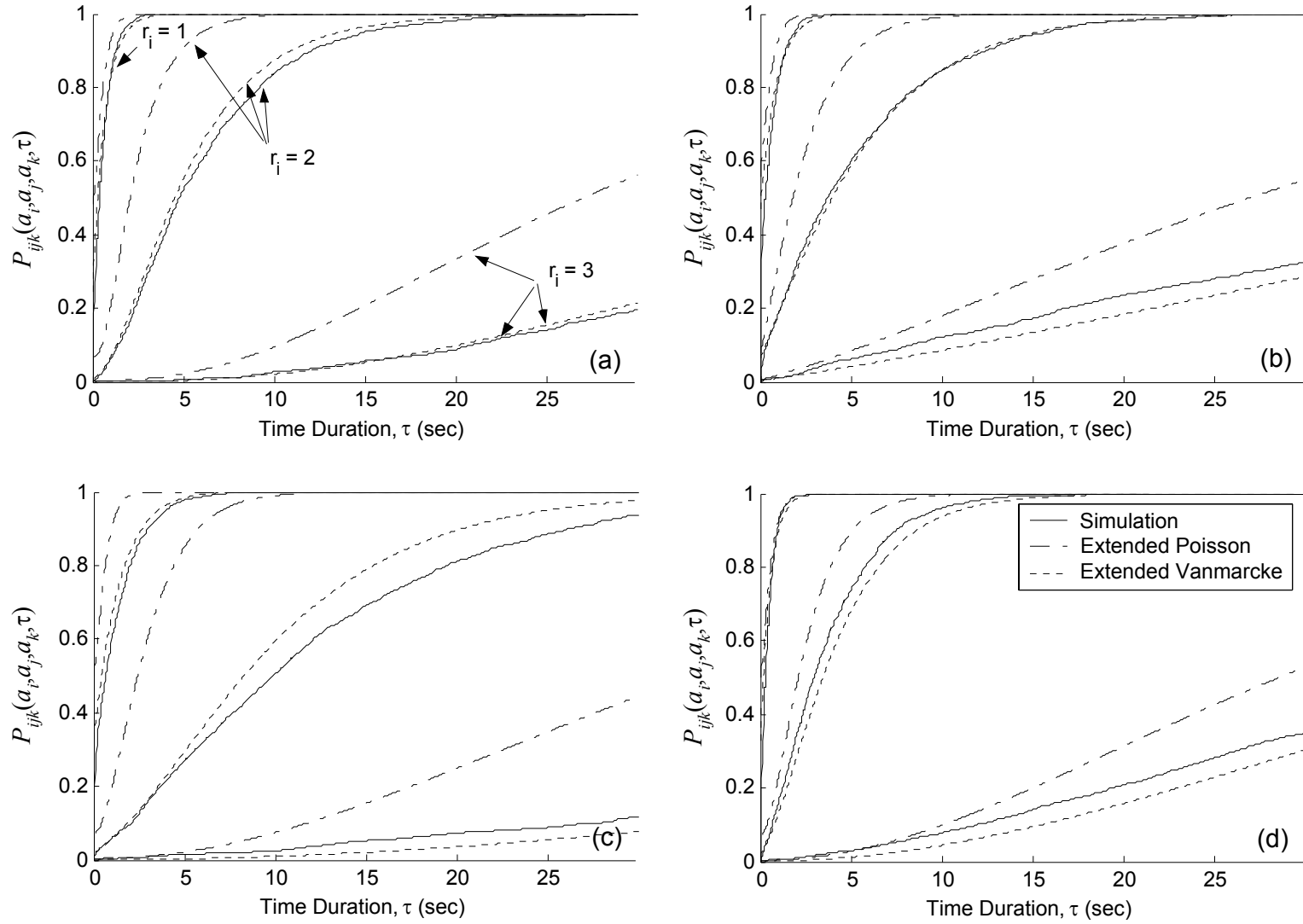


Figure 7.8 Joint first-passage probability  $P_{ijk}(a_i, a_j, a_k, \tau)$  for (a) 'Medium-Low', (b) 'Medium-High', (c) 'Narrow-Medium', (d) 'Wide-Medium' categories

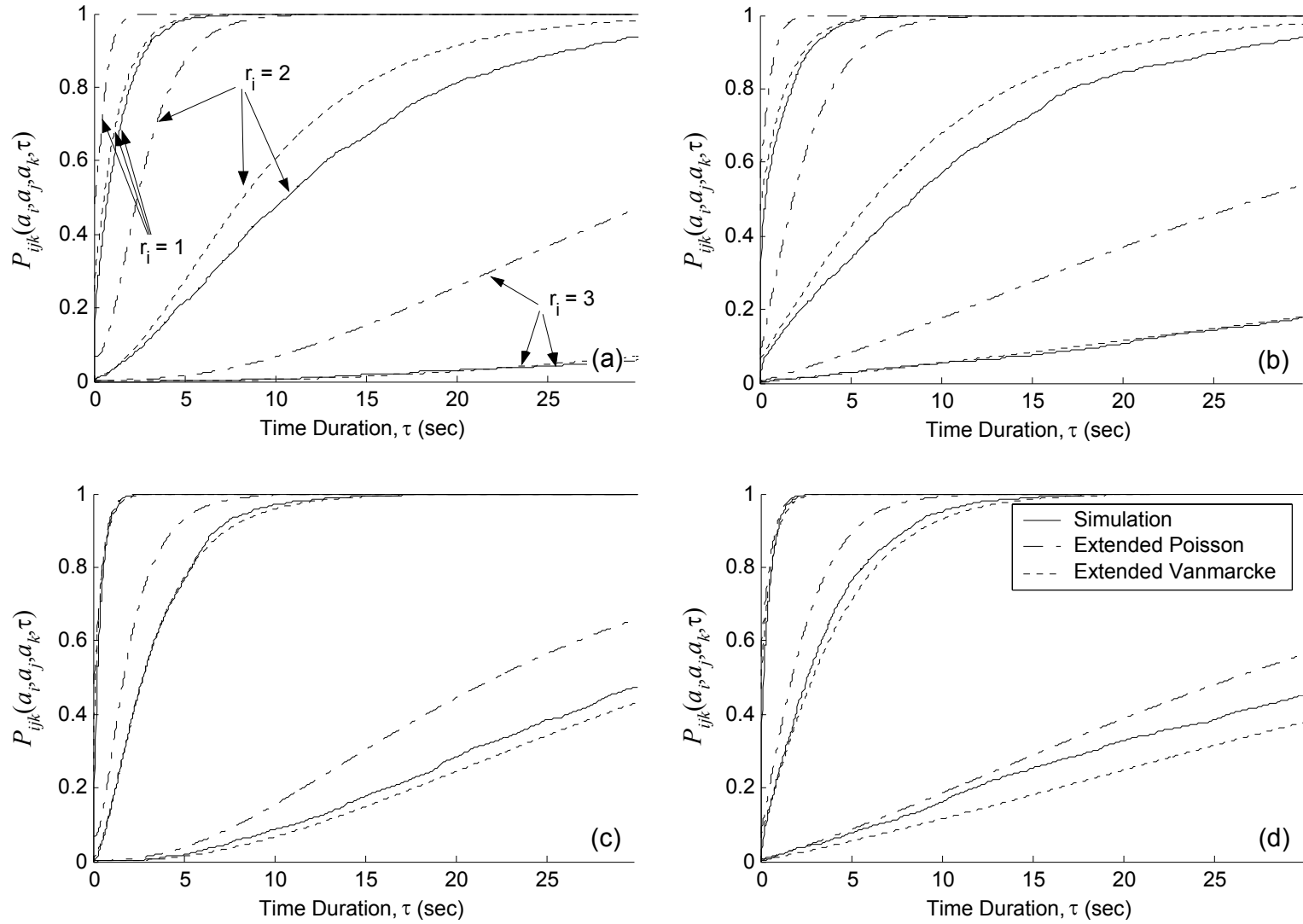


Figure 7.9 Joint first-passage probability  $P_{ijk}(a_i, a_j, a_k, \tau)$  for (a) 'Narrow-Low', (b) 'Narrow-High', (c) 'Wide-Low', (d) 'Wide-High' categories

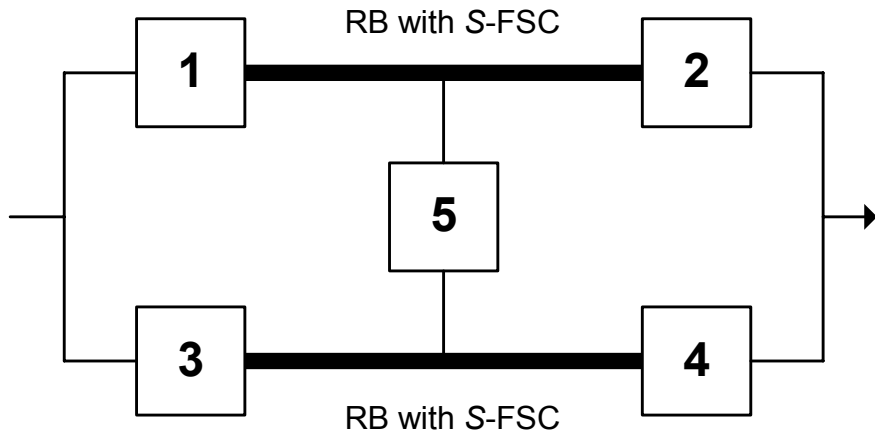


Figure 7.10 Substation system with five equipment items

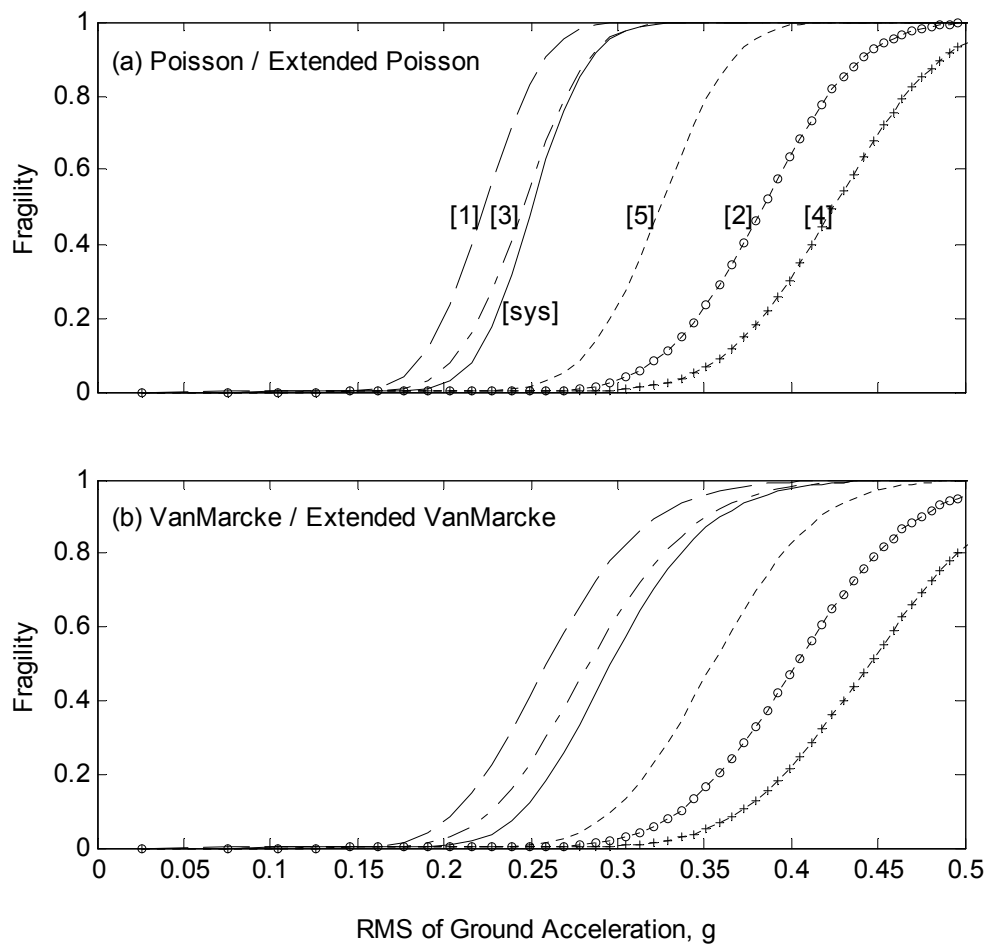


Figure 7.11 Equipment and system fragility estimates by (a) extended Poisson approximation; (b) extended VanMarcke approximation

## 8 Conclusions

### 8.1 SUMMARY OF MAJOR FINDINGS

This report develops analytical models and methods for assessing the seismic response of electrical substation equipment connected by assemblies of rigid bus and flexible connectors, and the reliability of electrical substation systems under stochastic earthquake loading. The results derived from the analytical models and methods are used to formulate practical design guidelines for reducing the adverse effect of dynamic interaction between connected equipment items under earthquake loading. Systematic methods for identifying critical components and cut sets in a system are also developed. The major findings of the study are summarized as follows:

- For the example connected system consisting of a disconnect switch and a bus support, the single-degree-of-freedom idealization of the equipment items provides reasonable approximations of the response ratios. The displacement shape under lateral self-weight is found to best represent the vibration of the equipment in the connected system. The example demonstrates wide variability in the estimated response ratios for different ground motions, which points to the need for stochastic modeling of the ground motion in the analysis of dynamic interaction between connected equipment items.
- A generalized Bouc-Wen model is newly developed to describe the hysteresis behavior of the existing flexible strap connectors (FSC). This model is capable of describing highly asymmetric hysteresis behavior with parameters that are invariant of the response. The hysteresis behaviors of the slider connector and the newly designed *S*-FSC are successfully described by a bi-linear differential equation model and the original Bouc-Wen model, respectively. The accuracy of these models in nonlinear dynamic analysis is verified through comparisons with the results of shake table tests or analytical estimates based on detailed finite element models.

- For the purpose of nonlinear random vibration analysis employing the equivalent linearization method (ELM), closed-form relations are derived for the coefficients of the equivalent linear system in terms of the second moments of the response for each hysteresis model. The ELM results, which are in close agreement with simulated time-history results, show significant reductions in the response ratios with increasing intensity of the ground motion. These are due to the softening and energy dissipation of the nonlinear rigid bus connectors.
- Using the ELM, an extensive parametric study on the dynamic interaction effect is performed, accounting for the nonlinear behavior of the rigid bus connectors and the stochastic nature of the ground motion. The influences of various structural parameters on the interaction effect are revealed by this parametric study. Based on these results, simple guidelines are suggested for reducing the hazardous effect of seismic interaction in practice.
- Electrical substation systems are usually too complex to be analyzed analytically, and the probability information on individual component items is often incomplete. The linear programming (LP) bounds are found to be useful for estimating and improving the reliability of these complex systems for any level of information on marginal- or joint-component probabilities. It is shown that the LP methodology can systematically identify the critical components and cut sets in a system. Once the bounds on the system failure probability are obtained by LP, simple calculations yield well-known importance measures, which provide the order of importance of the components or cut sets in terms of their contributions to the system failure probability.
- A new formulation is proposed to estimate the joint first-passage probability of a vector process. Monte Carlo simulations verify that the extended VanMarcke formulation provides accurate estimates on the joint first-passage probability of 2- and 3-dimensional vector process. The joint first-passage probability provides the means for obtaining narrow bounds on the reliability of general systems subjected to stochastic loading. An example application demonstrates the utility of this concept for assessing the reliability of electrical substation systems under stochastic earthquake loading.

## **8.2 RECOMMENDATIONS FOR FUTURE STUDIES**

In order to improve the applicability of the proposed methods in practice and to improve their



efficiency and accuracy, the following topics are recommended for future research.

- This study examined the effect of interaction between only two connected equipment items. The assembly of more than two interconnected equipment items is a more complicated system, which was not considered here. In some cases it is possible to combine several equipment items as a single SDOF system, which is then interacting with other such systems. An example is when two or more equipment items are connected by a run of rigid bus without a flexible connector. Due to the high axial rigidity of the rigid bus, the connected equipment items essentially move in a synchronized fashion and, therefore, can be idealized by a SDOF oscillator. However, more generally, multiply connected equipment items with flexible connectors must be modeled as multi-degree-of-freedom systems. While we believe the interaction results for two connected equipment items presented in this study provide good estimates of this effect, further studies are needed to better understand the nature of multiply interacting equipment items.
- Develop a method for assessing the reliability of large systems by use of the LP bounds methodology. The idea of employing “super-components” (see Chapter 6) to reduce the size of the LP problem should be explored. Specifically, it is desirable to develop a method for the optimal selection of “super-components,” which achieves the objective of problem size reduction, while minimizing the information loss.
- Develop a rigorous and practical decision framework for optimal upgrading of systems relative to specified performance and safety criteria and load hazard. This problem may take the form of a mixed integer-linear programming algorithm that aims at identifying the most effective and economical scheme for strengthening the components of a system to enhance its reliability, subject to prescribed constraints. Such an algorithm may also be used for developing optimal inspection and maintenance strategies for an electrical substation system.
- Improve the accuracy of the formulas for marginal and joint first-passage probability. As shown in Chapter 7, the accuracy of the formulas proposed for the joint first-passage probability is highly dependent upon the accuracy of the marginal first-passage probability formulas. Therefore, possible improvement of the marginal first-passage formula - especially for the case of strongly narrowband response - would lead to significant enhancement of the accuracy of the joint first-passage estimates as well.

- It would be highly desirable and instructive to apply the methods developed in this study to a real-world electrical substation system. Such an application would highlight the power and usefulness of these newly developed or extended methods, as well as identify shortcomings and areas needing further development. Furthermore, the system analysis methods developed in this study are applicable to any system, and applications to other lifelines may produce fruitful results. In particular, consideration may be given to applying these techniques to an entire power transmission network, or a subset of such a network, consisting of generation nodes, transmission lines, substations, and consumption nodes.

## REFERENCES

1. Anders, G.J. (1990). *Probability Concepts in Electric Power Systems*. J. Wiley & Sons, New York, NY.
2. ASCE. (1999) *Guide to Improved Earthquake Performance of Electric Power System*, Electric Power and Communications Committee Technical Council on Lifeline Earthquake Engineering (prepared), A.J. Schiff (edited). Reston: ASCE.
3. Atalik, T.S., and S. Utku (1976). Stochastic linearization of multi-degree-of-freedom nonlinear systems. *Journal of Earthquake Engineering and Structural Dynamics*, **4**: 411-420.
4. Baber, T.T., and M.N. Noori (1986). Modeling general hysteresis behavior and random vibration application. *Journal of Vibration, Acoustics, Stress and Reliability in Design*, **108**: 411-420.
5. Baber, T.T., and Y.K. Wen (1979). *Stochastic equivalent linearization for hysteretic, degrading, multistory structures*. Report UILU-ENG-80-2001. Urbana, Ill.: University of Illinois at Urbana-Champaign.
6. Bartels, R.H. and G.W. Stewart (1972). Solution of the matrix  $\mathbf{AX} + \mathbf{XB} = \mathbf{C}$ . *Communications of the ACM*, **15**(9): 820-826.
7. Bažant, Z. (1978). Endochronic inelasticity and incremental plasticity. *International Journal of Solid and Structure*, **14**: 691-714.
8. Belyaev, Y.K. (1968). On the number of exits across the boundary of a region by a vector stochastic process. *Theory of Probability and its Applications*, **13**: 320-324.
9. Bertsimas, D., and J.N. Tsitsiklis (1997). *Introduction to Linear Optimization*. Athena Scientific, Belmont, Mass.
10. Boole, G. (1854). *Laws of thought*, American reprint of 1854 ed. Dover, New York, NY.
11. Borgonovo, E., and G.E. Apostolakis (2001). A new importance measure for risk-informed decision making. *Reliability Engineering and System Safety*, **72**: 193-212.
12. Bouc, R. (1967). Forced vibration of mechanical system with hysteresis (Abstract). *Proceedings of 4th Conference on Nonlinear Oscillation*, Prague, Czechoslovakia.
13. Brown, R.E. (2002). *Electric Power Distribution Reliability*. Marcel Dekker Inc., New York,

NY.

14. Capecchi, D., and G. de Felice (2001). Hysteretic systems with internal variables. *Journal of Engineering Mechanics*, ASCE, **127**(9): 891-898.
15. Cheney, W., and D. Kincaid (1999). *Numerical Mathematics and Computing*, 4<sup>th</sup> edition. Brooks/Cole, Pacific Grove, CA.
16. Clough, R., and J. Penzien (1993). *Dynamics of Structures*. McGraw-Hill, New York, NY.
17. Cramer, H., and M.R. Leadbetter (1967). *Stationary and Related Stochastic Processes*. Wiley, New York, NY.
18. Crandall, S.H., and W.D. Mark (1963). *Random Vibration in Mechanical Systems*. Academic Press, New York, NY.
19. CSI, Inc. (1997). [http://www.csiberkeley.com/products\\_SAP.html](http://www.csiberkeley.com/products_SAP.html). Berkeley, CA.
20. Dantzig, G.B. (1951). Application of the simplex method to a transportation problem. *Activity analysis of production and allocation*, T.C. Koopmans, ed. Wiley, New York, NY.
21. Davenport, W.B., and W.L. Root (1958). *An Introduction to Theory of Random Signals and Noise*. McGraw-Hill, Inc., New York, NY.
22. Der Kiureghian, A. (2002). Bayesian method for seismic fragility assessment of lifeline components. *Acceptable Risk Processes – Lifelines and Natural Hazards*, ASCE: 61-77.
23. Der Kiureghian, A. (1981). A response spectrum method for random vibration analysis of MDF systems. *Earthquake Engineering and Structural Dynamics*, **9**(5): 419-435.
24. Der Kiureghian, A. (1980). Structural response to stationary excitation. *Journal of Engineering Mechanics Division*, ASCE, **106**(6): 1195-1213.
25. Der Kiureghian, A., J.L. Sackman, and K.-J. Hong (2001). Seismic interaction in linearly connected electrical substation equipment. *Earthquake Engineering and Structural Dynamics*, **30**: 327-347.
26. Der Kiureghian, A., J.L. Sackman, and K.-J. Hong (1999). *Interaction in interconnected electrical substation equipment subjected to earthquake ground motions*. PEER report 1999/01. Berkeley, Calif.: University of California.
27. Der Kiureghian, A., K.-J. Hong, and J.L. Sackman (2000). *Further studies on seismic inter-*

- action in interconnected electrical substation equipment*. PEER report 2000/01. Berkeley, Calif.: University of California.
28. Ditlevsen, O, and H.O. Madsen (1996). *Structural Reliability Methods*. J. Wiley & Sons, New York, NY.
  29. Ditlevsen, O. (1979). Narrow reliability bounds for structural systems. *Journal of Structural Mechanics*, **7**(4): 453-472.
  30. Fehlberg, E. (1969). Klassische Runge-Kutta formeln fünfter und siebenter ordnung mit schrittweitenkontrolle. *Computing*, **4**: 93-106.
  31. Filiatrault A., S. Kremmidas, A. Elgamal, and F. Seible (1999). *Substation equipment interaction – Rigid and flexible conductor studies*. Report SSRP-99/09. La Jolla, Calif.: Division of Structural Engineering, University of California, San Diego.
  32. Fréchet, M. (1935). Généralisations du théorème des probabilités totales, *Fund. Math.*, **25**: 379-387.
  33. Fussell, B.J. (1973). How to hand-calculate system reliability characteristics. *IEEE Trans. on Reliability*, **24**(3).
  34. Gilani, A.S., A.S. Whittaker, G.L. Fenves, C.-H. Chen, H. Ho, and E. Fujisaki (2000). *Seismic evaluation and analysis of 230-kV disconnect switches*. PEER report 2000/06. Berkeley, Calif.: University of California.
  35. Hailperin, T. (1965). Best possible inequalities for the probability of a logical function of events. *Am. Math. Monthly*, **72**(4): 343-359.
  36. Henley, E.J., and H. Kumamoto (1981). *Reliability Engineering and Risk Assessment*. Prentice-Hall, Inc., Englewood Cliffs, N.J.
  37. Hohenbichler, M., and R. Rackwitz (1983). First-order concepts in system reliability. *Structural Safety*, **1**(3): 177-188.
  38. Hunter, D. (1976). An upper bound for the probability of a union. *J. Appl. Prob.*, **13**: 597-603.
  39. Hurtado, J.E., and A.H. Barbat (2000). Equivalent linearization of the Bouc-Wen hysteretic model. *Engineering Structures*, **22**: 1121-1132.

40. Igusa, T., A. Der Kiureghian, and J.L. Sackman (1984). Modal decomposition method for stationary response of non-classically damped systems, *Earthquake Engineering and Structural Dynamics*, **12**(1): 121-136.
41. Kaul, M.K., and J. Penzien (1974). Stochastic analysis of yielding offshore towers. *Journal of Engineering Mechanics Division*, ASCE, **100**(5): 1025-1038.
42. Kimura, K., H. Yasumuro, and M. Sakata (1994). Non-Gaussian equivalent linearization for stationary random vibration of hysteretic system. *Probabilistic Engineering Mechanics*, **9**: 15-22.
43. Kounias, E.G. (1968). Bounds for the probability of a union, with applications. *Ann. Math. Stat.*, **39**(6): 2154-2158.
44. Kounias, S., and J. Marin (1976). Best linear Bonferroni Bounds. *SIAM (Soc. Ind. Appl. Math.) J. Appl. Math.*, **30**(2): 307-323.
45. Kozin, F. (1987). Parameter estimation and statistical linearization. *Stochastic Structural Mechanics*, Ed. Y.K. Lin and G.I. Schuëller, Springer-Verlag, Berlin, Germany.
46. Krylov, N., and N. Bogoliubov (1943). *Introduction to Nonlinear Mechanics*. Princeton University Press, New York, NY.
47. Lin, Y.K. (1967). *Probabilistic Theory of Structural Dynamics*. McGraw-Hill, New York, NY.
48. Liu, P.-L., and A. Der Kiureghian (1986). Multivariate distribution models with prescribed marginals and covariances. *Probabilistic Engineering Mechanics*, **1**(2): 105-112.
49. Lutes, L.D., and S. Sarkani (1997). *Stochastic Analysis of Structural and Mechanical Vibrations*. Prentice-Hall, Upper Saddle River, NJ.
50. Middleton, D. (1960). *An Introduction to Statistical Communication Theory*. McGraw-Hill, Inc., New York, NY.
51. Pradlwarter, H.J., and G.I. Schuëller (1991). The method of statistical equivalent linearization. *Structural Dynamics – Recent Advances*, Ed. G. I. Schuëller, Springer-Verlag, Berlin, Germany.
52. Prékopa, A. (1988). Boole-Bonferroni inequalities and linear programming. *Ope. Res.*, **36**(1): 145-162.

53. Rice, S.O. (1944&1945). Mathematical Analysis of Random Noise. *Bell System Technical Journal*, **23**: 282-332; **24**: 46-156.
54. Schuëller, G.I., M.D. Pandey, and H.J. Pradlwarter (1994). Equivalent linearization (EQL) in engineering practice for aseismic design. *Probabilistic Engineering Mechanics*, **9**: 95-102.
55. Sheppard, W.F. (1899). On the application of the theory of the error to cases of normal distribution and normal correlation. *Philosophical Transactions of the Royal Society of London, Series A*, **192**: 101-167.
56. Song, J., and A. Der Kiureghian (2003). Bounds on system reliability by linear programming. *Journal of Engineering Mechanics*, ASCE, **129**(6): 627-636.
57. Stearns, C., and A. Filiatrault (2003). *Electrical substation equipment interaction – Experimental rigid bus conductor studies*. Report SSRP-2003/11. La Jolla, Calif.: Division of Structural Engineering, University of California, San Diego.
58. VanMarcke, E.H. (1972). Properties of spectral moments with applications to random vibration. *Journal of Engineering Mechanics Division*, ASCE, **98**(2): 425-446.
59. VanMarcke, E.H. (1975). On the distribution of the first-passage time for normal stationary random processes. *Journal of Applied Mechanics*, ASME, **42**: 215-220.
60. Vinod, G., H.S. Kushwaha, A.K. Verma, and A. Srividya (2003). Importance measures in ranking piping components for risk informed in-service inspection. *Reliability Engineering and System Safety*, **80**: 107-113.
61. Wang, C.-H., and Y.K. Wen (1998). *Reliability and redundancy of pre-Northridge low-rise steel building under seismic excitation*. Report UILU-ENG-99-2002. Urbana, Ill.: University of Illinois at Urbana-Champaign.
62. Wen, Y.K. (1980). Equivalent linearization for hysteretic systems under random excitation. *Transactions of the ASME*, **47**: 150-154.
63. Wen, Y.K. (1976). Method for random vibration of hysteretic systems. *Journal of Engineering Mechanics Division*, ASCE, **102**(2): 249-263.
64. Zhang, Y.C. (1993). High-order reliability bounds for series systems and applications to structural systems. *Comput. Struct.*, **46**(2): 381-386.





## Appendix A Mean Crossing Rate of Vector Process over Finite Edges

Consider  $v_{ij}(a_i, t | a_j)$ , the mean crossing rate of a 2-dimensional vector process  $\mathbf{X} = \{X_i(t), X_j(t)\}$  over the finite edges defined by  $\{(x_i, x_j) : |x_i| = a_i, |x_j| < a_j\}$ . In the following, expressions for  $v_{ij}(a_i | a_j)$  (independent of time  $t$ ) are derived for the case of a zero-mean, stationary, Gaussian vector process.

By repeated conditioning of the joint probability density function (PDF) in (7.11), one can write for the mean rate

$$v_{ij}(a_i | a_j) = 2f_{X_i}(a_i) \int_{-a_j}^{a_j} f_{X_j|X_i}(x_j | a_i) \int_0^{\infty} \dot{x}_i f_{\dot{X}_i|X_i, X_j}(\dot{x}_i | a_i, x_j) d\dot{x}_i dx_j \quad (\text{A.1})$$

where  $f_{X_i}(x_i)$  denotes the marginal PDF of  $X_i(t)$ ,  $f_{X_j|X_i}(x_j | a_i)$  is the conditional PDF of  $X_j(t)$  given  $X_i(t) = a_i$ , and  $f_{\dot{X}_i|X_i, X_j}(\dot{x}_i | a_i, x_j)$  is the conditional PDF of  $\dot{X}_i(t)$  given  $X_i(t) = a_i$  and  $X_j(t) = x_j$ .

For a vector  $\mathbf{Y}$  of  $n$  jointly normal random variables, the joint PDF is given by

$$f_{\mathbf{Y}}(\mathbf{y}) = \frac{1}{(2\pi)^{n/2} \sqrt{\det \Sigma_{\mathbf{Y}\mathbf{Y}}}} \exp \left[ -\frac{1}{2} (\mathbf{y} - \mathbf{M}_{\mathbf{Y}})^T \Sigma_{\mathbf{Y}\mathbf{Y}}^{-1} (\mathbf{y} - \mathbf{M}_{\mathbf{Y}}) \right] \quad (\text{A.2})$$

where  $\mathbf{M}_{\mathbf{Y}}$  is the mean vector,  $\Sigma_{\mathbf{Y}\mathbf{Y}}$  is the covariance matrix, and  $\det \Sigma_{\mathbf{Y}\mathbf{Y}}$  denotes the determinant of  $\Sigma_{\mathbf{Y}\mathbf{Y}}$ . It is well known that any subset of  $\mathbf{Y}$  is also jointly normal. Suppose  $\mathbf{Y}$  is divided into two subsets  $\mathbf{Y}_1$  and  $\mathbf{Y}_2$  and the mean vector and covariance matrix are partitioned as

$$\mathbf{M}_{\mathbf{Y}} = \begin{Bmatrix} \mathbf{M}_1 \\ \text{---} \\ \mathbf{M}_2 \end{Bmatrix}, \quad \Sigma_{\mathbf{Y}\mathbf{Y}} = \begin{bmatrix} \Sigma_{11} & | & \Sigma_{12} \\ \text{---} & \text{---} & \text{---} \\ \Sigma_{21} & | & \Sigma_{22} \end{bmatrix} \quad (\text{A.3})$$

where  $\mathbf{M}_1$  (resp.  $\Sigma_{11}$ ) and  $\mathbf{M}_2$  (resp.  $\Sigma_{22}$ ) are the mean vectors (resp. covariance matrices) of  $\mathbf{Y}_1$  and  $\mathbf{Y}_2$ , respectively, and  $\Sigma_{12} = \Sigma_{21}^T$  is the covariance matrix of  $\mathbf{Y}_1$  and  $\mathbf{Y}_2$ . It is also well known that the conditional distribution of the subset  $\mathbf{Y}_1$  given  $\mathbf{Y}_2 = \mathbf{y}_2$  is jointly normal with the mean vector  $\mathbf{M}_{1|2}$  and covariance matrix  $\Sigma_{1|2}$  given by

$$\mathbf{M}_{1|2} = \mathbf{M}_1 + \Sigma_{12}\Sigma_{22}^{-1}(\mathbf{y}_2 - \mathbf{M}_2) \quad (\text{A.4a})$$

$$\Sigma_{1|2} = \Sigma_{11} - \Sigma_{12}\Sigma_{22}^{-1}\Sigma_{21} \quad (\text{A.4b})$$

In the case of a zero-mean, stationary, Gaussian process, therefore,  $f_{X_i}$ ,  $f_{X_j|X_i}$  and  $f_{\dot{X}_i|X_iX_j}$  in (A.1) are marginal PDF's of normal random variables. The means and standard deviations of  $f_{X_j|X_i}$  and  $f_{\dot{X}_i|X_iX_j}$  are computed by (A.4). Substituting these normal PDF's into (A.1) and analytically evaluating the integral over  $\dot{x}_i$ , one arrives at

$$v_{ij}(a_i | a_j) = \frac{2\phi(r_i)}{\sigma_{X_i}\sigma_{X_j}^{(i)}} \int_{-a_j}^{a_j} \phi\left(\frac{x_j - \mu_{X_j}^{(i)}}{\sigma_{X_j}^{(i)}}\right) \left[ \sigma_{\dot{X}_i}^{(ij)} \phi\left(\frac{\mu_{\dot{X}_i}^{(ij)}}{\sigma_{\dot{X}_i}^{(ij)}}\right) + \mu_{\dot{X}_i}^{(ij)} \Phi\left(\frac{\mu_{\dot{X}_i}^{(ij)}}{\sigma_{\dot{X}_i}^{(ij)}}\right) \right] dx_j \quad (\text{A.5})$$

where  $\phi$  and  $\Phi$  respective denote the PDF and cumulative distribution function (CDF) of the standard normal distribution,  $\sigma_{X_i}$  is the standard deviation of  $X_i(t)$ ,  $r_i = a_i/\sigma_{X_i}$  is the prescribed threshold normalized by the standard deviation, and

$$\mu_{X_j}^{(i)} \equiv E[X_j | X_i = a_i] = \frac{\sigma_{X_j}}{\sigma_{X_i}} \rho_{X_iX_j} a_i \quad (\text{A.6a})$$

$$\sigma_{X_j}^{(i)} \equiv \sqrt{\text{Var}[X_j | X_i = a_i]} = \sigma_{X_j} \sqrt{1 - \rho_{X_iX_j}^2} \quad (\text{A.6b})$$

$$\begin{aligned} \mu_{\dot{X}_i}^{(ij)} &\equiv E[\dot{X}_i | X_i = a_i, X_j = x_j] \\ &= \frac{\sigma_{\dot{X}_i}}{\sigma_{X_i}} \left( \frac{-\rho_{\dot{X}_iX_j} \rho_{X_iX_j}}{1 - \rho_{X_iX_j}^2} \right) a_i + \frac{\sigma_{\dot{X}_i}}{\sigma_{X_j}} \left( \frac{\rho_{\dot{X}_iX_j}}{1 - \rho_{X_iX_j}^2} \right) x_j \end{aligned} \quad (\text{A.6c})$$

$$\sigma_{\dot{X}_i}^{(ij)} \equiv \sqrt{\text{Var}[\dot{X}_i | X_i = a_i, X_j = x_j]} = \sigma_{\dot{X}_i} \sqrt{1 - \frac{\rho_{\dot{X}_iX_j}^2}{1 - \rho_{X_iX_j}^2}} \quad (\text{A.6d})$$

Next, consider  $v_{ijk}(a_i | a_j, a_k)$ , the mean crossing rate of a 3-dimensional zero-mean, sta-

tionary, Gaussian vector process  $\mathbf{X} = \{X_i(t), X_j(t), X_k(t)\}$  over the finite edges defined by  $\{(x_i, x_j) : |x_i| = a_i, |x_j| < a_j, |x_k| < a_k\}$ . By repeated conditioning of the joint PDF in (7.20), the crossing rate is written as

$$\begin{aligned} v_{ijk}(a_i | a_j, a_k) &= 2f_{X_i}(a_i) \times \\ &\int_{-a_j}^{a_j} f_{X_j|X_i}(x_j | a_i) \int_{-a_k}^{a_k} f_{X_k|X_i, X_j}(x_k | a_i, x_j) \int_0^{\infty} \dot{x}_i f_{\dot{X}_i|X_i, X_j, X_k}(\dot{x}_i | a_i, x_j, x_k) d\dot{x}_i dx_k dx_j \end{aligned} \quad (\text{A.7})$$

where  $f_{X_k|X_i, X_j}(x_k | a_i, x_j)$  denotes the conditional PDF of  $X_k(t)$  given  $X_i(t) = a_i$  and  $X_j(t) = x_j$ , and  $f_{\dot{X}_i|X_i, X_j, X_k}(\dot{x}_i | a_i, x_j, x_k)$  is the conditional PDF of  $\dot{X}_i(t)$  given  $X_i(t) = a_i$ ,  $X_j(t) = x_j$  and  $X_k(t) = x_k$ .

In the case of a zero-mean, stationary Gaussian vector process, all the marginal and conditional PDF's in (A.7) are normal. The means and standard deviations of the conditional PDF's are computed by (A.4). Substituting the normal PDF's in (A.7) and analytically evaluating the integral over  $\dot{x}_i$ , one can obtain

$$\begin{aligned} v_{ijk}(a_i | a_j, a_k) &= \frac{2\phi(a_i / \sigma_{X_i})}{\sigma_{X_i} \sigma_{X_j}^{(i)} \sigma_{X_k}^{(ij)}} \times \\ &\int_{-a_j}^{a_j} \phi\left(\frac{x_j - \mu_{X_j}^{(i)}}{\sigma_{X_j}^{(i)}}\right) \int_{-a_k}^{a_k} \phi\left(\frac{x_k - \mu_{X_k}^{(ij)}}{\sigma_{X_k}^{(ij)}}\right) \left[ \sigma_{\dot{X}_i}^{(ijk)} \phi\left(\frac{\mu_{\dot{X}_i}^{(ijk)}}{\sigma_{\dot{X}_i}^{(ijk)}}\right) + \mu_{\dot{X}_i}^{(ijk)} \Phi\left(\frac{\mu_{\dot{X}_i}^{(ijk)}}{\sigma_{\dot{X}_i}^{(ijk)}}\right) \right] dx_k dx_j \end{aligned} \quad (\text{A.8})$$

where

$$\begin{aligned} \mu_{X_k}^{(ij)} &\equiv E[X_k | X_i = a_i, X_j = x_j] \\ &= \frac{\sigma_{X_k}}{\sigma_{X_i}} \left( \frac{\rho_{X_i X_k} - \rho_{X_i X_j} \rho_{X_j X_k}}{1 - \rho_{X_i X_j}^2} \right) a_i + \frac{\sigma_{X_k}}{\sigma_{X_j}} \left( \frac{\rho_{X_j X_k} - \rho_{X_i X_k} \rho_{X_i X_j}}{1 - \rho_{X_i X_j}^2} \right) x_j \end{aligned} \quad (\text{A.9a})$$

$$\sigma_{X_k}^{(ij)} \equiv \sqrt{\text{Var}[X_k | X_i = a_i, X_j = x_j]} = \sigma_{X_k} \sqrt{\frac{\alpha}{1 - \rho_{X_i X_j}^2}} \quad (\text{A.9b})$$

$$\begin{aligned} \mu_{\dot{X}_i}^{(ijk)} &\equiv [\dot{X}_i | X_i = a_i, X_j = x_j, X_k = x_k] \\ &= \frac{\sigma_{\dot{X}_i}}{\alpha} \left( \frac{\alpha_i}{\sigma_{X_i}} a_i + \frac{\alpha_j}{\sigma_{X_j}} x_j + \frac{\alpha_k}{\sigma_{X_k}} x_k \right) \end{aligned} \quad (\text{A.9c})$$

$$\begin{aligned}
\sigma_{\dot{X}_i}^{(ijk)} &\equiv \sqrt{\text{Var}[\dot{X}_i | X_i = a_i, X_j = x_j, X_k = x_k]} \\
&= \sigma_{\dot{X}_i} \sqrt{1 - \frac{\rho_{\dot{X}_i X_j} \alpha_j + \rho_{\dot{X}_i X_k} \alpha_k}{\alpha}}
\end{aligned} \tag{A.9d}$$

in which

$$\alpha = 1 - \rho_{X_i X_j}^2 - \rho_{X_i X_k}^2 - \rho_{X_j X_k}^2 + 2\rho_{X_i X_j} \rho_{X_i X_k} \rho_{X_j X_k} \tag{A.10a}$$

$$\alpha_i = \rho_{\dot{X}_i X_j} (\rho_{X_j X_k} \rho_{X_i X_k} - \rho_{X_i X_j}) + \rho_{\dot{X}_i X_k} (\rho_{X_i X_j} \rho_{X_j X_k} - \rho_{X_i X_k}) \tag{A.10b}$$

$$\alpha_j = \rho_{\dot{X}_i X_j} (1 - \rho_{X_i X_k}^2) + \rho_{\dot{X}_i X_k} (\rho_{X_i X_j} \rho_{X_i X_k} - \rho_{X_j X_k}) \tag{A.10c}$$

$$\alpha_k = \rho_{\dot{X}_i X_j} (\rho_{X_i X_j} \rho_{X_i X_k} - \rho_{X_j X_k}) + \rho_{\dot{X}_i X_k} (1 - \rho_{X_i X_j}^2) \tag{A.10d}$$

In this study, the integrals in (A.5) and (A.8) are numerically evaluated once the statistics of the response vector process are known.

## Appendix B Joint Distribution of Envelopes of Two Gaussian Processes

A narrow-band random process  $X(t)$  can be represented in the form (Rice 1944 & 1945)

$$X(t) = E(t) \cos[\omega_c t + \Theta(t)] \quad (\text{B.1})$$

where  $E(t)$  is the envelope process,  $\omega_c$  is the central frequency around which the power spectral density is concentrated, and  $\Theta(t)$  is the phase process. When  $X(t)$  is a zero-mean, stationary, Gaussian process, the amplitude and phase processes can be defined as

$$E(t) = \sqrt{X(t)^2 + Z(t)^2} \quad (\text{B.2a})$$

$$\Theta(t) = \tan^{-1} \frac{Z(t)}{X(t)} - \omega_c t \quad (\text{B.2b})$$

where  $Z(t)$  is a conjugate process of  $X(t)$ . Various definitions of the envelope are available from alternative selections of  $Z(t)$ . The Cramer-Leadbetter envelope (Middleton 1960, Cramer & Leadbetter 1967) defines  $Z(t)$  as the Hilbert transform of  $X(t)$ . In that case, the conjugate process is given by

$$Z(t) = E(t) \sin[\omega_c t + \Theta(t)] \quad (\text{B.3})$$

It can be shown that  $Z(t)$  is also a zero-mean, stationary, Gaussian process, and  $X(t)$  and  $Z(t)$  are uncorrelated at the same time  $t$ .

Consider two zero-mean, correlated, stationary, Gaussian processes  $X_i(t)$  and  $X_j(t)$ . When the envelope processes defined by Cramer-Leadbetter are used,  $X_i(t)$  and  $X_j(t)$ , and their conjugate processes  $Z_i(t)$  and  $Z_j(t)$ , are represented as

$$X_i(t) = E_i(t) \cos[\omega_{c_i} t + \Theta_i(t)] \quad (\text{B.4a})$$

$$X_j(t) = E_j(t) \cos[\omega_{c_j} t + \Theta_j(t)] \quad (\text{B.4b})$$

$$Z_i(t) = E_i(t) \sin[\omega_{c_i} t + \Theta_i(t)] \quad (\text{B.4c})$$

$$Z_j(t) = E_j(t) \sin[\omega_{c_j} t + \Theta_j(t)] \quad (\text{B.4d})$$

In this case, the vector of processes  $\mathbf{Y} = [X_i(t) \ Z_i(t) \ X_j(t) \ Z_j(t)]^T$  is normal with a joint PDF as in (A.2) with

$$\Sigma_{\mathbf{Y}\mathbf{Y}} = \begin{bmatrix} \sigma_{X_i}^2 & 0 & R_{ij} & \hat{R}_{ij} \\ 0 & \sigma_{X_i}^2 & -\hat{R}_{ij} & R_{ij} \\ R_{ij} & -\hat{R}_{ij} & \sigma_{X_j}^2 & 0 \\ \hat{R}_{ij} & R_{ij} & 0 & \sigma_{X_j}^2 \end{bmatrix} \quad (\text{B.5})$$

and

$$\det \Sigma_{\mathbf{Y}\mathbf{Y}} = (\sigma_{X_i}^2 \sigma_{X_j}^2 - R_{ij}^2 - \hat{R}_{ij}^2)^2 \quad (\text{B.6})$$

where

$$R_{ij} \equiv E[X_i(t)X_j(t)] = \sigma_{X_i} \sigma_{X_j} \rho_{X_i X_j} \quad (\text{B.7a})$$

is the covariance of  $X_i(t)$  and  $X_j(t)$ , and

$$\hat{R}_{ij} \equiv E[X_i(t)Z_j(t)] = \int_0^\infty \text{Im}[G_{X_i X_j}(\omega)] d\omega \quad (\text{B.7b})$$

where  $\text{Im}(\cdot)$  denotes the imaginary part of a complex number and  $G_{X_i X_j}(\omega)$  is the one-sided cross-power spectral density function of  $X_i(t)$  and  $X_j(t)$ , is the covariance of  $X_i(t)$  and  $Z_j(t)$ .

The joint probability density function (PDF) of the envelope and phase processes  $E_i(t)$ ,  $E_j(t)$ ,  $\Theta_i(t)$  and  $\Theta_j(t)$ , denoted  $f_{E_i \Theta_i E_j \Theta_j}(e_i, \theta_i, e_j, \theta_j)$ , is obtained in terms of the joint PDF of  $\mathbf{Y}$ ,  $f_{\mathbf{Y}}(\mathbf{y}) = f_{X_i Z_i X_j Z_j}(x_i, z_i, x_j, z_j)$ , by applying the rules for transformation of random variables to (B.4). The result is

$$\begin{aligned}
f_{E_i \Theta_i E_j \Theta_j}(e_i, \theta_i, e_j, \theta_j) &= f_{X_i Z_i X_j Z_j}(x_i, z_i, x_j, z_j) \left| \det \mathbf{J}_{(x_i, z_i, x_j, z_j), (e_i, \theta_i, e_j, \theta_j)} \right| \\
&= \frac{e_i e_j}{4\pi^2 \sqrt{\det \boldsymbol{\Sigma}_{\mathbf{Y}\mathbf{Y}}}} \exp \left\{ -\frac{1}{2\sqrt{\det \boldsymbol{\Sigma}_{\mathbf{Y}\mathbf{Y}}}} \begin{bmatrix} \sigma_{X_i}^2 e_j^2 + \sigma_{X_j}^2 e_i^2 \\ -2R_{ij} e_i e_j \cos(\theta_j - \theta_i + \omega_{c_j} t - \omega_{c_i} t) \\ -2\hat{R}_{ij} e_i e_j \sin(\theta_j - \theta_i + \omega_{c_j} t - \omega_{c_i} t) \end{bmatrix} \right\} \\
&\quad 0 \leq e_i, e_j < \infty \quad \text{and} \quad 0 \leq \theta_i, \theta_j < 2\pi
\end{aligned} \tag{B.8}$$

where  $\mathbf{J}_{(x_i, z_i, x_j, z_j), (e_i, \theta_i, e_j, \theta_j)}$  denotes the Jacobian matrix of the transformation, whose elements are the partial derivatives of  $x_i$ ,  $z_i$ ,  $x_j$  and  $z_j$  with respect to  $e_i$ ,  $\theta_i$ ,  $e_j$  and  $\theta_j$ , as derived from (B.4).

Integrating the joint PDF in (B.8) with respect to  $\theta_i$  and  $\theta_j$  both over the interval  $[0, 2\pi)$ , one finally obtains the joint PDF of  $E_i(t)$  and  $E_j(t)$  as

$$\begin{aligned}
f_{E_i E_j}(e_i, e_j) &= \frac{e_i e_j}{\sqrt{\det \boldsymbol{\Sigma}_{\mathbf{Y}\mathbf{Y}}}} I_0 \left( \frac{e_i e_j \sqrt{R_{ij}^2 + \hat{R}_{ij}^2}}{\sqrt{\det \boldsymbol{\Sigma}_{\mathbf{Y}\mathbf{Y}}}} \right) \exp \left( -\frac{\sigma_{X_i}^2 e_j^2 + \sigma_{X_j}^2 e_i^2}{2\sqrt{\det \boldsymbol{\Sigma}_{\mathbf{Y}\mathbf{Y}}}} \right) \\
&\quad 0 \leq e_i, e_j < \infty
\end{aligned} \tag{B.9}$$

where  $I_0(\cdot)$  denotes the zeroth-order modified Bessel function of the first kind. One can easily show that the marginal distribution of each envelope is Rayleigh. This result is derived in an analogy to the joint PDF of the values of an envelope process at two different time points (Dav-  
enport & Root 1958, Middleton 1960).





## Appendix C Nataf Approximation of the Joint Distribution of Envelopes of Gaussian Processes

It is difficult to derive analytical expressions for the joint distribution of the envelopes of three or more processes. In this appendix, the Nataf joint distribution model (Liu & Der Kiureghian 1986) is used to construct an approximation to the joint distribution of the envelopes of any number of zero-mean, stationary, Gaussian processes. The exact distribution derived in Appendix B is used to examine the accuracy of this approximation for the envelopes of two processes.

In order to use the Nataf model for constructing the joint distribution, one needs to have the correlation coefficient between pairs of the envelopes. Consider two envelopes  $E_i(t)$  and  $E_j(t)$ . Using the bi-variate PDF of two envelope processes in (B.9), the expectation of  $E_i^\nu E_j^\eta$ , in which  $\nu$  and  $\eta$  are real numbers, is obtained as

$$\begin{aligned} E[E_i^\nu E_j^\eta] &= \int_0^\infty \int_0^\infty E_i^\nu E_j^\eta f_{E_i E_j}(e_i, e_j) de_i de_j \\ &= \sigma_{X_i}^\nu \sigma_{X_j}^\eta 2^{(\nu+\eta)/2} \Gamma(\nu/2 + 1) \Gamma(\eta/2 + 1) {}_2F_1(-\nu/2, -\eta/2; 1; k_{ij}^2) \end{aligned} \quad (C.1)$$

where  $\Gamma(\cdot)$  is the Gamma function,  ${}_2F_1$  denotes the Gauss hypergeometric function, and  $k_{ij}^2 = (R_{ij}^2 + \hat{R}_{ij}^2) / (\sigma_{X_i}^2 \sigma_{X_j}^2)$ , in which  $R_{ij}$  and  $\hat{R}_{ij}$  are as given in (B.7). This moment is analytically derived in an analogy to the derivation for the moment of the values of an envelope process at two different time points (Middleton 1960). When the Cramer-Leadbetter envelope is used, each envelope process has the Rayleigh marginal distribution

$$f_{E_i}(e_i) = \frac{e_i}{\sigma_{X_i}^2} \exp\left(-\frac{1}{2} \frac{e_i^2}{\sigma_{X_i}^2}\right) \quad (C.2)$$

The mean and standard deviation of  $E_i$  are

$$\mu_{E_i} = \sqrt{\frac{\pi}{2}} \sigma_{X_i} \quad (C.3)$$

$$\sigma_{E_i} = \sqrt{\frac{4-\pi}{2}} \sigma_{X_i} \quad (C.4)$$

The correlation coefficient between  $E_i$  and  $E_j$  is

$$\rho_{E_i E_j} = \frac{E[E_i E_j] - \mu_{E_i} \mu_{E_j}}{\sigma_{E_i} \sigma_{E_j}} \quad (C.5)$$

Substituting (C.1) with  $\nu = \eta = 1$ , (C.3) and (C.4) into (C.5), one obtains

$$\rho_{E_i E_j} = \frac{\pi}{4-\pi} \left[ {}_2F_1 \left( -\frac{1}{2}, -\frac{1}{2}; 1; k_{ij}^2 \right) - 1 \right] \quad (C.6)$$

The Nataf approximation of the joint PDF of  $n$  envelopes  $E_i$ ,  $i = 1, \dots, n$ , is given by (Liu & Der Kiureghian 1986)

$$f_{E_1 E_2 \dots E_n}(e_1, e_2, \dots, e_n) = f_{E_1}(e_1) f_{E_2}(e_2) \dots f_{E_n}(e_n) \frac{\varphi_n(\mathbf{u}; \mathbf{R}_0)}{\phi(u_1) \phi(u_2) \dots \phi(u_n)} \quad (C.7)$$

where  $\mathbf{u}$  is a vector with elements  $u_i = \Phi^{-1}[F_{E_i}(e_i)]$ ,  $i = 1, \dots, n$ , where  $\Phi^{-1}[\cdot]$  denotes the inverse of the standard normal cumulative distribution function (CDF),  $F_{E_i}(e_i)$  is the Rayleigh CDF of  $E_i$ ,  $\mathbf{R}_0$  is the correlation matrix of  $\mathbf{u}$ , and  $\phi(u_i)$  and  $\varphi_n(\mathbf{u}; \mathbf{R}_0)$  are the standard univariate and  $n$ -variate normal PDF's. The element  $\rho_{0,ij}$  of  $\mathbf{R}_0$  is related to the correlation coefficient  $\rho_{E_i E_j}$  of  $E_i$  and  $E_j$  through the double integral formula

$$\rho_{E_i E_j} = \int_{-\infty}^{\infty} \int_{-\infty}^{\infty} \left( \frac{e_i - \mu_{E_i}}{\sigma_{E_i}} \right) \left( \frac{e_j - \mu_{E_j}}{\sigma_{E_j}} \right) \varphi_2(u_i, u_j, \rho_{0,ij}) du_i du_j \quad (C.8)$$

For a given  $\rho_{E_i E_j}$  of (C.6), one can find the corresponding  $\rho_{0,ij}$  by iteratively solving (C.8) or using the approximate formulas developed by Liu and Der Kiureghian (1986). For the Rayleigh random variables  $E_i$  and  $E_j$ , the formula is

$$\rho_{0,ij} \cong \rho_{E_i E_j} (1.028 - 0.029 \rho_{E_i E_j}) \quad (C.9)$$

In order to examine the accuracy of the Nataf joint distribution for the envelopes, the

probability  $P_{i+j}(a_i, a_j, \tau)$  that a 2-dimensional, zero-mean, stationary Gaussian vector process out-crosses a rectangular domain during an interval of time  $t \in (0, \tau)$  are computed by use of (7.13) employing the exact bi-variate PDF in (B.9) and the approximate bi-variate PDF obtained by (C.7). The relative error  $\varepsilon_r$  is defined as

$$\varepsilon_r \equiv \frac{[1 - B_{ij}^{exact} \exp(-\eta_{ij}\tau)] - [1 - B_{ij}^{Nataf} \exp(-\eta_{ij}\tau)]}{[1 - B_{ij}^{exact} \exp(-\eta_{ij}\tau)]} \times 100 (\%) \quad (\text{C.10})$$

where  $B_{ij}^{exact}$  and  $B_{ij}^{Nataf}$  denote the probability that the vector of envelope processes is inside the rectangular domain at  $t = 0$ , computed by use of the exact and approximate bi-variate PDF's, respectively. The relative errors are computed for a total of 12 cases defined by the values of the mean number of out-crossings  $\eta_{ij}\tau$  and the aspect ratio  $r = (a_i / \sigma_{X_i}) / (a_j / \sigma_{X_j})$  of the rectangular domain. The specific values  $\eta_{ij}\tau = 0, 0.01, 0.1$  and  $1$ , and  $r = 1, 2$  and  $3$  are considered, and for each case the range of errors for the complete range of envelope correlation values  $0 \leq \rho_{E_i E_j} \leq 1$  is determined. Table C.1 lists the computed percent error values for each case. As expected, the errors are larger when the mean number of out-crossings is small, since in these cases the probability  $P_{i+j}(a_i, a_j, \tau)$  is dominated by the outcome at  $t = 0$ . The error is also larger and when the aspect ratio is close to 1, since in that case the probability is not dominated by one process. Error values are all small, with a maximum of slightly higher than 4% for  $\eta_{ij}\tau = 0$  and  $r = 1$  and values much smaller than 1% for  $\eta_{ij}\tau = 1$ . These results confirm that the Nataf model provides a good approximation of the bi-variate PDF of the envelopes for the purpose of computing the out-crossing probability of two processes. Although this examination is limited to the case of a 2-dimensional vector process, for which an exact solution of the bi-variate envelope distribution is available, we can conjecture that similar accuracy exists for higher-dimension cases.

Table C.1 Relative error  $\varepsilon_r$  (%) in estimate of  $P_{i+j}(a_i, a_j, \tau)$  based on the Nataf approximation of the bi-variate PDF of envelopes

$r \backslash \eta_{ij}\tau$	0	0.01	0.1	1.0
1	-4.31~2.31	-4.11~2.29	-2.86~2.07	-0.485~0.802
2	-0.551~1.52	-0.539~1.50	-0.451~1.37	-0.122~0.543
3	-0.0933~0.924	-0.919~0.914	-0.0806~0.833	-0.0262~0.332

## Appendix D Statistical Moments of Single-Degree-of-Freedom Oscillator Response to White Noise Input

Consider two single-degree-of-freedom (SDOF) oscillators having natural frequencies  $f_i$  and  $f_j$ , damping ratios  $\zeta_i$  and  $\zeta_j$ , and subjected to a zero-mean, stationary, white-noise base acceleration having a one-sided power spectral density  $G_0$ . In the following, the statistical moments of the stationary displacement responses  $X_i(t)$  and  $X_j(t)$  are presented. Most of these results are readily available in the literature.

The frequency-response function of the displacement  $X_i(t)$  relative to a base acceleration input is given by

$$H_i(\omega) = \frac{1}{\omega_i^2 - \omega^2 + 2i\zeta_i\omega_i\omega} \quad (\text{D.1})$$

where  $\omega_i = f_i/(2\pi)$  and  $i = \sqrt{-1}$ . The standard deviations of  $X_i(t)$  and  $\dot{X}_i(t)$  are the square-roots of the zeroth- and second-order spectral moments of  $X_i(t)$ , respectively:

$$\sigma_{X_i} = \sqrt{\lambda_{0,i}} = \left( \int_0^\infty |H_i(\omega)|^2 G_0 d\omega \right)^{1/2} = \left( \frac{\pi G_0}{4\zeta_i\omega_i^3} \right)^{1/2} \quad (\text{D.2})$$

$$\sigma_{\dot{X}_i} = \sqrt{\lambda_{2,i}} = \left( \int_0^\infty \omega^2 |H_i(\omega)|^2 G_0 d\omega \right)^{1/2} = \left( \frac{\pi G_0}{4\zeta_i\omega_i} \right)^{1/2} \quad (\text{D.3})$$

The standard deviations of  $X_j(t)$  and  $\dot{X}_j(t)$  can be obtained by replacing the index  $i$  in (D.2) and (D.3) with  $j$ .

The cross-correlation function of  $X_i(t)$  and  $X_j(t)$  is defined as

$$\begin{aligned}
R_{X_i X_j}(\tau) &= E[X_i(t)X_j(t-\tau)] \\
&= \frac{1}{2} \int_{-\infty}^{\infty} G_0 H_i(\omega) H_j^*(\omega) e^{i\omega\tau} d\omega
\end{aligned} \tag{D.4}$$

where  $H_j^*(\omega)$  denotes the complex conjugate of  $H_j(\omega)$ . When  $X_i(t)$  and  $X_j(t)$  are zero-mean processes, the correlation coefficient between them is given as (Igusa *et al.* 1984)

$$\begin{aligned}
\rho_{X_i X_j} &= \frac{R_{X_i X_j}(0)}{\sigma_{X_i} \sigma_{X_j}} \\
&= \frac{8\sqrt{\zeta_i \zeta_j \omega_i \omega_j} (\zeta_i \omega_i + \zeta_j \omega_j) \omega_i \omega_j}{(\omega_i^2 - \omega_j^2)^2 + 4\zeta_i \zeta_j \omega_i \omega_j (\omega_i^2 + \omega_j^2) + 4(\zeta_i^2 + \zeta_j^2) \omega_i^2 \omega_j^2}
\end{aligned} \tag{D.5}$$

The cross-correlation function between  $X_i(t)$  and  $\dot{X}_j(t)$  is obtained by differentiating  $R_{X_i X_j}(\tau)$ :

$$R_{X_i \dot{X}_j}(\tau) = -\frac{d}{d\tau} R_{X_i X_j}(\tau) \tag{D.6}$$

Therefore, the correlation coefficient  $\rho_{X_i \dot{X}_j}$  is derived as

$$\begin{aligned}
\rho_{X_i \dot{X}_j} &= \frac{R_{X_i \dot{X}_j}(0)}{\sigma_{X_i} \sigma_{\dot{X}_j}} \\
&= \frac{-dR_{X_i X_j}(\tau)/d\tau|_{\tau=0}}{\sigma_{X_i} \sigma_{\dot{X}_j}} \\
&= \frac{-4\sqrt{\zeta_i \zeta_j \omega_i^3 \omega_j} [(\zeta_i \omega_i + \zeta_j \omega_j)^2 - 2\zeta_i \omega_i (\zeta_i \omega_i + \zeta_j \omega_j) - (\omega_{D_i}^2 - \omega_{D_j}^2)]}{(\zeta_i \omega_i + \zeta_j \omega_j)^4 + 2(\omega_{D_i}^2 + \omega_{D_j}^2)(\zeta_i \omega_i + \zeta_j \omega_j)^2 + (\omega_{D_i}^2 - \omega_{D_j}^2)^2}
\end{aligned} \tag{D.7}$$

where  $\omega_{D_i} = \omega_i \sqrt{1 - \zeta_i^2}$  and  $\omega_{D_j} = \omega_j \sqrt{1 - \zeta_j^2}$ . The correlation coefficient  $\rho_{\dot{X}_i X_j}$  is obtained by interchanging the indices  $i$  and  $j$  in (D.7).

The shape factor of  $X_i(t)$  is defined as

$$\delta_i = \left( 1 - \frac{\lambda_{1,i}^2}{\lambda_{0,i} \lambda_{2,i}} \right)^{1/2} \tag{D.8}$$

Substituting the spectral moments  $\lambda_{0,i}$ ,  $\lambda_{1,i}$  and  $\lambda_{2,i}$  computed by use of the frequency response function into (D.8), one obtains (Igusa *et al.* 1984)

$$\delta_i = \left\{ 1 - \frac{4}{\pi^2(1-\zeta_i^2)} \left[ \tan^{-1} \left( \frac{\sqrt{1-\zeta_i^2}}{\zeta_i} \right) \right]^2 \right\}^{1/2} \quad (\text{D.9})$$

For small values of  $\zeta_i$ , the above expression can be approximated by  $2(\zeta_i / \pi)^{1/2}$  (VanMarcke 1972).